

Reynolds Stress Model for Hypersonic Flows

Von der Fakultät für Maschinenwesen der
Rheinisch-Westfälischen Technischen Hochschule Aachen
zur Erlangung des akademischen Grades
einer Doktorin der Ingenieurwissenschaften

vorgelegt von
Arianna Bosco

Berichter: Univ.-Prof. M. Behr, Ph.D.
apl. Prof. Dr. rer. nat. S. Müller

Tag der mündlichen Prüfung: 27. Mai 2011

“Diese Dissertation ist auf den Internetseiten der Hochschulbibliothek online
verfügbar.”

Acknowledgement

I would like to express my gratitude to Prof. Marek Behr who agreed to be my supervisor. A particular thanks goes to Birgit Reinartz, for her guidance through the three years of my PhD, for her encouragements, her inexhaustible patience and for being a source of inspiration as a scientist and as a woman. A big thank you to Siegfried Müller for his time, his help and his corrections. To my colleagues Martin Krause, Gero Schieffer and Frank Bramkamp for their invaluable help and support and for sharing my frustration, a big thank you.

I would like to thank Prof. Russel Boyce for inviting me to Brisbane; Fabrice Schloegel and Melrose Brown for their help in the preparation of the experimental campaign. A special thanks to four fantastic persons without whom I would have never been able to successfully conduct the experiment and survive to the T4 stress: Keith, Grant, James and Tom, you have helped, encouraged and praised me well beyond your duty as co-workers and friends and made me have a great time despite the hard work.

I would like to thank mum, dad and Giulia for being an inexhaustible source of inspiration and encouragement and for coming to visit me around the world. A special thanks to my friends at AICES Francesca and Markus, for the lunches and coffee breaks together and for listening to my complaints and to my friends at home who have no idea of what I am doing but are strongly convinced that I am doing it well.

The Financial support from the Deutsche Forschungsgemeinschaft (German Research Association) through grant GSC 111, the Forschungszentrum Jülich and the Rechenzentrum of RWTH Aachen are gratefully acknowledged.

Contents

1. Introduction	1
2. Hypersonic flows: a Brief Review	5
2.1. Main Characteristics of Hypersonic Flows	5
2.1.1. Thin Shock Layer and Shock-Shock Interaction	5
2.1.2. Entropy Layer	5
2.1.3. High Temperature Flows	7
2.1.4. Viscous Effects	7
2.2. Shock Wave/Boundary Layer Interaction (SWBLI)	9
2.2.1. SWBLI on a Compression Corner Configuration	10
2.2.2. Impinging-Reflecting Shock Wave	15
2.3. Turbulence Modeling in Hypersonic Flows	15
2.3.1. Experimental Databases	16
2.3.2. LES and DNS of SWBLI	17
2.3.3. Main RANS Results for Hypersonic 2D SWBLI	17
3. Physical Modeling of Turbulent Compressible Flows	21
3.1. The Navier-Stokes Equations	21
3.2. Material Laws and Thermodynamic Relations	21
3.3. Turbulent Flows	22
3.4. Reynolds Averaged Navier-Stokes Equations	25
3.4.1. RANS Equations for Compressible Flows	26
3.4.2. Closure for RANS Equations	27
3.4.3. Reynolds Stress Models	29
3.4.4. Eddy Viscosity Models	32
3.5. SSG/LRR- ω Model	33
3.5.1. Additional Terms	36
3.5.2. Boundary Conditions at Solid Walls	37
3.6. Reynolds Stress Models versus Eddy Viscosity Models	38
4. QUADFLOW code	39
4.1. General Features	39
4.1.1. Turbulence and Transition Models	40
4.1.2. Multiscale Analysis for Grid Adaptation	41
4.2. Computational Approach for the RSM	42

4.2.1.	Numerical Methods	42
4.2.2.	Initial and Boundary Conditions	43
4.2.3.	Convergence Criteria	45
4.3.	RSM Implementation	46
4.3.1.	Non-Dimensional Form of the RSM Equations	46
4.3.2.	Source Terms	47
4.3.3.	Turbulence Contribution to the Mean Flow	48
4.3.4.	Realizability Constraints	48
4.3.5.	Adaptive Simulations	49
5.	Model Validation	51
5.1.	Definition of Non-Dimensional Variables	51
5.2.	Model Sensitivity Studies	51
5.2.1.	Freestream Turbulence	52
5.2.2.	Grid Considerations	53
5.2.3.	ω -wall Condition	59
5.2.4.	Adaptive Simulations: Threshold Value and Refinement Levels	60
5.3.	Validation Results	64
5.3.1.	Hypersonic Flow over a Flat Plate	65
5.3.2.	Supersonic Flow over a Flat Plate	66
5.3.3.	Subsonic Flow over a Flat Plate	68
5.3.4.	Hypersonic Flow over a Double Wedge	70
5.3.5.	Comparison Between Adaptive and Structured Grids	75
6.	Scramjet Results	77
6.1.	Experimental Settings	78
6.2.	Numerical Approach	78
6.2.1.	2D Results	81
6.2.2.	3D Results	86
7.	Three-dimensional hypersonic SWBLI	93
7.1.	Experimental Investigation of a Compression Corner	93
7.1.1.	T4 Shock Tunnel	93
7.1.2.	Operating and Freestream Conditions	94
7.1.3.	Freestream Non-Uniformities	95
7.1.4.	Experimental Model and Sensors	97
7.1.5.	Analysis and Postprocessing Tools	102
7.2.	Numerical Approach	104
7.3.	40 degrees Compression Corner Results	104
7.3.1.	40 degrees 6 mm Condition with Boundary Layer Trip	108
7.3.2.	40 degrees 3 mm Condition with Boundary Layer Trip	117
7.3.3.	40 degrees 6 mm Condition without Boundary Layer Trip	120

7.3.4.	40 degrees 3 mm Condition without Boundary Layer Trip	122
7.4.	15 degrees Compression Corner Results	124
7.4.1.	15 degrees 6 mm Condition with Boundary Layer Trip	125
7.4.2.	15 degrees 3 mm Condition with Boundary Layer Trip	129
7.4.3.	15 degrees 6 mm Condition without Boundary Layer Trip	131
7.4.4.	15 degrees 3 mm Condition without Boundary Layer Trip	134
7.5.	Investigation Using an Adaptive Procedure	137
8.	Conclusions	141
A.	Sensor Positions	143
B.	Thermocouples Calibration	147
	Bibliography	149

List of Symbols

Scalar Variables

δ	: Boundary layer thickness
C_D	: Cross-diffusion term for ω
c	: Sound speed
c_p	: Specific heat at constant pressure, pressure coefficient
c_v	: Specific heat at constant volume
CFL	: Courant-Friedrichs-Levy number
D^ω	: Destruction of ω
d	: distance from the wall
e	: Specific internal energy
E	: Specific total energy
ϵ	: Turbulence dissipation rate, Adaptive threshold
γ	: Specific heat ratio
H	: Total specific enthalpy
I	: Turbulence intensity
k	: Turbulent kinetic energy
II	: Second invariant of the anisotropy tensor
L	: Separation length, Refinement level
λ_θ	: Thermal conductivity
μ	: Molecular viscosity
μ_t	: Turbulent viscosity
ω	: Specific turbulence dissipation rate
P^ω	: Production of ω
p	: Pressure
Q	: Heat flux
q_i	: Component of heat flux vector
$q_k^{(t)}$: Turbulent heat flux
R	: Radius, Specific gas constant
ρ	: Density
t	: Time
T	: Temperature
T_S	: Constant of Sutherland law
u_τ	: Shear stress velocity
u_i	: Velocity component

- visc – ratio : Ratio of turbulent to laminar viscosity
 x_i : Cartesian coordinates component
 x, y, z : Cartesian coordinates

Vector Notations

- \mathbf{u} : Velocity vector
 \mathbf{x} : Position vector

Tensor notations

- b_{ij} : Anisotropy tensor
 D_{ij} : Diffusion tensor for the Reynolds stresses
 ϵ_{ij} : Destruction tensor for the Reynolds stresses
 M_{ij} : Turbulent mass flux tensor for the Reynolds stresses
 Π_{ij} : Re-distribution tensor for the Reynolds stresses
 P_{ij} : Production tensor for the Reynolds stresses
 S_{ij} : Strain rate tensor
 \tilde{R}_{ij} : Reynolds stress tensor
 τ_{ij} : Viscous stress tensor
 W_{ij} : Rotation tensor

Operators

- $\frac{\partial \bullet}{\partial \bullet}$: Partial derivative
 $\frac{\partial \bullet}{\partial n}$: Partial derivative in normal direction

Dimensionless numbers

- M : Mach number
 Pr : Prandtl number
 Re : Reynolds number
 Re_x : Reynolds number based on the length x
 Re_θ : Boundary Layer momentum thickness Reynolds number, $\rho\theta U_\infty/\mu$

Superscripts

- ' : Reynolds fluctuation
- " : Favre fluctuation
- : Reynolds average
- ~ : Favre average
- ^ : Non-dimensional variable

Subscripts

- ∞ : Free stream value
- 0 ; Value at the interaction origin
- , • : Partial derivative
- ref* : Reference quantity
- x, y, z* : Cartesian coordinates
- w* : Wall data

1. Introduction

The study of hypersonic flows has been of interest for more than 50 years now. The main application in the field of hypersonics is the realization of a supersonic combustion ramjet (Scramjet), a propulsion system that operates above Mach 5 and at approximately 30-40 km altitude. As opposed to classical rockets, the air-breathing Scramjet does not need to carry oxygen for the combustion because this is taken directly from the atmosphere. The engine weight is therefore reduced and the payload mass can be increased, thus guaranteeing a cheaper access to space. One major impediment to the realization of such an engine lies in the uncertainties related to its design.

During the years, intense numerical analyses have been conducted on different hypersonic configurations. However, despite the improvement in computer power that allowed computational fluid dynamics (CFD) to be considered as a tool complementary to wind tunnel and flight test in the aircraft industry, its use for the prediction of hypersonic flows and in particular of heat fluxes, peak heating and flow separation is still far from satisfactory. For the aerodynamic design of hypersonic inlets, where large separations reduce the captured mass flow and thus the engine efficiency and severe heat loads can lead to structural failure, the correct prediction of these phenomena is critical to the overall performance and, thus, the realization of such engines.

Due to the high Reynolds number for hypersonic flight conditions, turbulence has to be taken into account. The lack of a satisfactory understanding of turbulence is one of the great fundamental challenges in flow simulations. When turbulent hypersonic flows are characterized by shock wave/boundary layer interaction (SWBLI), as it is always the case for practical applications, the only affordable numerical tool of investigation is the Reynolds Averaged Navier-Stokes method (RANS). This is a statistical approach to turbulence, where the conservative variables are divided into a mean and a fluctuating component and then the transport equations are averaged. From the averaging process, new variables, representing the contribution of turbulence to the mean flow, appear. The most widely used RANS models are the eddy viscosity ones, where a simplified assumption is made for the Reynolds stress tensor resulting in an isotropic behavior of turbulence inside the flow. For this class of models one or two additional equations need to be coupled to the averaged Navier-Stokes equations in order to relate the new turbulent variables to the mean flow equations. Eddy viscosity models, such as the famous Spalart-Allmaras or the SST $k - \omega$ model, have proven to be able to provide reliable solution, at a relatively cheap price, in many aerodynamic applications. However, they experience difficulties when dealing with wall dominated flows characterized by thick boundary layer, strong shock wave/boundary layers interaction and separation. Therefore, Reynolds stress models (RSM) are important. They are also called second-order

closure models, since they solve transport equations for the second-order correlations of the fluctuating velocity, which are the components of the Reynolds stress tensor. In addition, an equation for the turbulent length scale is needed. Due to their nature, these models account for the anisotropy of turbulence in the wall region, characteristic of wall-dominated flow, and are suitable for the integration through the boundary layer without the need of any wall function. Unfortunately, due to their increased computational cost and decreased stability, these models are not considered as standard design tools yet.

For the correct prediction of wall-bounded flows characterized by high Reynolds number and high Mach number, of interest for a Scramjet, the anisotropy of turbulence in the near wall region needs to be properly described by the turbulence model. For this reason, a differential RSM has been implemented in the in-house code QUADFLOW and tested on different hypersonic applications. QUADFLOW is a finite volume code that solves the compressible, time dependent Navier-Stokes equations, either on structured grids or on adaptive grids by means of an advanced multiscale technique. Several eddy viscosity models and one explicit algebraic Reynolds stress model are available in the code and have been used for validation and comparison. All the two-equations models available in QUADFLOW are based on an ω -equation for computing the turbulent length scale, since this variable is generally preferred for low-Reynolds number models where an integration through the viscous sublayer and down to the wall is required. For this reason, the SSG/LRR- ω model has been chosen to be implemented in QUADFLOW. The model is a combination of two existing RSM, one used near the wall and coupled to an ω -equation, and one used in the freestream and coupled to an ϵ -equation to profit from the low sensitivity of this variable to the incoming turbulence. The flow solver has been modified to accommodate seven turbulence equations, and a set of numerical methods and suitable boundary conditions have been chosen to be used in combination with the model for hypersonic flow simulations.

As it is a standard procedure in CFD, the model implementation has been tested against different configurations, starting from a zero pressure gradient flat plate at different Mach numbers, and subsequently on configurations characterized by SWBLI as a double wedge configuration. A Scramjet intake, designed in the frame of the Graduiertenkolleg GRK 1095 "Aero-Thermodynamic Design of a Scramjet Engine for Future Space Transportation Systems", has been investigated using both a block structured grid and an adaptive grid. The obtained results have been compared with available numerical solutions computed with QUADFLOW using other turbulence models, theoretical solutions and experimental results. In addition, the model has been assessed concerning important simulation parameters as the grid resolution, the incoming turbulence level and the boundary condition for the ω -equation. For most of the test cases considered, the possibility of using the SSG/LRR- ω model in combination with grid adaptation has been investigated.

The lack of fully turbulent results to be used for comparison and of measurement data from a fully three-dimensional SWBLI was the main motivation for the initiation of an experimental campaign that was conducted at the University of Queensland. The availability of a hypersonic shock tunnel and of a group of experienced hypersonics scientists, allowed

the successful completion of the experimental investigation and the interpretation and postprocessing of the collected data. The investigated compression corner flow provided useful results for testing the SSG/LRR- ω model and gaining insight into its prediction capability for hypersonic SWBLI.

A physical background on hypersonic flows with a focus on SWBLI is given in Chapter 2. There numerical results from turbulence modeling literature are presented to highlight the limitation of most models in correctly predicting such flows. The RANS approach to turbulence is shortly presented in Chapter 3. The Reynolds stress equations is derived step-by-step and the model chosen for this work is described in details. In the end of the chapter a comparison between eddy viscosity models and Reynolds stress models is given. In Chapter 4 the main features of the flow solver QUADFLOW are highlighted. The validation results and parametrical studies using different configurations and flow characteristics are presented in Chapter 5. In Chapter 6 results for a two dimensional and three dimensional Scramjet configuration are shown using both structured and adaptive grids. The outcomes of the experimental campaign and the comparison between numerical and experimental results are illustrated in Chapter 7. Finally some conclusion are drawn in Chapter 8.

2. Hypersonic flows: a Brief Review

In this chapter an overview of the main concepts of relevance to this thesis is presented. The characteristics of hypersonic flows are outlined with a major focus on shock wave/boundary layer interaction. A comprehensive description of this phenomenon is given. In the second part of the chapter the issues related to turbulence modeling of hypersonic flow are analyzed, the focus being on the results obtained using a statistical approach to turbulence.

2.1. Main Characteristics of Hypersonic Flows

There is no unanimous definition of hypersonic flow based solely on the Mach number, as it exists for supersonic flow. Depending on the problem at hand, the hypersonic flow regime begins somewhere between Mach 5 and Mach 7. The reason is that no abrupt changes occur in the flow characteristics when a supersonic flow is accelerated to higher speed, in contrast to what happens when a flow is accelerated from subsonic to supersonic speed. The hypersonic regime is better defined through certain flow phenomena that become of interest as the Mach number increases. In the next sections, an overview of these phenomena is given and hypersonic flows are described following the example by Anderson [4].

2.1.1. Thin Shock Layer and Shock-Shock Interaction

The shock layer is defined as the region that lies between the shock wave and the body surface. As the Mach number increases the shock wave angle decreases moving the shock closer to the surface. Because of the small inclination of the shock waves with respect to the body surface, shock interference is more likely to occur at hypersonic Mach number. In addition, it takes place close to the body surface, thus affecting the flow at the wall dramatically. Phenomena resulting from shock-shock interactions can have strong local effects because of the intensity of the shock waves in hypersonic flows and the high stagnation enthalpy level of the upstream flow [57]. In his work, Edney [39] classified the types of shock-shock interaction into six categories. These interactions produce high thermal loads on the surfaces that have to be accounted for in the design of high-speed applications.

2.1.2. Entropy Layer

In practical applications, in order to reduce the heat flux, the leading edge of each component of a hypersonic vehicle must be round or blunt in some way. At the stagnation point, where the maximum value is achieved, the heat flux, Q_w decreases with the square root of the nose radius R [4], so that:

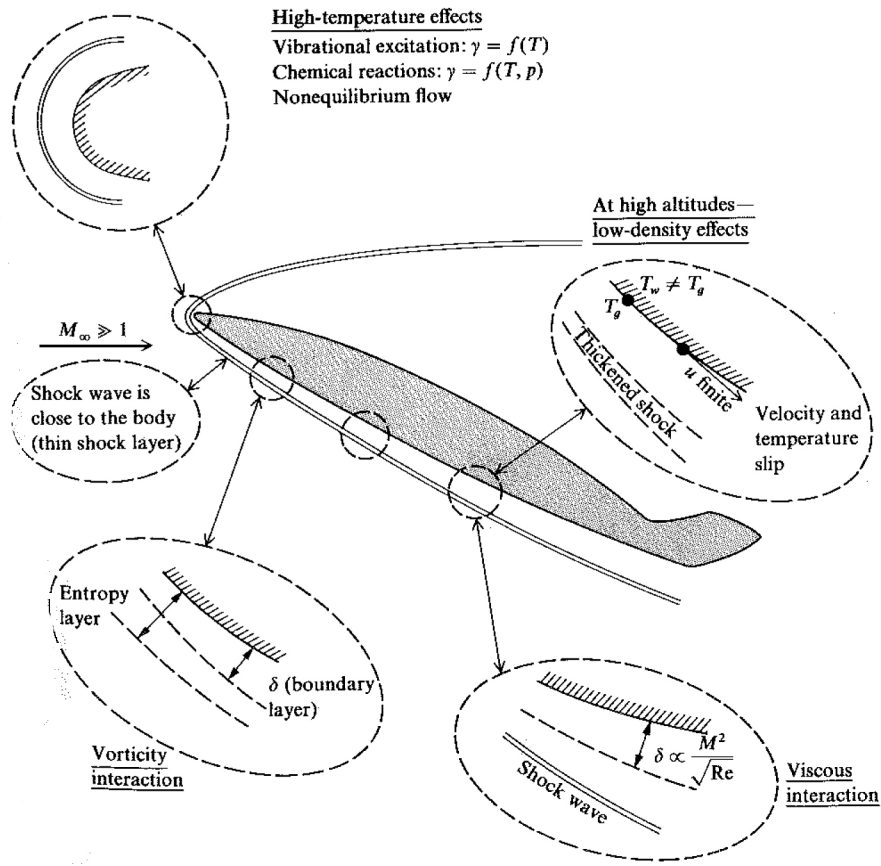


Figure 2.1. Main characteristics of hypersonic flows [4]

$$Q_w \propto \frac{1}{\sqrt{R}} \quad (2.1)$$

The use of a blunt leading edge causes the shock that originates in front of it to be curved. In addition, the bow shock is slightly detached from the solid surface and, for an ideal gas, this stand-off distance d can be computed from the nose radius and the Mach number [4]:

$$\frac{d}{R} = 0.386 \cdot e^{(4.67/M_\infty^2)} \quad (2.2)$$

From inviscid shock theory [4] it follows that the entropy increases across a shock and the larger the strength of the shock, the greater the entropy increase is. Since the portion of the shock in front of the nose is a normal shock, the flow that crosses it in that region experiences a larger entropy change than the flow further downstream along the body surface. At the nose, a layer characterized by high-temperature and high-pressure gas, called entropy layer, is generated. This layer flows downstream along the body surface, the boundary layer grows inside it and they interact. The effect of entropy layer on the viscous layer is ambiguous. The changes in pressure, temperature and local Mach number have to be considered. The increase in pressure generates a favorable pressure gradient that stabilizes the boundary layer.

The increase in temperature reduces the density of the flow so that, in order to pass the required mass flow through the boundary layer a thicker boundary layer, is necessary leading to a destabilizing effect. Finally the local Mach number is reduced. Considering that in hypersonic flows the boundary layer thickness increases with the square of the Mach number (see equation (2.4)), this phenomenon has a stabilizing effect reducing the boundary layer thickness [88]. Experimental results [59] have shown that when the nose bluntness (nose radius) is slightly increased, the size of a subsequent separation increases. When the nose bluntness is considerably increased an increase or decrease in the separation size can occur depending on the characteristics of the flow.

2.1.3. High Temperature Flows

While dealing with hypersonic flows, problems related to high temperature have to be considered. The deceleration of the high speed flow behind a shock or due to the viscous dissipation in the boundary layer, and the consequent transformation of kinetic energy into internal energy, provokes an increase in the temperature. When the temperature reaches 800 K, the vibrational energy of the molecules gets excited, and at 2500 K the molecules begin to dissociate. Under these conditions, the gas can no longer be considered as a perfect gas with constant ratio of specific heats. High temperature flows can be characterized by vibrational and chemical equilibrium if the vibrational excitation and the chemical reactions take place rapidly with respect to the mean movement of the fluid. If this does not happen, the flow has to be considered as a non-equilibrium flow. However, for the scope of this work only the perfect gas assumption is used. According to the work of Mallinson et al. [73], this assumption should not significantly affect the results for the flow conditions investigated in this thesis. This allows to focus on the influence of turbulence modeling on the flow prediction without having to deal with additional complexity of chemically reacting flows. In addition most of the experimental results available for hypersonic flows that can be used for validation are confined to perfect gases [105] due to the low enthalpy of the facilities where the experiments have been performed. For the Mach numbers that characterize the experiments used in this work for comparison, 7 and 8.3, no high temperature effects are observed. Data from the blow-down tunnel H2K at the DLR in Cologne are characterized by low freestream static temperatures, in the order of 50 K, and consequently low total temperatures. Data from shock tunnel such as TH2 at the Shock Wave Laboratory (SWL) in Aachen and T4 at the University of Queensland are characterized by high enthalpies and high total temperatures. However, due to the short test times, of a couple of milliseconds, the model surface does not heat up significantly so that also in this case high temperature effects are negligible at the wall. However, the cold walls lead to high heat flux in this region.

2.1.4. Viscous Effects

One of the key characteristics of hypersonic flows is the thickness of the boundary layer. For incompressible laminar flows, the boundary layer thickness δ decreases with an increase of

the Reynolds number, following the empirical law:

$$\delta \propto \frac{x}{\sqrt{Re_x}} \quad (2.3)$$

Additionally, turbulence increases the boundary layer thickness because of the turbulent energy dissipation [5].

In high-speed flows compressibility plays an important role and the Mach number influences the thickness of the boundary layer. When such flows pass a solid surface, they are decelerated due to viscous effects and the kinetic energy of the molecules is converted into heat and contributes to increase the temperature within the boundary layer. According to the boundary layer theory [98], the pressure is constant in the direction normal to a solid wall, so from the perfect gas relation it follows that an increase in temperature leads to a decrease in density. In order to pass the required mass flow through the boundary layer its thickness has to increase. As a consequence the boundary layer grows rapidly at hypersonic velocity; its thickness can be related to the local Reynolds number and the freestream Mach number as follows:

$$\delta \propto \frac{M_\infty^2}{\sqrt{Re_x}} \quad (2.4)$$

Because of the thick boundary layer, hypersonic flows are defined as boundary layer dominated. In order to numerically simulate them, particular care should be taken in the resolution of the boundary layer. The flow in this region is characterized by extremely high gradients, for example in the velocity, that varies from zero to hypersonic values at the boundary layer edge. The situation is even more critical for turbulent flows where the gradients at the wall are steeper than in the laminar case as shown in Figure 2.2.

As the Mach number increases, the displacement thickness caused by the thick boundary layer grows rapidly. This leads to the occurrence of displacement phenomena that make a hypersonic body to appear thicker than it actually is. This, in turn, affects the inviscid flow outside the boundary layer, as for example increasing the deflection of a shock. Finally the changes occurring in the outer flow influence the growth of the boundary layer. This is referred to as viscous interaction [4]. Viscous phenomena can affect the pressure distribution on the surface and thus the stability of a vehicle in flight. They also increase heat fluxes and friction at the wall [4]. Generally two phenomena are classified as viscous interaction. Firstly, the rapidly growing boundary layer at the leading edge increases the flow deflection and, consequently, a stronger shock wave is generated. The shock wave produces an increase in the pressure at the wall which in turn increases the density inside the boundary layer, making it thinner and reducing the deflection effect. Thus, shock wave strength and boundary layer growth (inviscid-viscous effects) mutually affect each other. Moving downstream the boundary layer displacement thickness grows more slowly. Then the so called weak interaction takes place where the inviscid outflow is only slightly affected and its feedback on the boundary layer is negligible. The second type of viscous interaction that is of higher

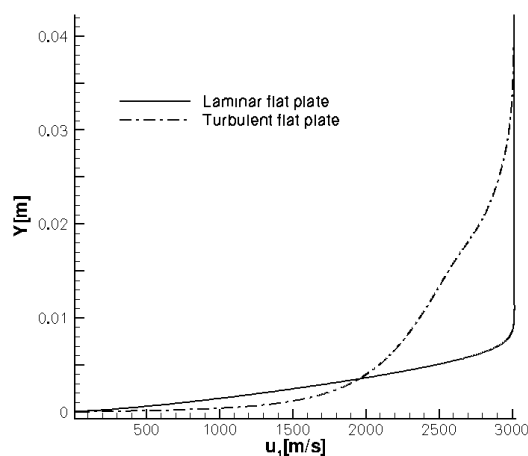


Figure 2.2. Comparison of the velocity profile in a laminar and turbulent boundary layer. Y is the wall normal distance and u_1 the first velocity component. Flat plate simulation at $M=6.3$ and $Re=1.7 \times 10^{-6}$ 1/m.

concern for this thesis is the so called shock wave/boundary layer interaction, and it is discussed in detail in the following section.

2.2. Shock Wave/Boundary Layer Interaction (SWBLI)

Under the name of shock wave/boundary layer interaction (SWBLI) mostly two phenomena are listed: the impinging-reflecting shock wave, which corresponds to the shock reflection inside an air-intake, and the compression corner flow, which corresponds to a control surface or an air-intake compression ramp. Such phenomena have been the subject of research studies during the past 50 years and are still actively investigated due to the difficulties in their prediction and the lack of understanding especially in the turbulent regime [7, 36, 55]. The study of the interaction between boundary layer and shock waves has both practical and theoretical importance. On the one hand, it is known that in high-speed flight SWBLI can strongly affect the vehicle performance and lead to the creation of regions of maximum mean and fluctuating pressure levels and severe peak heating. These phenomena can lead to structural failure as in the case of the X-15 flight in 1967 [81], so that a good understanding and prediction of these phenomena is an essential starting point for effective flow control. On the other hand, such flows provide one of the simplest occurrences of strong inviscid/viscous interaction which are of interest in fundamental research and are a challenging test case for Navier-Stokes flow solvers. A large amount of experimental data are available on the study of 2D shock wave/boundary layer interaction and provide a wide range of studies of the parameters involved [70, 100]. As far as 3D flows are concerned, the number of results available is considerably smaller and also the understanding of the phenomena and of the flow organization is not so satisfactory [7, 24]. The two type of SWBLI of interest for this

work are described in detail next.

2.2.1. SWBLI on a Compression Corner Configuration

A schematic sketch of SWBLI along a compression corner is shown in Figure 2.3. The flow moves along the plate following the undisturbed flat plate distribution. In the kink region the presence of a compression surface increases the pressure of the flow generating a shock and deflecting the flow to an angle equal to the ramp angle. In the subsonic viscous sub-layer of the boundary layer, information such as the pressure change can be propagated upstream.

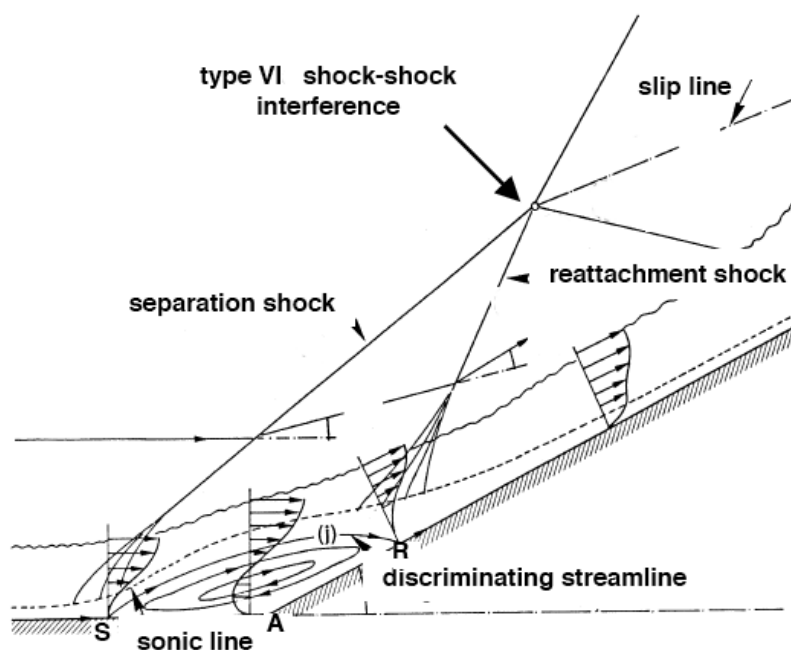


Figure 2.3. Schematic sketch of shock-wave/boundary layer interaction along a compression ramp [7].

For this reason the pressure rise is 'felt' also ahead of the kink. The upstream influence distance, defined as the distance between the point where the solution starts to differ from the flat plate one up to the kink, increases with increasing the ramp angle. A situation can occur where the adverse pressure gradient is strong enough to make the boundary layer undergo separation.

The ability of the boundary layer to prevent separation depends on how much momentum has been removed from the boundary layer due to viscous forces upstream of the interaction. Turbulent boundary layers are more resistant to separation than laminar ones because their velocity profiles increase more rapidly moving away from the wall as illustrated in Figure 2.2. In addition, the mixing due to turbulence increases the momentum thus assisting the flow to overcome the pressure gradient.

When separation occurs, a region of flow recirculation appears at the kink and, at the

separation onset, a shock wave is generated, since the thick separated boundary layer is an obstacle for the incoming flow. Along the compression ramp the boundary layer reattaches to the wall and becomes relatively thin inducing extremely high heat fluxes on the surface (peak heating). This feature is better shown in Figure 2.4 where the streamlines are strongly deviated toward the surface passing through the shock and get close to the solid wall. A so-called reattachment shock wave is generated to turn the flow parallel to the surface. At reattachment the flow field is similar to that near a stagnation point, since the high enthalpy gases from the freestream flow are transported to the wall causing large local heat transfer rates. At a certain downstream location the separation shock wave and the reattachment shock wave merge together into the ramp shock expected from inviscid shock theory. At the intersection point, a type VI shock-shock interference pattern is produced [39, 83]. For hypersonic Mach numbers a centered expansion propagates from the triple point where the two shocks meet in order to make the flows above and below it compatible. Due to the thin shock layer in hypersonic flow this expansion is so close to the wall that it is responsible for a remarkable pressure decrease when it impacts on the solid surface. A contact discontinuity (slip line) is generated between the region of the flow near the wall, that crosses the separation and the reattachment shock, and the region of flow away from the wall, that crosses the ramp shock.

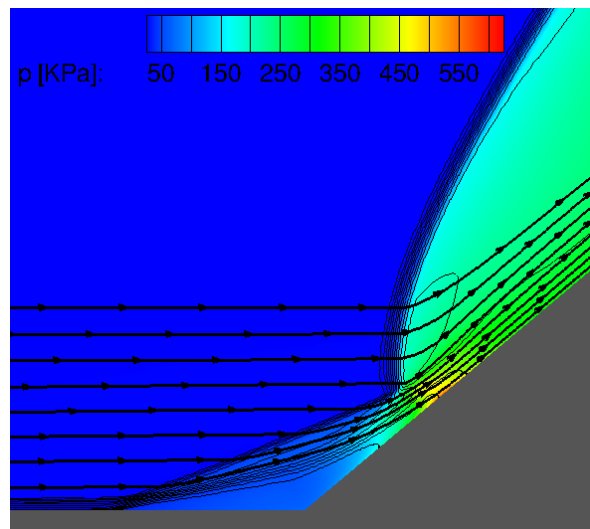


Figure 2.4. Pressure distribution, Mach number isolines and stream lines for a 40 degrees compression corner computed for turbulent flow conditions at $M=6.35$ and $Re=9.65 \times 10^6$ 1/m.

The pressure distribution along a hypersonic compression corner in a turbulent flow for different ramp angles has been the subject of detailed experimental investigations by Elfstrom [44] and Batham [10]. Furthermore, Colemann and Stollery investigated heat fluxes distribution for the same geometry [29]. Even though these studies were performed as early as 1971 and 1972, they have since then been considered as one of the most complete and reliable experimental database for hypersonic turbulent SWBLI. References to these works can be found in different reviews of hypersonic flows: in 1991 in Settles and Dodson [100],

in 2004 in Roy and Blotter [91] and in 2009 in Smits, Martin and Girimaji [105]. In the next paragraphs, selected results from the aforementioned studies are presented. Particularly the description of SWBLI in terms of two-dimensional flow is of concern here.

Mean Pressure

Figure 2.5 (left) presents a typical pressure distribution along a compression ramp in a hypersonic flow. The Mach number is 9.22, the Reynolds number is 47×10^6 1/m, the freestream temperature is 64.5 K and the wall temperature 295 K. The different lines describe the pressure at the wall for changing ramp angle. The origin of the x -axis coincides with the ramp edge. Moving downstream on the plate, the pressure distribution is constant until the presence of the compression ramp is felt. For an attached boundary layer, the upstream influence of the interaction, caused by the pressure rise from the shock transmitted through the subsonic part of the boundary layer, is limited to less than one boundary layer thickness (δ_L =boundary layer thickness at a distance L from the leading edge). For this reason it is considered to be a weak interaction [34]. For separated flow, the upstream influence increases rapidly with the ramp angle and a pressure plateau of approximately constant level, but of increasing length, develops.

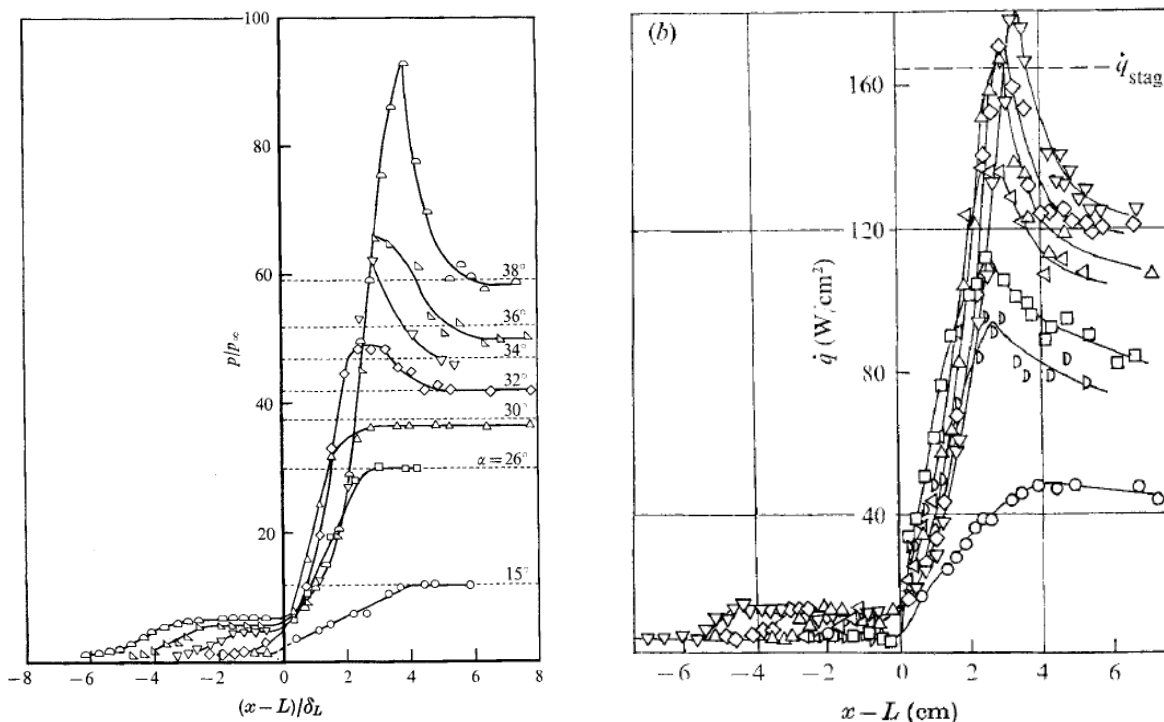


Figure 2.5. Wall pressure (left) and heat flux distribution (right) on a compression ramp at Mach 9.22 [44].

Results concerning the characteristics of the separation size and the respective pressure plateau have been first proposed by Chapman [27], and a complete description has later been

given by Delery and Marvin [35]. They developed the so-called free interaction theory that can be used to describe the pressure rise at the separation onset and along the pressure plateau. The relation for pressure is as follows:

$$\frac{p}{p_\infty} = 1 + \frac{1}{2} M_\infty^2 \gamma \mathcal{F} \cdot 2 \cdot (C_{f_0})^{1/2} \cdot (M_\infty - 1)^{-1/4} , \quad (2.5)$$

where \mathcal{F} is different for laminar and turbulent flows:

- at the separation point: $\mathcal{F} = 0.81$ for laminar flow, $\mathcal{F} = 4.22$ for turbulent flow;
- for the pressure plateau: $\mathcal{F} = 1.47$ for laminar flow, $\mathcal{F} = 6.00$ for turbulent flow;

M_∞ is the freestream Mach number, p_∞ the freestream pressure and C_{f_0} the skin friction coefficient at the interaction origin.

It follows that the separation and the development of the pressure plateau are independent of the flow downstream of the separation and of the phenomena that provokes the separation. Everything happens as if the flow characteristics were entirely determined by the properties at the onset of the interaction. The same applies to the separation length L :

$$L/\delta_0^* = k \cdot (C_f)^{1/2} \cdot (M_\infty^2 - 1)^{1/4} \quad (2.6)$$

where k is a constant independent of Mach or Reynolds number, but dependent on the ramp angle.

The free interaction theory predicts that the pressure levels in a separation (pressure at separation and pressure plateau) increase with the upstream Mach number and decrease with rising upstream Reynolds number. This is due to the fact that, for a flat plate, the skin friction decreases when the Reynolds number increases, so a stronger shock is required to separate the flow at lower Reynolds numbers. This trend is characteristic of both laminar and turbulent flows. However, the skin friction is considerably higher in turbulent flows, so that higher pressure levels are required to separate a turbulent boundary layer. The trend of a pressure decrease with increasing Reynolds number is valid for laminar flows and for turbulent flows up to Re_δ equal 10^5 ; above this value the pressure plateau is almost independent of the Reynolds number and even slightly increases with it [7]. An increase in the extent of the separation is promoted by an increase in the Reynolds number and a decrease in the Mach number. Finally, the pressure rise is independent of the ramp angle.

Considering the flow along the ramp, the pressure undergoes a rapid increase when the flow passes through the shock generated at the kink. For ramp angles up to 30 degrees the pressure levels downstream of the shock can be well predicted by inviscid flow theory using the Rankine-Hugoniot relations [4]. Increasing the ramp angle, a pressure overshoot appears and becomes more significant at higher values. The pressure distribution has a peak and then decreases to the predicted inviscid values. This is a typical characteristic of SWBLI for separated hypersonic flows. The pressure rise produced by the combined successive action of the separation shock and the reattachment shock is much larger than that due to

a unique oblique shock (as in the inviscid or attached case), therefore an expansion occurs at the triple point. As pointed out in Section 2.1.1, the angle between the shock and the solid wall decreases with increasing Mach number. This means that the triple point, where the separation and reattachment shock waves meet, lies very close to the surface; the intense expansion wave emanating from there hits the wall at a small distance downstream of the reattachment point producing a sudden pressure decrease toward the inviscid value. The characteristics of the pressure distribution described above hold for both laminar and turbulent flows. However, as said above, in a laminar flow the pressure rise required to separate the boundary layer is much lower than in a turbulent flow. From the free-interaction theory [35] it is estimated to be nearly five times smaller.

Mean Heat Fluxes

For attached flow, Coleman and Stollery [29] note that there are similarities between the pressure profile and the heat transfer profile, and that the upstream influence of the corner is extremely small. For separated boundary layers, laminar and turbulent heat flux distributions have to be discussed separately.

In the laminar case, the heat fluxes decrease along the plate following the flat plate solution until they undergo a fast decrease at the location of the separation onset. The heat transfer reaches a minimum in this region and then increases sharply upon reattachment.

A typical heat flux distribution for turbulent hypersonic flow over a compression corner at different ramp angles is presented in Figure 2.5 (right). The inflow conditions are the same as defined for Figure 2.5 and the different lines represent the same ramp angle as in Figure 2.5. The main feature of this kind of flow is the increase of the heat flux within the separation region. This rise is explained by the turbulence amplification in the vicinity of the separation point and further downstream. This leads to the formation of large eddies that enhance the exchange between the flow near the wall and the outer high enthalpy flow, leading to an increase in heat transfer [7]. Along the compression ramp, a peak heat flux, corresponding to the pressure overshoot, is detected just downstream of the reattachment point. In this location the separated flow impinges on the ramp generating heat transfer rates that exceed those obtained for a fully attached flow.

Between fully laminar and fully turbulent flows a wide range of transitional flows exists. The most relevant case, to this thesis, is the situation where the boundary layer at the separation onset is laminar, therefore leading to a decrease of the heat fluxes along the separation region, but turns turbulent in the shear layer above the separation, due to a turbulent amplification through the shock wave and the shear stresses generated in that region. In this case the heat fluxes measured at reattachment can be higher than in the fully turbulent case. A similar overshoot is detected along a flat plate where the flow undergoes a laminar to turbulent transition. In their work Arnal and Delery [34] suggest that this is due to presence of “large and well organized structure” characterizing a pre-turbulence state of the boundary layer and enhancing the heat transfer to the wall. Once the turbulent regime is established these

structures divide into smaller eddies and the heat fluxes approach the fully turbulent value.

2.2.2. Impinging-Reflecting Shock Wave

A schematic sketch of the main phenomena related to a shock wave impinging on a boundary layer is shown in Figure 2.6. The flow is deflected at first through the impinging shock C_1 . Next, in order for the flow to be parallel to the solid wall again, it is further deflected by the reflected shock C_2 by an angle of the same magnitude but opposite in sign than the one of C_1 .

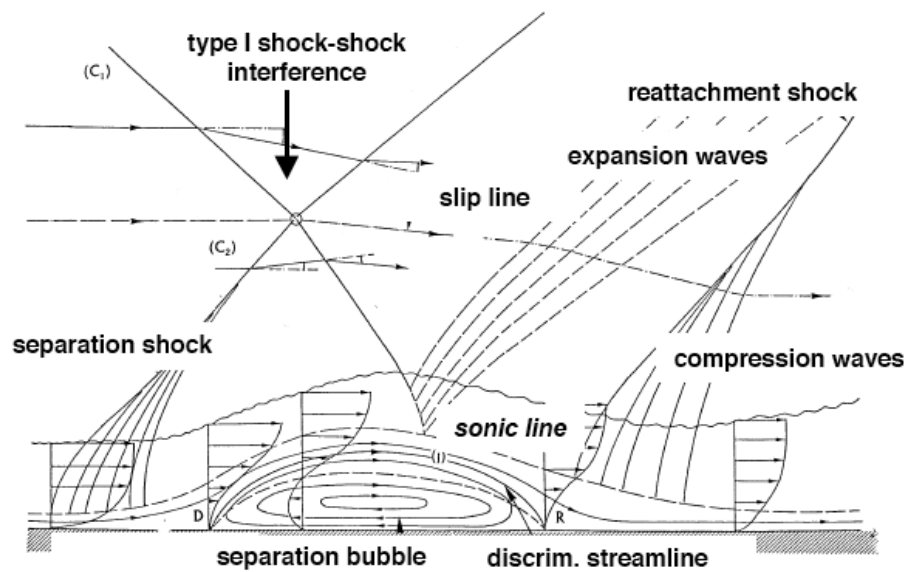


Figure 2.6. Schematic sketch of a shock wave/boundary layer interaction due to an impinging shock [7].

The impinging shock penetrates the incoming boundary layer and, through the subsonic part of it, the disturbance propagates upstream. If the pressure gradient generated at the impingement is strong enough, a region of separated boundary layer originates upstream of the impingement and a shock departs from the separation point. This shock merges with the impinging one creating a type I shock-shock interaction [39, 83]. In this configuration expansion waves and compression waves generate downstream of the impingement point and a complex flow pattern arises. The behaviour of the pressure and heat fluxes at the wall is similar to the compression corner case and is therefore not discussed here. The main difference is that the separation and reattachment shock waves do not intersect so that no overshoot is visible in the pressure distribution.

2.3. Turbulence Modeling in Hypersonic Flows

Despite remarkable advances in computational capabilities over the last decades, the simulation of hypersonic turbulent flows for engineering applications is still a challenge.

While Computational Fluid Dynamics (CFD) has become an analysis and design tool complementary to wind tunnel and flight test in the aircraft industry [90], there is not an easy way to directly transfer the methods used for transonic flows to highly compressible flows. Even well established turbulence models need to be tested again and assessed for their applicability to high Mach number flows.

Right now, the use of Direct Numerical Simulation (DNS) or Large Eddy Simulation (LES) for high speed regimes is limited to fundamental research. The use of hybrid LES/RANS (Reynolds Averaged Navier-Stokes equations) methods is still at an early stage and simulations of hypersonic shock wave/boundary layer interaction performed with these tools are not available [105]. On the contrary, RANS turbulence modeling, mainly in the form of algebraic and linear eddy viscosity models, has been widely used for different kinds of hypersonic applications, from basic research to the design and development of hypersonic vehicles, due to its relatively low computational cost and its suitability for two-dimensional simulations. In order to extend the applicability of the models to compressible flows, the original formulations, mainly developed for incompressible flows, have been enriched with terms to account for compressibility effects. Over the years, a variety of turbulence models for highly compressible flows has been proposed and compared with experimental findings, however the results obtained are far from being satisfactory, and important quantities such as separation size or peak heating still cannot be predicted accurately.

2.3.1. Experimental Databases

The well established way of validating turbulence models is by comparison with experimental (mostly wind tunnel and sometimes flight) data. Typically, the footprint of SWBLI is measured by surface measurement techniques such as pressure tabs, thermocouples and thin film gauges. In order to reproduce the experiments by numerical simulations, information about initial and boundary conditions as well as measurement uncertainties must be provided. In the early 1990s, Settles and Dodson [100] compiled a list of shock wave/ boundary layer interaction cases at Mach 3 or higher and found five experiments that satisfied their list of necessary criteria to be used as a validation test cases for turbulence models.

In 2006, Roy and Blottner [91] extended the existing database, adding new test cases. Also, they reported results obtained from well assessed one- and two-equation turbulence models for these test cases.

In 2010, Smits, Martin and Grimaji [105] reviewed the progress made in basic research on hypersonic turbulent flows. In their work, they point out that the experimental database for turbulent flows at hypersonic Mach number is extremely limited and that most of the studies available are confined to flow of perfect gases. They present different types of flows and selected results obtained using different approaches to turbulence. For RANS modeling the results presented in [91] are used. In the conclusions the paper gives some suggestions concerning the use and development of turbulence models and the authors state that: "for the foreseeable future the design and development of hypersonic vehicles will depend on

computations employing turbulence closure models".

For the scope of this thesis, experimental results obtained from both blow down tunnels and shock tunnels have been employed for comparison. The experiments were conducted in the frame of the German Research Training Group "Aero-Thermodynamic Design of a Scramjet Engine for Future Space Transportation Systems" (GRK 1095) [48]. The test case of a double wedge, investigated in the SWL in Aachen, was used as first validation test for SWBLI for the newly implemented RSM [80]. For simulations including a more complex geometry and consequently more complicated shock pattern, a Scramjet intake was studied both in 2D and 3D [53, 54]. Both test cases are characterized by moderate hypersonic Mach number of 8.3 and 7, respectively, and a cold wall condition due to either the low enthalpy of the flow or to the short test time. For each configuration, pressure and heat flux measurements were taken along the center line of the model using Kulite piezoresistive transducers and either k-type thermocouples or an infra-red camera. The results are characterized by moderate ramp angles which vary between 9 and 20.5 degrees, and by a large portion of laminar flow and subsequently transitional flow.

2.3.2. LES and DNS of SWBLI

LES and DNS of shock wave turbulent boundary layer interactions have been performed for about a decade now [116]. The first DNS simulation of a Mach 3 compression corner at 18 degrees and $Re_\theta = 1685$ was carried out in 2000 by Adams [3]. The results obtained were compared with experiments of the same configuration but at a higher Reynolds number, so the author was not able to draw definitive conclusions from the comparison. Generally there is a lack of experimental data obtained at Reynolds number accessible for LES and DNS. In 2006 Pirozzoli and Grasso [86] used DNS to study the characteristics of a shock impinging on a turbulent boundary layer at Mach 2.25 and a Reynolds number based on the boundary layer momentum thickness $Re_\theta=3725$. Also in this case no experimental results at the same inflow and boundary conditions were available. For this reason in 2007 a numerical and experimental project was conducted on a 24 degrees compression corner at Mach 2.9 by Wu and Martin [116], [89] and Bookey, Wyckham and Smits [14] who were responsible for the DNS simulation and the experiment at an appropriate Reynolds number, respectively. The results showed a discrepancy in the prediction of the separation size and of the pressure levels which were claimed to be due to the grid resolution and the dissipation of the WENO scheme employed.

Due to the grid constraints imposed by LES and DNS methods, no study exists of SWBLI at hypersonic speed performed with these tools, to the author's knowledge.

2.3.3. Main RANS Results for Hypersonic 2D SWBLI

A few representative comparisons between experimental data and results obtained using different RANS turbulence models are reported next. It is interesting to note that the authors of the studies limited their interest to one- and two-equation models. No results of SWBLI at

hypersonic speed performed using a differential Reynolds Stress Model are available to the author's knowledge. In their review, Roy and Blottner [91] state that one- and two-equation models are the standard tools used in design studies, while advanced turbulence models such as Reynolds stress models are still under development. In the NASA technical report by Olsen, Lillard and Coakley [84] it is stated that Reynolds stress models have been extensively investigated, but for complex flows they did not perform significantly better than simpler models; in addition, they are commonly considered more complicated and numerically stiff, and this prevents their wide application.

For the above reasons, only results obtained using one- and two-equation models are reported and briefly commented here. The experiment from Colemann and Stollery [29] was used by Roy and Blottner [91] for testing turbulence models in the hypersonic flight regime. The pressure and the heat fluxes at the wall are compared in Figure 2.7.

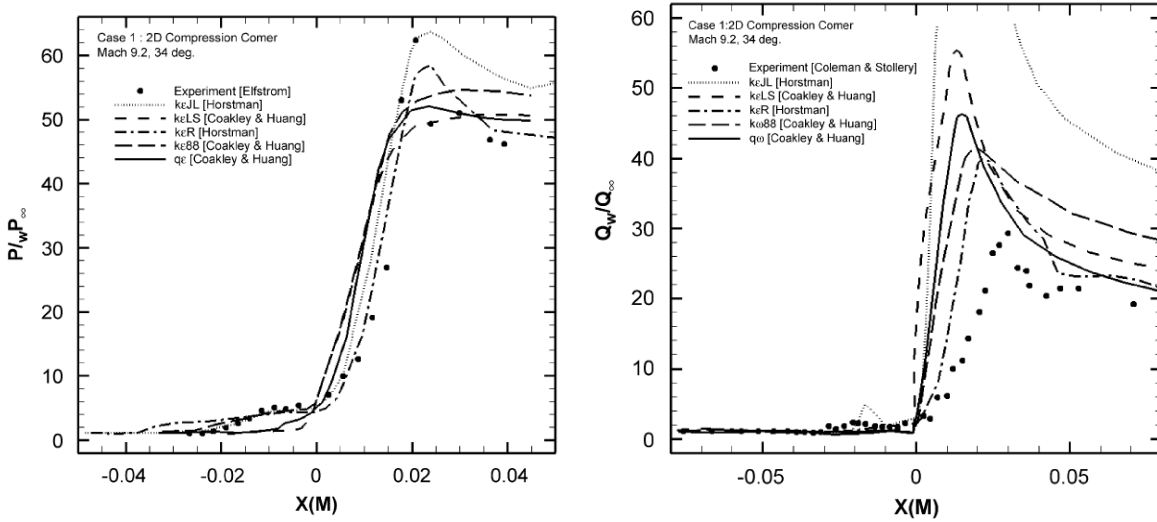


Figure 2.7. Pressure (left) and heat flux distribution (right) at Mach 9.2 for a 34 degrees compression corner [91]. Experimental results in comparison with numerical prediction from different turbulence models.

The experimental values are compared with five different two equations turbulence models listed in Table 2.1:

$k\epsilon JL$	Jones and Launder high Reynolds number $k - \epsilon$
$k\epsilon LS$	Launder and Sharma (standard) $k - \epsilon$
$k\epsilon R$	Rodi $k - \epsilon$
$k - \omega 88$	Wilcox 1988 $k - \omega$
$q - \omega$	Coakley $q - \omega$

Table 2.1. Turbulence models used in Figure 2.7.

The 34 degrees compression corner can be considered a critical test case, since the turbulent

boundary layer undergoes a separation as shown by the increase in pressure and heat fluxes ahead of the kink. The pressure distribution is captured relatively well by all turbulence models at least for what concerns the levels ahead and after the separation. Only two of the five turbulence models, the $k\epsilon JL$ and the $k\epsilon SL$ capture the separation size correctly and match the pressure increase and the plateau level. Concerning the heat flux in the interaction region, the numerical results provide predictions that are 2 to 5 times higher than those found in the experiments even for the models that were able to predict the separation size correctly.

A cylinder flare at Mach 7 was investigated at NASA by Olsen, Lillard and Coakley [84]. They developed a three-equation model starting from a standard $k-\omega$ model with the addition of an equation that accounts for non-equilibrium effects for the eddy-viscosity; in addition, a high-speed modification for k was used. Three grid resolutions are presented for this model and two for the Spalart-Allmaras and the Wilcox $k-\omega$ model from 1988. The numerical simulations are compared with experimental results. Different inclinations of the cone were analyzed from 20 up to 35 degrees. Here the case of 35 degrees, inducing boundary layer separation, is discussed. Figure 2.8 shows the pressure and heat flux distributions at the wall.

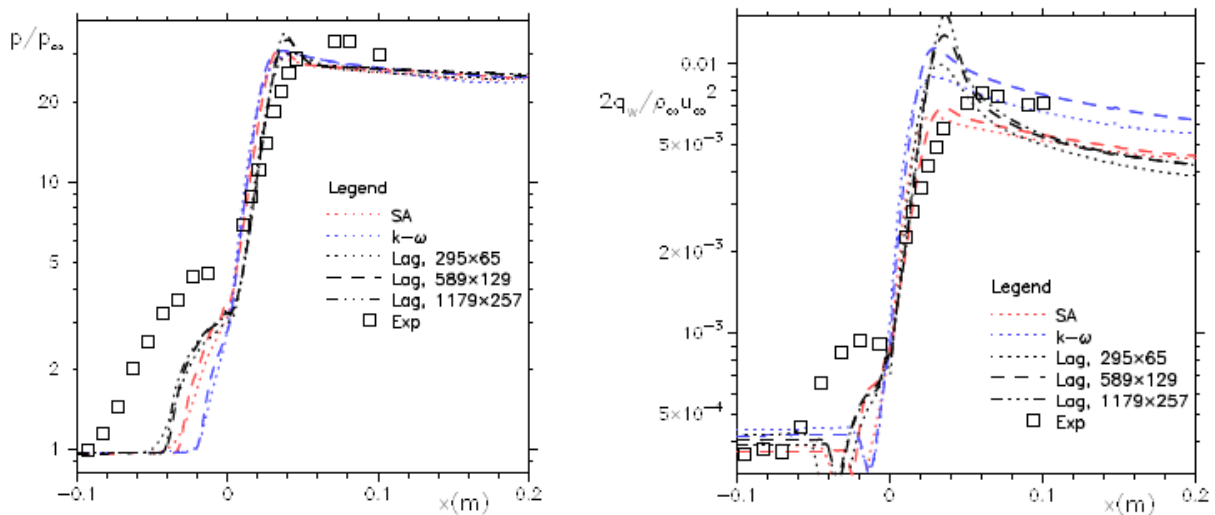


Figure 2.8. Pressure (left) and heat flux (right) distribution at Mach 7 for a 35 degrees cylinder flare [84]. Experimental results in comparison with numerical prediction from different turbulence models.

Concerning the pressure distribution, most of the models used predict boundary layer separation but the separation region is strongly underestimated. Downstream of the separation region, the pressure distribution is well captured. The heat flux distribution shows similar problems: the heat flux levels in the separation region are not predicted at all and at reattachment some models overpredict the peak heating while others underpredict it.

It is evident from these two basic examples that the capabilities of one- and two-equation models in the hypersonic flight regime are still very limited. The key issues are related to the prediction of the separation size and respective pressure and heat fluxes rise and the peak heating occurring at reattachment. The situation generally improves for attached boundary

layers. Similar results can be found in the works of Coratekin et al. [31], Shina et al. [101] and Goldberg [50]. While the two-dimensional SWBLI was repeatedly investigated both numerically and experimentally, this is not the case for three-dimensional interactions. The importance of the 3D SWBLI can be seen for configurations using side walls to increase the flow compression, as for example in the case of the Scramjet intake presented in Chapter 6. A 3D configuration of this type was studied numerically by Reinartz using the Reynolds Stress Model (RSM) of interest in this thesis, producing encouraging results [87] and showing the ability of the RSM to produce reliable results for complex geometries.

3. Physical Modeling of Turbulent Compressible Flows

In the first part of this chapter the Navier-Stokes equations for compressible viscous fluids are briefly introduced together with the constitutive equations needed for closing the system. In the second part the problem of turbulence modeling is addressed. The three main types of turbulence modeling are discussed and the Reynolds Averaged Navier-Stokes equation method is explained in detail. Finally, the Reynolds stress equations are derived and the 7-equation SSG/LRR- ω model is described.

3.1. The Navier-Stokes Equations

The general equations describing the time and space evolution of continuum compressible viscous fluids are the so-called Navier-Stokes equations [12], [5].

$$\frac{\partial \rho}{\partial t} + \frac{\partial(\rho u_i)}{\partial x_i} = 0 \quad , \quad (3.1)$$

$$\frac{\partial}{\partial t}(\rho u_i) + \frac{\partial(\rho u_i u_j)}{\partial x_j} = -\frac{\partial p}{\partial x_i} + \frac{\partial \tau_{ij}}{\partial x_j} \quad , \quad (3.2)$$

$$\frac{\partial}{\partial t}(\rho E) + \frac{\partial}{\partial x_j}(\rho H u_j) = \frac{\partial}{\partial x_j}(\tau_{ij} u_i) - \frac{\partial q_j}{\partial x_j} \quad . \quad (3.3)$$

The Einstein convention on repeated indices is applied. The system of equations (3.1)-(3.3) is not closed. For this reason some assumptions have to be made in order to provide suitable closure relations.

3.2. Material Laws and Thermodynamic Relations

In this work it is assumed that air (the fluid of interest) is a Newtonian fluid so that the viscous stresses can be considered proportional to the traceless strain rate tensor. Consequently, the viscous stress tensor, which characterizes the specific property of the fluid when subject to mechanical stresses, can be written as:

$$\tau_{ij} = 2\mu \left(\frac{1}{2} \left(\frac{\partial u_i}{\partial x_j} + \frac{\partial u_j}{\partial x_i} \right) - \frac{1}{3} \frac{\partial u_k}{\partial x_k} \delta_{ij} \right) \quad . \quad (3.4)$$

The variation of the dynamic viscosity, for a wide range of temperatures, can be described by the Sutherland's formula:

$$\frac{\mu(T)}{\mu_0} = \frac{T_0 + T_s}{T + T_s} \left(\frac{T}{T_0} \right)^{\frac{3}{2}}, \quad (3.5)$$

where the Sutherland constant is equal to $T_s = 110.6$ K for air and T_0 and μ_0 are 273.15 K and 1.716×10^{-5} kg/(m · s), respectively.

For what concerns the heat flux, Fourier's law for heat conduction, which states a proportionality between the heat flux and the temperature gradient, is assumed:

$$q_i = -\lambda \frac{\partial T}{\partial x_i}, \quad \lambda = \frac{c_p \mu}{Pr}, \quad (3.6)$$

where λ is the thermal conductivity of the fluid, c_p is the specific heat at constant pressure and Pr is the Prandtl number and is assumed constant and equal to 0.72.

In order to close the system, additional thermodynamic relations are needed. In this work the assumption of an ideal, calorically perfect gas is done. The static pressure p is derived by the equation of state for an ideal gas:

$$p = \rho RT, \quad (3.7)$$

where R is the universal gas constant. For air it is equal to 287.058 J · kg⁻¹ K⁻¹.

The total energy E in equation (3.3) is defined as the sum of the internal energy and the kinetic energy, and the internal energy is proportional to the temperature.

$$E = e + \frac{1}{2} u_k u_k, \quad e = c_v T. \quad (3.8)$$

The total enthalpy H , that appears in the total energy evolution equation, is defined as follows:

$$H = E + \frac{p}{\rho}. \quad (3.9)$$

Finally the following relations between the specific heat at constant pressure c_p and the specific heat at constant volume c_v hold:

$$R = c_p - c_v, \quad \gamma = \frac{c_p}{c_v}, \quad (3.10)$$

where γ is the isentropic exponent and is constant for a perfect gas and equal to 1.4 for air.

3.3. Turbulent Flows

Turbulence is that state of fluid motion which is characterized by apparently random and chaotic three-dimensional motion. Tennekes and Lumely [108] have characterized turbulent flows identifying six key features.

- **Irregularity:** turbulence is characterized by irregular and random motion. The flow is characterized by a spectrum of different scales related to the size of the eddies. The largest scale of turbulence are of the same order of the geometry under consideration and the smallest eddies are the ones where the energy of the flow is dissipated in internal energy.
- **Diffusivity:** turbulent flows are characterized by an increase in diffusivity. This also enhances the exchange of momentum between different flow regions. In the boundary layer this phenomenon delays flow separation from the wall. The increase in diffusivity also increases the wall friction.
- **Large Reynolds Number:** turbulent flows are a characteristic of high Reynolds number flows. It has been seen that flows with high Reynolds numbers usually undergo a transition to turbulence while flows characterized by lower Reynolds numbers tend to remain laminar.
- **Three-Dimensional:** by its nature, turbulence is always three-dimensional. However, using a time averaged approach the mean flow can be treated as two-dimensional.
- **Dissipation:** turbulence is characterized by the so called energy cascade. Most of the kinetic energy of a turbulent flow is contained in the large turbulent structures which extract it from the mean flow. This energy is partially passed to the smaller scales through a process called "energy cascade". During this process inviscid mechanisms occur so that the energy is mostly preserved. The cascade proceeds down to the dissipative (smallest) structures. At this point the eddies are so small that molecular diffusion becomes important and the energy is dissipated through viscosity. The scale of the dissipative eddies is called Kolmogorov length scale.
- **Continuum:** The smallest scales of turbulence are still much larger than the molecular scale so that the hypothesis of a continuum flow can be used.

When turbulence is present, it usually dominates all other flow phenomena and results in increased energy dissipation, mixing, heat transfer, and drag [49]. Since hypersonic vehicles operate in a high Reynolds number environment, turbulence needs to be taken into account when the flow around these bodies is simulated.

By the nature of the Navier-Stokes equations, turbulence, as continuum phenomenon, is automatically included in them. However, while simulating turbulent flows, one faces two main problems. On the one hand, the spectrum of turbulent scales is so wide that a Direct Numerical Simulation (DNS) of aerodynamic flows for engineering applications is computationally too expensive for current computer resources, since it requires extremely fine three-dimensional grids. On the other hand, if the small scales of turbulence are not resolved, due to the use of too coarse a grid, important turbulent dynamics are not captured so that the resulting solution describes a laminar flow. In order to address these problems

turbulence models, to be coupled to the Navier-Stokes equations, have been developed to take into account the effects of turbulence on the main flow. There are three fundamental approaches to turbulence: DNS where no turbulence model is required, LES where only the small scales of turbulence are modeled, and RANS where a statistical approach is used. Lately, hybrid approaches with combined RANS and LES have been developed. The different methods are now briefly described.

DNS: with the term Direct Numerical Simulation one refers to the complete spatial and temporal solution of the Navier-Stokes equations without the use of turbulence modeling. This means that three-dimensional, time dependent problems are addressed. In order to perform such simulations, a very fine grid is required since all the spatial scales from the dissipative Kolmogorov scales, introduced in Section 3.3, up to the large scales of turbulence need to be resolved. Since the range of the turbulent scales increases with the Reynolds number, and consequently the number of grid cells required for solving the problem, DNS of practical engineering problems is still prohibitive. Application of DNS technique is therefore limited to low Reynolds number flows.

Nowadays, DNS simulations are employed to investigate the nature of turbulent flows for gaining an understanding of turbulence structures and processes; in addition they can be used to compute statistics for testing closure approximation for engineering models. In order to get reliable results from this kind of simulation, attention should be paid to the specification of the boundary and initial conditions and to the numerical accuracy. Because of the elliptic nature of the problem at open boundaries, the flow characteristics at these locations need to be specified. Usually, to overcome this problem, periodic boundary conditions are used when applicable. For inhomogeneous flows, however, boundary conditions need to be generated and prescribed. For what concerns the initial conditions random fluctuations can be added to the velocity field and then let the flow evolve in time to develop the correct statistics.

LES: with the term Large Eddy Simulation one refers to numerical simulations in which the three dimensional, time dependent Navier-Stokes equations are solved for the large and medium scales of turbulence. These scales are anisotropic and directly affected by the boundary conditions. The smaller unresolved scales, which are nearly isotropic and have a universal behavior, are modeled. The separation between the grid and subgrid scales is generally performed using a low-pass filter and a Sub Grid Scale (SGS) model is coupled to the filtered flow.

Since the subgrid scales contain a significant portion of the turbulence spectrum, their modeling strongly affects the performances of LES simulations. During the years, lot of effort has been put into developing satisfactory SGS models, needed to model the SGS stresses deriving from the filtering procedure. Different models have been proposed, from algebraic, as the first model proposed by Smagorinsky in 1963 [102], to one-equation or more equation models.

Since in LES simulations the small eddies do not need to be captured by the grid, this allows

the use of coarser grids with respect to DNS techniques and thus the possibility to address problems at higher Reynolds numbers. LES is currently mostly used for the simulation of free flows as jet problems, combustion problems and weather prediction, when fully unsteady mechanisms have to be studied and provides reasonable agreement also for high-Reynolds-number flows. However, for high-Reynolds-number wall bounded flows, LES experiences some difficulties, because at the wall the flow is characterized by less universal properties than the free flow. The important scales of turbulence become smaller and smaller moving to the wall and the grid requirements in this region tighten. Unless one uses extremely fine grids at the wall (DNS grids) the anisotropy of the flow affects the subgrid scales so that the assumption upon which the LES approach relies breaks down. In these situations SGS models able to account for the anisotropy of the small scales are required. Usually the SGS model is then coupled with a wall model as it is done for high Reynolds number models in RANS simulations [47].

As it is the case for DNS, the numerical approach and even more importantly the way of imposing inflow and outflow conditions strongly affects the results.

RANS: Since the quantity of interest in a simulation are often averaged flow quantities, a statistical treatment of the turbulent Navier-Stokes equations can provide a cheap way of dealing with turbulent flows. In the Reynolds Averaged Navier-Stokes approach, the flow variables are divided into a mean and a fluctuating component. The equations are solved for the mean variables while the effect of the fluctuations (turbulence) on the mean flow, represented by additional terms appearing in the averaged equations, is modeled. A huge variety of turbulence models are available for RANS equations. Despite some intrinsic limitations, like the assumption that the turbulent time scale is much smaller than the mean flow time scale or the lack of accuracy in complex flows (separated flows), RANS modeling is at the moment the backbone of technical applications. A more detailed description of RANS modeling is given in Section 3.4.

Hybrid Methods: Since for some applications RANS simulations may not provide data with the desired accuracy, and LES for wall bounded flows at high Reynolds number is still too expensive, hybrid LES/RANS models have been proposed for more than a decade now. LES regions are placed in critical area of the flow (e.g. separation) and coupled with a RANS model in the remainder of the domain [46]. The most challenging aspect of this approach is to correctly treat the RANS-to-LES and LES-to-RANS interfaces.

3.4. Reynolds Averaged Navier-Stokes Equations

Since turbulence, by its nature, is a phenomenon characterized by random fluctuations of the flow quantities, the use of a statistical approach appears as a good way to obtain the main flow characteristic at an affordable computational cost. For the derivation of the RANS equations, the flow quantities are divided into a mean and a fluctuating component. Then the resulting

equations are averaged. Because of the nonlinearity of the Navier-Stokes equations, after the averaging process, new terms appear in the equations. They are momentum fluxes and act as apparent stresses. These quantities are unknown and equations for them need to be derived. The task of deriving enough equations for all the unknown is the so called closure problem [113].

3.4.1. RANS Equations for Compressible Flows

The general flow variable u_i is divided into a mean part \bar{u}_i and a fluctuating part u'_i :

$$u_i(\mathbf{x}, t) = \bar{u}_i(\mathbf{x}) + u'_i(\mathbf{x}, t) , \quad (3.11)$$

where the overbar represents the Reynolds averaging, which is a time-averaging defined as follows:

$$\bar{u}_i(\mathbf{x}) = \lim_{\tau \rightarrow \infty} \frac{1}{\tau} \int_{t_0}^{t_0+\tau} u_i(\mathbf{x}, t) dt . \quad (3.12)$$

Clearly τ can never really grow to infinity in any physical flow. For this reason a time τ is chosen that is very long with respect to the maximum period of the fluctuations. At this point the equations are averaged and the so called Reynolds Averaged Navier-Stokes equations are obtained.

This approach was first developed for incompressible flows. When moving to compressible flows, due to the appearance of density fluctuations in the equations, new terms originate from the averaging process which are not easy to model. In order to make the calculus easier the Favre averaging or mass-averaging is introduced defined as:

$$\tilde{u}_i(\mathbf{x}) = \frac{1}{\bar{\rho}} \lim_{\tau \rightarrow \infty} \int_{t_0}^{t_0+\tau} \rho(\mathbf{x}, t) u_i(\mathbf{x}, t) dt , \quad (3.13)$$

where the overline indicates the Reynolds averaging. Using the Favre averaging, a general flow variable u_i is divided in a mean component \tilde{u}_i and a fluctuating component u''_i .

$$u_i(\mathbf{x}, t) = \tilde{u}_i(\mathbf{x}) + u''_i(\mathbf{x}, t) . \quad (3.14)$$

The Favre averaging can also be rewritten in terms of the Reynolds averaging simply using the definition (3.13) as follows:

$$\bar{\rho} \tilde{u}_i = \overline{\rho u_i} = \bar{\rho} \bar{u}_i + \overline{\rho' u'_i} . \quad (3.15)$$

From equation (3.15) it is clear why the use of a Favre averaging is preferred to the Reynolds averaging when the density cannot be considered as a constant quantity. It is important to note that the weighted averages simplify the notation but not the physics and in case of constant density, Favre average reduces to Reynolds average.

The Reynolds averaged equations can be derived using the properties and definitions above

and read as follows:

$$\frac{\partial \bar{\rho}}{\partial t} + \frac{\partial}{\partial x_k} (\bar{\rho} \tilde{u}_k) = 0 \quad , \quad (3.16)$$

$$\frac{\partial}{\partial t} (\bar{\rho} \tilde{u}_i) + \frac{\partial}{\partial x_k} (\bar{\rho} \tilde{u}_i \tilde{u}_k) + \frac{\partial}{\partial x_k} (\bar{\rho} \tilde{R}_{ik}) = -\frac{\partial \bar{p}}{\partial x_i} + \frac{\partial \bar{\tau}_{ik}}{\partial x_k} \quad , \quad (3.17)$$

$$\frac{\partial}{\partial t} (\bar{\rho} \tilde{E}) + \frac{\partial}{\partial x_k} (\bar{\rho} \tilde{H} \tilde{u}_k) + \frac{\partial}{\partial x_k} (\bar{\rho} \tilde{R}_{ik} \tilde{u}_i) = \frac{\partial}{\partial x_k} (\bar{\tau}_{ik} \tilde{u}_i) - \frac{\partial \bar{q}_k}{\partial x_k} + \bar{\rho} D^{(k)} - \frac{\partial q_k^{(t)}}{\partial x_k} \quad , \quad (3.18)$$

The averaged continuity equation has the same form as the original one. In the momentum and energy equations, due to their nonlinearity, additional terms appear after the averaging process. For these terms, which represent the contribution of turbulence to the mean flow, a closure is needed. The term:

$$\bar{\rho} \tilde{R}_{ij} = \overline{\rho u_i'' u_j''} \quad (3.19)$$

is the Reynolds stress tensor and represents the correlation between two different fluctuating velocity components. The term:

$$\bar{\rho} D^{(k)} = -\frac{\partial}{\partial x_k} \left(\frac{1}{2} \overline{\rho u_i'' u_i'' u_k''} - \overline{u_i'' \tau_{ik}} \right) \quad (3.20)$$

is related to the turbulent transport and the diffusion term.

The term:

$$q_k^{(t)} = \overline{\rho h'' u_k''} \quad (3.21)$$

represents the turbulent heat flux. The material laws and the thermodynamic relations listed in Section 3.2 are averaged as above. For Sutherland's law, Fourier's law and the perfect gas equation it is assumed that they keep their original form.

3.4.2. Closure for RANS Equations

The RANS approach introduces new unknowns into the equations. These quantities need to be either solved using an additional equation or related to the mean variables so that the number of unknowns and equations is equal. In order to derive new relations one has to make some assumptions about the nature of the flow and the nature of turbulence itself based on the observation and on the study of the different terms appearing in the equations. Because of the scarcity of experimental results that measure turbulence quantities in compressible flows, as compared to incompressible ones, the development of reliable models that are applicable

to a wide range of flow is still a work in progress [113].

Since the closure of the RANS equations had started using the incompressible formulation, where the energy equation is not coupled with the continuity and momentum equations, the main focus of turbulence modeling was in writing an appropriate description for the Reynolds stress tensor in equation (3.19).

For all but second-order closure models, a closure approximation should be assumed for the Reynolds stress tensor. The modeling of this quantity relies on the similarity between the last term on the left hand side of equation (3.17) and the last term on its right hand side. These terms can be combined together as follows:

$$\frac{\partial}{\partial x_k} \left(\bar{\tau}_{ik} - \bar{\rho} \tilde{R}_{ik} \right) . \quad (3.22)$$

This means that both the terms in brackets have the dimension of stress. The first term represents indeed the viscous stress while the second one, even though it is not a stress, was named for sake of similarity, Reynolds stress. The eddy viscosity hypothesis assumes that the Reynolds stresses can be related to the mean velocity gradients and turbulent (eddy) viscosity by the gradient diffusion hypothesis, in a manner analogous to the relationship between the stress and the strain tensors in Newtonian flows. This assumption is called Boussinesq hypothesis and according to it a relation for the Reynolds stresses can be expressed as follows:

$$\bar{\rho} \tilde{R}_{ij} = \overline{\rho u_i'' u_j''} = - \left[\mu_t \left(\frac{\partial \tilde{u}_i}{\partial x_j} + \frac{\partial \tilde{u}_j}{\partial x_i} - \frac{2}{3} \frac{\partial \tilde{u}_k}{\partial x_k} \delta_{ij} \right) - \frac{2}{3} \bar{\rho} \tilde{k} \delta_{ij} \right] , \quad (3.23)$$

where μ_t is a scalar and is called turbulent viscosity. In comparison to the fluid viscosity, the turbulent viscosity is a property of the flow and not of the fluid. The turbulent kinetic energy \tilde{k} is related to the trace of the Reynolds stress tensor as:

$$\tilde{k} = \frac{1}{2} \bar{\rho} \tilde{R}_{ij} . \quad (3.24)$$

While formulating equation (3.23) it is important to guarantee that the trace of $\bar{\rho} \tilde{R}_{ij}$ is equal to $2\bar{\rho} \tilde{k}$.

Turbulence models can be divided in five classes according to the way the Reynolds stress tensor is treated.

- **Algebraic models (zero equation models):** one algebraic equation is solved for the turbulent (or eddy) viscosity. Then the Reynolds stress tensor is derived using equation (3.23).
- **One-equation models:** one transport equation is solved for a turbulent quantity. In many cases this is an equation for the turbulent kinetic energy and a second turbulent quantity representing a length scale is obtained from an algebraic equation. The eddy viscosity is then derived as a function of these two variables and some model

constant. A famous one-equation model in aerodynamic applications, the Spalart-Allmaras, solves one transport equation for a viscosity-like variable from which the eddy viscosity is then derived.

- **Two-equation models:** are the most well known and widely used turbulence models. Two transport equations are solved for two turbulent variables. Generally, the turbulent kinetic energy k and its dissipation ϵ or k and the specific dissipation ω are the primary variables. Then the eddy viscosity is obtained from the two transported scalars and from mean flow quantities.
- **Nonlinear eddy-viscosity models:** these models have been proposed in order to overcome some of the inaccuracies deriving from the Boussinesq hypothesis in equation (3.23). The most famous nonlinear models are the algebraic Reynolds stress models (ARSM), where a simplified description of the Reynolds stress tensor can be obtained in the form of an algebraic equation that needs to be solved iteratively. ARSM are known to be numerically unstable, so that explicit algebraic Reynolds stress model have been developed. Here the Reynolds stresses are described in an explicit formulation, and are thus more easily solved [56].
- **Reynolds stress models:** a transport equation for the Reynolds stresses is derived from the momentum equation so that no assumptions on the form of the Reynolds stress tensor need to be made. An additional transport equation for a turbulent length scale is needed, mostly an ϵ - or an ω -equation. A detailed description of this approach is given in the following section.

3.4.3. Reynolds Stress Models

The most accurate level of RANS modeling are the differential Reynolds Stress Models (RSM). RSM are also referred to as second-order closure models. This means that a transport equation is written for the second order correlations of the fluctuating velocity components while the higher correlations are modeled. In these models, an equation is written and solved for each component of the symmetric Reynolds stress tensor plus an additional equation is provided for the length scale. The Reynolds stress equation can be mathematically derived from the momentum equation (3.17) defined as $N(u_i) = 0$ in the following way:

$$\overline{N(u_i)u_j''} + \overline{N(u_j)u_i''} = 0 \quad . \quad (3.25)$$

It can be noticed that equation (3.25), as expected, is symmetric.

The explicit formulation of equation (3.25) reads as follow:

$$\begin{aligned} \overline{\rho u_j'' \frac{\partial u_i}{\partial t}} + \overline{\rho u_i'' \frac{\partial u_j}{\partial t}} + \overline{\rho u_j'' u_k \frac{\partial u_i}{\partial x_k}} + \overline{\rho u_i'' u_k \frac{\partial u_j}{\partial x_k}} = \\ -\overline{u_j'' \frac{\partial p}{\partial x_i}} - \overline{u_i'' \frac{\partial p}{\partial x_j}} + \overline{u_j'' \frac{\partial \tau_{ki}}{\partial x_k}} + \overline{u_i'' \frac{\partial \tau_{kj}}{\partial x_k}} \quad . \end{aligned} \quad (3.26)$$

3. Physical Modeling of Turbulent Compressible Flows

Now the different terms are developed. In order to make it easier to read, the time and space derivatives are indicated in tensor notation, i.e., $\frac{\partial}{\partial t} = (\cdot)_{,t}$, $\frac{\partial}{\partial x_i} = (\cdot)_{,i}$ and the equation is treated term by term.

Unsteady term

$$\begin{aligned}
 \overline{\rho u_j'' u_{i,t}} + \overline{\rho u_i'' u_{j,t}} &= \overline{\rho u_i'' (\tilde{u}_j + u_j'')_t} + \overline{\rho u_j'' (\tilde{u}_i + u_i'')_t} \\
 &= \overline{\rho u_i'' \tilde{u}_{j,t}} + \overline{\rho u_i'' u_{j,t}''} + \overline{\rho u_j'' \tilde{u}_{i,t}} + \overline{\rho u_j'' u_{i,t}''} \\
 &= \overline{(\rho u_i'' u_j'')_t} - \overline{\rho_t (u_i'' u_j'')} \\
 &= \frac{\partial}{\partial t} (\overline{\rho \tilde{R}_{ij}}) - \frac{\partial \rho}{\partial t} (u_i'' u_j'')
 \end{aligned} \tag{3.27}$$

Convective term

$$\begin{aligned}
 \overline{\rho u_i'' u_k u_{j,k}} + \overline{\rho u_j'' u_k u_{i,k}} &= \overline{\rho u_i'' ((\tilde{u}_k + u_k'') \tilde{u}_{j,k} + u_k u_{j,k}'')} + \overline{\rho u_j'' ((\tilde{u}_k + u_k'') \tilde{u}_{i,k} + u_k u_{i,k}'')} \\
 &= \overline{\rho u_i'' \tilde{u}_k \tilde{u}_{j,k}} + \overline{\rho u_i'' u_k'' \tilde{u}_{j,k}} + \overline{\rho u_k u_i'' u_{j,k}''} \\
 &\quad + \overline{\rho u_j'' \tilde{u}_k \tilde{u}_{i,k}} + \overline{\rho u_j'' u_k'' \tilde{u}_{i,k}} + \overline{\rho u_k u_j'' u_{i,k}''} \\
 &= \overline{\rho u_i'' u_k'' \tilde{u}_{j,k}} + \overline{\rho u_j'' u_k'' \tilde{u}_{i,k}} + \overline{(\rho u_k u_j'' u_i'')_k} - \overline{(\rho u_k)_k u_i'' u_j''} \\
 &= \overline{\rho \tilde{R}_{ik} \frac{\partial \tilde{u}_j}{\partial x_k}} + \overline{\rho \tilde{R}_{jk} \frac{\partial \tilde{u}_i}{\partial x_k}} + \frac{\partial}{\partial x_k} (\overline{\rho \tilde{u}_k \tilde{R}_{ij}}) \\
 &\quad - \frac{\partial}{\partial x_k} (\overline{\rho u_i'' u_j'' u_k''}) - \overline{(\rho u_k)_k u_i'' u_j''}
 \end{aligned} \tag{3.28}$$

Pressure term

$$\begin{aligned}
 \overline{u_i'' p_{,j}} + \overline{u_j'' p_{,i}} &= \overline{u_i'' (\overline{p}_{,j} + p'_{,j})} + \overline{u_j'' (\overline{p}_{,i} + p'_{,i})} \\
 &= \overline{u_i'' \overline{p}_{,j}} + \overline{u_j'' \overline{p}_{,i}} + \overline{u_i'' p'_{,j}} + \overline{u_j'' p'_{,i}} \\
 &= \overline{u_i'' \overline{p}_{,j}} + \overline{u_j'' \overline{p}_{,i}} + \overline{(u_i'' p')_{,j}} + \overline{(u_j'' p')_{,i}} - \overline{u_{i,j}'' p'} - \overline{u_{j,i}'' p'} \\
 &= \overline{u_i'' \frac{\partial \overline{p}}{\partial x_j}} + \overline{u_j'' \frac{\partial \overline{p}}{\partial x_i}} + \frac{\partial}{\partial x_k} (u_i'' p' \delta_{jk} + u_j'' p' \delta_{ik}) + p' \left(\frac{\partial u_i''}{\partial x_j} + \frac{\partial u_j''}{\partial x_i} \right)
 \end{aligned} \tag{3.29}$$

Viscous term

$$\begin{aligned}
 \overline{u_i \tau_{kj,k}} + \overline{u_j'' \tau_{ki,k}} &= \overline{u_i'' (\overline{\tau}_{kj,k} + \tau'_{kj,k})} + \overline{u_j'' (\overline{\tau}_{ki,k} + \tau'_{ki,k})} \\
 &= \overline{u_i'' \overline{\tau}_{kj,k}} + \overline{u_i'' \tau'_{kj,k}} + \overline{u_j'' \overline{\tau}_{ki,k}} + \overline{u_j'' \tau'_{ki,k}} \\
 &= \overline{u_i'' \overline{\tau}_{kj,k}} + \overline{u_j'' \overline{\tau}_{ki,k}} + \overline{(u_i'' \tau'_{kj})_k} - \overline{u_{i,k}'' \tau'_{kj}} + \overline{(u_j'' \tau'_{ki})_k} - \overline{u_{j,k}'' \tau'_{ki}} \\
 &= \overline{u_i'' \frac{\partial \overline{\tau}_{jk}}{\partial x_k}} + \overline{u_j'' \frac{\partial \overline{\tau}'_{ik}}{\partial x_k}} - \frac{\partial}{\partial x_k} (\overline{\tau'_{ik} u_j'' + \tau'_{jk} u_i''}) + \tau'_{ik} \frac{\partial u_j''}{\partial x_k} + \tau'_{jk} \frac{\partial u_i''}{\partial x_k}
 \end{aligned} \tag{3.30}$$

Combining the different terms listed above, the Reynolds stress equation can be written in its final form:

$$\frac{\partial}{\partial t}(\bar{\rho}\tilde{R}_{ij}) + \frac{\partial}{\partial x_k}(\bar{\rho}\tilde{u}_k\tilde{R}_{ij}) = \bar{\rho}P_{ij} + \bar{\rho}\Pi_{ij} - \bar{\rho}\epsilon_{ij} + \bar{\rho}D_{ij} + \bar{\rho}M_{ij} \quad . \quad (3.31)$$

The unsteady term and the convective term derive from the same terms of the momentum equation. The terms on the right hand side of the equation represent the production, the redistribution, the destruction, the diffusion and the contribution of the turbulent mass flux due to compressibility effects.

It has to be noticed that the sum of the last term in equation (3.27) and in equation (3.28) vanishes, since they are proportional to the two terms appearing in the instantaneous continuity equation (3.1).

The production term is derived from the convective terms and reads as follows:

$$\bar{\rho}P_{ij} = -\bar{\rho}\tilde{R}_{ik}\frac{\partial\tilde{u}_j}{\partial x_k} - \bar{\rho}\tilde{R}_{jk}\frac{\partial\tilde{u}_i}{\partial x_k} \quad . \quad (3.32)$$

It represents the way in which the kinetic energy can be interchanged between the mean flow and the fluctuations. As W. George wrote in *Lectures for turbulence in the 21st century*: "In order to understand how the overall exchange is accomplished one can think of the terms that appear in the production terms as the working of the Reynolds stresses against the mean velocity gradient of the flow, exactly as the viscous stresses resist deformation by the instantaneous velocity gradient. This energy expended against the Reynolds stresses during deformation by the mean motion ends up in the fluctuating motion [49]". From experimental results it has been observed that almost always the velocity gradient and the Reynolds stresses have opposite signs which means that kinetic energy is removed from the mean motion and added to the fluctuations.

The re-distribution (or pressure-strain correlation) derives from the pressure term and it reads:

$$\bar{\rho}\Pi_{ij} = \overline{p' \left(\frac{\partial u_i''}{\partial x_j} + \frac{\partial u_j''}{\partial x_i} \right)} \quad . \quad (3.33)$$

It is worth noting at this point that normally energy is transferred from the mean flow to only a single component of the fluctuating motions. Nevertheless it has been experimentally observed that all the components of the Reynolds stress tensor have more or less the same order of magnitude [49]. The pressure strain correlation term, also called the re-distribution term, is the factor that determines a uniform distribution of the energy among the components. The destruction term derives from the viscous term. It reads as:

$$\bar{\rho}\epsilon_{ij} = \overline{\tau'_{ik} \frac{\partial u_j''}{\partial x_k} + \tau'_{jk} \frac{\partial u_i''}{\partial x_k}} \quad . \quad (3.34)$$

The fluctuating energy is dissipated because of the work done by fluctuating viscous stresses in resisting deformation of the fluid material by the fluctuating strain stress. This term can be seen as a transfer of turbulent kinetic energy into internal energy.

The diffusion term contains parts that derive from different terms. The pressure diffusion appears in the pressure term, the viscous diffusion in the viscous term and the diffusion due to turbulence itself derives from the convective term. The diffusion reads as follows:

$$\bar{\rho}D_{ij} = -\frac{\partial}{\partial x_k} \left(\overline{\rho u_i'' u_j'' u_k''} + (\overline{p' u_i''} \delta_{jk} + \overline{p' u_j''} \delta_{ik}) - (\overline{\tau'_{ik} u_j''} + \overline{\tau'_{jk} u_i''}) \right) \quad (3.35)$$

This term is a divergence term. For this reason it cannot create or destroy fluctuating energy but only move it around the flow. The spatial transport (diffusion) of fluctuating energy is accomplished in three ways, the first term represents the turbulent transport of kinetic energy by the mean of turbulence itself, the second term the transport of kinetic energy by the mean of pressure diffusion and the last term the molecular diffusion.

The contribution of the turbulent mass flux due to the compressibility effects derives from both the pressure term and the viscous term:

$$\bar{\rho}M_{ij} = \overline{u_i''} \left(\frac{\partial \bar{\tau}_{jk}}{\partial x_k} - \frac{\partial \bar{p}}{\partial x_j} \right) + \overline{u_j''} \left(\frac{\partial \bar{\tau}_{ik}}{\partial x_k} - \frac{\partial \bar{p}}{\partial x_i} \right) \quad (3.36)$$

The pressure part of the above equation represents the pressure work and is another way in which energy is transferred from the mean motion, through the pressure field, to turbulence.

3.4.4. Eddy Viscosity Models

For comparison with the results obtained in this thesis, eddy viscosity models are used and are now shortly introduced. Most of the one- and two-equation turbulence models are based on an equation for the turbulent kinetic energy coupled, for two equations models, with an equation representing some sort of turbulent length scale, mainly ϵ or ω .

Since turbulent kinetic energy is defined as half of the trace of the Reynolds stress tensor, an exact transport equation for this quantity can be derived taking half of the trace of equation (3.31):

$$\begin{aligned} \frac{\partial}{\partial t} (\bar{\rho} \tilde{k}) + \frac{\partial}{\partial x_j} (\bar{\rho} \tilde{u}_j \tilde{k}) = & \bar{\rho} \tilde{R}_{ij} \frac{\partial \tilde{u}_i}{\partial x_j} + \overline{p' \left(\frac{\partial u_i''}{\partial x_i} \right)} + \overline{\left(\tau'_{ij} \frac{\partial u_i''}{\partial x_j} \right)} \\ & - \frac{\partial}{\partial x_j} \left(\overline{\rho \frac{1}{2} u_i'' u_i'' u_j''} + \overline{p' u_j''} - \overline{\tau'_{ij} u_i''} \right) + \overline{u_i''} \left(\frac{\partial \bar{\tau}_{ij}}{\partial x_j} - \frac{\partial \bar{p}}{\partial x_i} \right) \quad (3.37) \end{aligned}$$

It is worth noticing that the second term on the right hand side of equation (3.37) which is analogous to the re-distribution term in (3.33), also called pressure dilatation, vanishes for incompressible flows because the divergence of the velocity field is zero.

Concerning the second equation for the two-equation models, for both ω and ϵ a transport equation is written in analogy to the (modeled) k equation, considering that the physical processes normally observed in the motion of a fluid are unsteadiness, convection, diffusion, dissipation, dispersion and production.

A general $k - \omega$ model is now presented. This kind of models has been preferred to ϵ based models in this work, since it has been observed by Wilcox and Hung [60] that they present a smaller deviation from the law-of-the-wall in compressible regime and are less problematic for adverse pressure-gradient wall bounded flows. The k - and ω -equation in conservation form read as follow:

$$\frac{\partial(\bar{\rho}\tilde{k})}{\partial t} + \frac{\partial(\bar{\rho}\tilde{u}_j\tilde{k})}{\partial x_j} = P - \beta^*\bar{\rho}\omega\tilde{k} + \frac{\partial}{\partial x_j} \left[(\mu + \sigma_k\mu_t) \frac{\partial\tilde{k}}{\partial x_j} \right] \quad (3.38)$$

$$\frac{\partial(\bar{\rho}\omega)}{\partial t} + \frac{\partial(\bar{\rho}\tilde{u}_j\omega)}{\partial x_j} = \frac{\gamma\bar{\rho}}{\mu_t}P - \beta\rho\omega^2 + \frac{\partial}{\partial x_j} \left[(\mu + \sigma_\omega\mu_t) \frac{\partial\omega}{\partial x_j} \right] \quad (3.39)$$

where P is the k production terms and has different definitions depending on the turbulence model chosen.

The terms on the left hand side of equations (3.38) and (3.39) represent the unsteady term and the convection term while the terms on the right hand side define the production, the destruction and the diffusion. β^* , β , σ_k and σ_ω are model constants.

$k - \omega$ models have been developed for the case of incompressible flows, i.e. constant density and molecular viscosity, thus no term for the pressure diffusion, that is generally modeled together with the molecular diffusion, and for the pressure work and the pressure dilatation, which are not part of the incompressible formulation, appears in the equation. However, these models are largely used for the simulation of compressible flows since in many instances they are able to predict the flow characteristics with reasonable accuracy. For this kind of simulations, the compressibility of the flow is taken into account in the equations using a mass conservation equation based on variable mean density. This approach is based on the hypothesis of Morkovin who stated that one can account for the compressibility effects in turbulent flow just by mean density variations. Unluckily, incompressible models perform progressively worse in boundary layer flows with increasing Mach number, particularly for cold wall cases.

3.5. SSG/LRR- ω Model

The Reynolds stress model chosen to be implemented here is the SSG/LRR- ω [43] [41]. This model has been developed at DLR (Deutsches Zentrum für Luft- und Raumfahrt) by Eisfeld and is the combination of the Speziale, Sarkar and Gatski (SSG) model [107] in the far field and the Launder, Reece and Rodi (LRR) model [72] near the wall. The idea is to extend the applicability of the SSG model to wall-bounded flows in conjunction with an ω -equation. The LRR model chosen is a simplified version by Wilcox who coupled it with

his ω -equation [113]. The development of the SSG/LRR- ω model follows the ideas used by Menter for the SST model. On the one hand an ϵ -based model is preferred away from the wall to avoid the high sensitivity to freestream turbulence observed in ω -based models. On the other hand the choice of an ω based model near the wall is justified by the desire of having a low Reynolds number model allowing integration up to the wall. As Wilcox shows, the near-wall behavior of second-order closure models is strongly influenced by the scale-determining equation [113]. Models based on an ω -equation often predict acceptable values of the wall integration constant and are quite easy to integrate through the viscous sublayer with respect to models based on an ϵ -equations. The ω -equation of Menter [78] has been chosen to provide a turbulent length scale for the present model. The blending function of Menter has been employed to smoothly blend the coefficients of the two models. The production term does not need modeling, because it only depends on quantities for which an equation is solved. The other terms need to be modeled and the way the modeling is carried out determines the particular type of Reynolds Stress Model. Here the SSG/LRR- ω model is presented.

The re-distribution term is modeled as follows

$$\bar{\rho}\Pi_{ij} = -(C_1\bar{\rho}\epsilon + \frac{1}{2}C_1^*\bar{\rho}P_{kk})\tilde{b}_{ij} + C_2\bar{\rho}\epsilon(\tilde{b}_{ik}\tilde{b}_{kj} - \frac{1}{3}\tilde{b}_{mn}\tilde{b}_{mn}\delta_{ij}) \quad (3.40)$$

$$+(C_3 - C_3^*\sqrt{II})\bar{\rho}\tilde{k}\tilde{S}_{ij}^* + C_4\bar{\rho}\tilde{k}(\tilde{b}_{ik}\tilde{S}_{jk} + \tilde{b}_{jk}\tilde{S}_{ik} - \frac{2}{3}\tilde{b}_{mn}\tilde{S}_{mn}\delta_{ij}) + C_5\bar{\rho}\tilde{k}(\tilde{b}_{ik}\tilde{W}_{jk} + \tilde{b}_{jk}\tilde{W}_{ik}),$$

where all the coefficients are obtained inserting the values in Table 3.1 in the blending function (3.52) described below. In the above equation, \tilde{k} is the turbulent kinetic energy and ϵ is the specific dissipation. The tensors appearing in equation (3.40) are the anisotropy tensor and II its second invariant,

$$\tilde{b}_{ij} = \frac{\tilde{R}_{ij}}{2\tilde{k}} - \frac{\delta_{ij}}{3} \quad , \quad II = \tilde{b}_{ij}\tilde{b}_{ij} \quad , \quad (3.41)$$

\tilde{S} the strain rate tensor, \tilde{W} the rotation tensor (respectively the symmetric and skew part of the velocity gradient):

$$\tilde{S}_{ij} = \frac{1}{2} \left(\frac{\partial \tilde{u}_i}{\partial x_j} + \frac{\partial \tilde{u}_j}{\partial x_i} \right) \quad , \quad \tilde{W}_{ij} = \frac{1}{2} \left(\frac{\partial \tilde{u}_i}{\partial x_j} - \frac{\partial \tilde{u}_j}{\partial x_i} \right) \quad . \quad (3.42)$$

\tilde{S}_{ij}^* is the traceless strain rate tensor defined as:

$$\tilde{S}_{ij}^* = \frac{1}{2} \left(\frac{\partial \tilde{u}_i}{\partial x_j} + \frac{\partial \tilde{u}_j}{\partial x_i} \right) - \frac{1}{3} \frac{\partial \tilde{u}_k}{\partial x_k} \delta_{ij} \quad . \quad (3.43)$$

Finally, the specific dissipation is computed from the length scale.

$$\epsilon = C_\mu \tilde{k} \omega \quad , \quad (3.44)$$

where $C_\mu=0.09$.

Table 3.1. Coefficients of SSG and LRR model for the re-distribution term.

	C_1	C_1^*	C_2	C_3	C_3^*	C_4	C_5
SSG	3.4	1.8	4.2	0.8	1.3	1.25	0.4
LRR	3.6	0	0	0.8	0	2.0	1.11

The destruction term is modeled in an isotropic way as:

$$\bar{\rho}\epsilon_{ij} = \frac{2}{3}C_\mu\bar{\rho}\tilde{k}\omega\delta_{ij} \quad . \quad (3.45)$$

The role of the diffusion term is transporting the fluctuating kinetic energy from one place to another of the flow. It is known that on average the transport terms move the Reynolds stresses from region of higher concentration to region of lower concentration. For this reason, the diffusion term is modeled as proportional to the gradient of the Reynolds stresses themselves. Even though the assumption is not always locally true, i.e., Reynolds stresses can be transported from regions of low concentration to regions of high concentration, this simple idea, employed also in eddy viscosity models, has provided good results in many type of flows.

The generalized gradient diffusion model is chosen for this term:

$$\bar{\rho}D_{ij} = \frac{\partial}{\partial x_k} \left(\left(\bar{\mu}\delta_{kl} + D^{(GGD)}\frac{\bar{\rho}}{\omega}\tilde{R}_{kl} \right) \frac{\partial\tilde{R}_{ij}}{\partial x_l} \right) \quad . \quad (3.46)$$

The value of the constant $D^{(GGD)}$ is computed by the equation:

$$D^{(GGD)} = F\sigma^* + (1 - F)\frac{C_s}{C_\mu} \quad . \quad (3.47)$$

F is the blending equation in (3.52), $\sigma^* = 0.5$ and $C_s = 0.22$.

Finally the term $\bar{\rho}M_{ij}$, which represents a measure of the effects of compressibility through variations in density, is neglected. This term is generally neglected since it is difficult to model and no satisfactory models are presented in the literature yet.

Due to the nature of turbulence, an equation for the turbulence length scale is necessary to determine the dissipative length scale, i.e., the length scale of the eddies at which the energy cascade ends and the energy is dissipated into internal energy. In the chosen model, the Menter ω -equation is used for providing the turbulence length scale [78] and reads as follows:

$$\frac{\partial}{\partial t}(\bar{\rho}\omega) + \frac{\partial}{\partial x_k}(\bar{\rho}\tilde{u}_k\omega) = \bar{\rho}P^\omega - \bar{\rho}D^\omega + \frac{\partial}{\partial x_k} \left(\left(\bar{\mu} + \sigma_\omega\frac{\bar{\rho}\tilde{k}}{\omega} \right) \frac{\partial\omega}{\partial x_k} \right) + \bar{\rho}C_D \quad , \quad (3.48)$$

with the production term

$$\bar{\rho}P^\omega = -\alpha_\omega \frac{\omega}{\tilde{k}} \tilde{R}_{ik} \frac{\partial \tilde{u}_i}{\partial x_k} , \quad (3.49)$$

the destruction term

$$\bar{\rho}D^\omega = \beta_\omega \bar{\rho} \omega^2 , \quad (3.50)$$

and the cross-diffusion term

$$\bar{\rho}C_D = \sigma_d \frac{\bar{\rho}}{\omega} \max \left(\frac{\partial \tilde{k}}{\partial x_k} \frac{\partial \omega}{\partial x_k}; 0 \right) . \quad (3.51)$$

The coefficients of the ω -equation, listed in Table 3.2 as well as those of the Reynolds stresses are blended using the following function:

$$\phi = F\phi^{LRR} + (1 - F)\phi^{SSG} . \quad (3.52)$$

Table 3.2. Coefficients for the ω -equation.

	α_ω	β_ω	σ_ω	σ_d
SSG	0.44	0.0828	0.856	$2\sigma_\omega^{SSG}$
LRR	0.5556	0.075	0.5	0

The blending function of Menter is defined as:

$$F = \tanh(\zeta^4) , \quad \zeta = \min \left(\max \left(\frac{\sqrt{\tilde{k}}}{C_\mu \omega d}; \frac{500\bar{\mu}}{\bar{\rho}\omega d^2} \right); \frac{4\sigma_\omega^{(SSG)} \bar{\rho} \tilde{k}}{\bar{\rho} C_D^{(SSG)} d^2} \right) . \quad (3.53)$$

where d is the minimum distance to the wall.

3.5.1. Additional Terms

During the average process required by the RANS approach, some additional terms appear in the averaged Navier-Stokes equations representing the contribution of turbulence to the mean flow. The modeling of the Reynolds stress tensor has been largely discussed above. For the remaining terms an equation is needed for both RSM and eddy viscosity models.

The turbulent heat flux is generally modeled using a Fourier type approach. Alternatively it is possible to write an exact transport equation for the specific enthalpy, multiply it by a fluctuating velocity component and re-arrange the terms in a similar way as done for deriving the RANS equations. At this point new terms appear in the equation. For this reason this approach is rarely followed.

The Fourier assumption that state a proportionality between heat flux and the temperature gradient is commonly used in both eddy viscosity and Reynolds stress models:

$$q_k^{(t)} = -\lambda_t \frac{\partial \tilde{T}}{\partial x_k}, \quad \text{with} \quad \lambda_t = \frac{C_p \mu_t}{Pr_t}, \quad (3.54)$$

where \tilde{T} is the mean temperature and λ_t the eddy heat conductivity. In this work the turbulent Prandtl number (Pr_t) is treated as a constant and is equal to $Pr_t = 0.9$. The turbulent eddy viscosity can be obtained from the other turbulence variables using the equation:

$$\mu_t = \frac{\bar{\rho} \tilde{k}}{\omega} = \bar{\rho} C_\mu \frac{k^2}{\epsilon}. \quad (3.55)$$

The relations in equation (3.55) are the standard definition of the turbulent viscosity for $k - \epsilon$ and $k - \omega$ based models (and also for the RSM described above). However, many authors have used modified definitions with additional constants or variables limitation. As an example of the latter approach one can refer to the Wilcox $k - \omega$ model of 2008 [114].

The last term is the diffusion of the turbulent kinetic energy associated with the turbulent transport and diffusion terms. For eddy viscosity models, it is often neglected while for the Reynolds stress model it is modeled as half the trace of the Reynolds stresses diffusion term:

$$\bar{\rho} D^{(k)} \approx \frac{\bar{\rho} D_{kk}}{2}. \quad (3.56)$$

3.5.2. Boundary Conditions at Solid Walls

The natural boundary condition for the Reynolds stresses, which are velocity fluctuations, is that of a zero value at wall. For the ω -equation it is harder to define a suitable condition since its value tends to infinity close to a solid wall. Let us consider the transport equation for ω (3.48). A steady state flow is assumed. Moving close to the wall the viscous forces dominate so that the convective fluxes, the production and the cross-diffusion can be considered negligible [63]. Under these assumptions, the ω -equation can be rewritten as:

$$\frac{\partial}{\partial x_k} \left(\mu \frac{\partial \omega}{\partial x_k} \right) = \beta^* \bar{\rho} \omega k. \quad (3.57)$$

The asymptotic solution for this equation moving close to the wall has the following form:

$$\omega_w = \lim_{d \rightarrow 0} \frac{6\mu}{\bar{\rho} \beta^* d^2} = \frac{6\mu_w}{\rho_w \beta^*} \lim_{d \rightarrow 0} \frac{1}{d^2}, \quad (3.58)$$

where d is the distance from the wall. This analysis shows that ω goes to infinity when approaching a solid wall. Clearly an infinite value cannot be prescribed in a numerical simulation and for this reason different approaches have been proposed during the years to find a satisfactory solution to this problem. The different approaches used in this work are presented in Section 4.2.2

3.6. Reynolds Stress Models versus Eddy Viscosity Models

The main reason to use a Reynolds stress model instead of an eddy viscosity model is to account for non-isotropic effects in turbulence. Even though eddy viscosity models are able to produce reliable results for attached boundary layer flows, they experience deficiencies concerning the prediction of shock location, separation or free vortices and more generally for flows that undergo a sudden change in mean strain rate. Since the Reynolds stresses adjust to changes in the mean flow at a rate unrelated to it, it is not surprising that the Boussinesq hypothesis fails. Furthermore eddy viscosity models predict isotropic normal Reynolds stresses at the wall or in flows that experience rapid dilatation or significant streamlines curvatures as opposed to what observed in experiments. Indeed the Boussinesq approach, which implies that turbulence is an isotropic phenomenon, breaks down in flows characterized by strong curvature, swirling flows and flows with strong acceleration or retardation.

One of the main reasons for the prediction superiority of second order closure models relies in the production term. Even though the production term clearly has the same form in the k equation (3.38) and in the Reynolds stresses equations (3.32), for the RSM, which needs no modeling, it is an exact term. This allows the model to be able to naturally include effects of stresses increase or decrease due to curvature, acceleration or deceleration, swirling flow and so on. In this way, second order closure models represent a potential gain in universality since all these effects are intrinsic to the model itself and do not need ad-hoc modification and corrections. In addition, RSM take into account non-equilibrium effects in the sense that the Reynolds stresses do not respond instantaneously to changes in the strain rate, as it happens in eddy viscosity models, but realistically delay their response in time and space. The presence of terms as the dissipation and the turbulent transport that refer to a time scale different from the scale of the mean flow indicates that history effects are better represented than in eddy viscosity models. Finally in Reynolds stress transport equations there appear no a-priori reason for the normal Reynolds stresses to be equal when the mean strain rate vanishes. This allows the model to capture flows in which a sudden change in the strain rate occurs.

From a numerical point of view, beside the increased computational effort due to the 7-equations from the turbulence model, RSM are characterized by a decreased numerical stability which has prevented their use for industrial applications. Eddy viscosity models increase the diffusion coefficient of the momentum and the heat flux which are the dissipative terms of the mean flow equations. This has a positive effect on the stability of the models especially in the boundary layer where the eddy viscosity can exceed the fluid viscosity by one order of magnitude. On the contrary in Reynolds stress models there is no additional dissipation since there is no eddy viscosity that sums up to the fluid viscosity but the turbulence equations are coupled to the mean flow via a divergence term which could potentially destabilize the solution.

4. QUADFLOW code

The results presented in this thesis have been obtained using an in-house flow solver. QUADFLOW [21] has been developed in the framework of the Collaborative Research Center SFB 401 *Flow Modulation and Fluid-Structure Interaction at Airplane Wings* at the RWTH Aachen University. QUADFLOW relies on an integrated concept consisting of grid generation, grid adaptation and a flow solver. A general overview of the code is now given with particular emphasis on the two features which have been the focus of this work: turbulence models and adaptive simulations. In the second part of the chapter, the implementation of the RSM described in Section 3.5 is discussed in detail together with the numerical method used in combination with the turbulence model.

4.1. General Features

QUADFLOW solves the Reynolds Averaged Navier-Stokes equations for unsteady, compressible fluid flow in two and three dimensions. Furthermore, it is able to solve aeroelastic problems using a partitioned approach [9,97], real gas problems considering air as composed by five species [69, 115] and gas mixture problems employing a modified Jachimowski model [51]. The flow solver in QUADFLOW is based on a cell-centered finite volume discretization. The mesh is treated as fully unstructured and composed of simply connected elements with otherwise arbitrary topology. This approach, also called "grid-independent", is especially suited for dealing with hanging nodes appearing in adaptive meshes. For the discretization of the convective fluxes, upwind methods based on both flux-vector splitting and flux-difference splitting are available. A linear reconstruction of the primitive variables is performed to locally achieve second order accuracy in space, and the Venkatakrishnan slope limiter is employed to avoid oscillations typical of second order schemes [111]. For the discretization of the viscous fluxes, a modified central difference method is used [20]. For the time integration, a second order accurate explicit Runge-Kutta scheme and first and second order fully implicit methods are available. In the latter case, the non-linear system of equations is solved by a Newton-Krylov method. Details on the schemes implemented in the code can be found in [20, 22]. The flow solver has been parallelized using the Message Passing Interface (MPI) and is portable across a wide range of computer architectures [23].

Two grid generators have been employed in this work. The grid generator Gnagg is part of the QUADFLOW paradigm and generates block structured grids for adaptive simulations. It provides grid mappings for each block of a multiblock topology. These mappings are B-splines that are characterized typically by a small number of control points. From these mappings, locally refined grids are constructed during the simulation by point

evaluation. This grid generator has been developed at the Institut für Geometrie und Praktische Mathematik (IGPM) at RWTH Aachen University within the frame of the SFB 401 [71]. The grid generator MegaCads is part of the MEGAFLOW project of the DLR [68] and generates structured multiblock grids which can also be used in QUADFLOW simulations.

4.1.1. Turbulence and Transition Models

For the treatment of turbulent flows, the user can choose from a wide choice of eddy viscosity models. All the turbulence models present in the solver have been implemented as in the original papers and no constants tuning has been performed afterwards. From the class of one-equation turbulence models, the classical Spalart-Allmaras model in its original version [106], in the version modified by Ashford [8], and in the version proposed by Edwards and Chandra [40] is available. Concerning two-equation linear eddy viscosity models, the LLR $k-\omega$ model [94], the Menter SST $k-\omega$ model [78] and the Wilcox $k-\omega$ model in the original version of 1988 [113] and in the latest version of 2008 [114] are available. A $k-\omega$ explicit algebraic Reynolds stress model (EARSM) developed by Hellsten [58] is also implemented. The turbulence models have been used for the prediction of different flow regimes from subsonic to hypersonic [21, 66, 95, 97]. An assessment of the available turbulence models for high-speed wall-bounded flows can be found in Nguyen et al. [82]. For the simulation of hypersonic flows mainly the SST model has been employed [64, 65].

Furthermore, the SST turbulence model can be extended by the two-equation $\gamma-Re_\theta$ -transition model from Menter [77] in order to predict flows characterized by laminar to turbulent transition. The coupling of the SST model with the $\gamma-Re_\theta$ -transition model has been driven by the need of reproducing results from wind tunnel experiments. Even though the flow around a hypersonic vehicle in flight is turbulent everywhere, this is not the case for small scale wind tunnel experiments where a large portion of the model lies in a laminar flow region. For this reason laminar to turbulent transition plays an important role for this kind of configuration in which the location of the transition point strongly affects the overall flow.

Another way to reproduce the laminar to turbulent transition measured in the experimental results is the use of a fixed transition point. The location of the transition point is defined by the user prescribing a region in the computational domain where the source terms of the turbulence equations are set to zero. The results obtained from the RSM, using a transition points for transitional test cases, have been mainly compared with the SST model, coupled with the transition model for the transitional test cases. This has been done since the two models employ the same ω -equation for the prediction of the turbulence length scale so that the differences visible between the models are mainly related to the way the Reynolds stress tensor is treated. For simulations where substantial differences between the two models have been observed, additional comparisons have been performed using the $k-\omega$ models of Wilcox and the $k-\omega$ EARSM from Hellsten.

4.1.2. Multiscale Analysis for Grid Adaptation

The mesh adaptation is performed by means of multiscale techniques similar to those used in data compression. Starting point of this strategy is a sequence of nested grids $G_l := \{\Omega_{li}\}_{i \in I_l}$ that can be obtained by successfully refining the cells on a given coarsest scale $l = 0$, i.e., each cell on a coarse scale l is the union of cells on the finer scale $l + 1$. The index set I_l represents the enumeration of the cells corresponding to the grid G_l and corresponding averages $\bar{\mathbf{u}}_l$. By means of this sequence, the average $\bar{\mathbf{u}}_L$ on the finest level L is successively decomposed into a sequence of averages on the coarsest level $\bar{\mathbf{u}}_0$ and details $\bar{\mathbf{d}}_l$, $l = 0, \dots, L - 1$. This is realized by a multiscale analysis using biorthogonal wavelets [21].

The detail coefficients can be interpreted as differences between successive refinement levels, which become negligibly small in regions where the solution is sufficiently smooth. The set of significant details can now be introduced $D_\epsilon := \{(l, i) : |d_{l,i}| > \epsilon_l\}$, where $\epsilon_l = 2^{l-L}\epsilon$ is a level-dependent threshold value. The user defined parameter ϵ determines the sensitivity of the adaptation. At this point one has to determine the adaptive grid on the new time level. Since the corresponding averages, respectively details are not yet available, one has to predict all details on the new time level that can become significant due to the evolution by means of the details on the old time level. In order to do that, a heuristic approach is applied taking into account the finite speed of propagation and the fact that gradients may become steeper causing significant details in the local neighborhood and on higher refinement levels, respectively. By means of D_ϵ a locally refined grid with hanging nodes is determined by proceeding from coarse to fine. If there exists a significant detail the corresponding cell is refined. For the flow fields considered, the number of significant detail coefficients $N_D := \#D_\epsilon$, is much smaller than the number of averages N_L corresponding to the uniform finest scale, i.e., the computational time and memory requirements may be significantly reduced. In order to perform an adaptive simulation, the user needs to set certain parameters:

- L : number of refinement levels. This value should be chosen in a way that the grid on the finest level satisfies requirements related for example to the desired wall resolution and the cell size in particular flow regions.
- ϵ : threshold value for performing grid adaptation. If a detail is larger than ϵ_l the adaptation is activated for that cell. The choice of this parameter strongly affects the grid refinement. A too large value of the threshold leads to a grid that is not able to properly capture the flow structures while a too small value leads to an almost uniformly refined grid.
- variables by which to perform grid adaptation: the adaptation process can be driven by any of the conserved flow variables including turbulent ones. The user can chose which variable should be considered for activating the adaptation. This means that their details are compared with the threshold and if one of them is larger than ϵ in a cell adaptation is performed.

- adaptation method: adaptation can be performed after a user defined number of iterations or once the averaged density residual has dropped by a user defined factor.

Simulations on adaptive grids have been performed to investigate different configurations [97], [20]. The influence of the adaptation parameters on the results and the best choice for the hypersonic simulations are discussed Section 4.3.5.

4.2. Computational Approach for the RSM

The SSG/LRR- ω 7-equations differential Reynolds stress model by Einfeld [41], described in Section 3.5, has been implemented in the flow solver QUADFLOW. An overview on the choice of the numerical methods, boundary conditions and convergence criteria used to perform the simulations is presented in the next sections.

4.2.1. Numerical Methods

For the discretization of convective fluxes, flux-difference splitting methods are preferred for the solution of hypersonic flows since they are less dissipative than the flux-vector splitting method [30, 110]. Particularly two methods are employed: the HLLC scheme by Batten and Leschziner [11] and the AUSMDV scheme by Wada and Liou [112].

In order to obtain second order accuracy, a linear reconstruction is performed and the Venkatakrisnan slope limiter is employed to avoid oscillations typical of second-order schemes. In order to accelerate the convergence, simulations are often run using first-order scheme in space until the residual drops under a user-defined level (usually 10^{-2}) and then second-order accuracy is prescribed.

For the treatment of viscous fluxes, only one approach is available in QUADFLOW so that a modified central difference method is always used [20].

The simulations considered in this work are all steady state problems so that time plays the role of an iteration parameter to achieve asymptotically stationary flow in the computation. Unsteady simulations using the RSM are possible but are not considered in this thesis. The numerical methods employed for time integration are a five-stage second-order-accurate Runge-Kutta explicit scheme and the first-order-accurate implicit Euler integration scheme. Generally, an implicit integration is preferred because it allows for larger CFL numbers and consequently a faster convergence rate. However, since the simulations are always started using uniform variables in the whole field, the flow undergoes a period of transient evolution where it cannot be considered stationary. In several cases this behavior leads to difficulties in the solution convergence during the first time steps. Simulations that experience these kind of difficulties are started using an explicit time integration and after the residuals have started to drop the time integration is changed to implicit to achieve faster convergence to the steady state. For simulations with strong shock waves and significant boundary layer separation it is necessary to run the simulations solely explicitly. Three dimensional simulations are run explicit in time due to the very high memory requirements for implicit integration.

4.2.2. Initial and Boundary Conditions

The turbulent variables are initialized by the user-defined freestream values. First of all, the turbulent kinetic energy (which is not a model variable) is computed from the freestream turbulence intensity I , the Mach number M_∞ and the reference speed of sound c_∞ .

$$\tilde{k}_\infty = \frac{3}{2}(I \cdot M_\infty \cdot c_\infty)^2, \quad I = \frac{u_\infty''}{\tilde{u}_\infty}. \quad (4.1)$$

Then the initial values for the Reynolds stresses are computed by uniformly distributing the turbulent kinetic energy among the diagonal components of the tensor and considering the off-diagonal terms as zero:

$$\tilde{R}_{ii\infty} = \frac{2}{3}\tilde{k}_\infty, \quad \tilde{R}_{ij\infty} = 0 \quad \forall i \neq j. \quad (4.2)$$

The initial value for ω_∞ can be written using the definition of the turbulent viscosity as follows:

$$\tilde{\omega}_\infty = \frac{\bar{\rho}_\infty \cdot \tilde{k}_\infty}{\mu_{t\infty}}; \quad (4.3)$$

where the initial value for the turbulent viscosity is computed by means of the user-defined ratio between the turbulent and the laminar viscosity:

$$\text{visc - ratio} = \frac{\mu_{t\infty}}{\mu_{l\infty}}. \quad (4.4)$$

For solid walls, two conditions need to be imposed: the no-slip condition and a condition for the energy equation [33]. For what concerns the no-slip condition, two kinds of implementations are available:

- **Strong boundary conditions:** at the wall, the coordinate location that is associated with the vector of the unknowns, is shifted from the cell center to the midpoint of the corresponding wall edge. Advantages are that at each iteration the boundary conditions are strongly enforced for the wall cells. The no-slip condition at the wall is then imposed modifying the momentum equation.
- **Weak boundary conditions:** the no-slip condition is imposed modifying the viscous fluxes at the wall. The component of the gradient in wall normal direction is computed by the difference between the value in the cell center and the value at the wall which is forced to be zero. In this way, the tangential component of the gradient is always zero [33].

For the energy equation two choices are available as described below:

- **Isothermal wall:** a constant temperature is imposed at the wall.

- **Adiabatic wall:** the normal derivative of the temperature is set to zero by imposing that the temperature at the wall face is the same as the temperature in the cell center so that there is no heat transfer between the wall and the fluid.

Generally, a strong condition at the wall is chosen together with an isothermal wall. For simulations where an adiabatic wall is assumed, a weak boundary condition has to be used because right now adiabatic flow conditions are only implemented in combination with weak conditions.

For what concerns turbulent quantities, the Reynolds stresses, which are velocity fluctuations, are set to zero at the solid walls:

$$\tilde{R}_{ij} = 0 \quad \forall i, j \quad . \quad (4.5)$$

Furthermore, three possible ω -wall conditions are considered.

ω -wall condition by Menter

The Menter approach is considered as the natural choice for the Reynolds stress model since the ω -equation chosen is by Menter [78], as well. In his approach, Menter uses the asymptotic behavior of ω from equation (3.58) and prescribes as wall condition:

$$\omega_w = C_M \frac{6\mu_w}{\rho_w \beta^* d^2} \quad . \quad (4.6)$$

Here d is defined as the distance of the cell center (for strong boundary conditions this is the value before moving the cell center to the wall) to the solid wall. The subscript $_w$ refers to values at the wall. The constant C_M is the Menter constant and is generally set to 10. This condition is clearly dependent on the grid resolution.

ω -wall condition by Rudnik

In his approach, Rudnik tries to improve the disadvantages of the direct dependence of the Menter condition on the grid resolution [92]. The wall value for ω is prescribed using a reference length, L_{ref} , that should depend on the model geometry. In this way the wall distance d is defined as:

$$d = C_R \cdot L_{ref} \quad . \quad (4.7)$$

The ω -value at the wall can then be imposed as follows:

$$\omega_w = \frac{6\mu_w}{\rho_w \beta^* (C_R \cdot L_{ref})^2} \quad , \quad (4.8)$$

where the constant C_R has to be prescribed in the order of magnitude of the first grid spacing.

ω -wall condition by Wilcox

The ω -wall condition proposed by Wilcox relies on the definition of the surface roughness [113] and reads as:

$$\omega_w = \frac{u_\tau^2 \rho_w}{\mu_w} S_R \quad , \quad (4.9)$$

where

$$S_R = (50/k_R^+)^2 \quad , \quad k_R^+ < 25 \quad \text{and} \quad u_\tau = \sqrt{\frac{\mu_w}{\rho_w} \left| \frac{\partial \mathbf{u}}{\partial n} \right|_w} \quad (4.10)$$

The variable $k_R^+ = u_\tau k_R \rho_w / \mu_w$ is the scaled surface roughness height. For smooth walls k_R^+ is required to be smaller than 5.

For hypersonic flows, the inflow conditions are prescribed using the freestream values while the outflow conditions are determined by quantities being extrapolated from the interior of the domain.

4.2.3. Convergence Criteria

In order to prove that a simulation has reached the steady state solution, each code controls that some convergence criteria have been satisfied. In QUADFLOW, convergence is measured by the relative residual of density which is defined as the L^1 -norm of the density residuals normalized by the initial density residual. To the author's experience, steady state simulations can be considered converged when the relative density residual drops below 10^{-6} . This has been proven to be sufficient to obtain a converged solution in terms of pressure, skin friction coefficient and heat fluxes at the wall.

To confirm this, for some test cases the computation has been continued until the density residual decreased below 10^{-8} and no differences were visible between the obtained solution and the solution obtained using the standard convergence criteria. Generally, once the convergence criteria has been satisfied, the simulation is continued for 10,000 iterations for an explicit time integration or 500 iterations for an implicit time integration. The results before and after are compared and in case differences between the two solutions are found the simulation is continued. Figure 4.1 shows the behavior of the density residual relative to two solutions obtained by applying explicit and implicit time integration. Details of the test case are given in Section 5.2.2. After a certain amount of iterations, 5,000 for implicit and 25,000 for explicit integration, the residual starts to drop steadily and reaches the desired value. At this point the convergence of the solution has been verified as explained above.

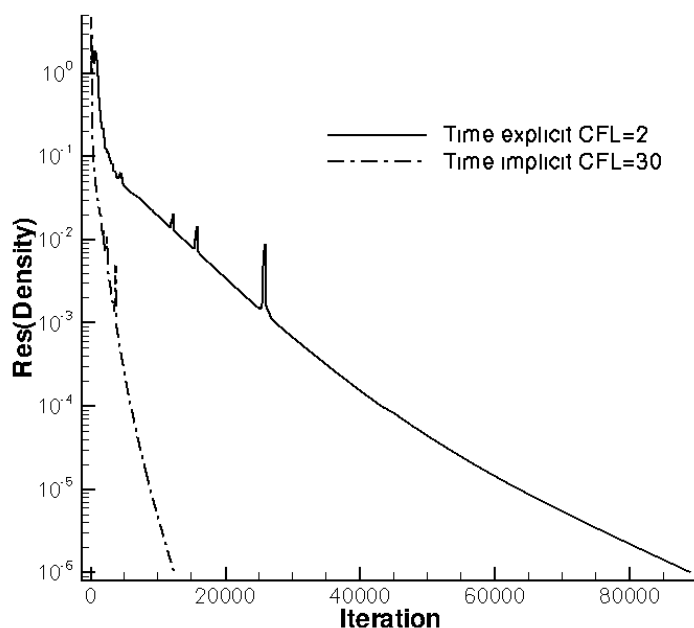


Figure 4.1. Convergence rate for explicit and implicit time integration for the 15 degrees compression corner.

4.3. RSM Implementation

In order to accommodate the seven equations of the turbulence model, the QUADFLOW solver has been modified. Modifications of the input routines to allow the call to the RSM as well as of the output routines for getting results concerning the values of the additional turbulence variables have been required. Some details of the main changes required are given in the next sections.

4.3.1. Non-Dimensional Form of the RSM Equations

For the numerical solution of the conservation laws in QUADFLOW, a dimensionless form of the governing equations is employed [20]. In order to derive it, a set of reference values is needed. These are, in our case, the reference length l_{ref} , the reference velocity u_{ref} , the reference density ρ_{ref} , the reference pressure p_{ref} and the reference viscosity μ_{ref} . Using these reference values a transformation of variables is performed.

$$\begin{aligned}
 \hat{t} &:= \frac{t}{t_{ref}} , & \hat{x} &:= \frac{x}{l_{ref}} , \\
 \hat{\rho} &:= \frac{\rho}{\rho_{ref}} , & \hat{u} &:= \frac{u}{u_{ref}} , \\
 \hat{p} &:= \frac{p}{p_{ref}} , & \hat{\tau} &:= \frac{\tau}{\mu_{ref} u_{ref} / l_{ref}} , \\
 \hat{R}_{ij} &:= \frac{\tilde{R}_{ij}}{u_{ref} u_{ref}} , & \hat{\omega} &:= \frac{\tilde{\omega}}{t_{ref}} .
 \end{aligned} \tag{4.11}$$

Finally some important non-dimensional coefficients are defined. These are the Reynolds number and the Strouhal number, respectively:

$$Re_{ref} := \frac{\rho_{ref} u_{ref} l_{ref}}{\mu_{ref}} , \quad Sr_{ref} := \frac{l_{ref}}{u_{ref} t_{ref}} . \tag{4.12}$$

The state of reference for the time t_{ref} and for the velocity u_{ref} are chosen in such a manner that the Strouhal number (as well as the Euler number that appears in the momentum equation) are equal to one.

The differential operators deriving from this change of coordinates are:

$$\frac{\partial}{\partial \hat{t}} = t_{ref} \frac{\partial}{\partial t} , \quad \frac{\partial}{\partial \hat{x}_j} = l_{ref} \frac{\partial}{\partial x_j} , \quad \frac{\partial^2}{\partial \hat{x}_i \partial \hat{x}_j} = l_{ref}^2 \frac{\partial^2}{\partial x_i \partial x_j} \tag{4.13}$$

The non-dimensional formulation of the Reynolds stresses, in equation (3.31), is derived here.

$$\begin{aligned}
 Sr_{ref} \frac{\partial}{\partial \hat{t}} (\hat{\rho} \hat{R}_{ij}) + \frac{\partial}{\partial \hat{x}_k} (\hat{\rho} \hat{U}_k \hat{R}_{ij}) = & \tag{4.14} \\
 \hat{\rho} \hat{P}_{ij} + \hat{\rho} \hat{\Pi}_{ij} - \hat{\rho} \hat{\epsilon}_{ij} + \frac{\partial}{\partial \hat{x}_k} \left(\left(\frac{1}{Re_{ref}} \hat{\mu} \delta_{kl} + D^{(GGD)} \frac{\hat{\rho}}{\hat{\omega}} \hat{R}_{kl} \right) \frac{\partial \hat{R}_{ij}}{\partial \hat{x}_l} \right)
 \end{aligned}$$

The non-dimensional form of the ω -equation in (3.48), reads as:

$$\begin{aligned}
 Sr_{ref} \frac{\partial}{\partial \hat{t}} (\hat{\rho} \hat{\omega}) + \frac{\partial}{\partial \hat{x}_k} (\hat{\rho} \hat{U}_k \hat{\omega}) = & \tag{4.15} \\
 \hat{\rho} \hat{P}^\omega - \hat{\rho} \hat{D}^\omega + \frac{\partial}{\partial \hat{x}_k} \left(\left(\frac{1}{Re_{ref}} \hat{\mu} + \sigma_\omega \frac{\hat{\rho} \hat{k}}{\hat{\omega}} \right) \frac{\partial \hat{\omega}}{\partial \hat{x}_k} \right) + \hat{\rho} \hat{C}_D
 \end{aligned}$$

4.3.2. Source Terms

For the computation of the source terms, some preliminary steps need to be performed. In order to minimize the number of operations required, the cross diffusion term in equation (3.51) needs to be computed at first. Using the cross diffusion, a value for the blending function in equation (3.53) can be obtained. This is subsequently used for blending the

coefficient of the source terms. After these two operations, the different terms can be called in any order.

During the implementation of the source terms, the difference between the traceless strain rate tensor and the strain rate tensor appearing in the re-distribution term in equation (3.40) has been dropped, as it is also assumed in the original paper by Einfeld [41]. For the implicit time integration the Jacobian of the source terms has been computed using Maple [1], and the so derived derivatives have been implemented into the flow solver.

4.3.3. Turbulence Contribution to the Mean Flow

For the contribution of turbulence to the mean momentum equation a modification of the viscous fluxes is required. In the eddy-viscosity models, the following term needs to be implemented:

$$\frac{\partial}{\partial x_k} \left(\bar{\rho} \tilde{R}_{ik} + \bar{\tau}_{ik} \right) = \frac{\partial}{\partial x_k} \left(\bar{\rho} \tilde{R}_{ik} + 2\mu_l S_{ij}^* \right) = \frac{\partial}{\partial x_k} \left(2(\mu_l + \mu_t) S_{ij}^* \right) . \quad (4.16)$$

When applying the RSM, the Reynolds stresses are explicitly computed, therefore the last step of equation (4.16) is not valid and the Reynolds stresses are inserted directly in the formulation at the step before.

Considering the energy equation in (3.18), three additional terms appear as contribution of the turbulent motion to the mean flow. The term containing the Reynolds stress tensor is added to the viscous stresses. For the turbulent heat fluxes a value of the turbulent viscosity is required, which is obtained computing the turbulent kinetic energy from the Reynolds stress tensor as in equations (3.55) and (3.24). Finally the term $\bar{\rho} D^{(k)}$, in equation (3.56), which is related to the diffusion of the Reynolds stresses and which is always neglected in QUADFLOW for eddy viscosity models, has been added to the energy equation.

4.3.4. Realizability Constraints

Based on simple mathematical considerations, realizability constraints have been added to the flow solver.

For the Reynolds stresses on the diagonal line a positive value is imposed, since each of them represents the square of one fluctuating velocity component. At each iteration the values of these variables are checked and in case they are negative, they are set to a minimum value defined in the code.

$$\tilde{R}_{ii} = \max(\tilde{R}_{ii}, 10^{-12}) \quad (4.17)$$

The value of the Reynolds stresses out of the main diagonal line can be easily bounded from above and below as follows:

$$-\sqrt{\tilde{R}_{ii}\tilde{R}_{jj}} \leq \tilde{R}_{ij} \leq \sqrt{\tilde{R}_{ii}\tilde{R}_{jj}} \quad \forall i \neq j . \quad (4.18)$$

If one of the off-diagonal Reynolds stresses is found to be outside these bounds, its value is overwritten so that equation (4.18) is satisfied. For the ω -equation, a limitation analogous to that described by equation (4.17) is used to enforce the positivity of the variable, since ω is assumed to be proportional to the square root of \tilde{k} and the turbulent length scale.

4.3.5. Adaptive Simulations

As explained in Section 4.1.2, in order to run adaptive simulations some parameters need to be defined by the user.

For adaptive simulations using the RSM, the adaptation procedure uses all the mean flow variables and the first component of the Reynolds stress tensor (\tilde{R}_{11}). From different tests using both $k - \omega$ models and the RSM, it has been seen that using ω as a variable to trigger adaptation is a bad choice, because this leads to the generation of a too fine grid even in far field areas where it is not required. This is due to the fact that there is no ω production in the freestream and the value of this variable decays quickly moving toward the inside of the domain. The adaptive procedure detects this change and refines the grid in that location triggered by the numerical approach and not by the physics.

In order to compare the details of all variables used for adaptation against the same threshold, the details has to be normalized by some representative quantity. Considering that in hypersonic flow, the variables take values among the domain that differ by many orders of magnitude, as for example the velocity which increase from zero to a value of few thousand (m/s) in the boundary layer, a local maximum is used for rescaling before the thresholding. The local maximum is computed among the cell and its neighbors.

5. Model Validation

In the first part of this chapter results concerning the behavior of the chosen RSM are shown. Its sensitivity to different parameters like freestream turbulence and wall spacing is presented as well as the evolution of the solution depending on the choice of the adaptive strategy. In the second part, selected two-dimensional simulations used for validating the model implementation are discussed. The results are compared with the solution obtained using other turbulence models implemented in QUADFLOW, particularly the SST $k - \omega$ model of Menter as well as experimental data and analytical solutions, when available.

5.1. Definition of Non-Dimensional Variables

For the studies presented in this work, non-dimensional variables are often used for comparison with experimental results or numerical solutions. Particularly three quantities are considered: the pressure coefficient C_p , the (skin) friction coefficient C_f and the Stanton number St defined as follows:

$$C_p = \frac{p - p_\infty}{\frac{1}{2}\rho_\infty|\mathbf{u}_\infty|^2} , \quad (5.1)$$

$$C_f = \frac{\tau_w}{\frac{1}{2}\rho_\infty|\mathbf{u}_\infty|Re_\infty} , \quad (5.2)$$

$$St = \frac{q_w}{\rho_\infty|\mathbf{u}_\infty|c_p(T_{0,\infty} - T_w)} , \quad (5.3)$$

where q_w is the heat flux at the wall and τ_w is the wall shear stress. The symbol c_p in equation (5.3) refers to the specific heat at constant pressure.

5.2. Model Sensitivity Studies

The sensibility of the Reynolds stress model has been assessed against different simulation parameters. First, the freestream turbulence in the form of turbulence intensity and ratio between laminar and turbulent viscosity is taken into exam. Then, grid studies are presented focusing on the changes of the variables at the wall depending on the grid refinement. Subsequently, three ω conditions at the wall are compared. Finally, the adaptive parameters are considered and the convergence of the wall variables is presented as well as the error relative to the results obtained on a uniform grid at the finest prescribed level.

5.2.1. Freestream Turbulence

For the comparison of numerical results with wind tunnel experiments, a value of the freestream turbulence intensity (I), defined in equation (4.1), has to be provided describing the flow characteristics in the facility. However, measurements of such a quantity are difficult to perform and normally are not reported in the literature. For this reason a study on the influence of the freestream turbulence intensity for the RSM has been conducted. This quantity is generally given in percent. The values used here are 0.5%, 2%, 5% and 10%. The analysis has been performed on the supersonic flow over a flat plate and the inflow conditions are given in Table 5.1. The Riemann solver used is the AUSMDV and the viscosity ratio (equation 4.4) is 0.001.

p [Pa]	ρ [kg/m ³]	Re [1/m]	Ma [-]	T [K]	T_w [K]
24191	0.497	2.5×10^7	2.25	169.44	320.9

Table 5.1. Inflow conditions for a supersonic flow over a flat plate.

The results presented in Figure 5.1 (left) clearly show that the flow along the plate is scarcely influenced by the turbulence intensity imposed at the inflow boundary, as is also reported in the literature [91].

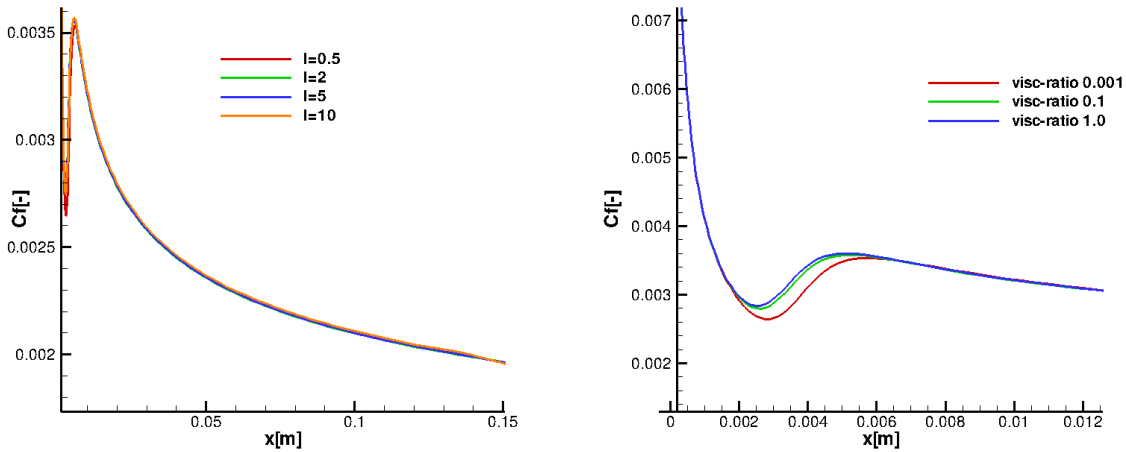


Figure 5.1. Parametric study on the influence of the freestream turbulence intensity (left) and of the viscosity ratio (right) on the skin friction coefficient of a supersonic flat plate at $M=2.25$ and $Re=2.5 \times 10^7$ 1/m.

The definition of the turbulence characteristics in QUADFLOW depends also on the viscosity ratio defined in equation (4.4). This quantity mostly influences the location of the (numerical) transition from laminar to turbulent flow that occurs along a solid wall in proximity of the leading edge [91]. This is a well known phenomenon in CFD due to the

fact that near the inflow boundary the high value of the turbulent dissipation terms exceeds the turbulent production terms [113], [93]. An increase in the value of the viscosity ratio leads to a lower value for the incoming ω , which means lower dissipation, and consequently the flow transition occurs closer to the leading edge. Figure 5.1 (right) shows the influence of the viscosity ratio for values of 0.001, 0.1 and 1 using a value of $I=0.5\%$. The picture only shows the portion of the flat plate near the leading edge to have a better focus on the phenomenon. The friction coefficient distribution shows that the transition region moves upstream for increasing values of the viscosity ratio but also that the distribution downstream of the transition region is not affected by this parameter.

5.2.2. Grid Considerations

The problem of generating grids with an appropriate resolution for hypersonic flows is well known in the CFD literature. The presence of high gradients of the variables across the boundary layer makes hypersonic simulations extremely grid sensitive with respect to lower Mach number flows as mentioned in Section 2.1.4. For example, Candler et al. show, in the case of laminar hypersonic flow, how much care has to be taken in the grid generation to get a grid-converged solution [26,37]. For turbulent flows, which are of interest in this thesis, the situation is even more critical since wall quantities such as skin friction and Stanton number are subject to substantially larger variations than in the laminar case and the flow variables present steeper gradients close to the solid walls as seen in Figure 2.2 for the velocity.

In order to quantify the quality of a grid at the wall, a non-dimensional wall distance called y^+ is defined as in equation (5.4). For low-Reynolds number turbulence models, which are models that solve the governing equations up to the wall without employing wall functions, the value of y^+ should be less or equal to one everywhere in order to properly resolve the viscous sublayer of the boundary layer [113].

$$y^+ = \frac{u_\tau y}{\nu} , \quad u_\tau = \sqrt{\frac{\tau_w}{\rho}} , \quad \tau_w = \mu \left(\frac{\partial u}{\partial y} \right)_{y=0} . \quad (5.4)$$

The inflow conditions, and especially the Reynolds number, influence the grid resolution required. The definition of y^+ is similar to the one of the Reynolds number and for a given value of y , y^+ increases with the Reynolds number. This means that in order to have $y^+ < 1$ at the wall, for increasing Reynolds number, a smaller grid resolution is required.

Description of the Test Case

The hypersonic flow over a compression corner at 15 degrees has been chosen as an appropriate test case for grid studies since large variable gradients are produced at the wall due to the presence of SWBLI. In this sense the chosen configuration is representative of most of the problems addressed in this thesis. The inflow conditions are listed in Table 5.2

5. Model Validation

p [Pa]	ρ [kg/m ³]	Re [1/m]	Ma [-]	T [K]	T_w [K]	I [-]	visc-ratio [-]
9681	0.08624	9.65×10^6	6.35	396	300	5%	0.001

Table 5.2. Inflow conditions for a hypersonic compression corner at 15 degrees.

Particular care has been placed in the generation of the grid for hypersonic flow simulations. For the test case considered here, the base grid, used for the grid studies presented in the next sections, has been built using constant grid spacing in the flow direction and refrains from clustering point in the area of separation in order to avoid any unphysical triggering of separation due to the grid spacing. The only region where the grid points are clustered is at the leading edge in order to capture the growth of the boundary layer and the viscous interaction described in Section 2.1.4, correctly. A uniform first grid spacing of 10^{-6} m has been used and the first cell at the leading edge has an aspect ratio of 2.5. The cell size in the flow direction increases smoothly up to 5×10^{-4} m and the grid spacing along the ramp is constant. In the cross flow direction the grid spacing increases up to 5×10^{-4} m in order to have squared cells in the freestream. The grid has been generated trying to have the grids line as orthogonal as possible to the wall in order to minimize the numerical error introduced by the cells skewness. The grid contains approximately 160,000 cells. The computational domain is presented in Figure 5.2

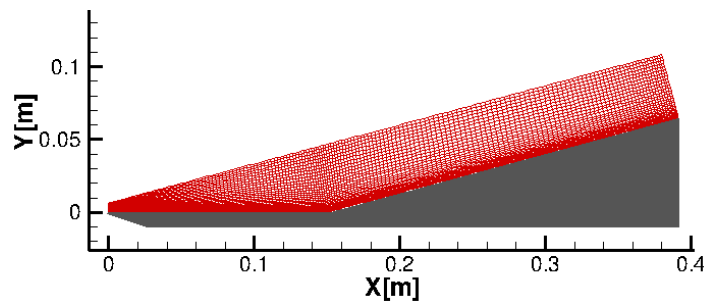


Figure 5.2. Computational domain for a 15 degrees compression corner at $M=6.35$ and $Re=9.65 \times 10^6$ 1/m. Every fourth grid line displayed.

For what concerns the boundary conditions at the wall the no-slip condition is enforced using strong boundary conditions as described in Section 4.2.2 and the wall is considered isothermal. At the inflow boundaries, supersonic inflow conditions have been prescribed and at the outflow boundary, supersonic outflow conditions. The AUSMDV Riemann solver is used for the convective fluxes.

Grid Refinement Study

Different grid refinements have been used in order to investigate the effects of grid variation on the wall variables of interest here. The grids used for the refinement study are described in

Table 5.3. The maximum aspect ratio (AR) is given with respect to the base grid (AR/AR_{base}) which has a value of aspect ratio of 500.

	base grid	xy-refinement	x-refinement	y-refinement	y-ref, large y^+
points x-dir	845	1690	1690	845	845
points y-dir	190	380	190	380	380
Δy_w [m]	10^{-6}	5×10^{-7}	10^{-6}	5×10^{-7}	10^{-6}
AR/AR_{base}	1	1	0.5	2	1

Table 5.3. Characteristics of the grids used for the refinement study.

The variables considered for evaluating the grid convergence of the solution are the Stanton number and the pressure at the wall. Since the Stanton number is a function of the temperature gradient, which takes large values at the wall, in hypersonic flows, its correct computation is challenging and extremely sensitive to the grid resolution. For this reason, it is considered an appropriate variable for testing grid convergence. For what concerns the pressure at the wall, it is expected to be not sensitive to grid variation and it is shown for completeness only. At first a xy-refinement has been performed doubling the number of grid points in each direction with respect to the base grid. In addition, two grids have been generated refining the base grid once only in the flow direction (x-refinement grid) and once only in the crossflow direction (y-refinement grid), in order to see whether the refinements in the x- and y-direction equally affect the convergence of the wall variables. The pressure and Stanton number for the three grids mentioned above and the base grid are compared in Figure 5.3.

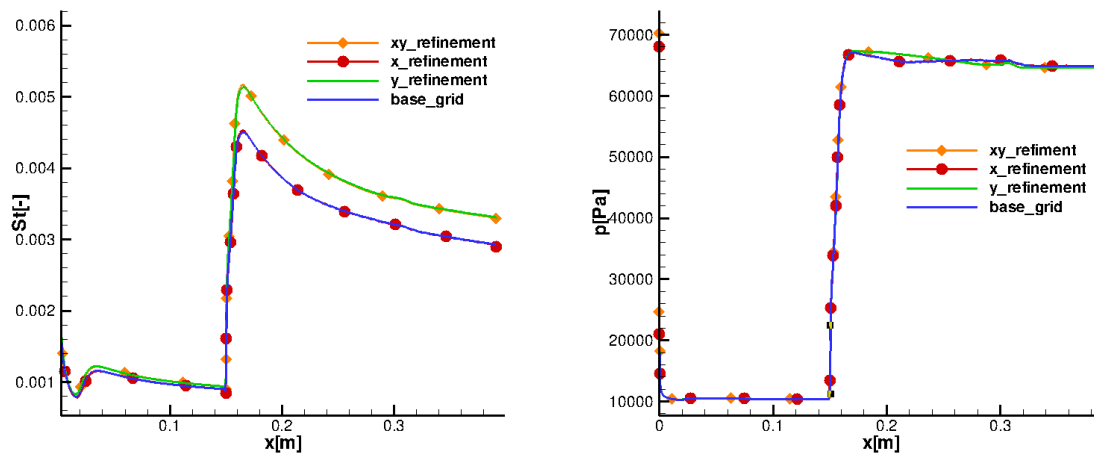


Figure 5.3. Grid convergence study on Stanton number and pressure for a 15 degrees compression corner using different refinement techniques. $M=6.35$ and $Re=9.65 \times 10^6$ 1/m.

On the one hand it can be seen that the x-refinement does not influence the wall values for either pressure or Stanton number distribution. On the other hand the Stanton number

is strongly affected by the grid changes introduced by the xy-refinement grid and the y-refinement grid and a visible increase in its value is visible. The differences are particularly appreciable where the variable has its peak values, which means where the temperature gradient is steeper; this corresponds to the peak heating along the compression ramp where the flow passes through the compression shock wave. The results obtained with the y-refinement grid are the same as using the xy-refinement grid which means that the grid variation in the y-direction accounts for all the changes in the Stanton number distribution. As expected the pressure is not affected by the grid refinement since at each location it has a constant value across the boundary layer.

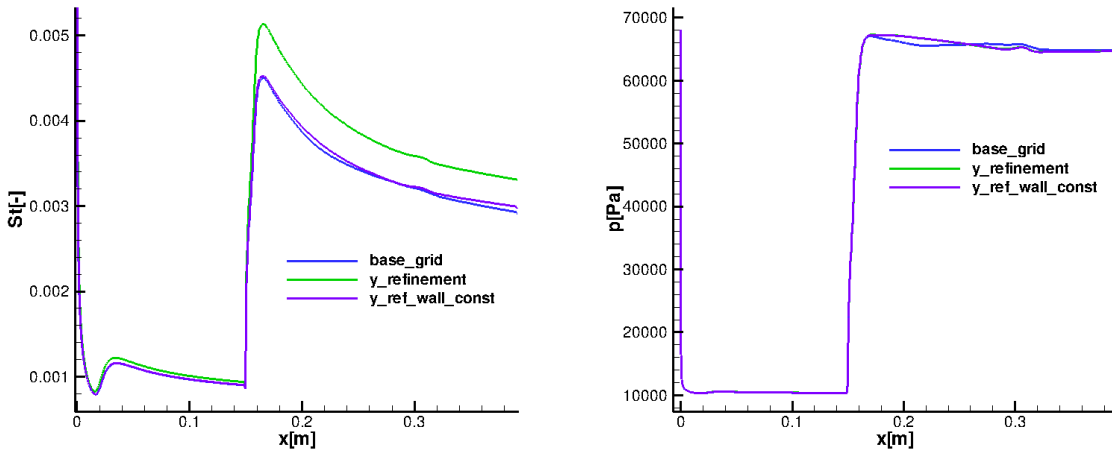


Figure 5.4. Grid convergence study on Stanton number and pressure for a 15 degrees compression corner at $M=6.35$ and $Re=9.65 \times 10^6$ 1/m.

The previous results do not indicate whether the changes in the solution are due to the better refinement in the whole field or just to the change in the wall resolution. For this reason a further comparison is done between the results obtained for the base grid, the y-refinement grid and the y-refinement grid with large y^+ i.e. without changing the resolution at the wall with respect to the base grid. The results are shown in Figure 5.4. Only negligible differences in both Stanton number and pressure values are visible between the base grid and the y-refinement grid with the same wall spacing. These differences do not justify the use of twice as many points. From these results it is evident that, for a reasonably refined grid, the quantity that considerably affects the grid-convergence is the first grid spacing rather than the number of cells away from the wall. Such a large difference in the Stanton number distribution along the ramp between the base grid and the y-refinement grid shows that the grid resolution prescribed at the wall is not sufficient for the chosen geometry subject to these inflow conditions.

Wall refinement study

The results shown in the previous section indicate a strong sensitivity of the surface distribution of the Stanton number on the first grid spacing. Thus, the number of grid points is now kept constant but the first grid spacing at the wall is changed in order to determine which wall resolution is required. It must be considered that this procedure, that only slightly changes the grid resolution in the field, strongly affects the maximum aspect ratio of the cells. For this study, seven grids are considered as shown in Table 5.4.

	base grid	grid 2	grid 3	grid 4	grid 5	grid 6	grid 7
Δy_w [m]	10^{-6}	5×10^{-7}	2.5×10^{-7}	1.25×10^{-7}	6.5×10^{-8}	3.25×10^{-8}	1.6×10^{-8}
AR/AR_{base}	1	2	4	8	16	32	64

Table 5.4. Characteristics of the grids used for the wall refinement study.

The y^+ distributions relative to the grids used in this section are presented in Figure 5.5. It can be noticed that all the grids apart the base grid have a y^+ lower than 1 everywhere. For the finest grid this value even drops below 0.05 everywhere.

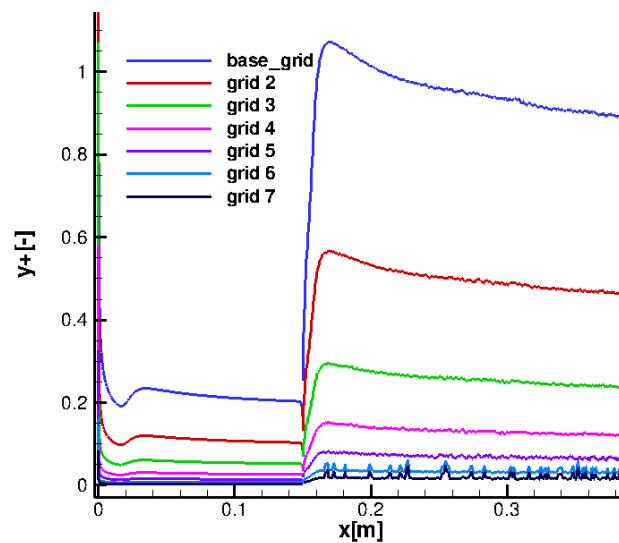


Figure 5.5. Effect of wall refinement on y^+ for a 15 degrees compression corner at $M=6.35$ and $Re=9.65 \times 10^6$ 1/m..

First of all, grid 2 is compared with the y -refined grid since the two grids have the same resolution at the wall but a different number of grid points. The results in Figure 5.6 show that there are only negligible differences in the results for both pressure and Stanton number indicating that the large differences found in Figure 5.3 are due to the refinement of the first cell off the wall only.

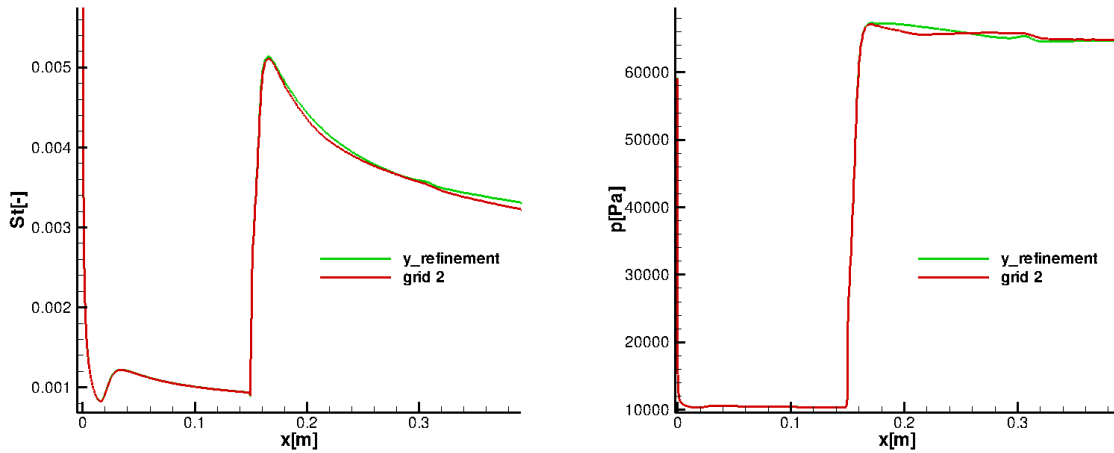


Figure 5.6. Comparison of Stanton number and pressure distribution for grids having the same wall resolution but different number of cells. 15 degrees compression corner at $M=6.35$ and $Re=9.65 \times 10^6$ 1/m.

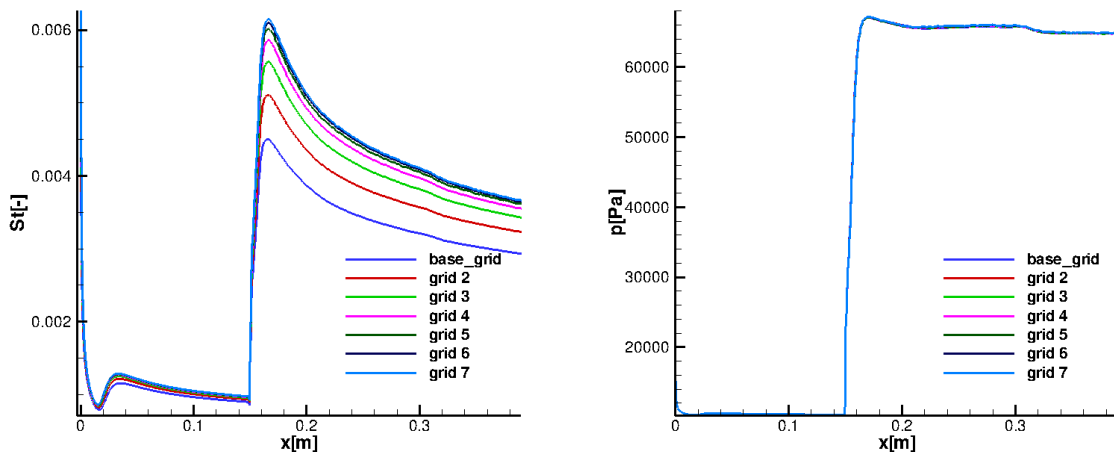


Figure 5.7. Study of the influence of the wall resolution on Stanton number and pressure for a 15 degrees compression corner at $M=6.35$ and $Re=9.65 \times 10^6$ 1/m.

In Figure 5.7, the influence of the resolution at the wall on Stanton number and pressure is analyzed using the seven grids described in Table 5.4. It can be noticed that, as expected, all seven grids predict the same pressure distribution while the differences in Stanton number are significant. Decreasing the wall resolution leads to a considerable increase in Stanton number and no grid convergence is achieved even with a wall resolution almost 100 times smaller than in the base grid.

The grid study presented here shows that the Stanton number is extremely sensitive to the grid resolution at the wall while the pressure levels are not affected by wall refinement.

In addition, the use of a y^+ smaller than one does not guarantee a grid-independent solution. The discretization error present in the computation of the Stanton number decreases monotonically with reducing the wall spacing. This means that the result obtained for the Stanton number on a given grid is a conservative approximation of the result one can obtain on a grid characterized by a smaller cell size at the wall. In order to choose the grid to be used for the computations in Section 7.2, a compromise between accuracy and efficiency needs to be done. For this reason grid 4 has been chosen since it provides a solution with an error of 5% at peak heating (where the largest discrepancy is displayed) with respect to the finest grid and the simulation converges properly in a reasonable time.

5.2.3. ω -wall Condition

As described in Section 4.2.2, three different approaches for the definition of ω at a solid wall have been tested in this work. Only the influence of the ω -wall boundary condition needs to be analyzed, while for the Reynolds stresses the definition of the boundary condition is straightforward. On the contrary, the ω -condition presents a singularity and is thus not uniquely defined numerically and the different approaches prescribe a value that depends, more or less directly, on the resolution at the wall.

The Stanton number distribution for the test case presented in the previous section is now analyzed for the Menter, Rudnik and Wilcox ω -boundary conditions. However, the Menter condition, in equation (4.6) is regarded as the natural choice for the RSM since its equation for the turbulent length scale is employed in the SSG/LRR- ω model and is used as a standard in this thesis. A detailed analysis of the influence of the ω -wall conditions for different turbulence models and grid resolutions using QUADFLOW can be found in [63].

The Rudnik condition, in equation (4.7) requires the definition of a parameter that has to be of the same order of the first grid spacing. A first comparison between the Menter condition and the Rudnik condition has been performed varying the grid resolution at the wall and the value of the Rudnik parameter. The base grid and grid 4, described in Section 5.2.2, have been employed. The results are presented in Figure 5.8 (left). For a Rudnik parameter equal to the wall distance, the Menter and the Rudnik conditions produce the same results, since under these conditions they prescribe exactly the same value for ω at the wall. For the grid with a wall resolution of 1.25×10^{-7} m a value of 10^{-7} has been employed for the Rudnik approach and only small differences can be seen with respect to the Menter solution for the same grid. For a value of the parameter one order of magnitude different from the wall resolution, large differences are observed and the predicted Stanton number is much larger than in the previous case. For a Rudnik parameter close to the grid resolution at the wall the results are in good agreement with those obtained using the ω condition of Menter. However it should be noticed that changing the Rudnik parameter on the base grid, it is possible to get a Stanton number close to the solution obtained on the finest grid. It is not known whether this is a general trend but it should be considered that the problem of getting a grid converged solution may also depend on the definition of ω at the wall which varies with the grid resolution.

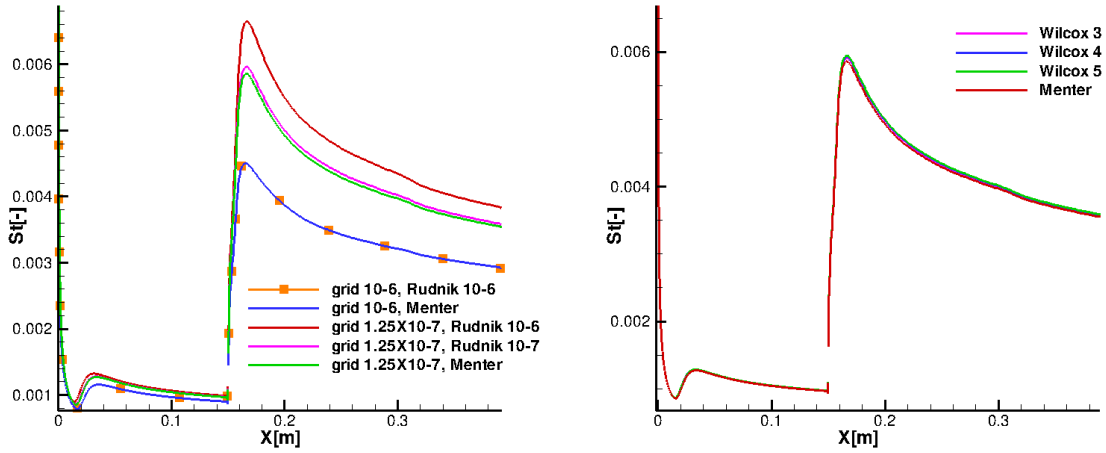


Figure 5.8. Comparison of different approaches for the definition of ω at the wall for a 15 degrees compression corner at $M=6.35$ and $Re=9.65 \times 10^6$ 1/m.

A second comparison is made between the Menter and the Wilcox approach. The grid used here has a wall resolution of 1.25×10^{-7} m (grid 4). For a smooth wall, as it is the case here, a value of k_R^+ smaller or equal to 5 should be prescribed in equation (4.9). Three values of this parameter have been tested: 3, 4 and 5. In Figure 5.8 (right) it can be observed that the differences in the parameter almost do not affect the solution and the Wilcox approach produces results similar to the Menter approach.

The results presented in this section are encouraging and show that these three conditions for ω at the wall, used with appropriate parameters produce similar wall distribution so that the solution does not strongly depend on the choice of the boundary conditions for this variable.

5.2.4. Adaptive Simulations: Threshold Value and Refinement Levels

For a clear understanding of the capabilities of the adaptive procedure a distinction between discretization error and perturbation error needs to be done. For each given problem three solutions can be defined as follows:

- V is the exact solution;
- \bar{U}_L is the adaptive solution projected on the uniform reference mesh for L refinement levels;
- U_L is the non adaptive solution computed on the uniform reference mesh for L refinement levels.

In order to bound the error for the adaptive solution committed with respect to the exact solution, the error is split into two contributions:

$$\|V - \bar{U}_L\| \leq \underbrace{\|V - U_L\|}_{\text{discretization error}} + \underbrace{\|U_L - \bar{U}_L\|}_{\text{perturbation error}} \leq Tol , \quad (5.5)$$

where the tolerance Tol has to be defined by the user. The discretization error of the reference scheme tends to zero for L that goes to infinity, i.e. for an infinitely fine grid. The perturbation error of the adaptive scheme tends to zero for ϵ that goes to zero for a fixed number of refinement levels L .

An efficient solution of the problem is obtained when the two errors are balanced, i.e.; they are of the same order.

From a theoretical point of view, the ideal strategy for the choice of the best parameters for an adaptive computation would be to first choose the number of refinement levels L so that the discretization error is smaller than half of the tolerance:

$$\|V - U_L\| \leq Tol/2 , \quad (5.6)$$

and then chose ϵ so that the perturbation error is of the same order as the discretization error in the equation above:

$$\|U_L - \bar{U}_L\| \leq Tol/2 . \quad (5.7)$$

Unfortunately, in practical application, there is no error estimation available by which one can bound the discretization error. In the case of 1D nonlinear conservative laws, it has been proved [28] that, h_L being the size of a mesh element on the finest scale and α the order of the reference scheme, the optimal choice for the threshold would be:

$$\epsilon \sim h_L^{1+\alpha} \quad (5.8)$$

This prediction is by far too pessimistic and cannot be used in practice. For practical two-dimensional applications, the experience shows that a value of the threshold $\epsilon \sim 10^{-3}$ provides reasonable results [21].

The hypersonic flow over a flat plate has been studied to analyze the error arising from the adaptation procedure and the influence of the adaptive parameters on the solution. In the following analysis, only the perturbation error is considered. The inflow conditions used for this test case are listed in Table 5.5.

p [Pa]	ρ [kg/m ³]	Re [1/m]	Ma [-]	T [K]	T_w [K]	I	visc-ratio
2781.6	0.017	1.7×10^6	6.3	570	288	0.5%	0.001

Table 5.5. Inflow conditions for a hypersonic flat plate.

The coarse grid has 50 points in the streamwise direction and 20 points in the wall normal direction. The points are clustered near the leading edge and in the boundary layer in order to capture the boundary layer growth and have a higher resolution in that region. For $L=0$

which is the coarsest level the grid contains 1,000 cells. For $L=1$ which is the initial grid, the grid contains 4,000 cells. In order to obtain the desired refinement at the wall, the maximum number of refinement levels has been set to 4. The threshold value has been set to 10^{-3} as mentioned above. The adaptation procedure is triggered by the mean flow variables and by the first component of the Reynolds stress tensor $\rho\tilde{R}_{11}$. An option is chosen to have, at any time, the maximum refinement level at the wall. This technique is adopted to avoid the presence of hanging node close to the wall that can trigger non-physical oscillations in the solution. The reason for this is not yet clear. Most probably it is related to the reconstruction procedure on grids with high aspect ratio. The maximum difference of refinement levels between two adjacent cells, as prescribed by the adaptive algorithm, is one so that a smooth decrease in the refinement levels is performed moving away from the wall.

Three simulations using different threshold values ϵ of 10^{-1} , 10^{-2} and 10^{-3} and a fixed number of refinement levels ($L=4$) have been performed. Successively, the number of refinement levels has been varied from 1 to 2 to 3 keeping the threshold value fixed at 10^{-3} . All simulations, except for the choice of parameters $(L, \epsilon) = (4, 10^{-3})$, have been run on 4 processor, on the Linux Xeon cluster at the Center for Computing and Communication (CCC) at the RWTH Aachen University using implicit time integration and a maximum CFL number of 30 so that the computational time can be compared. For the case $(4, 10^{-3})$, 6 processors have been employed. The simulation performed on the uniform grid has been performed using explicit time integration due to convergence problems.

The error induced by the thresholding process in the adaptation has been estimated using as reference a uniform grid at the finest refinement level ($L=4$). This grid contains $1000 \cdot 4^4$ cells, i.e., 256,000 cells. The adaptive solution for each case has been projected on the uniform grid and then the error between the projected adaptive solution and the reference solution has been estimated for the wall and the field variables. Calling M the number of wall cells and $|S_i|$ the wall length of the i -th wall cell, the formula used for the computation of the error for wall variables reads as follows:

$$E_w = \frac{1}{\|U_L\|_\infty} \sum_{i=1}^M |\bar{U}_{L,i} - U_{L,i}| |S_i| . \quad (5.9)$$

For the field variables, calling N the number of cells and $|V_i|$ the volume of the i -th cell, the error has been evaluated as follows:

$$E_f = \frac{1}{\|U_L\|_\infty} \sum_{i=1}^N |\bar{U}_{L,i} - U_{L,i}| |V_i| , \quad (5.10)$$

where $\|U_L\|_\infty = \max_i |(U_L)_i|$.

The errors computed for a decreasing value of the threshold value using 4 levels of refinement are presented in Table 5.6. The error has been computed using the pressure as variable. The total number of grid cells after the last adaptation and the computational time are reported in the last two columns.

Threshold value	E_w	E_f	cells	time
10^{-1}	3.63778×10^{-4}	0.01032	10627	00:34:53
10^{-2}	1.16164×10^{-4}	0.00863	31355	01:51:34
10^{-3}	4.123251×10^{-5}	0.00770	72833	14:59:20
uniform	-	-	256000	-

Table 5.6. Perturbation error computed on the pressure at the wall and in the whole field. The number of refinement levels is kept constant to $L=4$.

The pressure and skin friction distribution along the wall for the same threshold values are illustrated in Figure 5.9. It can clearly be seen that a large value of the threshold produces non-physical oscillations in the solution for both pressure and skin friction. The oscillations gradually decrease when the threshold value is decreasing.

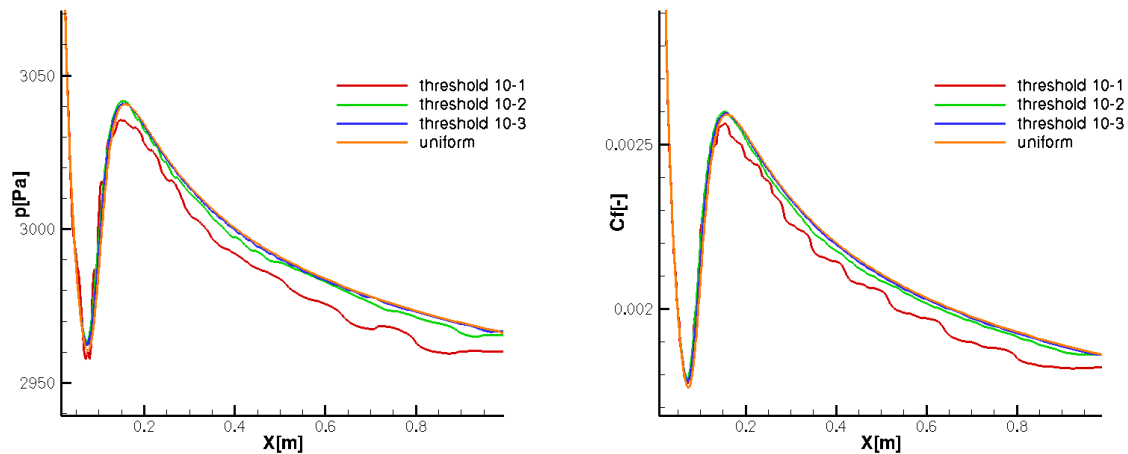


Figure 5.9. Study of the influence of the change in the threshold value for the pressure (left) and skin friction (right) distributions at the wall for a fixed number of refinement levels $L=4$. Hypersonic flow over a flat plate at $M=6.3$ and $Re=1.7 \times 10^6$ 1/m.

The errors obtained for an increasing value of the refinement levels and a threshold value of 10^{-3} are presented in Table 5.7. The error has been computed using the pressure as variable. The pressure and skin friction distribution along the plate are presented in Figure 5.10. The variables steadily increase for an increased number of refinement level and the solution obtained at the highest level almost coincides with the uniform solution.

Naming the solution using the two parameters (L, ϵ) one can notice that $(2, 10^{-3})$ and $(4, 10^{-1})$ have a comparable computational time. The first one shows a smooth behavior but clearly underestimates the skin friction coefficient, while the second one gives a general better approximation of the skin friction but strong non-physical oscillations of this quantity can be seen. Even for an 'easy' test case as the flat plate, a threshold of at least 10^{-2} is

Refinement levels	E_w	E_f	cells	time
$L=1$	0.00405	0.00906	3334	00:05:25
$L=2$	0.00187	0.00832	11977	00:40:22
$L=3$	8.38076×10^{-4}	0.010099	33277	08:00:48
$L=4$	4.123251×10^{-5}	0.00770	72833	14:59:20
uniform	-	-	256000	-

Table 5.7. Wall and field error for different values of refinement levels and a fixed threshold value of $\epsilon=10^{-3}$.

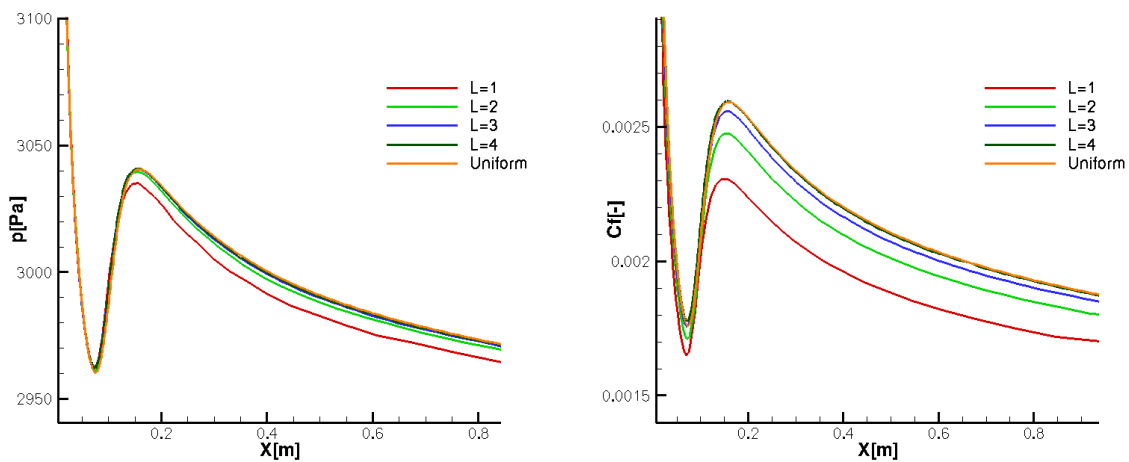


Figure 5.10. Pressure (left) and skin friction (right) distribution for varying value of the refinement levels for an adaptive flat plate.

required to get a smooth solution. The effect of the change in the number of refinement levels is similar to the effect observed in the grid resolution study. A higher L leads to smaller spacing at the wall and consequently higher values of the friction coefficient.

The difference between the uniform grid and the grid ($4,10^{-3}$) is small both for what concerns the field and the wall variables. In terms of number of cells the adaptive grid has one third of the cells with respect to the uniform grid. The performance in terms of CPU time cannot be compared since different integration procedures have been employed for the two simulations as explained above.

5.3. Validation Results

The newly implemented Reynolds stress model has been validated for different configurations. The obtained results have been compared with analytical solutions, experimental results and numerical results obtained with QUADFLOW using other turbulence models.

5.3.1. Hypersonic Flow over a Flat Plate

The hypersonic flow over a flat plate has been used as first validation simulation in order to test the RSM on a zero pressure gradient configuration. The inflow conditions are the same used in the previous section and listed in Table 5.5. The geometry considered consists of a 2 meters long flat plate with a sharp leading edge. A grid study has been performed using the three grids described in Table 5.8.

grid	points x-dir	points y-dir	Δx_{\max} [m]	Δx_{\min} [m]	Δy_{\max} [m]	Δy_{\min} [m]
coarse	150	60	4×10^{-2}	2×10^{-6}	10^{-2}	10^{-6}
medium	300	120	2×10^{-2}	10^{-6}	5×10^{-3}	5×10^{-7}
fine	600	240	1×10^{-2}	5×10^{-7}	2.5×10^{-3}	2.5×10^{-7}

Table 5.8. Grid resolution for the three grids used for the study of a hypersonic flat plate at $M=6.3$ and $Re=1.7 \times 10^6$ 1/m.

The values of the skin friction coefficient for the three grids are presented in Figure 5.11 (left) for the Reynolds stress model.

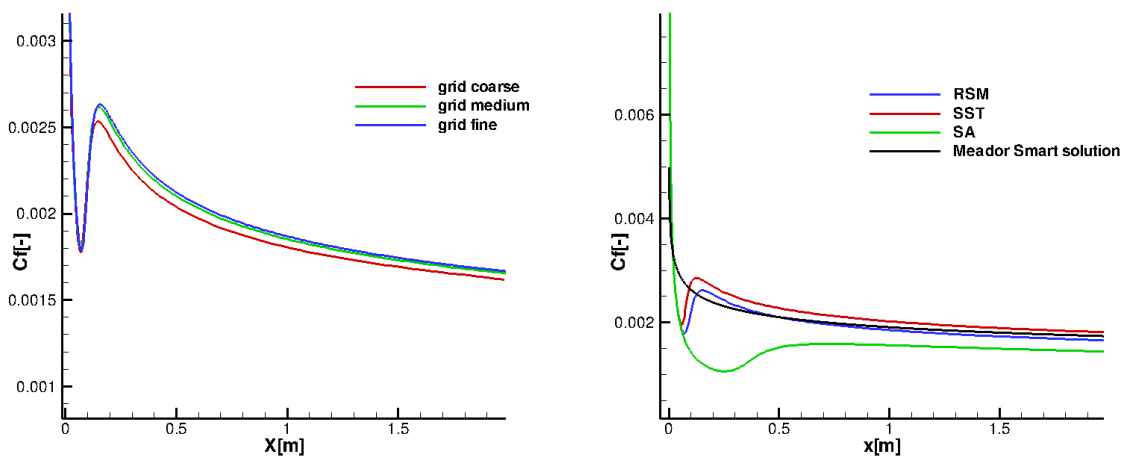


Figure 5.11. Grid convergence study (left) and comparison of skin friction distribution (right) for a hypersonic flat plate at $M=6.3$ and $Re=1.7 \times 10^6$ 1/m.

The coarse grid provides a value of the skin friction coefficient considerably lower than the other two grids while the results of the medium and fine grid are comparable and the maximum difference between the two solutions is smaller than 2%. The grid chosen for the comparison is the medium grid and it guarantees a y^+ smaller than 0.05 everywhere. The RSM solution is compared with the SST $k - \omega$ model and the Spalart-Allmaras (SA) model using the same grid for all turbulence models. Additionally an analytical solution is provided. The solution has been obtained using the reference enthalpy method by Meador and

Smart [74] as recommended in [6]. The skin friction coefficient distribution is presented in Figure 5.11 (right). It can be seen that the Spalart-Allmaras model strongly underpredicts the distribution along the whole plate. An excellent agreement between the analytical solution and the RSM model has been obtained. The SST model slightly overpredicts the skin friction distribution.

5.3.2. Supersonic Flow over a Flat Plate

The supersonic flow over a flat plate has been studied in order to compare the behavior of the Reynolds stress model in the cross flow direction with experimental results. The same test case has been studied with QUADFLOW by Schieffer in the frame of the SFB 405 [96]. The test case is the number 5501-05 in reference [45] and consists of a flat plate flow at Mach 2.25. The inflow conditions are the same as used in Section 5.2.1 and are given in Table 5.1. For what concerns the turbulent variables $I=0.5\%$ and $\text{visc-ratio}=0.001$ are used.

The grid resolution for this test case is similar to the one used for the hypersonic flat plate. The outflow boundary has been made larger to allow the Mach wave that generates at the leading edge to exit the domain at the outflow edge and to avoid unphysical reflections from the upper boundary. This was not a problem for the hypersonic test case since the shock that generates at the leading edge lies closer to the surface as explained in Section 2.1.1. The grid is presented in Figure 5.12.

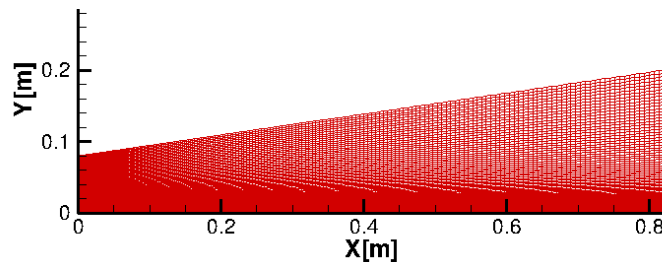


Figure 5.12. Computational grid used for the simulation of a supersonic flat plate at $M=2.25$ and $Re=2.5 \times 10^7$ 1/m.

The comparison of the skin friction coefficient with the experimental results is presented in Figure 5.13. The distribution compares well with the experimental results and the difference at each measurement location is smaller than 5%. No error bars are provided by the authors. At the same locations where the skin friction coefficient is measured, the Mach number and temperature distributions in the boundary layer have been experimentally investigated.

A comparison between the numerical and experimental results is presented in Figure 5.14. In order to make the picture more clear the Mach number distributions have been shifted by +0.5, +1.0 and +1.5 respectively starting from the second measurement point in the flow direction. The picture shows an excellent agreement between the experimental measurements and the simulation. For what concerns the temperature distribution, the results have been shifted by 10 K, 20 K and 30 K respectively starting from the second measurement point. An

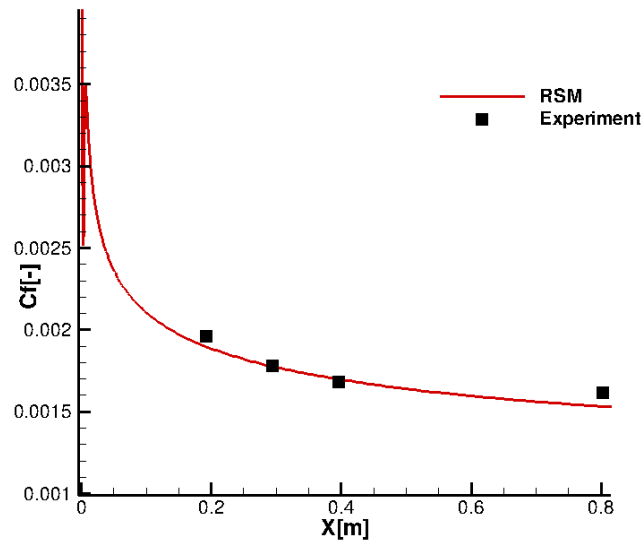


Figure 5.13. Skin friction distribution along a supersonic flat plate at $M=2.25$ and $Re=2.5 \times 10^7$ 1/m and comparison with experimental results in [45].

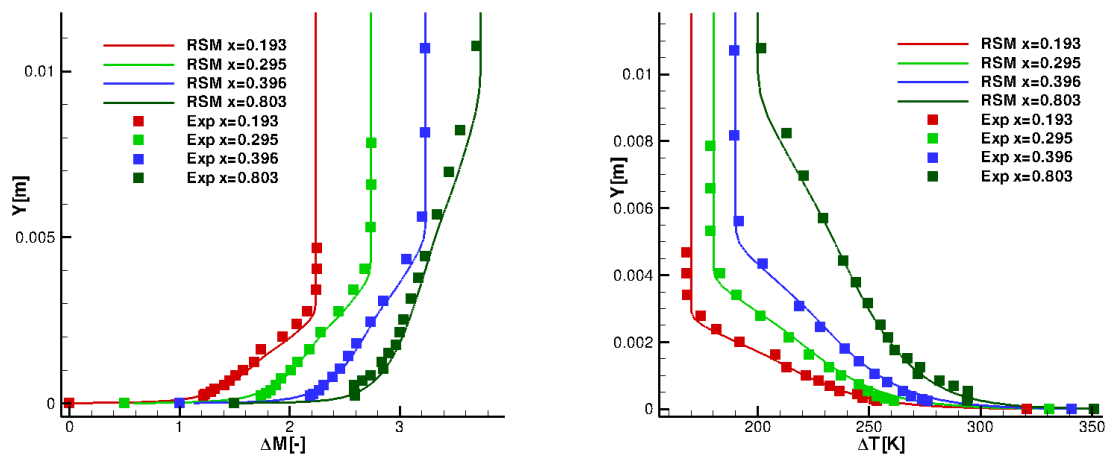


Figure 5.14. Mach number (left) and temperature (right) distribution in the wall normal direction at different streamwise locations for a flat plate at $M=2.5$ and $Re=2.5 \times 10^7$ 1/m. The Mach curves are shifted progressively starting from $x=0.295$, the second location, by +0.5, +1.0 and +1.5 Mach, respectively. The temperature distributions are shifted progressively starting from $x=0.295$, the second location, by +10 K, +20 K and +30 K, respectively.

excellent agreement is shown at each location also for the temperature distribution. This test case clearly shows the ability of the Reynolds stress model to correctly predict not only wall variables, as the skin friction coefficient, but also the velocity and temperature profiles inside the boundary layer.

5.3.3. Subsonic Flow over a Flat Plate

In order to test the capability of the Reynolds Stress Model to reproduce the so-called logarithmic law of the wall the subsonic flow over a flat plate has been considered. The inflow conditions for this test case are listed in Table 5.9.

p [Pa]	ρ [kg/m ³]	Re [1/m]	Ma [-]	T [K]	T_w [K]	I	visc-ratio
143000	1.7475	10^7	0.3	285	300	0.5%	0.001

Table 5.9. Inflow conditions for a subsonic flat plate.

The numerical grid is composed by two blocks: a freestream block of 0.2 m and the flat plate block of 1 m length. The height is 0.4 m. The characteristics of the grid are listed in Table 5.10. Characteristic boundary conditions are imposed at the inflow and upper boundary, while at the outflow boundary all the variables are extrapolated. The no-slip condition at the wall is enforced using the strong boundary conditions. A symmetry condition is imposed at the lower boundary between the inflow and the leading edge of the flat plate. The AUSMDV Riemann solver is used for the convective fluxes.

points x-dir	points y-dir	Δx_{\max} [m]	Δx_{\min} [m]	Δy_{\max} [m]	Δy_{\min} [m]
250	100	10^{-2}	10^{-6}	10^{-2}	5×10^{-7}

Table 5.10. Grid resolution for the study of a subsonic flat plate at $M=0.3$ and $Re=10^7$ 1/m.

First the distribution of the skin friction coefficient at the wall is considered and shown in Figure 5.15. The numerical results are compared with those reported in [42]. The results show that at subsonic speed the RSM underpredicts the skin friction coefficient slightly.

The velocity in the cross flow direction at the middle of the plate is shown in Figure 5.16 (left) in terms of the non-dimensional variables y^+ defined in equation 5.4 and u^+ defined as follows:

$$u_i^+ = \frac{\tilde{u}_i}{u_\tau} = \sqrt{\frac{2}{C_f}} \frac{1}{\sqrt{\gamma} M_\infty} \left(\frac{\tilde{u}_i}{\sqrt{R\tilde{T}_\infty}} \right). \quad (5.11)$$

The figure shows that the RSM correctly predicts the velocity profile in the boundary layer both in the laminar layer and in the logarithmic layer. For the same reason the skin friction coefficient is underpredicted, the velocity profile is slightly shifted toward higher u^+ .

Finally the distribution of the Reynolds stress components R_{ij}^+ is given in Figure 5.16 (right). Where R_{ij}^+ are defined as:

$$R_{ij}^+ = \frac{\tilde{R}_{ij}}{u_\tau} = \frac{2}{C_f} \frac{1}{\gamma M_\infty^2} \left(\frac{\tilde{R}_{ij}}{R\tilde{T}_\infty} \right). \quad (5.12)$$

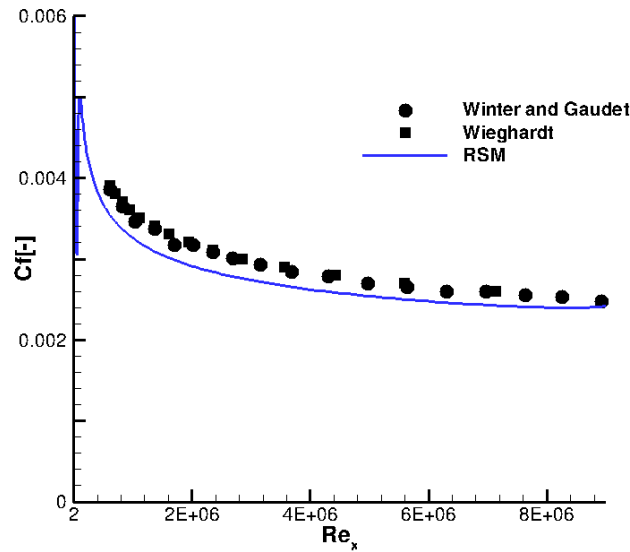


Figure 5.15. Skin friction distribution along a subsonic flat plate at $M=0.3$ and $Re=10^7$ 1/m. The results are compared with the values reported in [42].

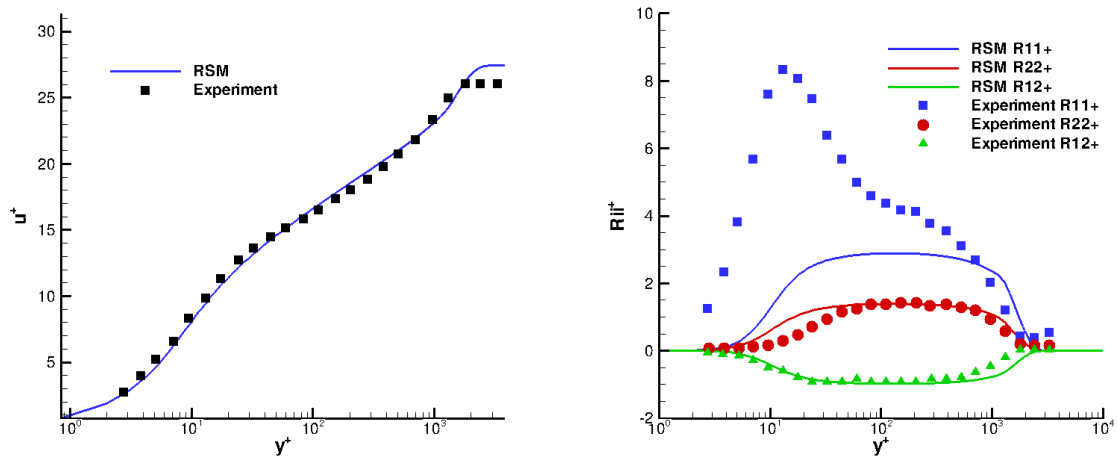


Figure 5.16. Velocity distribution (left) and Reynolds stresses distribution (right) inside the boundary layer at $x=0.5$ m for a subsonic flat plate at $M=0.3$ and $Re=10^7$ 1/m. The results are compared with the values reported in [42].

For the R_{11}^+ component of the normal stresses a visible underprediction is shown in the numerical results in comparison with the experiments. Nevertheless the component R_{12}^+ shows a good agreement with the experimental results. This behavior has already been observed by Eisfeld when testing his model on the same test case [42] and is a characteristic of the model itself. Eisfeld explains that this is expected because of the missing wall-reflection term in the Wilcox (LRR) model. The results show then the correctness of the

implementation.

5.3.4. Hypersonic Flow over a Double Wedge

After the validation on the flat plate, the RSM has been tested on a configuration characterized by SWBLI at hypersonic speed [18]. The results obtained are compared with experimental findings and numerical results from QUADFLOW using the SST $k - \omega$ turbulence model.

5.3.4.1. Experimental Setting

The double wedge configuration has been experimentally investigated at the Shock Wave Laboratory (SWL) in Aachen in the TH2 shock tunnel [80], [79]. It consists of two ramps inclined at 9 and 20.5 degrees respectively with the horizontal. The first ramp is 0.18 m long, the second ramp 0.255 m long and the model width is 0.27 m to ensure a two-dimensional flow along the center line. Two different leading edges have been considered. A sharp leading edge and a blunt one of 0.5 mm radius. In the second case the first ramp length has been reduced to 0.1773 m. The inflow conditions used in the experiment are listed in Table 5.11.

p [Pa]	ρ [kg/m ³]	Re [1/m]	Ma [-]	T [K]	T_w [K]
463.6	0.0158	3.76×10^6	8.3	102	300

Table 5.11. Experimental inflow conditions for the double wedge configuration.

Heat flux and static pressure measurements were collected along the center line of the model using K-type thermocouples and Kulite piezoresistive sensors, respectively. The error bars are set to 5% for the pressure and to 10% for the Stanton number.

5.3.4.2. Numerical Approach

In order to numerically reproduce the experimental findings, the inflow conditions used in the experimental campaign have been prescribed as numerical inflow. Supersonic inflow boundary conditions have been imposed at the inflow boundaries, supersonic outflow boundary conditions at the outflow boundary and the no-slip condition has been enforced at the solid wall using the strong boundary condition described in Section 4.2.2. The wall is considered isothermal and the experimental wall temperature is prescribed. A turbulence intensity of 0.5% and a viscosity ratio of 0.001 are chosen. The HLLC Riemann solver is used to match the conditions chosen by Krause [64] whose results, obtained with the SST $k-\omega$ model, are used for comparison.

A grid study has been performed using the three grids described in Table 5.12 for the configuration with blunt leading edge. This configuration contains all the physical phenomena of the configuration with sharp leading edge but also the entropy layer that makes it a more challenging test case.

grid	points x-dir	points y-dir	Δx_{\max} [m]	Δx_{\min} [m]	Δy_{\max} [m]	Δy_{\min} [m]
Coarse	452	76	2×10^{-3}	10^{-6}	2×10^{-3}	10^{-6}
Medium	576	128	10^{-3}	10^{-6}	10^{-3}	10^{-6}
Fine	700	200	5×10^{-4}	10^{-6}	5×10^{-4}	10^{-6}

Table 5.12. Grid resolutions used for the grid study on the double wedge configuration with blunt leading edge at $M=8.3$ and $Re=3.76 \times 10^6$ 1/m.

The medium grid is presented in Figure 5.17. The grid has been created by Krause [64] taking care of having orthogonal grids line at the wall and a good refinement in the leading edge region.

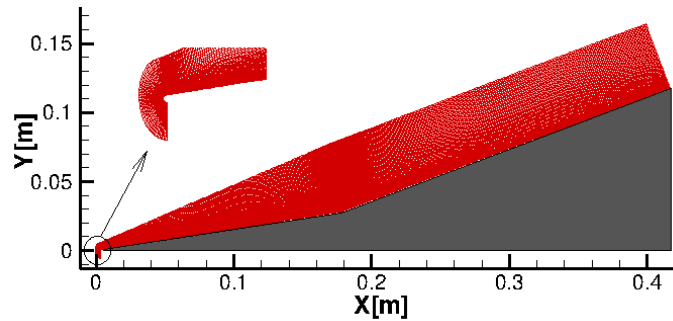


Figure 5.17. Computational grid for a hypersonic double wedge with blunt leading edge.

The results of the grid study are presented in Figure 5.18. For the coarse grid the simulation produces unreliable results. The results obtained with the medium and fine grids show a close behavior and allow us to use the medium grid for further analysis of this test case.

The same grid has also been used for the sharp leading edge configuration using 64 fewer points in the x -direction. These points have previously been used to resolve the blunt leading edge.

5.3.4.3. Results

For each configuration, a fully turbulent simulation as well as a laminar simulation has been performed but none of them could reproduce the experimental findings correctly. The measurements indicate that the boundary layer is laminar along the first ramp giving origin to a laminar separation, but then turns turbulent at some location along the separation due to the turbulence amplification across the ramp shock and in the shear layer above the separation where high shear stresses are generated. To reproduce this phenomenon a laminar/turbulent simulation has been performed setting the transition point at the kink and forcing the turbulence source terms to be zero upstream of it.

In order to describe the physics involved in the transitional (laminar/turbulent simulation) and fully turbulent configurations, the Mach number contours are shown in Figure 5.19 for

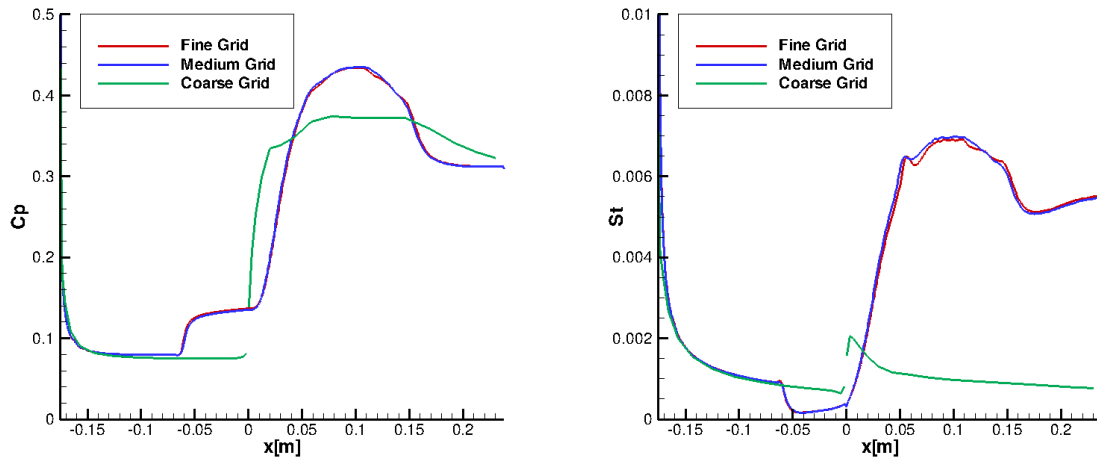


Figure 5.18. Grid convergence study on pressure coefficient and Stanton number for a double wedge configuration with blunt leading edge at $M=8.3$ and $Re=3.76 \times 10^6$ 1/m.

the blunt leading edge configuration. The whole computational domain is displayed and the main features are highlighted. A zoom of the leading edge is given to show the detached bow shock wave.

In Figure 5.19 (top), the laminar/turbulent solution is illustrated. The flow features visible at separation and reattachment are the same as described in Section 2.2.1. Along the first ramp the boundary layer separates, as visible in the low Mach number region at the kink, and a separation shock wave generates. This shock wave meets the first ramp shock at the first triple point. At the location where the boundary layer reattaches to the ramp, a reattachment shock is generated. Further downstream it meets the shock wave generated from the separation and the first ramp shock and gives origin to a shock corresponding to the superposition of the first and second ramp shock. After the second triple point a slip line can be seen in the Mach number distribution and an expansion wave is originated in order to make the pressure levels before and after the expansion compatible.

In 5.19 (bottom), the fully turbulent solution is reported. A detached bow shock wave originates in front of the leading edge and produces the first ramp shock moving downstream along the straight wall. At the kink a second shock wave is originated. The flow that passes through the first and second ramp shock waves experiences a higher pressure rise than the flow that passes through the combined shock that originates at the triple point where the two shock waves merge. From this point an expansion wave emanates and the slip line, between the fluids coming from the two different regions described above, is visible.

In Figure 5.20 (left), the pressure coefficient distribution for a sharp leading edge is shown. The black horizontal lines represent the values obtained from the oblique shock theory. The computational values obtained from the transitional simulations match well the experimental results along the first ramp. No substantial differences between the laminar result and the result obtained with the laminar/turbulent RSM or the SST Menter model with transition can

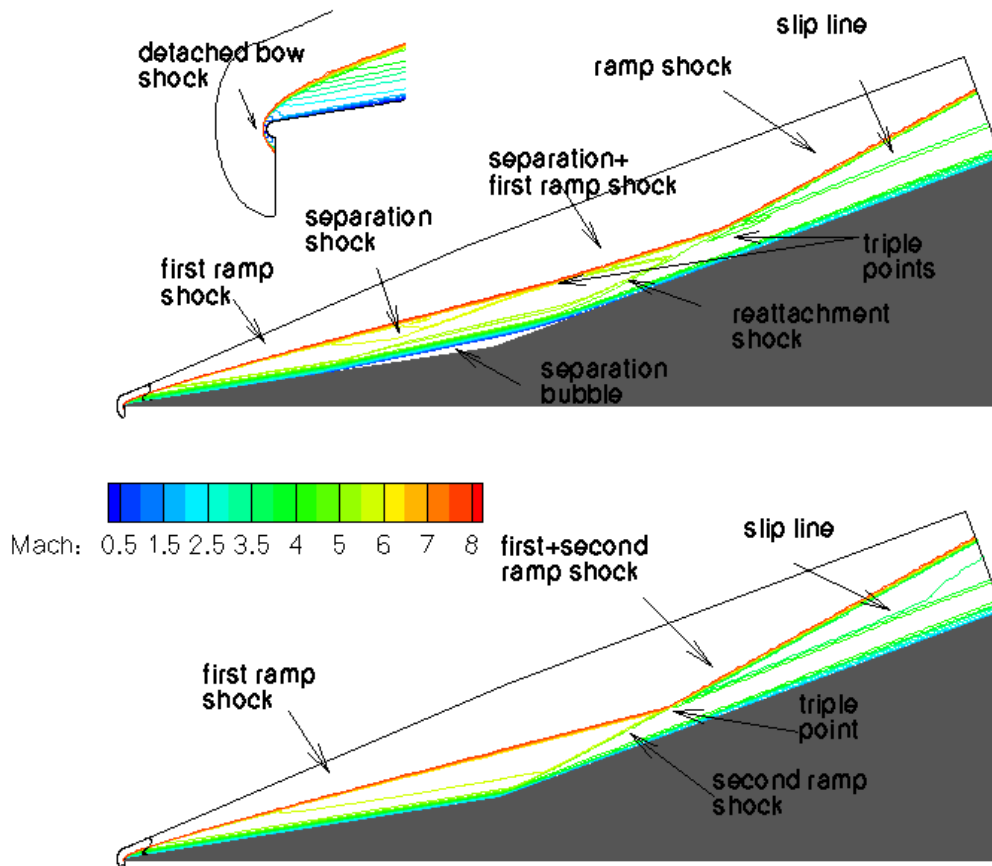


Figure 5.19. Mach number distribution for the laminar/turbulent (top) and for the turbulent (bottom) double wedge configuration with blunt leading edge at $M=8.3$ and $Re=3.76 \times 10^6$ 1/m.

be seen in the prediction of the separation size. For both the RSM and the SST model, the value of the pressure along the separation and up to the peak value are well predicted even though the peaks are not reached. For what concerns the results toward the end of the second ramp, a good agreement between the computational results is observed.

Figure 5.20 (right), shows the Stanton number for a sharp leading edge double wedge configuration. As expected, the fully turbulent simulations largely overpredict the value of the experimental Stanton number along the first ramp. Considering the transitional simulations, the laminar/turbulent RSM result and the SST transition result match the laminar profile and the differences in the size of the separation region are small. Near the kin,k the boundary layer undergoes a separation and the separation size is well captured by both transitional simulations and by the laminar one. After decreasing because of the laminar separation, the Stanton number increases passing through the second shock wave and the RSM results

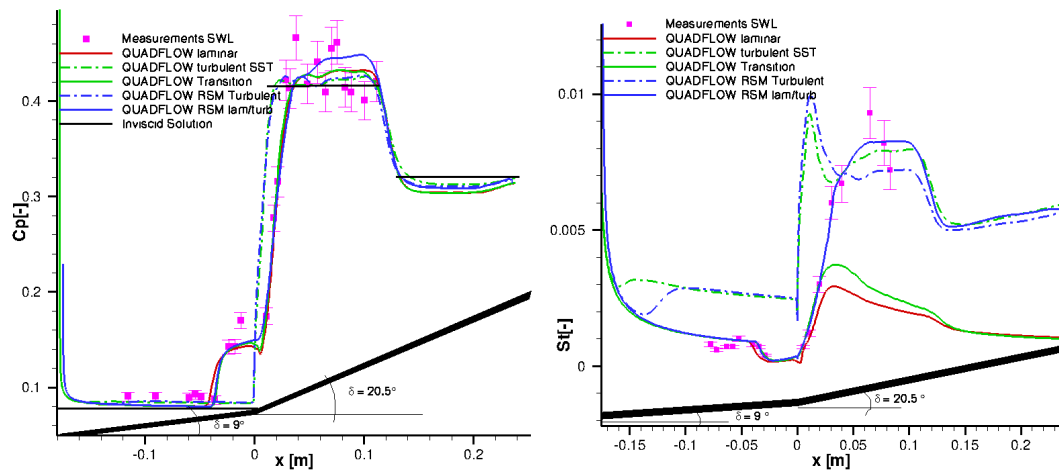


Figure 5.20. Pressure coefficient distribution (left) and Stanton number distribution along a double wedge configuration with sharp leading edge at $M=8.3$ and $Re=3.76 \times 10^6$ 1/m.

show a good agreement with the experimental ones but the peak value on the second ramp is not reached. For the RSM the turbulent and laminar/turbulent profiles are in good agreement toward the end of the second ramp. The SST model coupled with the transition model predicts a Stanton number close to the laminar solution along the second ramp.

In the case of a blunt leading edge surface loads similar to the one observed for the sharp leading edge are expected but in addition the effect of the entropy layer on the boundary layer has to be taken into account as explained in Section 2.1.2. Considering the small radius of the leading edge an increase of the separation size is expected as reported in the literature [59]. Figure 5.21 (left) shows the behavior of the pressure coefficient along the wall for a configuration with blunt leading edge. The black horizontal lines represent the pressure values obtained from the oblique shock theory. One can notice that the pressure value along the first ramp is the same for all the computational results but it is lower than the experimental one. This suggests that probably the inflow conditions for the experimental test were different from the nominal ones later used for the simulations. Higher pressure values are also observed along the second ramp where the pressure-peak measured in the wind tunnel is not reached by the simulations as it was the case for the sharp leading edge. The fully turbulent profile obtained with the RSM is in good agreement with the SST model in all flow regions.

For what concerns the laminar/turbulent computation, a boundary layer separation is observed along the first ramp and the size of the separation is smaller than that shown by the laminar solution. This is due to the fact that the turbulent flow along the second ramp affects the flow upstream of the kink making it more resistant to separation. After the kink the pressure increases, as predicted by the theory, with a slope larger than in the laminar case and reaches the inviscid value. Along the second ramp a further change in the pressure coefficient can be observed due to the merging of the two shock waves and the consequent generation of an

expansion fan at the triple point.

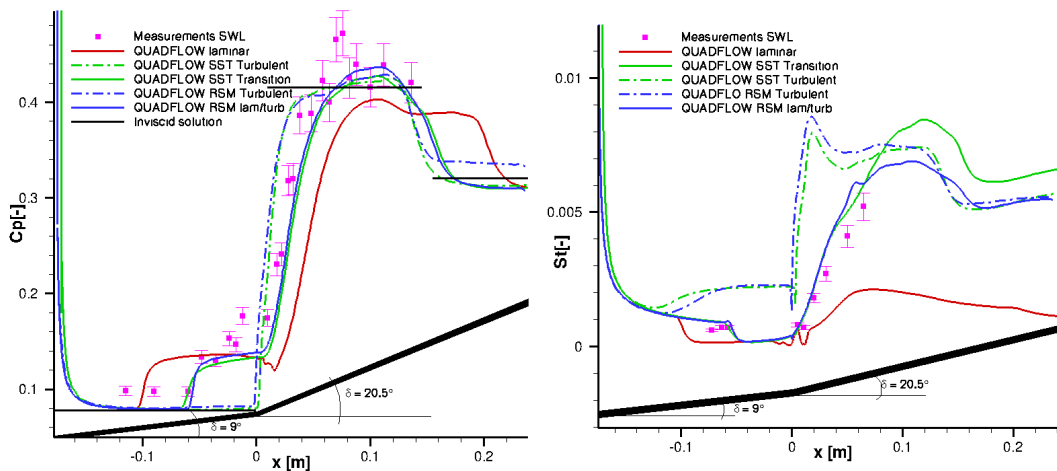


Figure 5.21. Pressure coefficient distribution (left) and Stanton number distribution along a double wedge configuration with blunt leading edge at $M=8.3$ and $Re=3.76 \times 10^6$ 1/m.

The Stanton number is shown in Figure 5.21 (right). As expected, the fully turbulent solution does not capture the separation of the boundary layer and shows values significantly different from the experimental results. For what concerns the laminar/turbulent simulation performed with the RSM, the Stanton number decreases along the first ramp correctly following the laminar ramp result and a further abrupt decrease occurs when the separation takes place. As also shown by the pressure distribution, the size of the separation detected by the heat flux is smaller than that observed in the fully laminar simulation. After the kink the Stanton number increases to turbulent values. With respect to the SST model, the RSM shows a smaller Stanton number peak along the second ramp but no experimental results are available for comparison in this region. The results presented in this section clearly show the ability of the RSM to simulate complex flows with SWBLI in hypersonic regime and producing results in good agreement with experimental findings and numerical results obtained with another turbulence model.

5.3.5. Comparison Between Adaptive and Structured Grids

This comparison has been performed in order to investigate the possibility of studying complex flow geometries by the mean of adaptive simulations in combination with the RSM. The test case and the simulation parameters are the same as the one described in the previous section apart from the Riemann solver: here the AUSMDV has been used.

The results obtained for a sharp leading edge and a fully turbulent flow are now compared with the adaptive results. The starting grid for the adaptive simulation has been chosen relatively fine: 200×30 points, in the stream and cross flow direction respectively, for the first ramp block and 80×30 point for the second ramp block. The points are uniformly distributed along the edges. The maximum number of refinement levels is $L=6$ and the threshold value

5. Model Validation

used for adaptation is $\epsilon = 10^{-2}$. The final grid contains approximately 900,000 cells and has a minimum wall resolution of 10^{-7} m at the leading edge which increases up to 10^{-6} m moving toward the kink and remains constant along the second ramp.

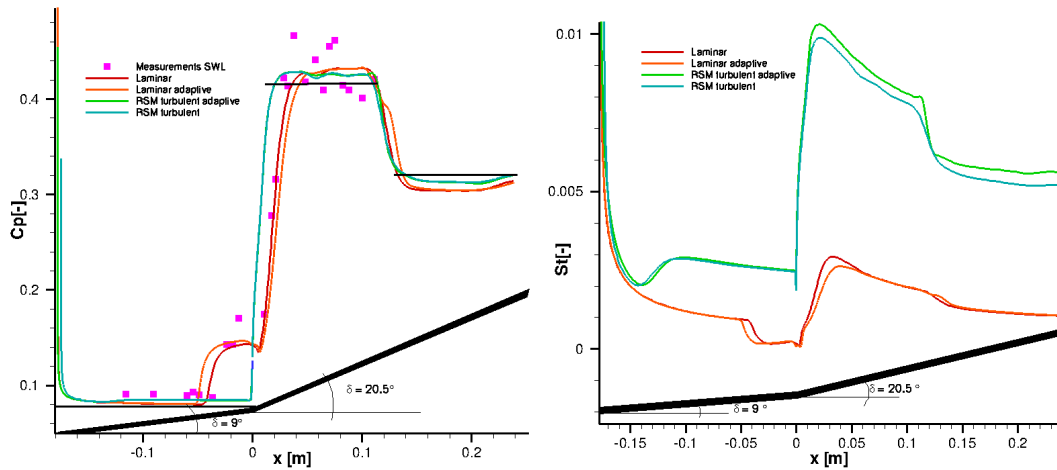


Figure 5.22. Pressure coefficient distribution (left) and Stanton number distribution along a double wedge configuration with sharp leading edge at $M=8.3$ and $Re=3.76 \times 10^6$ 1/m for adaptive and structured grids.

In Figure 5.22 the pressure distributions obtained using a structured and an adaptive grid do not present visible differences. The Stanton number distribution shows that the (numerical) laminar to turbulent transition occurs earlier in the adaptive grids due to the larger number of point along the first ramp. Along the ramp, the Stanton number is slightly higher in the adaptive case but the difference at the peak heating, where the error is the largest, is smaller than 5%.

The same adaptive grid has also been used to study the laminar solution. The main influence of the grid changes lies in the prediction of a slightly larger separation size. This is probably due to the sensitivity to the grid resolution in the separation region.

This test case shows the ability of the adaptive procedure, combined with the Reynolds stress model, to successfully reproduce the results obtained using structured grids.

6. Scramjet Results

A Scramjet (supersonic combustion ramjet) is a ramjet characterized by supersonic combustion. A ramjet is a supersonic air-breathing engine which uses the forward motion through the air to compress the incoming flow, without a rotary compressor as in the case of classical transonic vehicles. In order to achieve a supersonic combustion, the Scramjet has a minimal functional speed which lies in the range of hypersonic velocities.

A Scramjet is a highly integrated system: the forebody and the afterbody are integrated with the complete propulsion system. No moving parts are necessary for a Scramjet and thus the mechanical complexity of the system itself is low. However, the Scramjet will always have to be part of a combination engine.

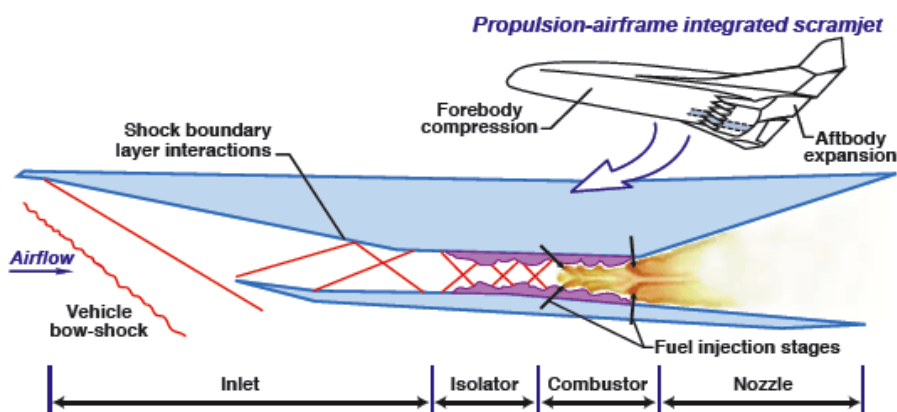


Figure 6.1. Main features of a Scramjet (source: NASA)

A Scramjet propulsion system is the subject of study for the Graduiertenkolleg GRK 1095 "Aero-Thermodynamic Design of a Scramjet Engine for Future Space Transportation Systems" [48]. This project involves three German universities: the Universität Stuttgart, the RWTH Aachen and the Technische Universität München and the German Space Agency (DLR) in Cologne. A Scramjet consists mainly of four components as illustrated in Figure 6.1. These components are now briefly described illustrating the characteristics chosen in the frame of the GRK 1095. The inlet consists of a double ramp that provides homogeneous high-pressure flow to the engine through a series of oblique shock waves. The isolator, as the name says, isolates the pressure sensitive inlet from the combustion chamber and allows the flow to adapt to the back pressure of the combustion chamber using a shock train. In the combustion chamber, liquid hydrogen is injected as fuel using a strut-injector, it mixes with high pressure air and the supersonic combustion takes place. Finally in the Single Expansion

Ramp Nozzle (SERN) the gas expands, accelerates to a speed higher than that at the inlet and exits the vehicle producing positive thrust.

A detailed description of Scramjet propulsion can be found in the book of Heiser and Pratt [57] or in the NASA report [38].

6.1. Experimental Settings

A Scramjet intake configuration has been studied experimentally in the framework of the GRK 1095 in the blow down tunnel H2K at the DLR in Cologne [52], [54], [53].

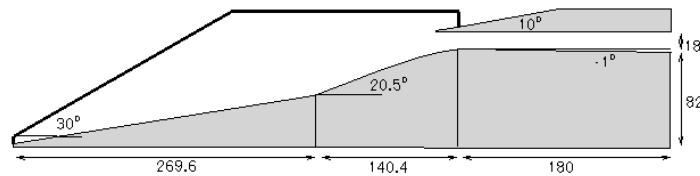


Figure 6.2. Scramjet intake geometry. The dimensions are given in millimeters.

The geometry of the experimental model is presented in Figure 6.2. The model is 100 mm wide and has side walls on both sides which are represented in the picture by the black bold line. The leading edge and the cowl tip are blunt with a radius of 0.5 mm. Measurement of pressure using pressure transducers and heat fluxes using an infrared camera were taken along the central line of the model. Measurement of Pitot pressure and Mach number have been taken at the isolator exit plane along the vertical center line.

The inflow conditions used within the experimental campaign are listed in Table 6.1.

p [Pa]	ρ [kg/m ³]	Re [1/m]	Ma [-]	T [K]
163	0.012	4×10^6	7	46

Table 6.1. Inflow conditions for the Scramjet intake configuration.

The wall temperature during the experiment was not uniform and its value varied between 300 K and 350 K.

6.2. Numerical Approach

This intensively applied test case has been already computed using the QUADFLOW solver on a structured grid using the SST two equation turbulence model and has been considered a valuable configuration for comparing the performance of structured and adaptive grids and for using the fully three dimensional formulation of the RSM. The inflow conditions used here are the same as the experimental one, the turbulence intensity is set to 0.2% and the viscosity ratio to 0.001. The Riemann solver used is the AUSMDV. For the boundary

conditions, supersonic inflow and supersonic outflow are used at the inflow and outflow boundaries, respectively. The no-slip condition at the wall is enforced using the strong boundary conditions. The wall is considered isothermal and its temperature set to 300 K. Since it was known that the experiment had revealed a laminar to turbulent transition along the inlet, a combined laminar/turbulent approach is adopted and the fixed transition point is set at $x=0.290$ m for all the results presented in this chapter.

First a two-dimensional analysis is performed using a structured grid and an adaptive grid [17]. The characteristics of the structured grid are given in Table 6.2 and the grid is presented in Figure 6.3. The grid has a constant wall spacing at the wall and has grid lines that are orthogonal to the walls. The grid has been generated by Krause and is described in details in his PhD thesis [64].

points x-dir	points y-dir	Δx_{max} [m]	Δx_{min} [m]	Δy_{max} [m]	Δy_{min} [m]
616	96	4×10^{-3}	10^{-6}	4×10^{-3}	10^{-6}

Table 6.2. Structured grid resolution for the two-dimensional Scramjet configuration at $M=7$ and $Re=4 \times 10^6$ 1/m.

The two-dimensional structured grid contains 60,000 cells. The points have been clustered in the boundary layer region both along the ramps and inside the isolator and in the kink region where boundary layer separation is expected.

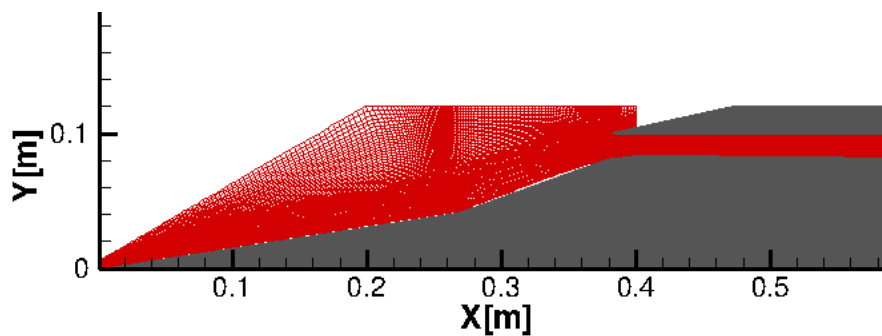


Figure 6.3. Computational structured grid for a two-dimensional Scramjet intake at $M=7$ and $Re=4 \times 10^6$ 1/m.

For what concerns the adaptive simulation, a number of refinement levels $L=5$ and a threshold value $\epsilon = 10^{-2}$ have been chosen. Given the initial resolution, the number of refinement levels has been determined in order to guarantee a first wall spacing of 10^{-6} m in the kink region and along the second ramp for the finest grid. The grid resolution along the first ramp is below 10^{-6} m. The grid on level 1 contains 4,600 points and is shown in Figure 6.4. The grid is generated using a multiblock topology and for the starting grid each block shows a coarse grid discretization. Afterwards the same adaptive procedure is adopted in all blocks.

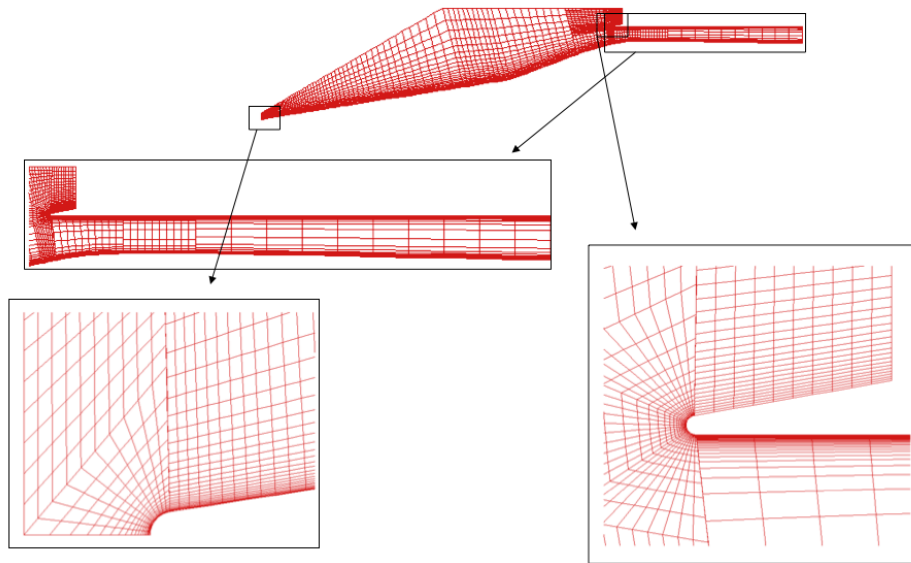


Figure 6.4. Computational grid for an adaptive computation of a Scramjet intake. Initial grid on uniform level 1.

adaptation	1	2	3	4	5
cells	19192	38218	64069	68971	144208

Table 6.3. Grid size for a 2D Scramjet configuration after each adaptation

Zooms of the interesting regions, such as the round leading edge, the cowl area and the isolator are presented. These are the regions where the majority of the shocks are generated and for this reason, more grid refinement is triggered here. The evolution of the grid resolution during the adaptive procedure is illustrated in Table 6.3.

It is worth noticing that only small differences in the grid size appear between the third and the fourth adaptation. This is not due to the fact that the grid has reached a good resolution since at the fifth adaptation the number of cells increases considerably, but due to the ability of the adaptive procedure to reduce the number of cells in regions where the flow solution has a smooth behavior. Between step 3 and 4 a new sorting of the cells in the flow takes place: some cells in the freestream are coarsened while in the regions close to the shocks or in the boundary layer regions grid refinement is performed. In case of coarsening the four child cells are replaced by their parent cell.

The final grid obtained after five adaptations is presented in Figure 6.5. Details of the blunt nose, the cowl tip and the isolator are given. The grid refinement in the location of the leading edge shock wave is visible in the global picture as well as the refinement at the wall triggered by the boundary layer. At the blunt leading edge, the bow shock is well captured by the grid as well as the boundary layer at the wall. At the cowl tip, the bow shock is clearly visible in the refinement of the grid and also the ramp shock impinging on the bow shock triggers the

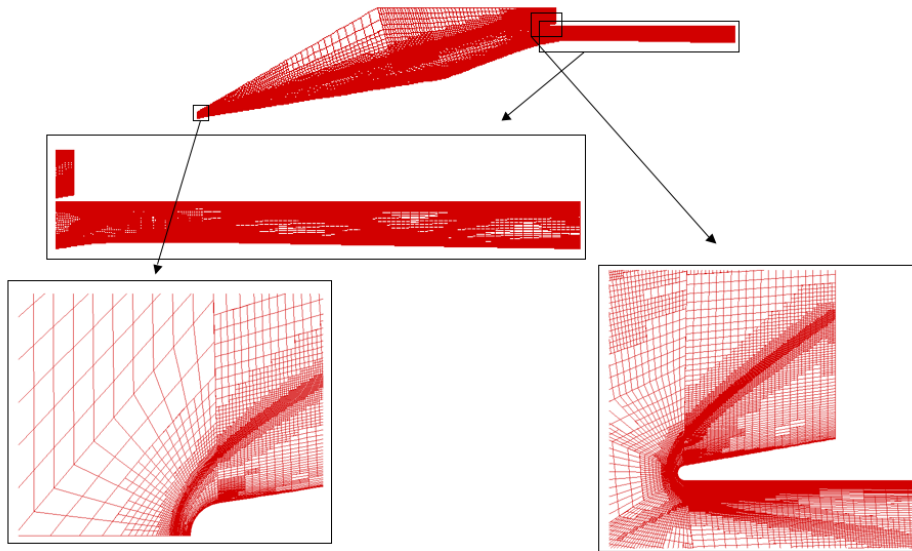


Figure 6.5. Computational grid for a Scramjet intake after the adaptation procedure using 5 refinement levels.

adaptation procedure. In the isolator, the pattern of the impinging-reflecting shock wave can be recognized in the way the grid has been refined. In the far field, regions are visible where no differences in the grid resolution appears between the initial and the final grid since the flow remains almost unchanged there.

For the three-dimensional grid the two-dimensional block-structured grid has been used as base and extruded in the z-direction for 100 mm. The characteristics of the grid are given in Table 6.4. The grid is refined in the z-direction near the side walls to capture the boundary layer growth. At the side walls the no-slip condition and the isothermal condition have been imposed.

	x-dir	y-dir	z-dir
min spacing	10^{-6} m	10^{-6} m	10^{-6} m
max spacing	4×10^{-3} m	4×10^{-3} m	8×10^{-4} m
points	616	96	88

Table 6.4. Structured grid resolution for the three-dimensional Scramjet configuration at $M=7$ and $Re=4 \times 10^6$ 1/m.

Some details concerning the resolution of the three-dimensional grid in the leading edge region and in the spanwise direction are given in Figure 6.6

6.2.1. 2D Results

The Mach contours for the two-dimensional Scramjet intake computed using the 2D structured grid are displayed in Figure 6.7. The whole field as well as a zoom of the blunt

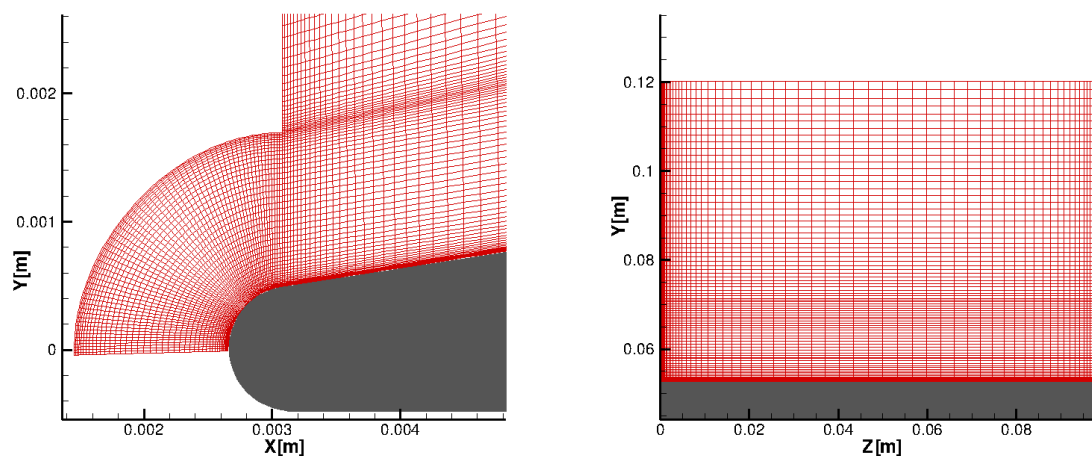


Figure 6.6. Details of the three-dimensional grid. Leading edge region (left), along the ramp at $x=0.29$ m (right).

leading edge and of the cowl tip are shown. In front of the blunt leading edge a detached bow shock is generated. The bow shock straightens along the first ramp generating the first ramp shock that exits the domain without interacting with other shock waves.

Along the first ramp, a boundary layer separation occurs and a separation forms at the kink. At the separation onset the separation shock is visible. Moving downstream along the second ramp, the separated boundary layer reattaches to the wall and a reattachment shock wave is generated. This shock wave impinges on the cowl shock that is generated in front of the cowl tip. Because of the blunt edge, the shock is a curved bow shock. The upper part of this shock wave simply exits the domain while the lower part impinges on the lower isolator wall giving origin to a large separation which size is approximately one half of the isolator height. The shock reflects on the wall and gives origin to an impinging reflected shock pattern, in the end, the reflected shock wave exits at the end of the isolator.

In Figure 6.8, the pressure distribution along the ramp and the lower isolator wall (left) is presented as well as the pressure along the upper isolator wall (right). The Mach number contours in both regions are also presented for clarity on the top of each figure. The results obtained using the structured grid and the adaptive procedure are compared with the experimental measurements. The numerical results are presented in blue and red respectively, the symbols represent the experimental values. The experimental error for the static pressure is 4-6% and is comparable with the symbol size.

The profile along the ramp clearly shows that the laminar boundary layer undergoes a large separation; this is visible from the early pressure rise at $x=0.14$ m. At the separation onset a separation shock wave is generated. In a location above the separation the flow turns turbulent due to the turbulence amplification across the shock wave and to the shear stresses generated in the shear layer. Along the second ramp the boundary layer reattaches to the wall giving origin to a considerable pressure rise. Due to the second ramp curvature the flow expands,

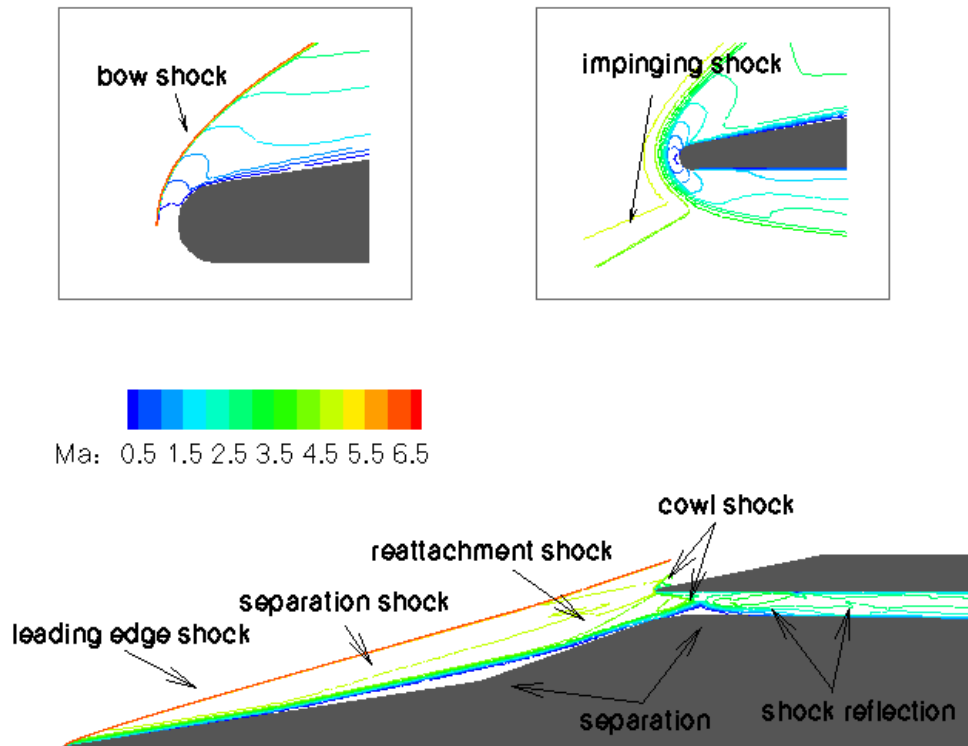


Figure 6.7. Mach distribution for a two-dimensional Scramjet configuration at $M=7$ and $Re=4 \times 10^6$ 1/m. On the top of the picture a zoom of the blunt leading edge (left) and of the cowl tip (right) are given.

accelerates and the pressure level decreases. In addition the expansion wave emanating from the triple point further enhances the pressure decrease. This process leads to a reduction of the turbulent content of the boundary layer which undergoes a 'relaminarization' even though a complete revers transition from turbulent to laminar does not occur. In the location where the cowl shock impinges on the lower isolator wall, the boundary layer shows a large separation due to the combined strength of the impinging shock wave and the reduced turbulent content of the flow. The latter can be seen in the distribution of the first component of the Reynolds stress tensor \tilde{R}_{11} at the isolator entrance shown in Figure 6.9.

The region of high \tilde{R}_{11} visible near the wall on the left side of the picture is followed by a region of decreasing value moving downstream due to the expansion of the flow. A local minimum is visible in the location where the cowl shock impinges on the boundary layer at the lower isolator wall. Two regions of high \tilde{R}_{11} are generated behind the impinging and the reflecting shock due to the turbulence amplification across the shock.

The physics at the impingement corresponds to the type I shock-shock interaction introduced in Section 2.2. A separation and a reattachment shock originate ahead and behind the separation, respectively. The reattachment shock impinges on the upper wall and an impinging-reflected pattern is established in the unthrottled isolator. The peaks visible in

6. Scramjet Results

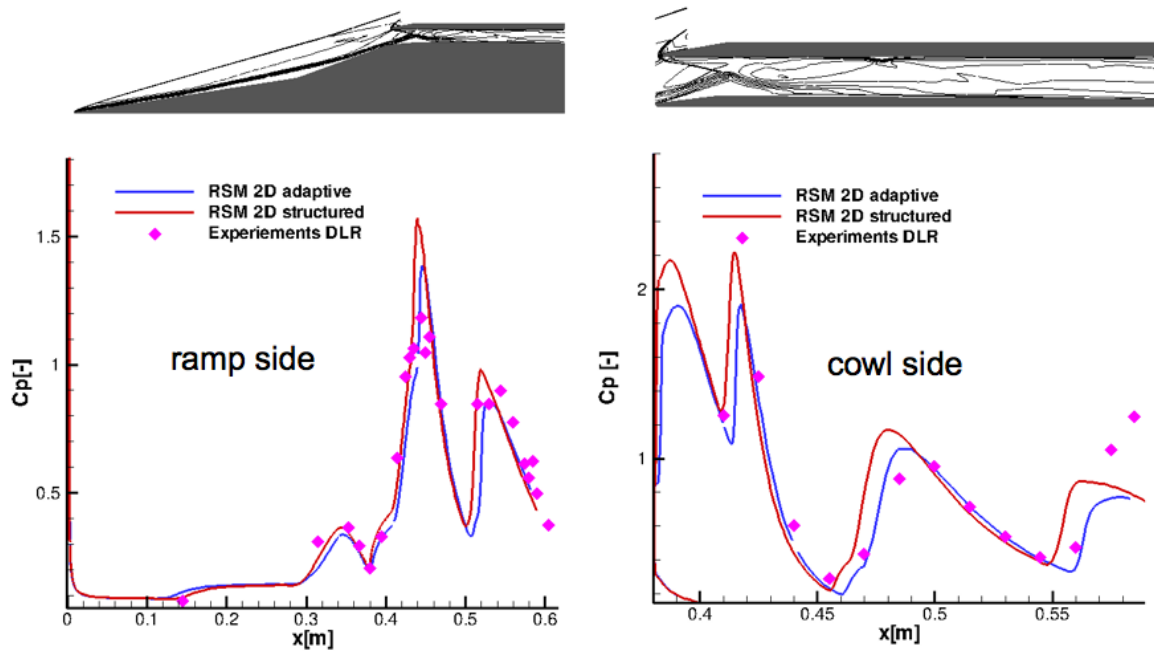


Figure 6.8. Pressure coefficient distribution along the ramp and the lower isolator wall (left) and along the cowl and upper isolator wall (right) for a 2D Scramjet intake configuration at $M=7$ and $Re=4 \times 10^6$ 1/m. On the upper part the Mach contours for the regions of interest are shown.

the pressure distributions at the wall on the ramp and cowl sides correlate with the shock wave reflections. On the ramp side, the numerical and the experimental results are in good agreement. The solution obtained from the structured grids shows more intense pressure peaks probably due to some small differences in the interaction pattern. On the cowl side, the solution from the structured grid does not match the exact location of the shock waves and the pressure rises occur further upstream than detected by the measurements. The adaptive solution agrees well with the experiment up to the last two measurement points where the predicted pressure is much lower than the measured one. The same behaviour is observed for the solution obtained using a structured grid. These two points show a pressure value that exceeds the previous peak while it would be expected that the shock waves weaken producing lower pressure peaks moving downstream.

The skin friction distributions along the wall for the ramp and the cowl side are presented in Figure 6.10 for the adaptive and the structured two-dimensional grids. The black horizontal lines correspond to a value of $C_f=0$ and have been drawn to identify the regions where the boundary layer is separated. These correspond to negative values of the skin friction coefficient. The values of the separation and reattachment points along the ramp side and the cowl side of the model are given in Table 6.5.

The adaptive simulation predicts the first separation point upstream with respect to the structured grid, probably due to the finer grid resolution along the first ramp. For both simulations, the skin friction coefficient takes negative values close to zero from the

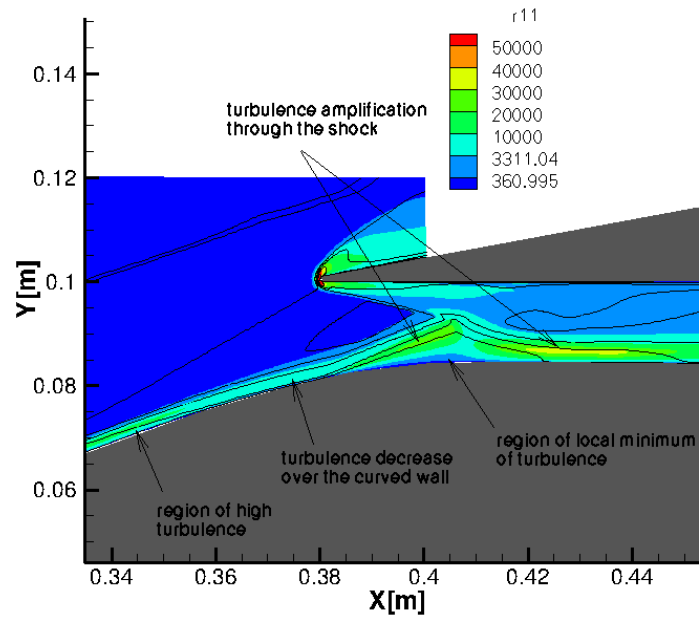


Figure 6.9. Distribution of \tilde{R}_{11} at the isolator entrance for a two-dimensional Scramjet configuration at $M=7$ and $Re=4 \times 10^6$ 1/m.

Ramp	separation 1 [m]	reattachment 1 [m]	separation 2 [m]	reattachment 2 [m]
Structured	0.159	0.312	0.383	0.418
Adaptive	0.143	0.319	0.381	0.416
Cowl	separation 1 [m]	reattachment 1 [m]	separation 2 [m]	reattachment 2 [m]
Structured	0.458	0.469	-	-
Adaptive	0.464	0.474	0.562	0.563

Table 6.5. Location of separation and reattachment point for the solutions obtained using a structured and an adaptive grid. The separations are numbered moving downstream.

separation point to the kink and then shows an abrupt decrease when the flow moves to the second ramp. Reattachment occurs slightly earlier for the structured grid. A second boundary layer separation is then numerically detected due to the cowl shock impingement on the lower isolator wall. Both simulations predict a similar behavior in this area.

Moving downstream, the adaptive simulation shows a larger decrease in correspondence of the second shock wave impingement. On the cowl side a pattern similar to that detected in the pressure distribution is visible. Also in this case the structured grid predicts the skin friction peaks earlier than the structured grid. In addition, the adaptive simulation predicts a small separation in correspondence to the last shock impingement which is not detected in the structured grid. The differences noticed for both pressure and skin friction distribution in the isolator are most probably due to the better resolution of the adaptive grid in correspondence of the shocks. The grid refinement in these locations decreases the numerical diffusion

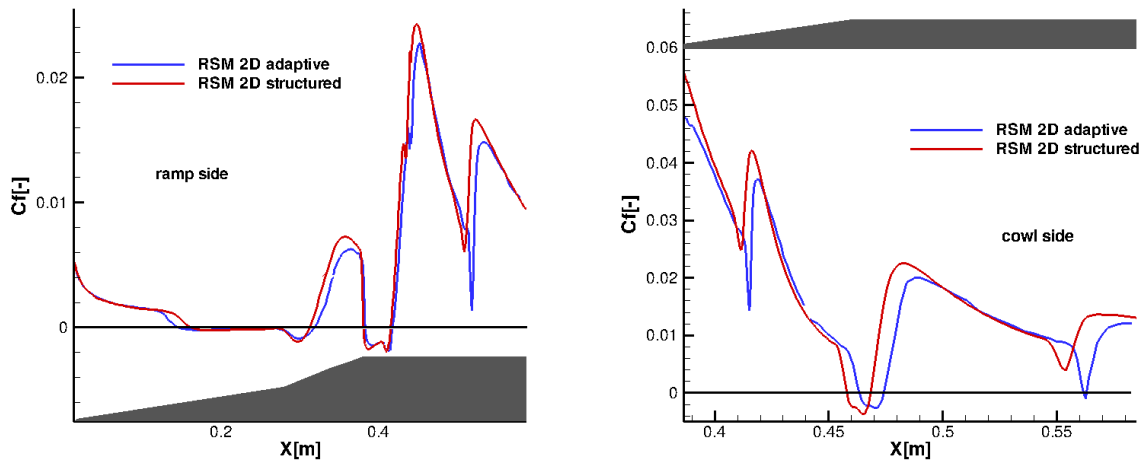


Figure 6.10. Skin friction coefficient distribution along the ramp and the lower isolator wall (left) and along the cowl and upper isolator wall (right) for a 2D Scramjet intake configuration at $M=7$ and $Re=4 \times 10^6$ 1/m.

allowing the solver to better capture the shock waves structure. A comparison of the grid resolution inside a portion of the isolator is shown in Figure 6.11. A comparison of the adaptive simulation with a simulation performed on a uniform grid at the highest refinement level ($L=5$) was not performed due to the high computational cost related to the huge number of cells. The adaptive procedure allows to get the same accuracy but at an affordable cost.

6.2.2. 3D Results

In order to increase the flow compression and improve the performance, side walls can be used for Scramjet intakes configurations. Clearly the presence of the walls affects the physics of the flows and new flow features appear. A three-dimensional simulation has been performed using the grid described in Table 6.4. The Mach number distribution along different planes is shown in Figure 6.12.

From the figure, some of the main flow features are visible. The first ramp shock wave can clearly be identified in the change of color at the locations $x=7$ mm, $x=88$ mm and $x=180$ mm. The separation above the kink can be seen in the blue region close to the wall visible on the planes $x=180$ mm and $x=250$ mm. The second separation, occurring at the isolator entrance is visible at the plane $x=410$ mm. At the corner between the wall and the side walls corner vortices formed. They are visible on both sides of the planes $x=88$ mm to $x=335$ mm. Inside the isolator, the traces of these vortices are also visible. In order to have a better look at the flow features and at the effects that the side walls have on the flow, the skin friction coefficient is considered.

Figure 6.13 shows the skin friction coefficient along the ramp wall and one side wall. The areas where the skin friction coefficient is negative are in grey color and correspond to regions

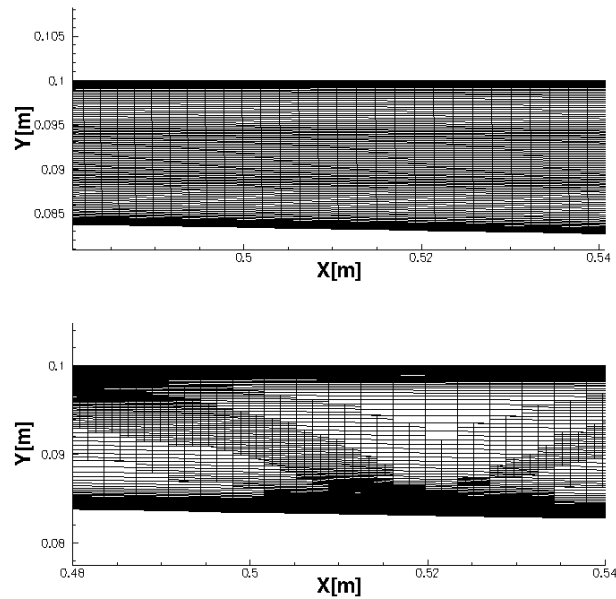


Figure 6.11. Grid resolution inside the isolator for a structured grid (top) and and adaptive grid (bottom) for a two-dimensional Scramjet configuration at $M=7$ and $Re=4 \times 10^6$ 1/m.

where the boundary layer has separated. Due to the presence of the side walls the separation and reattachment points show large variations in the crossflow direction. A huge separation is visible along the kink region characterized by two small areas, one at each side, where the flow reattaches, for a short distance, to the wall. The separation and reattachment points along the center line for both turbulence models are listed in Table 6.6.

The pressure distribution along the ramp and the lower isolator wall is shown in Figure 6.14 (left). For this configuration, the results are compared with those obtained using the SST model, coupled with the Menter transition model, in reference [64]. The results from the two-dimensional simulation on the structured grid are also reported for comparison. The results obtained using a 3D grid produce an improvement in the agreement with the experiments especially along the second ramp where the pressure rise and decrease is correctly predicted and also toward the end of the isolator where the 2D grid underpredicted the pressure levels while the 3D grid agrees well with the next-to-last measurement point. The reliability of the value of the last pressure measurement, which is higher than the ones from the previous peak, has been discussed in the previous section.

The results produced by the SST model combined with the transition model clearly show that the separation is considerably reduced with respect to the RSM. The pressure rise along the second ramp occurs upstream and the simulation does not match the experimental values in that region. Moving further downstream, the RSM and the SST model produce very similar results. On the cowl side of the isolator the numerical solutions provide similar results. The 3D simulations predict higher pressure level at the end of the isolator with respect to the 2D one. The RSM both in 2D and 3D capture a higher pressure peak in correspondence of the

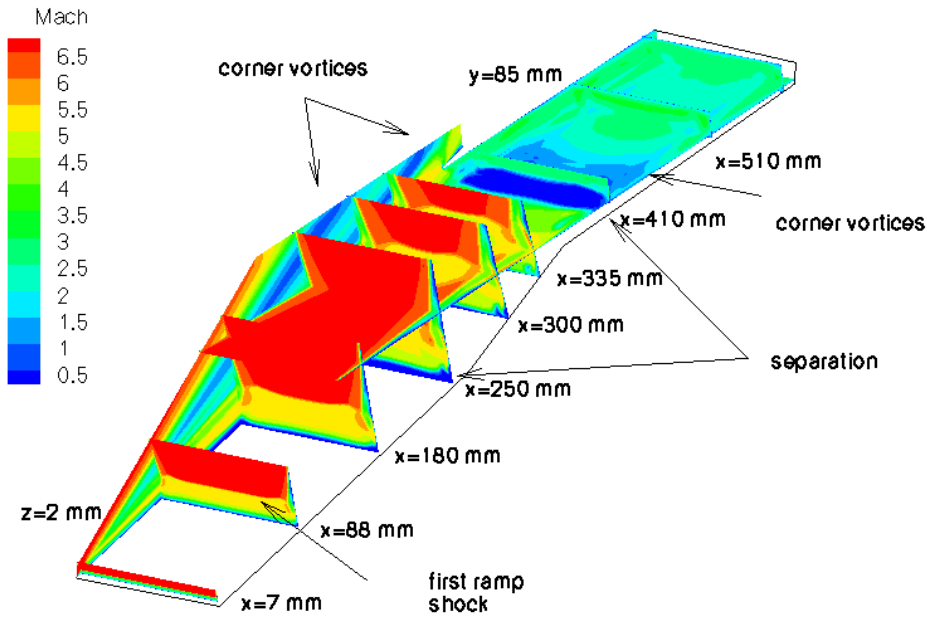


Figure 6.12. Mach distribution for a three-dimensional Scramjet configuration at $M=7$ and $Re=4 \times 10^6$ 1/m.

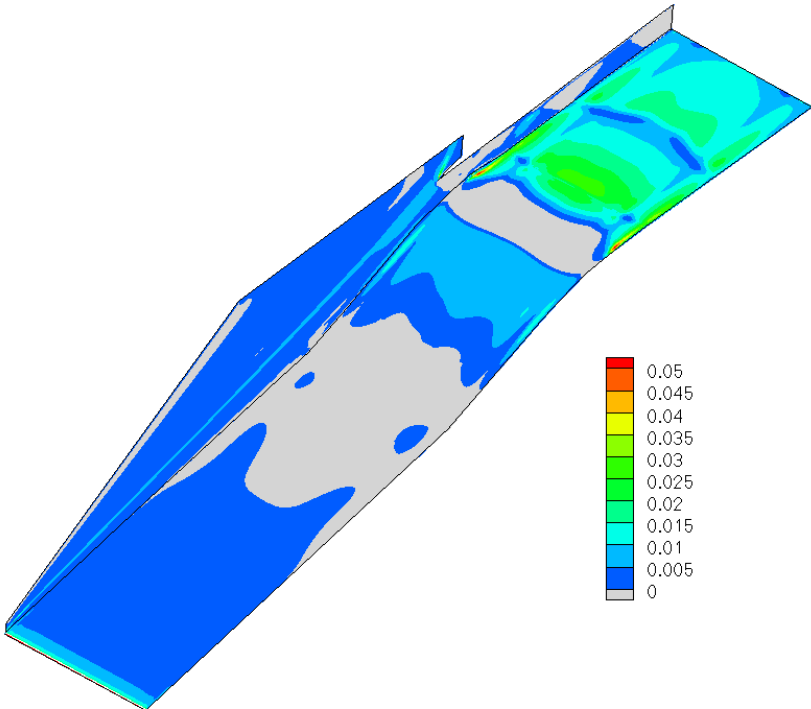


Figure 6.13. Skin friction coefficient along the wall of a three-dimensional Scramjet at $M=7$ and $Re=4 \times 10^6$ 1/m.

location of the separation due to the impingement of the cowl shock. This is due to the fact that the differences in the separation size noticed both in the pressure and in the heat flux

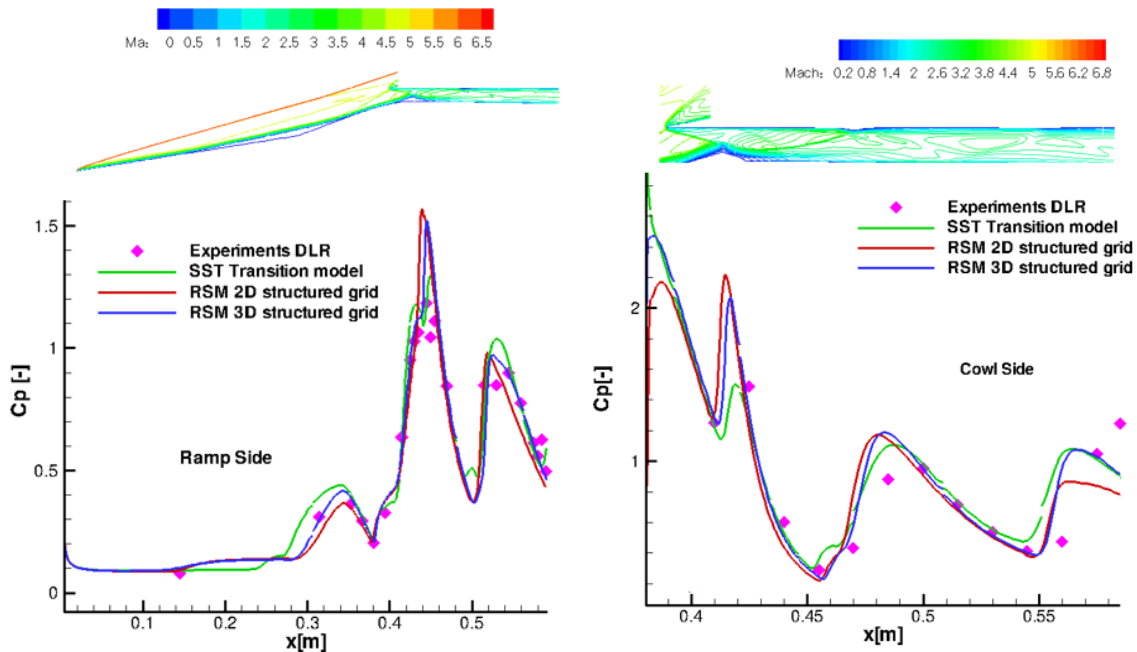


Figure 6.14. Pressure coefficient distribution along the ramp and the lower isolator wall (left) and along the cowl and upper isolator wall (right) for a 3D Scramjet intake configuration at $M=7$ and $Re=4 \times 10^6$ 1/m. On the upper part the Mach contours for the region of interest are shown.

results affect the shock pattern. The reattachment shock hits the bow shock from the blunt cowl tip at different locations depending on the turbulence model used as visible in Figure 6.15. For the RSM, the shock wave hits the bow shock below the cowl and the two shocks merge giving origin to a stronger shock wave that produces a higher pressure rise at the wall when it impinges. In the case of the SST model the shock wave hits the bow shock above the cowl.

The Stanton number along the kink is presented in Figure 6.16. A visible increase in the Stanton number is observed using a three-dimensional domain, with respect to a two-dimensional one due to the side wall compression. The RSM prediction starting at $x=0.30$ m lays among the measurement error. The SST model shows a better agreement along the second ramp near the kink. The prediction along the first ramp is difficult to interpret. The RSM always predicts a large separation but the Stanton number levels along this region are different in 2D and 3D. The SST model predicts a small separation near the kink and the experiment show a small decrease in the Stanton number and then a steady increase over the kink where the values are much higher than in all the numerical simulations.

Pitot measurements have been taken placing a pitot rake, containing 5 pitot probes vertically lined up, at the exit of the isolator. The Pitot pressure and the Mach number are presented in Figure 6.17 (right). As before, the blue line represents the RSM and the green line the SST model combined with the transition model; in both cases the 3D grid has been

6. Scramjet Results

Ramp	separation 1 [m]	reattachment 1 [m]	separation 2 [m]	reattachment 2 [m]
3D RSM	0.163	0.307	0.383	0.415
3D SST+trans	0.247	0.292	0.383	0.417
Cowl	separation 1 [m]	reattachment 1 [m]	separation 2 [m]	reattachment 2 [m]
Structured	0.460	0.471	0.554	0.558
Adaptive	0.455	0.472	0.551	0.554

Table 6.6. Location of separation and reattachment point for the solutions obtained using the 3D RSM and the 3D SST model coupled with the transition model. The separations are numbered moving downstream.

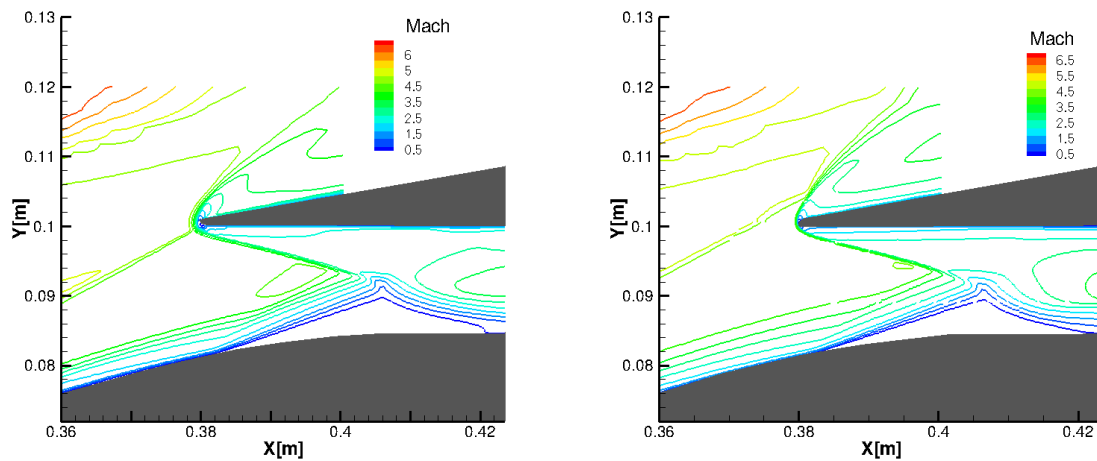


Figure 6.15. Mach number distribution in the cowl region for the RSM (left) and the SST model (right) for a three-dimensional simulation along the center line.

employed. The pressure distribution is better captured by the RSM even though the pressure peak is not reached. Due to the differences in the shock train occurring in the isolator, the second Pitot probe from the top is not hit by a shock wave as in the experiment. For what concerns the Mach distribution, the RSM overestimates the values at each location but seems able to better capture the general behavior such as the decrease of the Mach number at the third measurement probe.

The results presented in this chapter show that a differential Reynolds stress model can be successfully used to simulate highly complex three-dimensional simulations characterized by SWBLI. The model is able to correctly predict the flow features and to produce results in good agreement with both experimental findings and another turbulence model. In addition, the adaptive procedure tested on this geometry has been able to further improve the agreement with the experimental data.

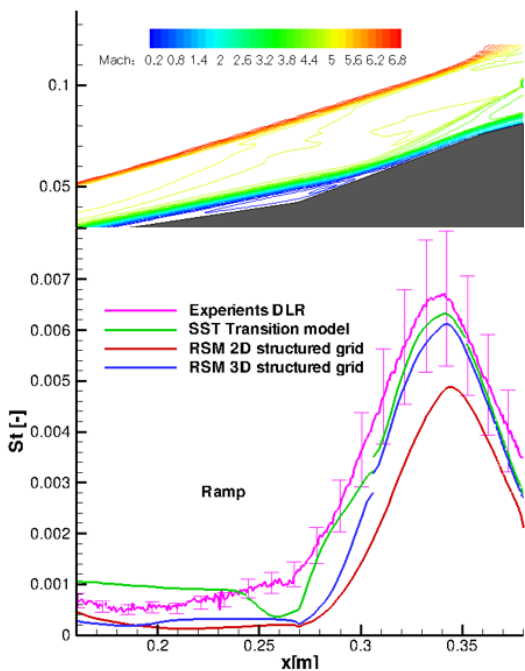


Figure 6.16. Stanton number distribution along the kink region for a 3D Scramjet intake configuration at $M=7$ and $Re=4 \times 10^6$ 1/m.

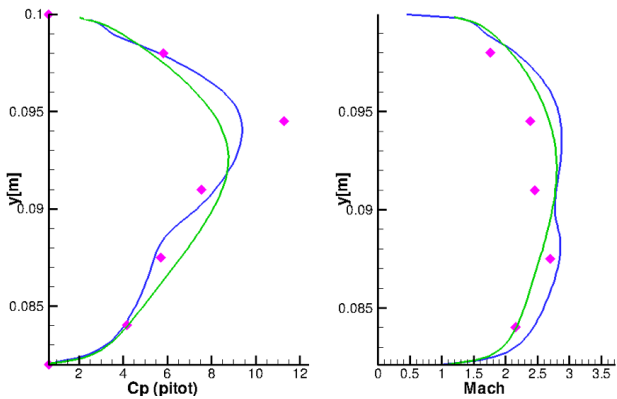


Figure 6.17. Pitot pressure and Mach number distribution at the isolator exit along the central vertical plane for a 3D Scramjet intake configuration at $M=7$ and $Re=4 \times 10^6$ 1/m.

7. Three-dimensional hypersonic SWBLI

In this chapter the results obtained during an experimental campaign are compared with numerical simulations to test the prediction capability of the RSM for a flow characterized by three-dimensional SWBLI. In the first part, the preparation of the experimental campaign, the analysis conducted to assess the tunnel flow conditions, the sensors manufacturing and the choice of the sensors location along the model surface are discussed. In the second part, the experimental results, for each investigated condition, are compared with the solution obtained with the RSM. For two representative test cases numerical results from two linear eddy viscosity models and an explicit algebraic Reynolds stress model are also presented.

7.1. Experimental Investigation of a Compression Corner

The experiment has been a cooperation between three institutions: the Aachen Institute for advances studies in Computational Engineering Science at the RWTH Aachen University (AICES, Germany), The University of Queensland, Centre for Hypersonics (UQ, Australia), where the experiment has been conducted, and the University of New South Wales at the Australian Defence Force Academy (UNSW@ADFA, Australia). The collaboration initially focused on the analysis of previous SWBLI experiments, which had been instrumented on the assumption that the interaction would be fundamentally two-dimensional and that the data collected along the center line of the model were not affected by the finite model width [13]. In order to quantify the effect of three-dimensionality and to test the prediction capabilities of the RSM for fully turbulent conditions on a three-dimensional SWBLI, an experimental campaign has been initiated funded by the AICES graduate school. A compression corner, which consists of a flat plate with a compression ramp at its end, has been chosen as the object of investigation. The full definition of the model and test conditions has been specified through numerical design and the sensors position optimized to collect data from key regions such as the boundary layer separation and the reattachment. The aspect ratio of the flat plate, defined as the ratio between its length and its width has been chosen equal to one to minimize the spillage effects occurring at the model side and two ramp angles have been investigated to collect results for both a turbulent attached boundary layer and a turbulent separated boundary layer. Preliminary simulations with varying ramp angles have been performed and values of 15 degrees and 40 degrees have been considered suitable for the campaign purposes.

7.1.1. T4 Shock Tunnel

The experiment has been performed in the T4 free-piston tunnel at the University of Queensland (Australia) [75]. The facility is capable of producing flows with total enthalpies

in the range of 2.5 to 15 MJ/Kg and sub-orbital flow speed at a range of Mach numbers from 4 to 10.

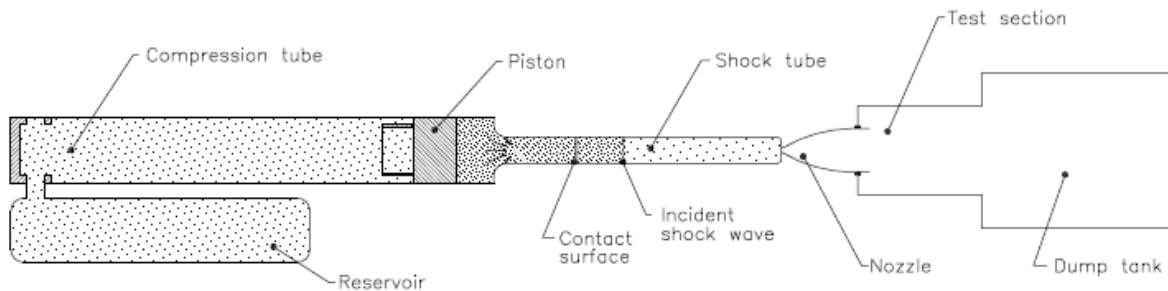


Figure 7.1. Schematic of the T4 shock tube as from [103].

The T4 shock tunnel, shown in Figure 7.1 consists of five main sections: a high-pressure reservoir, a compression tube, a shock tube, a test section and a dump tank. The test section and the dump tank are evacuated before each run to a pressure below 130 Pa (1 Torr) to ensure a rapid nozzle startup and flow establishment. When the tunnel is fired a 92 kg piston is driven by the high pressure air coming from the reservoir, through the compression tube. At the end of the compression tube a metal-diaphragm breaks once a sufficient pressure is reached. At this moment a shock wave is generated in the test gas inside the shock tube and a contact surface separates the driver gas from the test gas. Once the shock wave reaches the end of the shock tube it is reflected in the shock tube and traveling backwards it stagnates the test gas. The test gas breaks a thin secondary diaphragm at the nozzle throat, expands inside the nozzle and finally enters the test section. The unsteady nozzle process starts and is followed by a steady established flow. The gases are then collected in the dump tank. For the experimental campaign a Mach 6.68, axisymmetric, contoured nozzle is used. The experiment is performed using air as test gas, argon as driver gas, a nozzle-supplied enthalpy of about 3 MJ/kg and a unit Reynolds number of about $10 \times 10^6 \text{ m}^{-1}$ for a 6 mm diaphragm thickness and $5 \times 10^6 \text{ m}^{-1}$ for a 3 mm diaphragm thickness. Under these operational conditions the tunnel provides approximately 2 ms of steady test time. The test section, where the model is located, has a size of $0.45 \times 0.45 \text{ m}$ in the cross flow direction and a length of about 0.8 m; the usable part of the test section depends on the extent of core flow region generated by the chosen nozzle.

7.1.2. Operating and Freestream Conditions

The choice of the testing conditions has been dictated both by the need of getting high Reynolds number flow, which allows the generation of turbulent conditions, and by the need of keeping the total enthalpy low enough for high temperature effects to be negligible. Two conditions have been investigated that satisfy these requirements. They are listed in table 7.1. The freestream total enthalpy produced by these conditions is 3.19 MJ/Kg and 3.58 MJ/Kg, respectively.

Condition	Reservoir pressure (MPa)	Compression Tube pressure (KPa)	CT Gas	Shock Tube pressure (KPa)	Test Gas
3 mm	5.6	80.5	Argon	240	Air
6 mm	2.8	40.2	Argon	150	Air

Table 7.1. Shock tunnel filling conditions.

	ρ [Kg/m ³]	p [Pa]	U [m/s]	M [-]	Re [1/m]	T [K]
Condition 6 mm	0.08624	9681	2516	6.35	9.65×10^6	396
Condition 3 mm	0.0485	5186	2465	6.38	5.51×10^6	386

Table 7.2. High and low Reynolds number inflow conditions, named by the diaphragm thickness.

The tunnel conditions listed in Table 7.1 lead to the freestream conditions at the nozzle exit reported in Table 7.2. Considering the short test time of 2 ms, the model surface temperature remains constant during one test run.

7.1.3. Freestream Non-Uniformities

The contoured nozzle used for the campaign generates a core flow of almost uniform flow which is bounded by the expansion waves that propagate at the edges of the nozzle itself. A Pitot pressure survey has been conducted at the end of the test campaign, for both conditions in Table 7.1, to quantify the non-uniformities of the freestream flow, to prove the repeatability of the flow characteristics between different runs for the same nominal tunnel conditions and to determine the appropriate Pitot-to-nozzle-supply pressure ratio (p_p/p_s) to be used for postprocessing the results. The nozzle-supplied pressure is the pressure measured by the stagnation probes at the end of the shock tube. A typical trace of a stagnation probe is given in Figure 7.7. The Pitot pressure, which is the pressure measured by the Pitot probe, is defined as [76]:

$$p_p = p_\infty \left[\frac{(\gamma + 1)M_\infty^2}{2} \right]^{\frac{\gamma}{\gamma-1}} \left[\frac{\gamma + 1}{2\gamma M_\infty^2 - (\gamma - 1)} \right]^{\frac{1}{\gamma-1}}, \quad (7.1)$$

with γ being the isentropic coefficient equal to 1.4 for air considered as a perfect gas. Previous pressure survey results have been used before the campaign to detect the core region and determine an appropriate position of the model inside the test section.

The Pitot rake, consisting of 33 PCB piezoelectric pressure transducers, has been located 33 mm away from the nozzle exit, which corresponds to a position 80 mm downstream of the flat plate leading edge for the considered model. Taking into account the limited extension of the model in the flow direction, only one horizontal position of the rake has been investigated but measurements have been taken for two vertical positions to increase the spatial resolution. Before use, all PCBs have been calibrated in situ so that the effects of mounting, amplifier

7. Three-dimensional hypersonic SWBLI

and cabling were included in the obtained calibration coefficients. Details of the mounting of a Pitot probe in its shell in order to avoid vibrations can be found in [104].

For each configuration, two runs have been performed which means four runs per inflow condition. Apart from one run at the 3 mm condition, that has been excluded from the post-processing, the results show, for each condition, values consistent with the one registered during the campaign, in terms of stagnation pressure and shock speed inside the shock tunnel. The data collected from gauges that saturated (experienced pressure levels above their working range) during the test time have been excluded from the analysis.

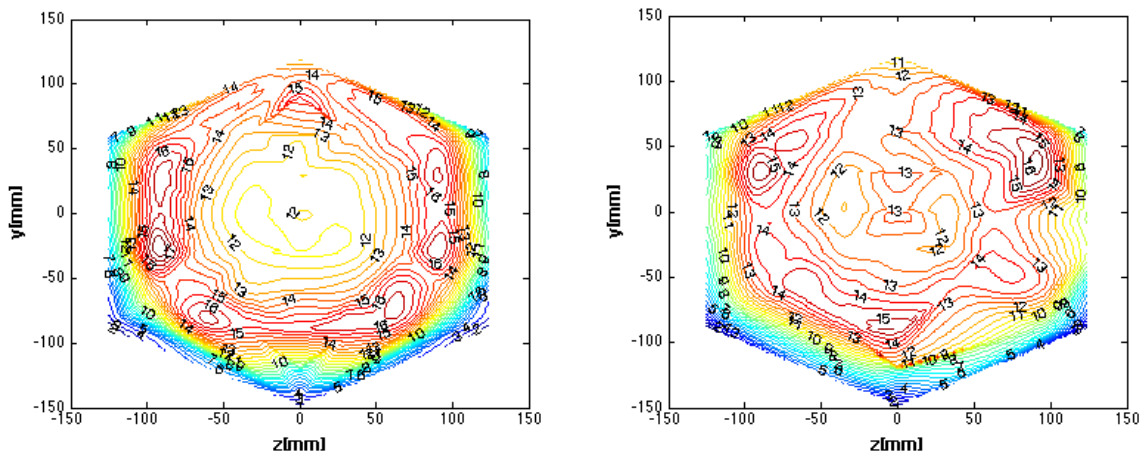


Figure 7.2. Isocontours of Pitot-to-nozzle supply pressure ratio (p_p/p_s) for the 3 mm condition (left) and the 6 mm condition (right). Levels given as $1000p_p/p_s$.

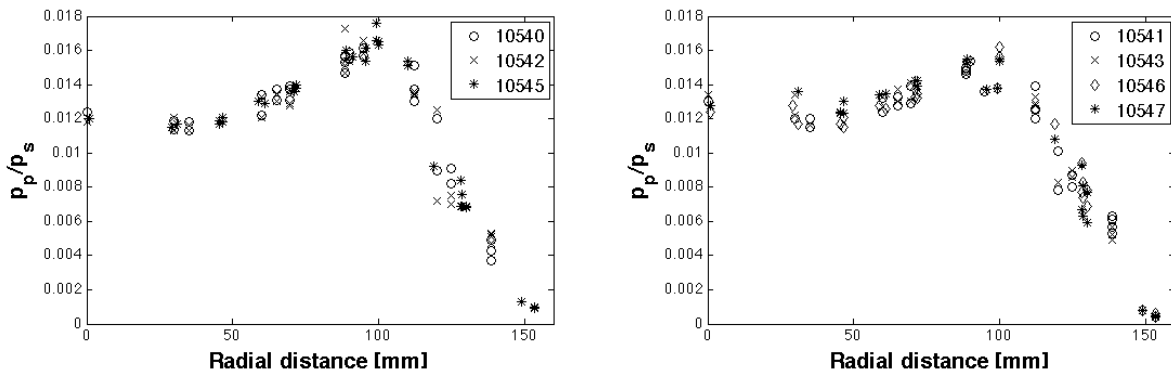


Figure 7.3. Pitot-to-nozzle supply pressure ratios plotted against radial distance from the nozzle centerline. 3 mm condition (left) and 6 mm condition (right).

The results from both conditions are shown in Figure 7.2 as contour plot. The value of the Pitot-to-nozzle pressure supply ratio is shown over the area captured by the Pitot rake and the values written along the isolines are given as $1000 p_p/p_s$. In Figure 7.3, the radial distribution

of the same quantity, with respect to the nozzle center, is displayed to test the symmetry of the flow. The two pictures show a good repeatability for the 3 mm condition, especially in the flow region where the model has been located, i.e., z -values between +75 mm and -75 mm in Figure 7.2 corresponding to a radial distance below 75 mm in Figure 7.3. For the 6 mm condition, the p_p/p_s value shows a slightly larger spread particularly near the center of the flow. The p_p/p_s has been computed as a weighted average of the value over the area captured by the model at 15 degrees. The average is calculated allocating to each PCB the portion of the flow which is closer to that gauge than to any other one. A value of p_p/p_s equal to 0.0013 has been found for both conditions and has been used for the postprocessing as explained in Section 7.1.5.

7.1.4. Experimental Model and Sensors

A three-dimensional CAD image of the compression corner used for the campaign is shown in Figure 7.4 for a ramp angle of 15 degrees. The CAD design of the model and the manufacturing of the parts has been done at UQ. The dimension of the model and the sensor positions have been accurately optimized in order to collect data in sensible flow regions and to obtain the desired conditions along the model.

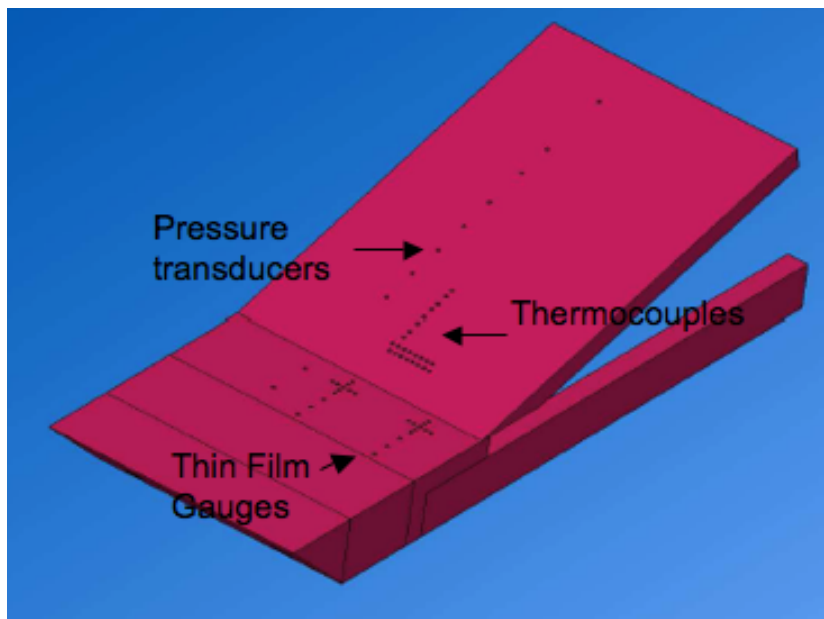


Figure 7.4. Three-dimensional view of the experimental model at an angle of 15 degrees. The location of the different sensors along the surface is shown.

Figure 7.5 shows the model inside the tunnel for a ramp angle of 40 degrees. On the left picture the model is visible from the side. With respect to Figure 7.4 the model is mounted into the test section upside down. The picture on the right has been rotated of 180 degrees for clarity. For this experiment, the flat plate is 150 mm long and 150 mm wide. From the design process an aspect ratio of 1, defined as the ratio between the plate length and plate

7. Three-dimensional hypersonic SWBLI

width, has been chosen to minimize the three-dimensional effects due to the flow spillage at the sides. The maximum plate dimension was then subject to constraints deriving from the extension of the nozzle core flow. From existing experimental and numerical analysis, this region was found to have a crossflow extension of approx. 200 mm. For this reason 150 mm has been considered as an appropriate width to ensure an almost uniform flow above the plate. The plate is composed of three parts visible in Figure 7.5 (left). A removable sharp leading edge of 45 mm length was chosen to keep the manufacturing process as straightforward as possible and avoid errors coming from the need of re-manufacturing this part during the campaign. Connected to the leading edge is a removable plate of 50 mm length. This part allows a reduction of the plate length and consequently of the local Reynolds number to obtain a laminar flow above the model (for a diaphragm thickness of 1 mm). The laminar investigation was not in the aim of this thesis so that only results using the full plate length are presented here. The last component is an instrumented plate of 60 mm length; the last 5 mm of its surface are used for connecting the plate to the ramp so that the effective total plate length, from the leading edge to the ramp, is 150 mm.



Figure 7.5. Photographs of the investigated model inside the test section of the T4 shock tunnel. Side view (left). Front view (right), this picture is rotated of 180 degrees for clarity.

The compression ramp is 250 mm long, so that when inclined at 40 degrees only a small portion of the back of the ramp lies outside the core flow. At 15 degrees, the whole model lies inside the core flow. The ramp is connected to the plate using two metal supports on the side to keep it at the right inclination. A thin layer of silicon gel was applied along the last 5 mm of the plate to ensure a proper adherence between the two metal surfaces. To enhance the laminar to turbulence transition and obtain a fully turbulent flow along the model, a boundary layer trip constituted by triangular roughness elements was positioned between the leading edge and the removable plate as visible in Figure 7.5 (right). The triangular teeth are 2.1 mm high and 4.2 mm wide.

The main focus of the campaign was the measurement of the heat flux in the separation

and reattachment regions. For this reason the collocation of the heat flux sensors, thin film gauges (TFG) and thermocouples (TC), was a priority with respect to the pressure sensors. The last downstream sensor location along the plate and the first upstream sensor location along the ramp were imposed by manufacturing constraints. It was not possible to locate any sensor closer to the hinge line without compromising the structural integrity of the model when subject to the high Reynolds number flow chosen as inflow. Along the instrumented plate, two TFG stencils are visible in Figure 7.4. Each stencil is composed of twelve sensors: eight sensors disposed in the streamwise direction and five in the crossflow direction forming a cross (one sensor is counted twice). For one stencil the streamwise gauges are distributed along the center line of the model. The other stencil is located 46.85 mm on the side in order to gain an insight of the flow away from the center line and estimate the effect of the three-dimensionality of the flow. In the streamwise direction the gauges cover the whole length of the instrumented plate within the manufacturing constraints. In the crossflow direction the ten gauges (five from each stencil) are disposed along a line that is inside the separated region for each examined condition where a boundary layer separation occurs. For the measurement of the heat flux in the reattachment region 38 TC have been employed. The TC have been located along the model surface to measure the heat flux in the reattachment region to detect variations in both the streamwise and the crossflow direction. Four rows of eight sensors are spaced orthogonal to the flow, each line slightly displaced with respect to the adjacent ones. In Figure 7.4 only two of these rows are visible. At one end, each row has a sensor on the center line or two sensors at its side. Six additional TC are disposed along the center line of the model to make a series of ten (almost aligned) gauges.

Finally, 10 Kulite pressure sensors have been distributed along a line parallel to the center line of the model and displaced of 23 mm due to the presence of heat flux sensors along the center line. Two sensors are located along the flat plate and eight along the compression ramp. The first Kulite along the ramp is located substantially away from the kink since the ramp thickness in that region is decreased to allow the ramp to lie on the tip of the flat plate at an angle of 15 degrees. The reduced model thickness did not allow the drilling of the holes necessary for the Kulite mounting.

The signal collected by each sensor was sampled every microsecond. The exact location of each sensor along the model is given in Appendix A.

Thin Film Gauges

For the measurement of the moderate heat fluxes along the flat plate and the separation region 24 thin film gauges have been employed. They are cylinders of 2.3 mm diameter and 3.3 mm length. The response time of these gauges is about 1 μ s. The advantage of this kind of sensors is that they allow measurement of temperature changes in the order of 0.1 K and heat flux as small as 0.5 W/cm². However due to the design their thin film can easily get damaged. The gauges have been bought from the Shock Wave Laboratory (SWL) in Aachen and an accurate description of their characteristics can be found on the SWL website [2]. No

calibration was needed for these gauges since they were calibrated after manufacturing. The TFG have a diameter of 2.3 mm and a length of 6 mm. They have been mounted into the model by inserting them into cylindrical holes flash to the surface and gluing the back to the model, as shown for the TC in Figure 7.6. Each group of 12 TFG has been connected to a 12 pins D-connector. An appropriate amplifier has been used. For the estimation of the error on the heat flux, the analysis conducted by A. Dann in a similar facility has been used and the error for the heat flux has been estimated as +/- 10% [32].

Thermocouples

For the measurement of heat fluxes along the compression ramp, fast response surface junction K-type thermocouples have been chosen for their robustness since they can withstand harsh flow conditions as the extremely high heat flux, in the order of $2 \times 10^7 \text{ W/m}^2$, registered at the peak heating during the campaign. The principle of thermocouple is to generate a voltage using the difference in properties between two different materials. In the case of K-type TC the components are chromel (chrome and aluminium alloy) and alumel (nickel and aluminium alloy). The voltage is generated by the temperature gradient between the two metals. For the range of temperatures between 300 K and 1300 K the change in voltages registered at the TC surface is directly proportional to the change of the flow temperature. In order to reduce the experimental costs, the thermocouples have been self-manufactured. The manufacturing and calibration were performed using a concept and a technique similar to the one of Buttsworth in [25].

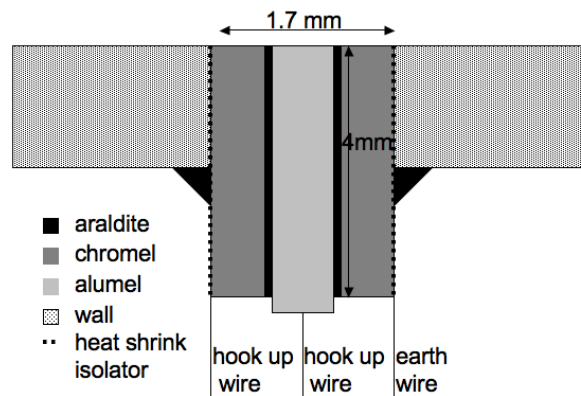


Figure 7.6. Section of a cylindrical thermocouple mounted inside the model wall.

For the manufacturing of the thermocouples, 4 mm long and 1.7 mm wide diameter chromel annulus have been used as external material and alumel wires as internal material. A section of a thermocouple is shown in Figure 7.6. A hook up wire was soldered to each of the two components and connected to a multimeter. An earth wire was soldered on the chromel cylinder opposite the hook up wire. Five minute araldite was used to electrically isolate the two materials. The alumel wire covered in araldite was inserted into the chromel annulus

and rotated until the glue covered both metals inhibiting any contact and an open circuit was reached. At this point, the TC was covered using a heat shrink tube to electrically isolate the TC from the model body. In order to get a fast response gauge, a low mass junction was formed at the exposed surface by scratching the top of the TC with rough sandpaper in order to transport chromel particles in contact with alumel particles, or vice versa. The process was continued until the multimeter, set to 200 Ohm read a value below 1 Ohm. The thermocouples have been mounted into the model using the same technique described for the TFG. For the error estimation the same value used for the TFG has been used knowing that due to the manufacturing this is a conservative value.

Sets of ten TC have been grouped using 12-pins D-connectors and their signal amplified using an appropriate amplifier.

In order to relate the temperature change registered by one TC to the heat flux at that location along the wall, the value of the thermal product is needed to be used in the procedure explained in Section 7.1.5. The thermal product is a characteristic of the materials used for manufacturing the TC, in this case alumel, chromel and araldite, and of the surface junction generated at its top. It is defined as $\sqrt{\rho c_p k}$ ($J/m^2 K s^{1/2}$) where ρ is the density, c_p is the specific heat at constant pressure and k is the heat conductivity. The water droplet technique has been employed for the calibration. The instrumented plate containing the TC has been put inside an oven and heated up to a temperature of approximately 50° C. One TC has been connected to an amplifier and the amplifier to an oscilloscope. A droplet of water from a melted ice-cube at 5° C has been made impact on the TC. It is assumed that no temperature changes occur while the droplet moves toward the gauge. The impact with the droplet causes an abrupt change in the TC surface temperature and consequently a jump function is registered by the oscilloscope. Considering that K-type thermocouples have a sensitivity of 40 $\mu V/K$ [85], the temperature change experienced by the TC can be measured. This value is then used to compute the thermal product (TP_s) of the TC using the properties of water at 5° C. The following formula is used for this purpose [61]:

$$\frac{T - T_s}{T_w - T_s} = \frac{TP_w}{TP_w + TP_s} , \quad (7.2)$$

where the subscript w stands for water, T_s is the temperature of the TC before the contact and T is the temperature of the TC after the contact. One should consider that this formula holds only in the hypothetical case of a one-dimensional droplet impact with no rebound and one-dimensional heat contact. The procedure has been repeated for five TC four times getting consistent values and an averaged thermal product of 9500 has been used for all TC. The results of the calibration are reported in Appendix B.

Kulites

Kulite piezoresistive transducers are devices that correlate changes in the voltages registered at their surface with changes in the surrounding pressure. For a wide range of pressure,

including those of interest here (5-500 kPa), the changes in voltages are linearly proportional to changes in the surface pressure.

Consequently, for the calibration of the pressure gauges a two points calibration has been performed. The Kulites are mounted in the model, located inside the test section, and connected to the amplifiers and the data acquisition system. The test section is closed and evacuated. At this point signals from the Kulites start to be recorded at low frequency for 20-30 seconds. The averaged value over this time is used as first calibration point considering the level measured as zero pressure. Then the valve is opened and air is allowed to enter in the test section. After a couple of minutes the test section reaches the atmospheric pressure. The signal is then recorded for 30 seconds and averaged. The correct atmospheric pressure of the day has been taken from the meteorological station at the UQ which provides highly accurate atmospheric pressure values each 10 minutes. For each Kulite an offset value and a calibration coefficient are extracted. The offset are the voltages recorded at zero pressure. The coefficient is the slope of the line passing between the two points of calibration. The measurement error for these gauges is set to 5%.

PCBs

For the calibration of the PCB transducers a procedure different than the one employed for the Kulites is needed since the nature of the PCB transducer inhibits the measurement of absolute pressure. The technique described in [62], [109] has been used. The calibration is performed by rapidly applying a pressure to the front of each Pitot probe. A conical fitting, connected to a pressure reservoir, was placed on top of the probe and sealed. Inside this device a calibrated Kulite was inserted and experienced the same pressure as the Pitot probe. Opening a fast acting valve a high pressure of about 200 kPa was applied to the gauges for a short time and the peak pressure measured by the Kulite was related to the value measured by the PCB.

7.1.5. Analysis and Postprocessing Tools

Previous to the postprocessing of the collected data, the definition of the steady test time for each run is necessary. This is done using the trace of two stagnation probes that measure the variation of the stagnation pressure at the end of the shock tube during each run. Figure 7.7 shows a typical trace collected by the stagnation probes. The two probes show a good agreement which is the sign that they are correctly calibrated and can therefore be used for the determination of the flow characteristics. Under the chosen condition 2 ms of usable test time followed the unsteady start process of the nozzle and the flow establishment time.

The onset of flow in the test section is indicated by the sharp pressure rise. After the nozzle starting and the flow establishment, the steady test time begins. The end of the test time is characterized by a reduction in the mass flow rate and a consequent decrease in the pressure (by more than 10%) and by a contamination due to the driver gas reaching the test section.

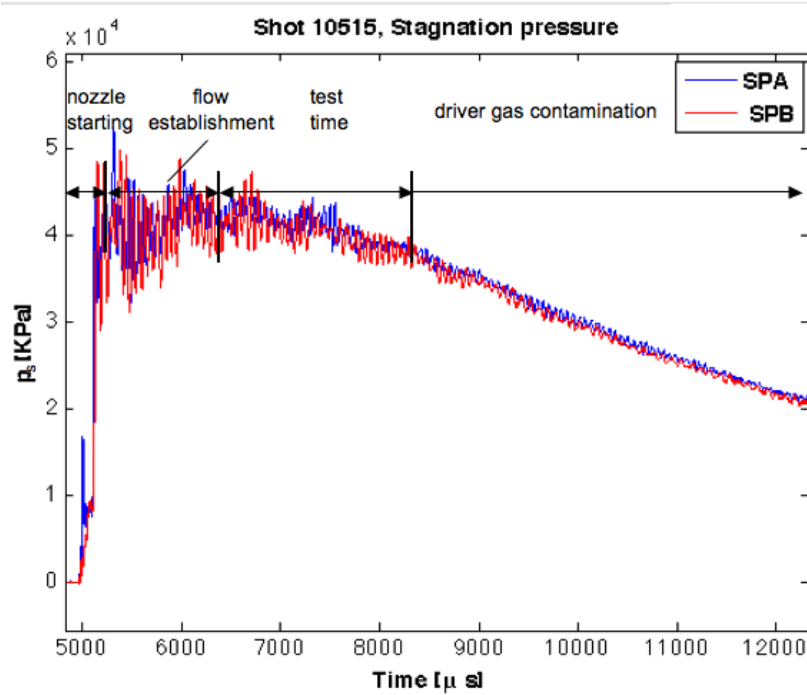


Figure 7.7. Trace of the stagnation pressure probes during a shot at the high Reynolds condition. The name SPA and SPB identify the two stagnation probes used at the end of the shock tube.

The nozzle exit conditions, which are the inflow conditions for the test section, are estimated using a software called STN (Shock Tube and Nozzle Calculations for Equilibrium Air) [67], which calculates the flow properties in a reflected shock tunnel. The input data required by the program are: (1) the initial shock tube fill pressure, (2) the initial temperature of the test gas in the shock tube, (3) the incident shock speed, (4) the measured nozzle supply stagnation pressure (over the steady test time) and (5) the Pitot-to-stagnation pressure ratio. The program then computes the properties of the flow in different locations: (1) the conditions following the incident shock, (2) the conditions just after the shock reflection, (3) the stagnation conditions after relaxation to the measured nozzle supply pressure, (4) the conditions at the nozzle throat and (5) the conditions at the nozzle exit.

For the calculation of the heat flux (Q), using the data collected by the TFG and the TC, the time history of the measured surface temperature variation is used in the formula:

$$Q = \frac{\sqrt{\rho c_p k}}{\sqrt{\pi}} \int_0^t \frac{dT/d\tau}{(t - \tau)^{1/2}} d\tau , \quad (7.3)$$

where $\sqrt{\rho c_p k}$ is the thermal product of the gauge. For the numerical integration the discrete form of equation (7.3) obtained by Schultz and Jones [99] has been implemented in a Matlab routine and it reads as follows:

$$Q_s(t_n) = \frac{\sqrt{\rho c_p k}}{\sqrt{\pi}} \sum_{i=1}^n \frac{T(t_i) - T(t_{i-1})}{(t_n - t_i)^{1/2} + (t_n - t_{i-1})^{1/2}} . \quad (7.4)$$

After the postprocessing the pressure and heat flux values obtained have been averaged over the test time and used for comparison with numerical simulations.

7.2. Numerical Approach

In order to reproduce the experimental findings, the inflow conditions computed by the experimental data, listed in Table 7.2, have been prescribed as numerical inflow for the simulations. At the numerical inflow and outflow boundaries, supersonic inflow and outflow conditions have been prescribed. At the solid wall, the no-slip condition is enforced using the strong boundary condition. Due to the short test time the model surfaces is treated as an isothermal wall and the temperature is set to 300 K corresponding to room temperature. A turbulence intensity of 0.5% and a viscosity ratio of 0.001 has been chosen. The AUSMDV Riemann solver is used for the treatment of the convective fluxes together with the Venkatakrishnan limiter. Both explicit and implicit time integrations have been used. For the simulation of the flow conditions characterized by a clear laminar to turbulent transition in the interaction region, a transition point has been defined corresponding to the location of the model kink.

The experimental runs differ with respect to the diaphragm thickness and consequently the Reynolds number, use of the boundary layer trip or not and the compression ramp angle. A list of the runs performed and of the characteristics is given in Table 7.3. As it can be seen from the table some run numbers are missing in the upper part of the table. This is due to the fact that the campaign was started using a new piston that weighted 4 kg more than the old one and produced different flow conditions so that the pressure in the different tunnel sections had to be tuned again. The missing runs correspond to flow conditions where no steady flow was visible. From now on, the results from the experimental runs, used for comparison with the numerical simulations, are referenced by their specific run number.

7.3. 40 degrees Compression Corner Results

For the simulation of the 40 degrees compression corner, a two-dimensional structured grid was created to simulate the flow along the center line of the model. The grid has been generated trying to keep the grid resolution as smooth as possible in order not to trigger unphysical phenomena. The only regions where the grid lines are clustered are the leading edge, in order to capture the boundary layer growth, and at the wall. The grid has a reduced ramp length of 150 mm with respect to the 250 mm of the experimental model. This has been done since no data were collected on the back of the model or they were affected by the reflection of the expansion waves occurring at the nozzle exit, on the test section walls. In

run	40 degrees	15 degrees	6 mm cond	3 mm cond	with trip	without trip
10512	X			X	X	
10515	X		X		X	
10516	X		X			X
10517	X		X			X
10518	X		X			X
10519	X		X			X
10520	X		X			X
10521	X		X		X	
10522	X		X		X	
10523	X			X		X
10524		X		X		X
10525		X	X			X
10526		X	X		X	
10527		X	X		X	
10528		X	X		X	
10529		X	X			X
10530		X	X			X
10531		X		X		X
10532		X		X	X	
10533		X		X	X	

Table 7.3. List of experimental runs and their characteristics.

addition this region is of no interest for the study of the SWBLI which occurs close to the kink.

The characteristics of the numerical grid are given in Table 7.4.

points x-dir	points y-dir	Δx_{\max} [m]	Δx_{\min} [m]	Δy_{\max} [m]	Δy_{\min} [m]
450	230	10^{-3}	10^{-6}	10^{-3}	1.25×10^{-7}

Table 7.4. Grid resolution for the simulation of a two-dimensional 40 degrees compression corner.

The grid study has been based on the results of the grid study conducted for the compression corner at 15 degrees in Section 5.2.2. Since the two test cases involve similar physical features (SWBLI), it is assumed that the same grid refinement is sufficient to ensure grid-independent results. The grid is depicted in Figure 7.8 where each fourth grid line is shown. The grid contains 112,500 cells.

For the three-dimensional simulation, performed at the higher Reynolds number the grid presented above (named 2D RSM 1.25×10^{-7}) was used as a base, to be extruded in the third

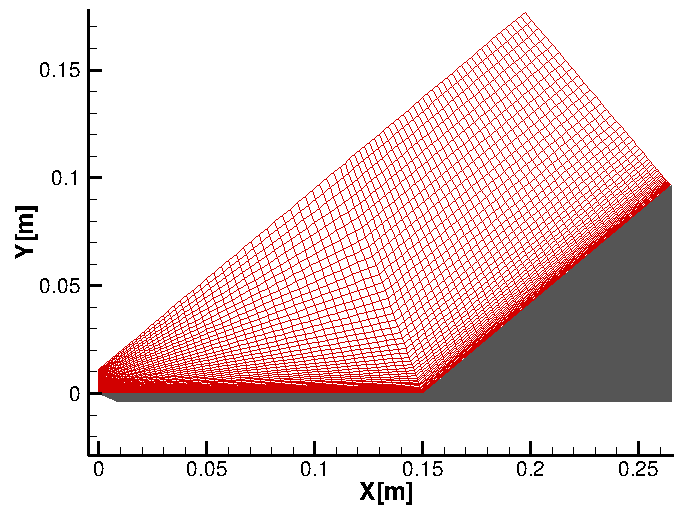


Figure 7.8. Computational domain for a 40 degrees compression corner at $M=6.35$ and $Re=9.65 \times 10^6$ 1/m and at $M=6.38$ and $Re=5.51 \times 10^6$ 1/m. Every fourth grid line displayed.

direction, but the first grid spacing at the wall was increased for accelerating the convergence. The effect of this change on the y^+ at the wall is presented in Figure 7.9 together with the Stanton number distribution. The two-dimensional grid with increased resolution is called 2D RSM 10^{-6} . The result of the three-dimensional grid is shown along the center line, using the name 3D RSM center line. The results show that, as expected, the y^+ has a huge increase when changing the grid resolution and the condition $y^+ < 1$ is not satisfied. The heat flux shows that the main difference between the 2D simulations on the 2D RSM 10^{-6} grid and the 2D RSM 1.25×10^{-7} grid is on the heat flux value on the ramp, as seen in Section 5.2.2 while no appreciable differences in the separation size can be seen.

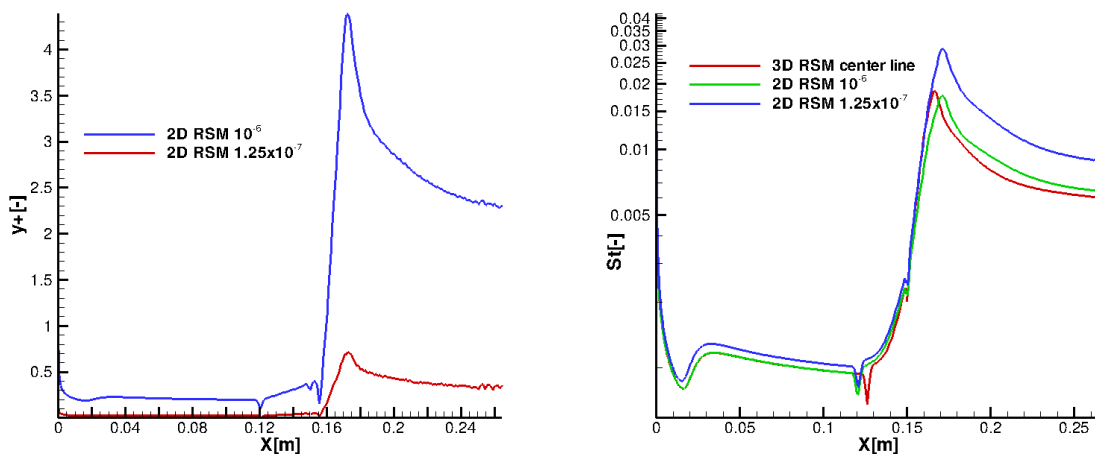


Figure 7.9. y^+ (left) and heat flux (right) distribution along a 40 degrees compression corner for different grids at $M=6.35$ and $Re=9.65 \times 10^6$ 1/m .

In order to simulate the flow spillage at the model sides, two freestream blocks were added. Only half of the plate is simulated and a symmetry condition is used along the symmetry plane. A front view of the three-dimensional domain, in a streamwise location near the leading edge, is given in Figure 7.10. The grid is divided into three blocks as shown by the numbers in the picture.

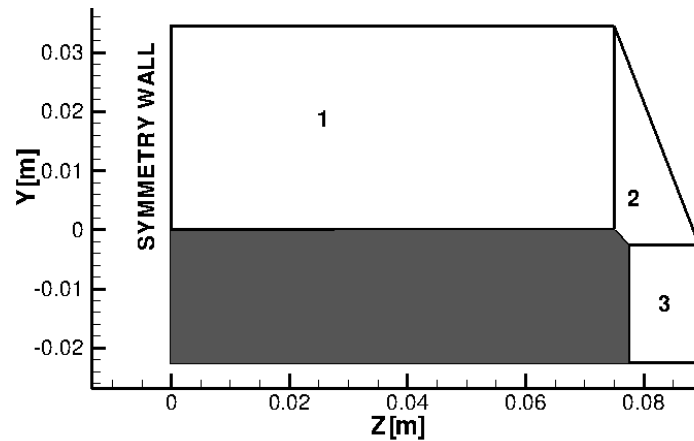


Figure 7.10. Computational domain for a three-dimensional 40 degrees compression corner on a plane orthogonal to the incoming flow at $M=6.35$ and $Re=9.65 \times 10^6$ 1/m and at $M=6.38$ and $Re=5.51 \times 10^6$ 1/m. The number refers to the different grid blocks.

For each block the grid characteristics are listed in Table 7.5. For block 2 the inclined lines are considered as z-direction while the other 2 walls are listed as y-direction. The grid contains approx. 11 million points.

	block 1	block 2	block 3
points x-dir	450	450	450
points y-dir	230	230	20
points z-dir	75	20	230
Δx_{\max} [m]	10^{-3}	10^{-3}	10^{-3}
Δx_{\min} [m]	10^{-5}	10^{-5}	10^{-5}
Δy_{\max} [m]	10^{-3}	10^{-3}	10^{-3}
Δy_{\min} [m]	10^{-6}	10^{-6}	10^{-3}
Δz_{\max} [m]	10^{-3}	uniform	10^{-6}
Δz_{\min} [m]	10^{-3}	uniform	10^{-4}

Table 7.5. Grid resolution for the three-dimensional simulation of the 40 degrees compression corner.

The use of block 2 instead of a sharp edge was necessary due to a problem occurring on a grid with a sharp edge deriving from the formulation of the boundary conditions. The inclined edge is 3.54 mm long and is rotated by -45 degrees with respect to the plate line.

7.3.1. 40 degrees 6 mm Condition with Boundary Layer Trip

The first configuration to be analyzed is the compression corner at 40 degrees for the higher Reynolds number inflow condition which is considered as representative and of main interest since it is characterized by a turbulent separation [19], [16]. This test case has been extensively investigated. From the numerical point of view, the two-dimensional case has been analyzed using the $k - \omega$ SST model of Menter, the $k - \omega$ model of Wilcox in its latest version of 2008, the EARSM of Hellsten and the RSM. In addition, a three-dimensional simulation using the RSM has been performed. The three-dimensional simulation has been run on the supercomputer JUROPA at the Forschungszentrum Jülich [15].

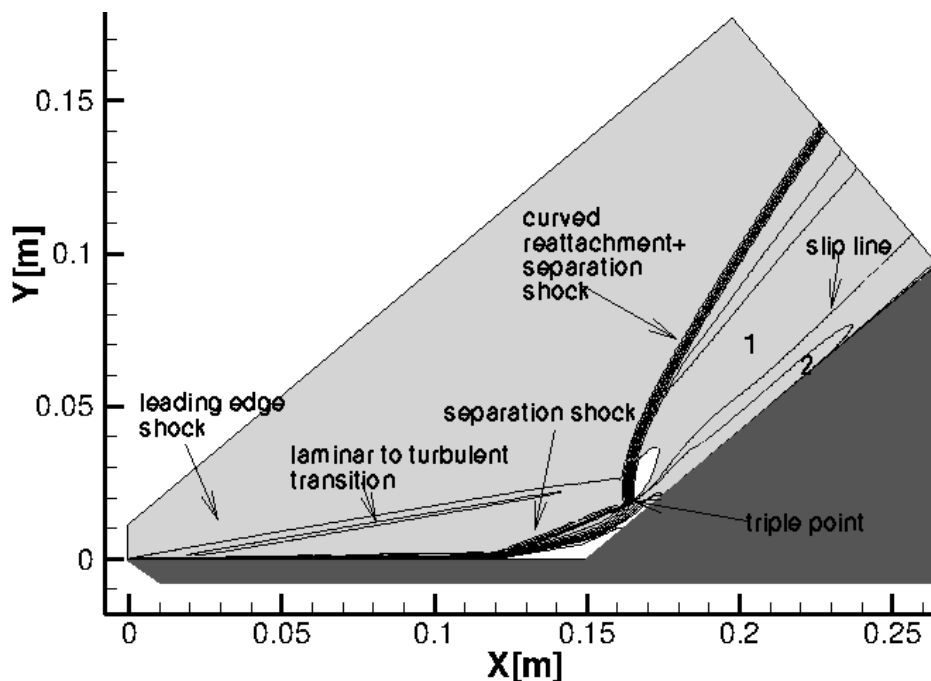


Figure 7.11. Main flow features of a 40 degrees compression corner investigated numerically using fully turbulent conditions at $M=6.35$ and $Re=9.65 \times 10^6$ 1/m. The Mach contours are shown and the subsonic regions are highlighted in white color. The number 1 identifies the flow that passed through the shock wave originated at the triple point by the merging of the separation and the reattachment shock waves. The number 2 identifies the flow that passed first through the separation shock wave and then through the reattachment shock wave separately.

Figure 7.11 shows the main features detected numerically for a two-dimensional fully turbulent simulation using the RSM. At the leading edge, a weak shock wave forms due to the boundary layer thickness. Moving downstream, a second weak shock wave is generated where the numerical laminar to turbulent transition occurs due to the sudden change in boundary layer thickness. The boundary layer is visible along the flat plate and its thickness increases quickly along the plate. Moving toward the kink, the boundary layer feels the adverse pressure gradient, produced by the compression ramp, and separates. A separation

shock wave is generated at the separation onset. The boundary layer reattaches along the second ramp and a strong curved reattachment shock wave is generated. The separation shock and the reattachment shock waves meet in a location close to the wall due to the high deflection angle. At the triple point a slip line emanates. The flow in region 1 has crossed only the curved shock wave generated from the merging of the separation and reattachment shock waves, while the flow in region 2 has passed through the separation shock wave first and then through the reattachment shock wave. For such a large ramp angle (under the given inflow conditions) it is impossible for the flow in region 1 to be generated by a single shock wave and be compatible with the conditions in region 2. For this reason the shock is curved and its strength is such that a small subsonic region is generated behind it and is visible in the picture in light-grey color. The shock wave resulting from the interaction between the separation and the reattachment shock waves interacts with the leading edge shock, but this interaction does not visibly affect the flow field.

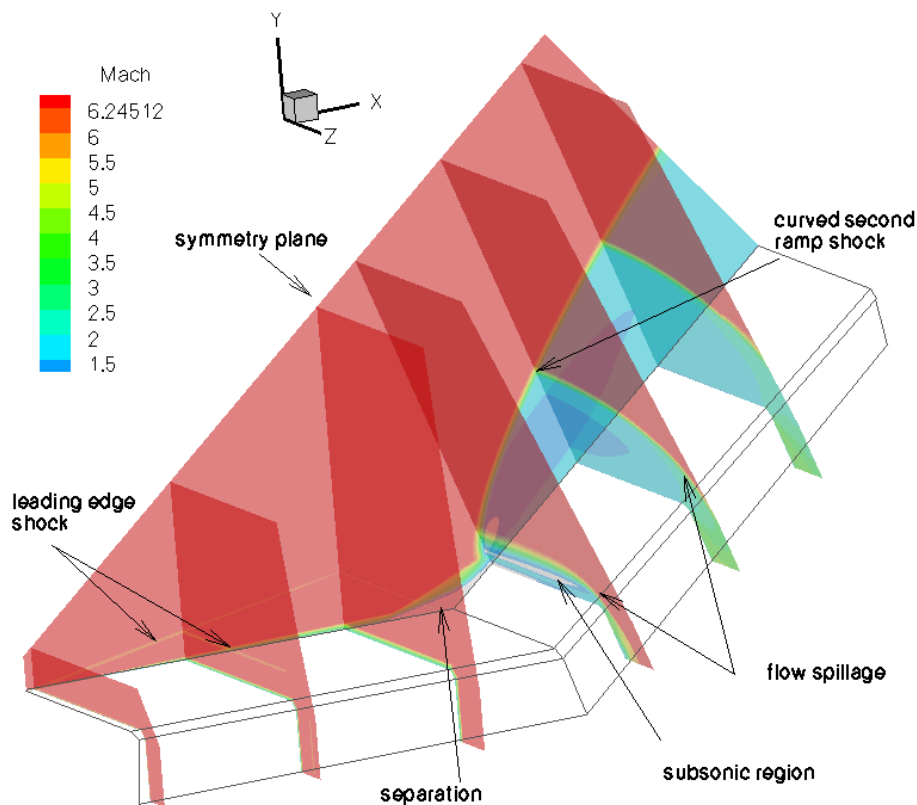


Figure 7.12. Main flow features of a three-dimensional 40 degrees compression corner investigated numerically using fully turbulent conditions at $M=6.35$ and $Re=9.65 \times 10^6$ 1/m.

The same features observed in the two-dimensional simulation are also detected by the three-dimensional one. In Figure 7.12, the Mach distribution along different planes is shown and the main flow features are highlighted. The plane at constant z corresponds to the

symmetry plane of the grid (and to the center line of the model). The weak shock that originates at the leading edge due to the thick boundary layer is visible along the symmetry plane. Moving downstream, the flow undergoes a separation whose size reduces moving toward the plate side. The strong shock that is visible along the ramp decelerates the flow behind it to subsonic speed in a small region. The areas of subsonic flow are visible in the figure in grey color. The subsonic region extends for the whole crossflow direction but it shrink moving toward the side. The flow spillage at the plate side is visible in the decrease of the Mach number in the crossflow direction.

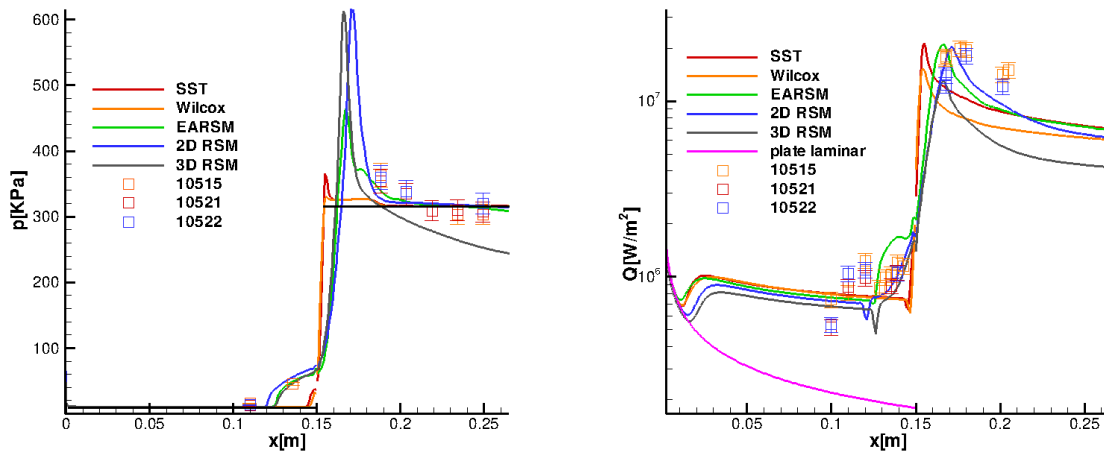


Figure 7.13. Pressure (left) and skin friction coefficient (right) distribution for a 40 degrees compression corner at $M=6.35$ and $Re=9.65 \times 10^6$ 1/m. Comparison between experiments and simulations. Runs with boundary layer trip.

Figure 7.13 (left) shows the experimental pressure distribution along the pressure measurement line (0.023 m away from the center line). The experimental data along the flat plate show that the boundary layer is attached at the first measurement location. The measured pressure value matches the inflow value computed from the experimental data and used for the numerical simulation. Moving forward along the plate, the boundary layer undergoes a separation as shown by the pressure increase at the second measurement point. The pressure rise along the compression ramp and the peak at the reattachment are not visible in the measurements since it was not possible to mount pressure sensors close enough to the kink, as explained in Section 7.1.4. Along the compression ramp the last part of the pressure decrease is captured in the measurements. Further downstream, the pressure reaches the value from the inviscid shock theory shown by the black horizontal line.

The experimental results are compared with two-dimensional computations for all turbulence models listed above and a three-dimensional computation performed with the RSM. For this last simulation, the numerical pressure distribution shown in the picture correspond to the correct location with respect to the experimental model. From the numerical point of view, significant differences can be observed looking at the predicted pressure distribution. The

two-equation linear eddy-viscosity models do not predict a boundary layer separation and show the typical profile for an attached boundary layer along a compression corner. The RSM correctly predicts the boundary layer separation, and the agreement with the pressure level in the separated region is increased in the three-dimensional simulation due to the reduction of the separation size moving away from the center line. A large pressure increase is visible along the ramp followed by a steep decrease due to the expansion fan that emanates from the triple point which, as visible in Figure 7.11, lies very close to the surface. For the two-dimensional simulation, the pressure drops to the inviscid value and remains constant while in the three-dimensional simulation the pressure decreases steadily until the outflow boundary due to the flow spillage at the side and underestimates the pressure measurements. The solution obtained using an explicit algebraic Reynolds stress model (EARSM) also predicts a boundary layer separation of a slightly smaller size than the 2D RSM. Its pressure distribution has a peak along the ramp corresponding to the boundary layer reattachment, and this peak is visibly lower than the one predicted by the RSM. The pressure then decreases and reaches the inviscid solution for a 40 degrees ramp.

Since the numerical simulation shows different separation sizes and location of separation and reattachment points, these values are listed in Table 7.6 for clarity. For the three-dimensional simulation, the values reported correspond to the separation size along the center line.

	separation point [m]	reattachment point [m]	separation size [m]
2D RSM 1.25×10^{-7}	0.121	0.156	0.035
2D RSM 10^{-6}	0.121	0.156	0.035
RSM 3D center line	0.126	0.155	0.029
2D EARSM	0.126	0.158	0.032

Table 7.6. Comparison of separation size for different turbulence models and grids for a 40 degrees compression corner at $M=6.35$ and $Re=9.65 \times 10^6$ 1/m. For the three-dimensional grid the separation size along the center line is considered.

The maximum separation size is obtained using the 2D RSM and this value decreases by 13% when moving to the 3D simulation. The behavior of the separation size in the 3D simulation is presented in Figure 7.14. Starting from the leading edge, the location of the laminar to turbulent transition is visible in the increase of the skin friction coefficient. As expected, the flow spillage at the side has an influence on the separation size, visible in the picture in white color. Moving toward the outflow edge, the separation point moves downstream, the reattachment point moves upstream and the total separation size decreases.

In Figure 7.13 (right), the heat flux distribution along the center line is presented. The first measurement location shows variant states of turbulence. The second and third measurement locations consistently detect turbulent values. From the pressure measurements, it is known that the boundary layer undergoes a separation and the heat flux values measured in the kink region clarify that it is a turbulent separation because their values grow well above the

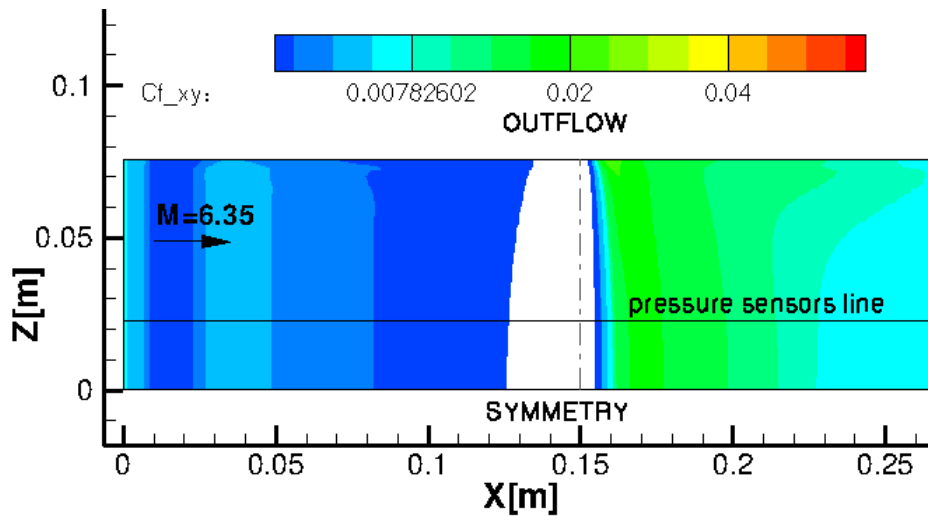


Figure 7.14. Skin friction coefficient at the wall for a 40 degrees 3D compression corner and fully turbulent conditions using a RSM at $M=6.35$ and $Re=9.65 \times 10^6$ 1/m. The dash dotted line corresponds to the location of the kink. The white area corresponds to the region where the boundary layer is separated.

turbulent level for a flat plate. From the data available, it is difficult to correctly identify the separation point that can either be located near the second TFG or near the fourth TFG. Along the ramp, the high heat flux level correspond to the values expected for a turbulent boundary layer.

For better analyzing the behavior of the heat flux inside the separation, a zoom of the heat flux along the instrumented plate is given in Figure 7.15. The measurement taken in the part of the flow where the simulations predict boundary layer separation, clearly shows an increasing behavior and values characteristic of a turbulent separation. The third measurement point shows heat fluxes corresponding to a local maximum for each experimental run. The fact that the heat flux along the first three TFG is increasing, in contrast to what is expected for a flat plate, suggests that the boundary layer is transitional in that region and that separation occurs between the third and the fourth TFG.

Considering the comparison between the numerical solutions, visible differences can be seen in the heat flux level along the flat plate. In Figure 7.16, the skin friction coefficient, which for a flat plate is proportional to the heat flux, is presented for the flat plate. The analytical solution of Meador-Smart [74] is shown for comparison, as well as the laminar solution. All turbulence models show a (numerical) laminar to turbulent transition displaying values above the theoretical turbulent solution. Moving forward, the skin friction decreases and approaches the level predicted by the analytical solution. As expected, the 3D simulation underpredicts the skin friction due to the larger grid spacing at the wall. Toward the end of the figure, the RSM shows the better agreement with the analytical solution.

As already discussed in the case of the pressure distribution, neither the SST nor the $k-\omega$ model of Wilcox are able to predict the boundary layer separation. The RSM shows

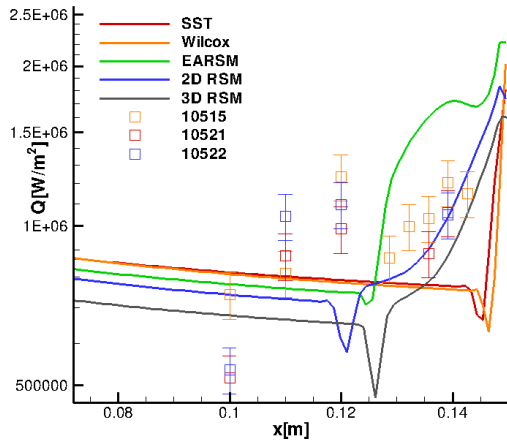


Figure 7.15. Heat flux distribution along the flat plate for a 40 degrees compression ramp at $M=6.35$ and $Re=9.65 \times 10^6$ 1/m. Runs with boundary layer trip.

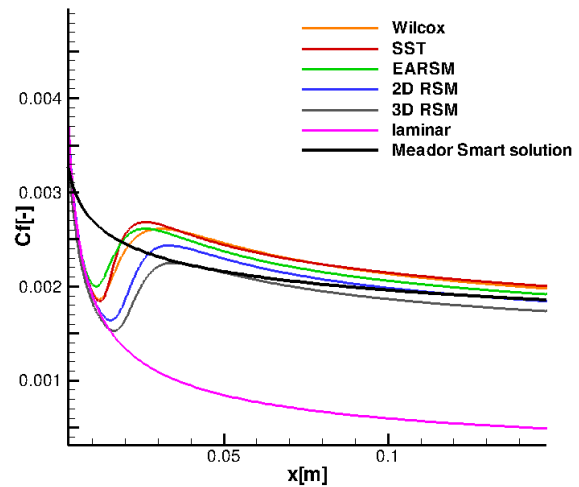


Figure 7.16. Skin friction coefficient distribution along a flat plate at $M=6.35$ and $Re=9.65 \times 10^6$ 1/m.

a boundary layer separation that occurs just upstream of the fourth TFG. The heat flux decreases in a small region and then increases sharply above the separation region in excellent agreement with the experimental results in that area even though the experimental results suggest a slightly larger separation size. The decrease in the heat fluxes corresponds to the region where the skin friction coefficient decreases from the flat plate solution to the zero value. The minimum in the heat flux corresponds to a value of $C_f=0$. Once the boundary layer separates the heat flux increases monotonically over the plate. Along the ramp, the agreement with the measurement point is also good but the RSM predicts a faster decrease in the heat flux than the experiment captured. The three-dimensional simulation predicts lower heat fluxes, as expected due to the lower grid resolution at the wall, and a slightly reduced separation size as already observed in the pressure distribution and in Table 7.6.

The EARSM also predicts the boundary layer separation in proximity of the fourth TFG but predicts a different increase in the heat flux with respect to the RSM. Along the compression ramp a sharp increase in the heat flux occurs, corresponding to the peak heating at the reattachment point and then a fast decrease is shown. The agreement with the experimental results along the compression ramp is not as good as for the RSM. From the pressure and heat flux profile, it can be seen that even though the RSM and the EARSM predict a similar separation size visible differences are displayed. The cause for this is to be found in the different shock interaction predicted by the two models. The Mach contours for the RSM and the EARSM in the kink region are shown in Figure 7.17. As observed above, the RSM predicts a strong curved shock wave at reattachment which generates a region of subsonic flow behind it. This shock wave is the cause of the high pressure peak detected at the wall by this model. The EARSM, on the contrary, does not predict a strong shock at the reattachment

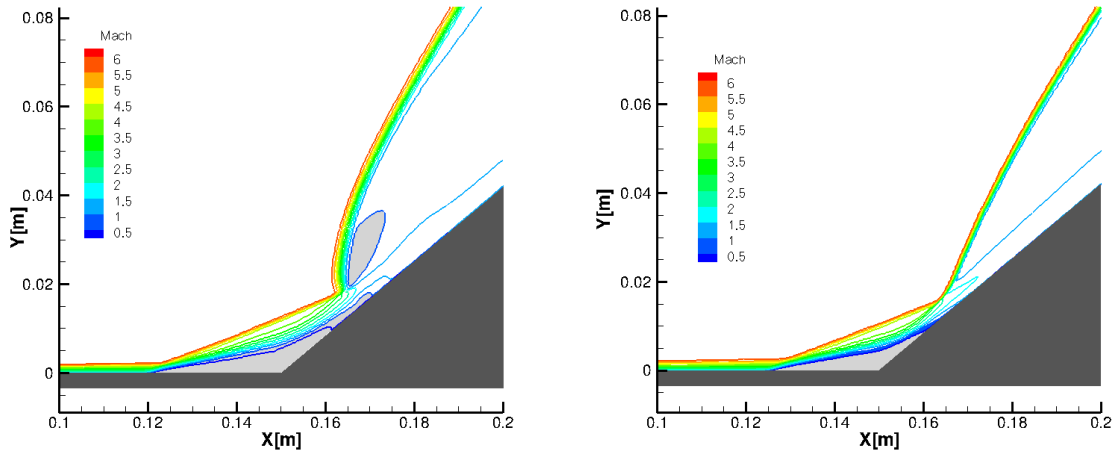


Figure 7.17. Mach number distribution in the kink region for a fully turbulent simulation using a RSM (left) and an EARSM (right) at $M=6.35$ and $Re=9.65 \times 10^6$ 1/m. The grey regions correspond to areas of subsonic flow.

and the pressure rise is, consequently, less pronounced.

In order to better identify the correct separation point and to gain some insight into the problem, the measurements taken away from the center line are analyzed.

Figure 7.18 (left) shows the heat flux distribution along a line parallel to the center line displaced by 46.85 mm toward the side. The right picture shows an enlargement of the heat flux along the instrumented plate. The measurements corresponding to the first three TFG correspond to a turbulent attached boundary layer. Also in this case, as for the center line, the heat flux values displayed by the first three gauges increase moving downstream in contrast to what is expected for a flat plate, indicating a transitional behavior. Moving downstream, the results clearly show that the boundary layer separation does occur between the third and the fourth TFG leading to the assumption that this is the case also for the heat flux along the center line. The gauges downstream of the third TFG clearly measure a turbulent boundary layer separation. While the first value is in excellent agreement with the EARSM profile, the last two measurements are in much better agreement with the RSM.

Figure 7.19 displays the heat flux distribution along a line in the crossflow located 0.1357 m downstream of the leading edge. On the left side, the line under consideration is highlighted on the model assembly. The third measurement from the right corresponds to the sixth TFG in Figure 7.18 (which is the center sensor in the cross of TFG) . The point $z=0$ corresponds to the symmetry wall. The experimental results show a high repeatability. The heat flux measured away from the center line are higher than the one displayed near $z=0$. The result from the shot 10515 at $z=0$ is in good agreement with the measurement on the left side of the picture. The reason why the runs 10521 and 10522 show a lower value can lie in the mounting of the gauges. These gauges had to be replaced due to a damage. The new gauges have a smaller diameter than the original one and slightly sunk into the model during the mounting.

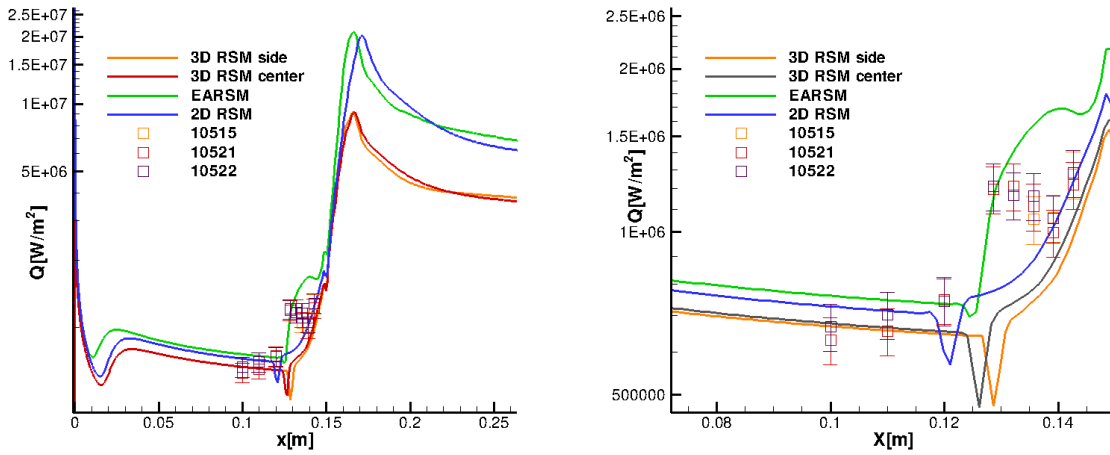


Figure 7.18. Heat flux distribution for a 40 degrees compression corner at $M=6.35$ and $Re=9.65 \times 10^6$ 1/m along a line parallel to the center line. Whole model (left) and flat plate (right). Runs with boundary layer trip.

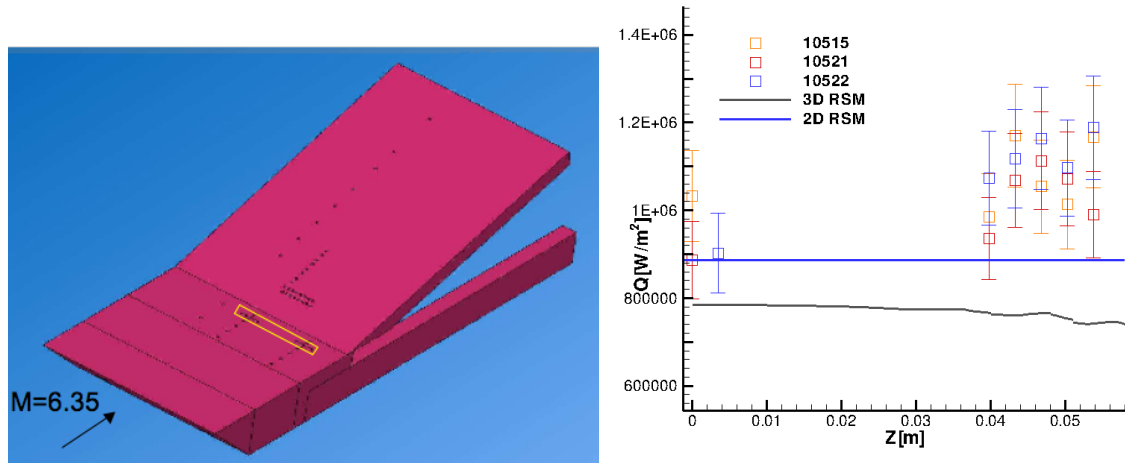


Figure 7.19. Heat flux distribution for a 40 degrees compression corner at $M=6.35$ and $Re=9.65 \times 10^6$ 1/m along a line orthogonal to the flow (right). The exact location of the line is highlighted in the model picture (left). Runs with boundary layer trip.

They collect good quality results in term of noise and steadiness of the measurement but, as a trend, register lower heat fluxes than the gauges that have not been changed. The 3D simulations predict at each location a lower heat flux value. One reason for the discrepancy is that the 3D grid has a lower resolution at the wall.

Finally the heat flux collected by the TC along the compression ramp are shown along four lines orthogonal to the flow in Figure 7.20. The blue horizontal lines represent the heat flux value measured at the same streamwise location in the 2D simulation. The 3D data are not

7. Three-dimensional hypersonic SWBLI

used since, due to the higher grid size at the wall, they systematically underestimate the heat flux level. The TC are located at the furthest 0.025 m away from the symmetry line.

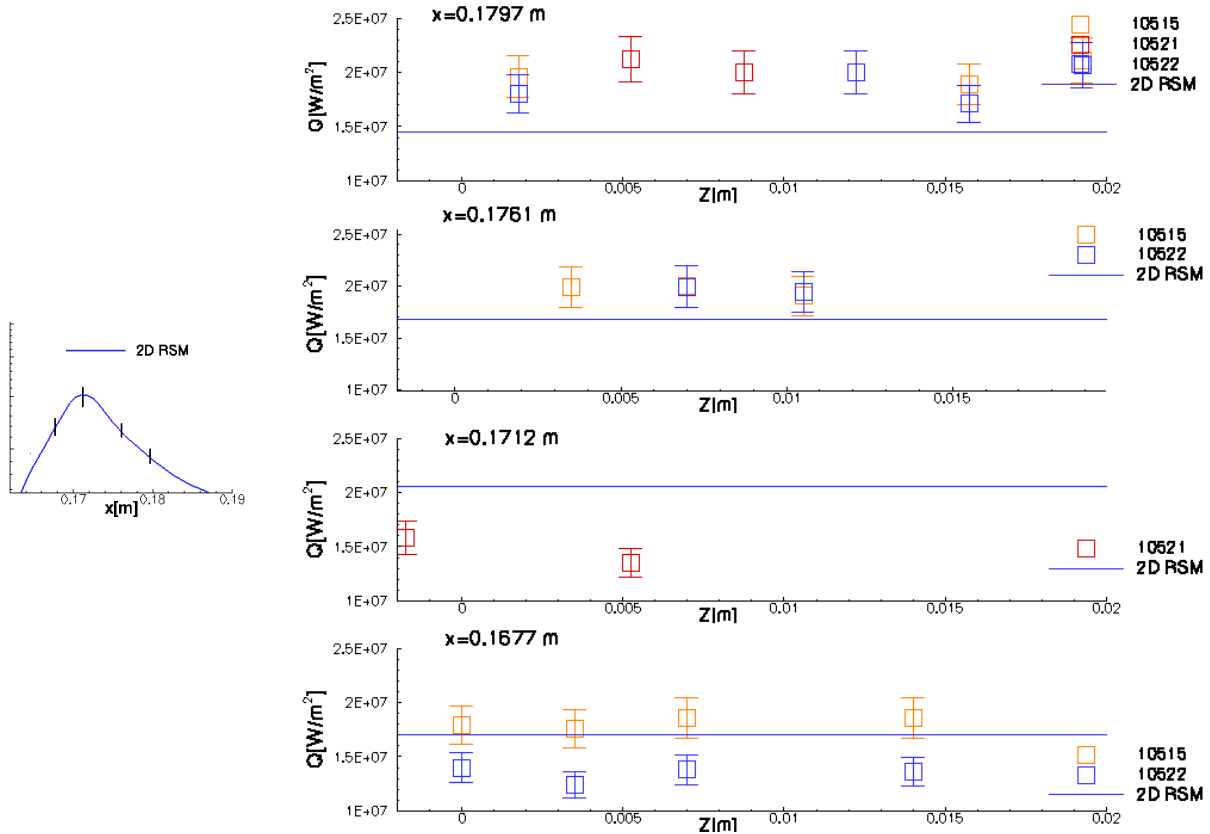


Figure 7.20. Heat flux distribution for a 40 degrees compression corner at $M=6.35$ and $Re=9.65 \times 10^6$ 1/m. On the left a zoom of the numerical peak heating region is given and the locations of the four lines shown on the right figure are highlighted. On the right the heat flux distribution along these four crossflow lines is presented. Runs with boundary layer trip.

Furthermore, the measurements show a spanwise consistency, indicating no 3D structures in this flow region. Visible differences are displayed between the measurements and the numerical results. The numerical solution is higher at the peak heating (second line) than the measurements and the trend is inverted for the third and fourth line confirming what was observed before. These differences are related to the fact that the numerical solution predicts a smaller separation size than the experiment. For a larger separation, the reattachment point and the peak heating at the wall would move downstream and the numerical result would get closer to the measurements.

The numerical results obtained from this configuration show that two-equation eddy-viscosity models, that are known to perform well at subsonic and transonic speed, fail to reproduce a key feature as the turbulent boundary layer separation. On the other hand, both the RSM and the EARSM predict the boundary layer separation, where the RSM shows a better agreement with the experimental results in the separated region and the heat flux in the

reattachment region.

7.3.2. 40 degrees 3 mm Condition with Boundary Layer Trip

The 40 degrees compression corner investigated with boundary layer trip at the lower Reynolds number is now considered. Due to technical problems no measurements from the TFG are available for the run conducted at this condition. The Mach distribution resulting from the 2D RSM computation is similar to the one in Figure 7.11 and, also in this case, a subsonic region appears behind the curved shock.

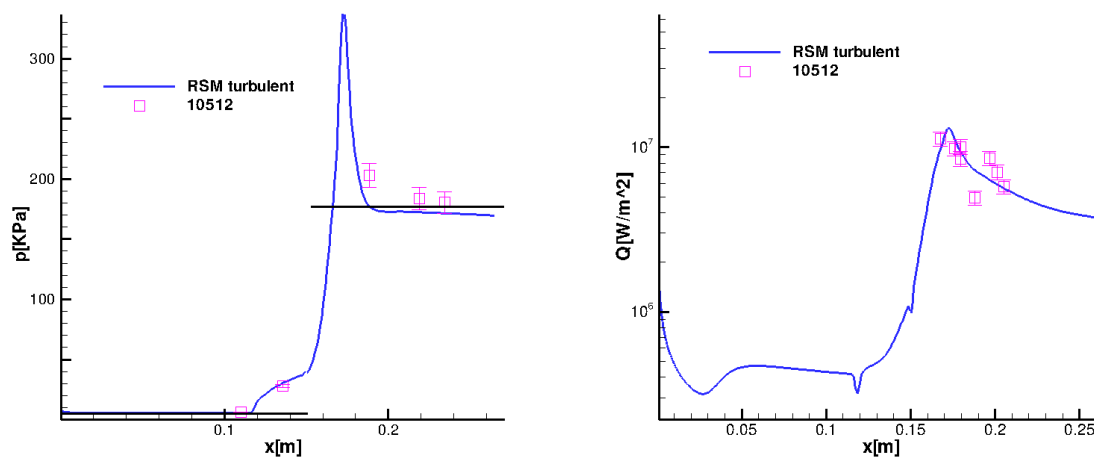


Figure 7.21. Heat flux distribution for a 40 degrees compression corner at $M=6.38$ and $Re=5.51 \times 10^6$ 1/m along a line parallel to the center line (left) and in the crossflow direction (right). Runs with boundary layer trip.

In Figure 7.21 (left), the pressure measurements are compared with the numerical result. The boundary layer, at the first measurement point, is attached both in the simulation and in the experiment and is separated at the second. The agreement at both location is excellent. The numerical solution shows that, going through the ramp shock, the pressure has a sudden increase followed by a decrease due to the flow passing through the expansion wave generated at the triple point. Finally, the pressure values reach the inviscid solution indicated by the black horizontal line. The first measurement value along the ramp indicates that the peak heating in the experiment is located a bit downstream of the numerical one.

In order to understand whether the pressure measurements predict a laminar or a turbulent separation, the theoretical pressure level of the plateau p_P is computed by the mean of the free interaction theory presented in Section 2.2.1. The theory is used for computing the value for both a laminar and a turbulent separation. In order to compute these values the skin friction coefficient obtained numerically from a laminar and a turbulent (RSM) flat plate simulation at $x=0.11$ m has been used. The obtained values are compared with the experimental data and the numerical solution. For what concerns the measurement, only one data is available

7. Three-dimensional hypersonic SWBLI

in the separated region (at $x=0.1357$ m). For the numerical solution, the value at the same location where the pressure is measured is considered, as well as the value at the end of the flat plate ($x=0.15$ m). It should be noted that, due to the small separation size, the pressure never reaches a constant plateau distribution. The pressures are listed in Table 7.7.

	p at $x=0.1357$ m [Pa]	p_P or $x=0.15$ m [Pa]
RSM 2D	29760	38670
Experiment	27910	-
Free-interaction laminar	-	10700
Free-interaction turbulent	-	43700

Table 7.7. Comparison of the pressure level between the experimental and numerical findings and the free interaction theory for the plateau.

The simulation and the experiment are in good agreement at the measurement locations and both show a value approximately double than the laminar value predicted by the free-interaction theory for the plateau. A much better agreement is shown with the turbulent theoretical value. However, since the pressure has not yet reached the plateau level, these values are smaller than the values predicted by the theory for a turbulent boundary layer. The pressure predicted by the RSM at the end of the plate gets close to the theoretical value. This means that the experimental results, in agreement with the simulation, predict a turbulent separation of the boundary layer. In Table 7.8, the characteristics of the separation are listed. In comparison to the higher Reynolds number test case, the separation size increases. This is to be expected from equation (2.5), because for this test case, with respect to the previous one, the Mach number is slightly higher, the skin friction coefficient is higher since it increases for decreasing Reynolds number, and the boundary layer thickness should be higher since it is directly proportional to the Mach number squared and inversely proportional to the square root of the Reynolds number.

	separation point [m]	reattachment point [m]	separation size [m]
RSM 2D	0.118	0.156	0.038

Table 7.8. Details of the numerical separation for a 40 degrees compression corner at $M=6.38$ and $Re=5.51 \times 10^6$ 1/m.

In Figure 7.21 (right), the heat flux along the separation ramp is shown; the three black vertical lines identify the streamwise locations used in Figure 7.22. The agreement between the numerical simulation and the measurement is good and confirms that the boundary layer is fully turbulent at reattachment. The presence of a measurement that lies visibly below the others, at $x=0.189$ m, is probably due to the manufacturing differences. As described in

Section 7.1.4 only one calibration value has been used for all the TC taken as an averaged value.

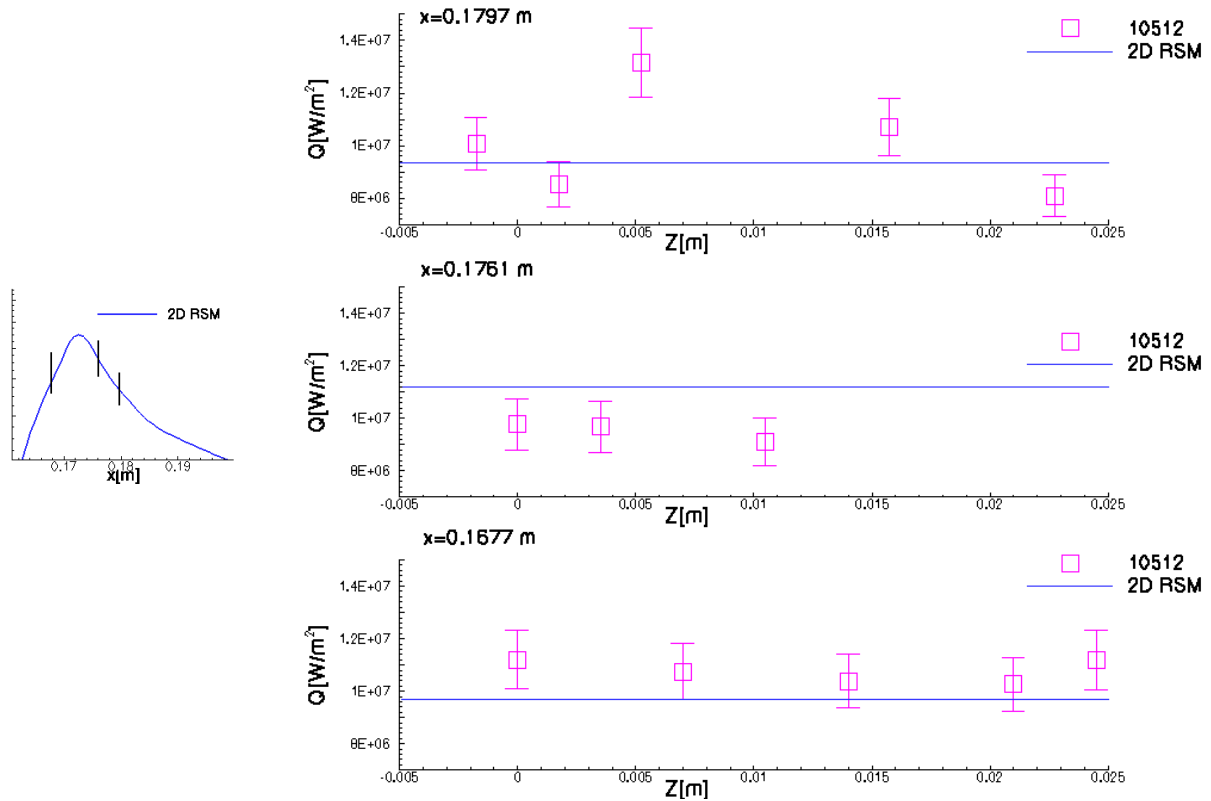


Figure 7.22. Heat flux distribution for a 40 degrees compression corner at $M=6.38$ and $Re=5.51 \times 10^6$ 1/m. On the left a zoom of the numerical peak heating region is given and the locations of the three lines shown on the right figure are highlighted. On the right the heat flux distribution along these three crossflow lines is presented. Runs with boundary layer trip.

Finally, the heat fluxes along the ramp for three different cross flow lines are presented in Figure 7.22. The value predicted by the 2D RSM is also reported as reference for each measurement line. The results at $x=0.1677$ show that the heat flux rise is well captured by the numerical simulation. At the second location, the numerical simulation overestimates the experimental findings and at the last location the values are in good agreement again. These results indicate that there are some small differences between the measurements and the numerical values and probably the reattachment point has not the same position in the experiment and the simulation. However, the results show a general good agreement for both pressure and heat flux and the model can correctly predict the peak heating measured in the shock tunnel.

7.3.3. 40 degrees 6 mm Condition without Boundary Layer Trip

The experimental pressure distribution for the compression corner at 40 degrees without boundary layer trip and at the higher Reynolds number is presented in Figure 7.23. The measurements along the plate show that the boundary layer has separated and the pressure levels are visibly higher than the inflow value. Along the ramp the first measurement point captures the pressure decrease after the pressure peak while the pressure at the other measurement locations follows the solution from the inviscid shock theory presented in the figure using a black horizontal line. In order to understand the state of the boundary layer during the separation, measured pressure values are compared with the theoretical values from the free interaction theory for both laminar and turbulent flows. The value of theoretical pressure plateau are computed using the skin friction coefficient obtained from a laminar and turbulent (RSM) flat plate at $x=0.1$ m and the results are shown in Table 7.9. Clearly this is an approximation since the data do not provide any information on where the separation occurs.

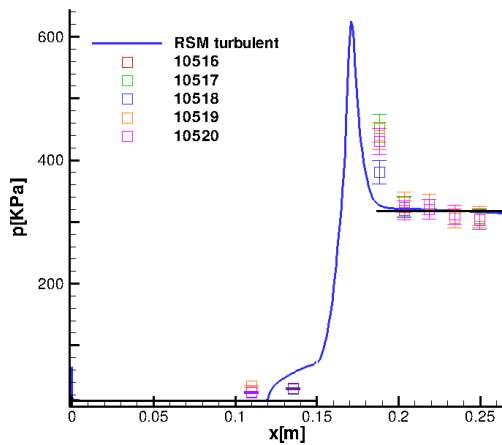


Figure 7.23. Pressure distribution along a 40 degrees compression corner at $M=6.35$ and $Re=9.65 \times 10^6$ 1/m. Runs without boundary layer trip.

	p[kPa]
Free-interaction laminar	18.8
Free-interaction turbulent	77.9
10516	n.a. - 30.6
10517	24.1 - 28.9
10518	23.5 - 29.5
10519	33.7 - n.a.
10520	24.3 - n.a.

Table 7.9. Pressure plateau estimation from the free interaction theory for a laminar and a turbulent flow and experimental values at the two locations along the flat plate for different runs.

The comparison shows that the values measured during the experiment exceed the laminar prediction by 25% and are less than half the turbulent one. Equation 2.5, for the computation of the theoretical pressure plateau level shows that the pressure plateau value increases with an increase of the skin friction coefficient at the separation onset. In this case, it means that the skin friction coefficient, that generates the pressure plateau measured in the experiment, has a value between the laminar and the turbulent one, i.e., at the separation onset the boundary layer is transitional. This conclusion is supported by the heat flux distribution measured along the instrumented plate.

In Figure 7.24, the heat flux distribution along the center line are displayed together with a zoom of the values along the instrumented plate. Along the plate the heat flux increases from

an almost constant value and near the kink it exceeds the level predicted for a fully turbulent flat plate showing the typical feature of a turbulent separation. At reattachment, the heat flux takes values characteristic of a turbulent boundary layer.

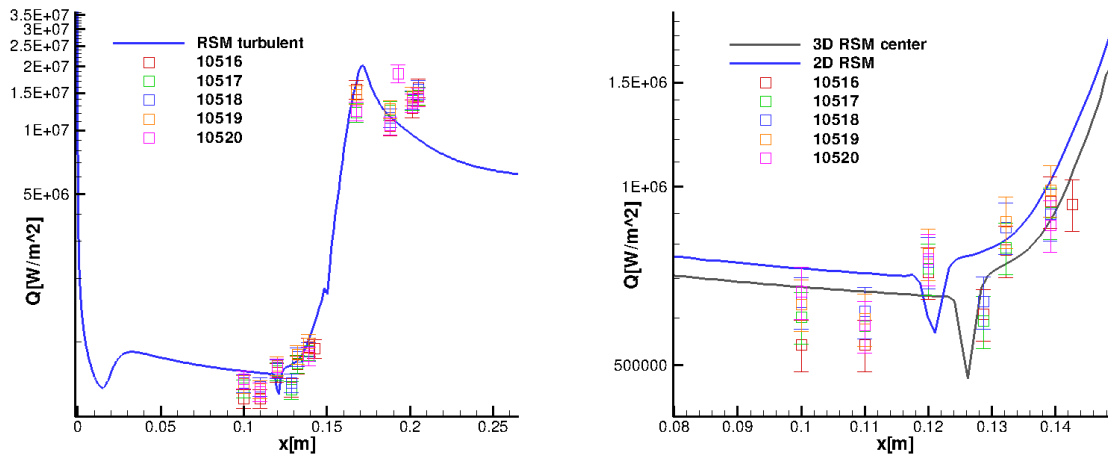


Figure 7.24. Heat flux distribution for a 40 degrees compression corner at $M=6.35$ and $Re=9.65 \times 10^6$ 1/m along the center line (left) with a zoom of the separation region (right). Runs without boundary layer trip.

On the right part of the picture the heat flux behavior in the separation region is visible. From the pressure measurement it is known that, the boundary layer is separated at least starting from the second TFG (which is aligned in the crossflow direction with the first Kulite).

The values displayed by the first and second TFG are below the turbulent value, but nevertheless, the boundary layer shows the characteristics of a turbulent separation, i.e. an increase of the heat flux above the turbulent flat plate level. The boundary layer at these two locations shows transitional values in agreement with the results obtained for the pressure. The comparison with the numerical results shows that the fully turbulent solution underpredicts the separation size but that the heat flux distribution in the separation region, where the flow has turned to turbulent, is in qualitatively good agreement with the RSM. The values collected from the TFG along the side line, presented in Figure 7.25, show a similar behavior. The heat flux shows a monotonic increase from a value lower than the turbulent one up to a level higher than that. This result is in agreement with the discussion above.

Finally, the measurements from the TC along four lines in the crossflow direction are shown in Figure 7.26. Despite the not so good agreement with the numerical levels presented in the picture, all the data show that the boundary layer at reattachment is turbulent. At the first measurement location, the numerical result overestimate the heat flux showing that in the experiment this quantity has a less steep increase. The same is seen for the second measurement point, which corresponds to the numerical peak heating. Along the third and fourth line, the trend is inverted and the numerical simulation predicts a much faster

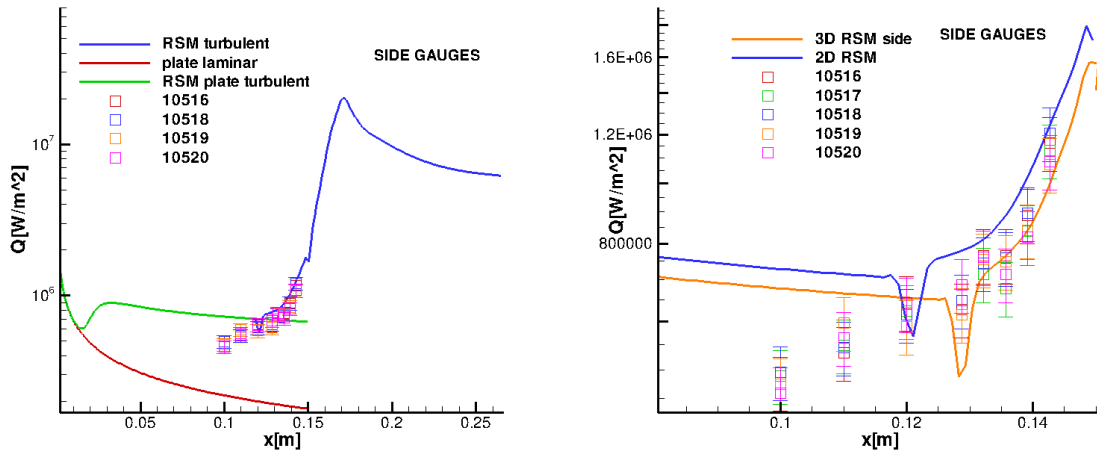


Figure 7.25. Heat flux distribution for a 40 degrees compression corner at $M=6.35$ and $Re=9.65 \times 10^6$ 1/m along a line parallel to the center line (left) with a zoom of the separation region (right). Runs without boundary layer trip.

decrease of the heat flux than seen in the measurement. This is due to the fact that the peak heating in the experiment is downstream of the numerical one so that before the peak heating the numerical solution overestimates the experimental data and after the peak heating the opposite is true. This happens only in the proximity of the peak heating.

The results discussed in this section show that a separation, characterized by a distribution of the heat flux typical of turbulent flow, can be achieved also without employing a boundary layer trip. However, the flow at the interaction region is affected by the laminar to turbulent transition which takes place in that area and the separation size is larger than in the case where a boundary layer trip is used. The fully turbulent solution is unable to predict the flow transition thus showing a different heat flux profile but is used to interpret the results and to determine the state of the boundary layer.

7.3.4. 40 degrees 3 mm Condition without Boundary Layer Trip

The 40 degrees compression corner at the lower Reynolds number condition without the use of a boundary layer trip is discussed here. The pressure and heat flux profile along the pressure line and the center line, respectively, are displayed in Figure 7.27. The pressure value measured along the plate shows that the boundary layer at that location has separated. The measurements along the ramp show the profile expected for a boundary layer that reattaches: a higher pressure is registered near the kink and then the value decreases toward the inviscid solution. The low value displayed by the last kulite probably shows a problem with the gauge during the run since, from the physical point of view, it is known that the pressure should remain constant and this has been seen in all the previous experimental test cases. The numerical solution for a fully turbulent flow underpredicts the separation size.

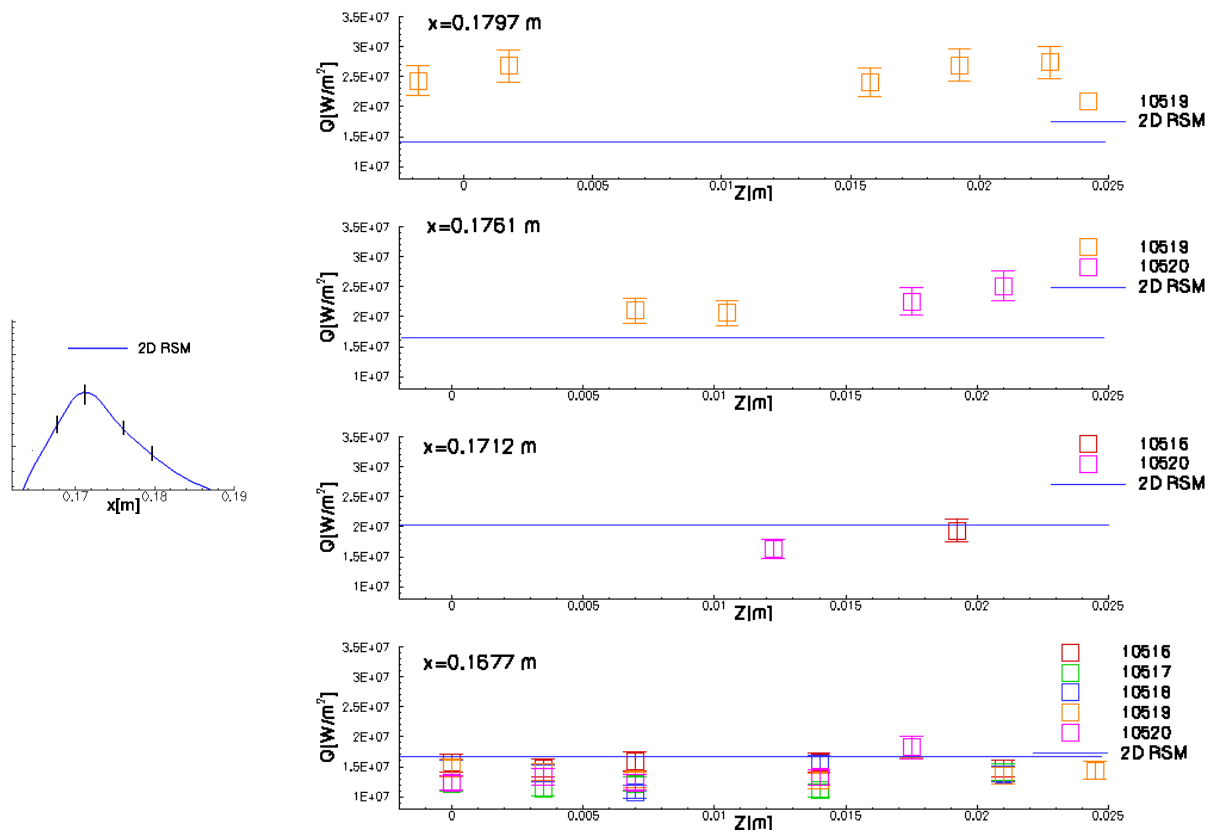


Figure 7.26. Heat flux distribution for a 40 degrees compression corner at $M=6.35$ and $Re=9.65 \times 10^6$ 1/m. On the left a zoom of the numerical peak heating region is given and the locations of the four lines shown on the right figure are highlighted. On the right the heat flux distribution along these four crossflow lines is presented. Runs without boundary layer trip.

The heat flux measurements shown on the right picture are difficult to interpret. The values along the plate are neither turbulent nor laminar. On the contrary, the heat flux on the ramp clearly show turbulent values. For getting a better insight into the problem, the heat flux values along a line parallel to the center one and 46.85 mm at its side are shown in Figure 7.28 (left). The flow shows a typical profile of a laminar to turbulent transition in correspondence of the first four gauges. At some point during the transition, the boundary layer separates and a turbulent separation occurs as shown by the values increasing above the turbulent level for a flat plate.

In Figure 7.28 (right), the same trend observed on the TFG in the flow direction is visible. The TFG measured a heat flux value between the laminar and turbulent solution. From the pressure measurement, assuming that the separation size increases moving toward the center, it is known that the value shown by the first TFG from left corresponds to a separated boundary layer. This means that also the other gauges, which display a similar value, are located inside the separation region.

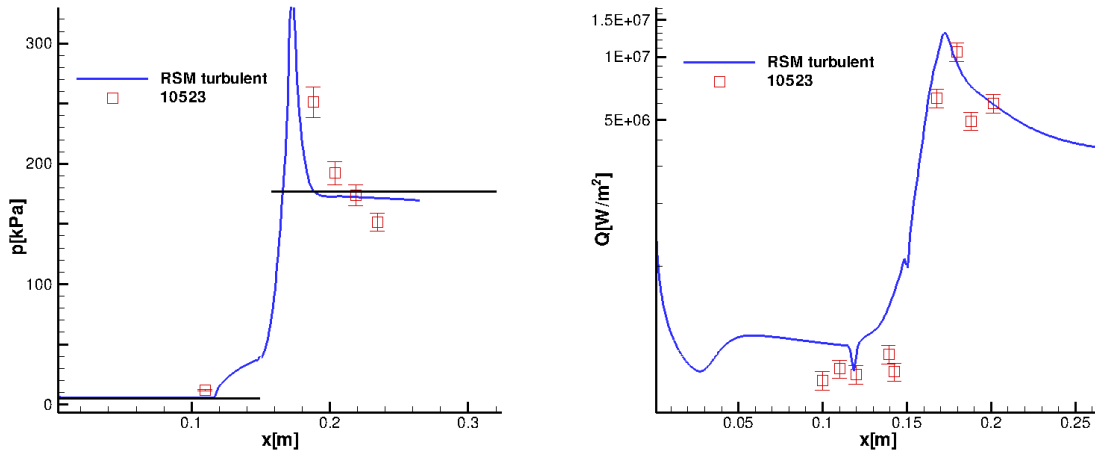


Figure 7.27. Pressure (left) and skin friction coefficient (right) distribution for a 40 degrees compression corner at $M=6.38$ and $Re=5.51 \times 10^6$ 1/m. Comparison between experiments and simulations. Runs without boundary layer trip

Finally, the heat flux on the separation ramp are discussed and presented in Figure 7.29. The first location along the ramp shows that the numerical solution predicts a steeper increase in the heat flux then registered by the TC. At the second measurement point, the values are in good agreement while at the third point the numerical solution predicts a faster decrease of the heat flux.

7.4. 15 degrees Compression Corner Results

For the 15 degrees compression corner test case, the two-dimensional grid described in Section 5.2.2 has been used. For the three-dimensional simulation, a two-dimensional grid with a reduced ramp length of 150 mm has been extruded for 75 mm and two side blocks have been added to allow flow spillage. In Figure 7.30, the plane on a line orthogonal to the flow direction is shown and three blocks are highlighted.

The characteristics of each block in terms of number of cells and grid spacing in each direction are described in Table 7.10.

For this test case, the performance of four turbulence models has been compared. The configuration at the high Reynolds number has been studied using the $k-\omega$ SST model, the Wilcox $k-\omega$ model (2008), the EARSM by Hellsten and the RSM. The performance, in terms of total number of iterations, CPU time for 1000 iteration and total CPU time, is compared in Table 7.11. The simulations are run on the Xeon cluster at the Rechenzentrum in Aachen using 8 processors. The integration in time is performed explicitly using a maximum CFL number equal to 3. All the simulation parameters are unchanged between the models.

The results show that all the chosen turbulence models require approximately the same number of iterations for solving the problem. However, the CPU time per iteration varies

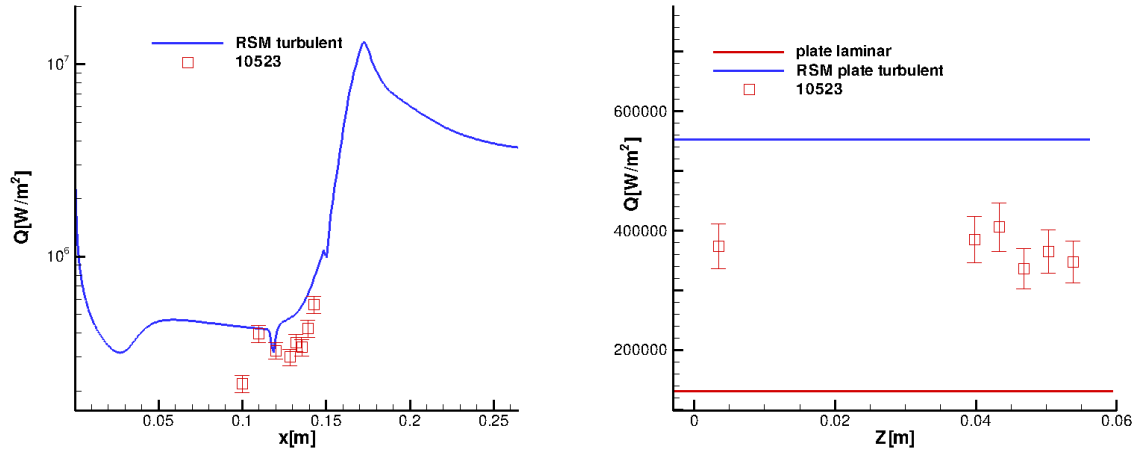


Figure 7.28. Heat flux distribution for a 40 degrees compression corner at $M=6.38$ and $Re=5.51 \times 10^6$ 1/m along a line parallel to the center line (left) and in the crossflow direction (right). Runs without boundary layer trip.

	block 1	block 2	block 3
points x-dir	450	450	450
points y-dir	190	190	20
points z-dir	55	20	20
Δx_{\max} [m]	10^{-3}	10^{-3}	10^{-3}
Δx_{\min} [m]	10^{-5}	10^{-5}	10^{-5}
Δy_{\max} [m]	10^{-3}	10^{-3}	10^{-3}
Δy_{\min} [m]	10^{-7}	10^{-7}	10^{-6}
Δz_{\max} [m]	2×10^{-3}	2×10^{-3}	2×10^{-3}
Δz_{\min} [m]	10^{-6}	10^{-6}	10^{-6}

Table 7.10. Grid resolution for the simulation of the 40 degrees compression corner.

visibly and consequently, also the total CPU time required. As expected, the linear eddy-viscosity models are the cheapest ones in terms of CPU time, followed by the EARSM and then the RSM, which requires 1.85 times the CPU time of the linear eddy-viscosity models.

7.4.1. 15 degrees 6 mm Condition with Boundary Layer Trip

As for the 40 degrees case, the higher Reynolds number condition has been investigated numerically using the same four turbulence models and a three-dimensional simulation performed with the RSM. The simulations have been performed fully turbulent. In Figure 7.31, the main features detected numerically on a two-dimensional grid using the RSM are presented. Along the flat plate the leading edge shock is visible, as well as the shock

7. Three-dimensional hypersonic SWBLI

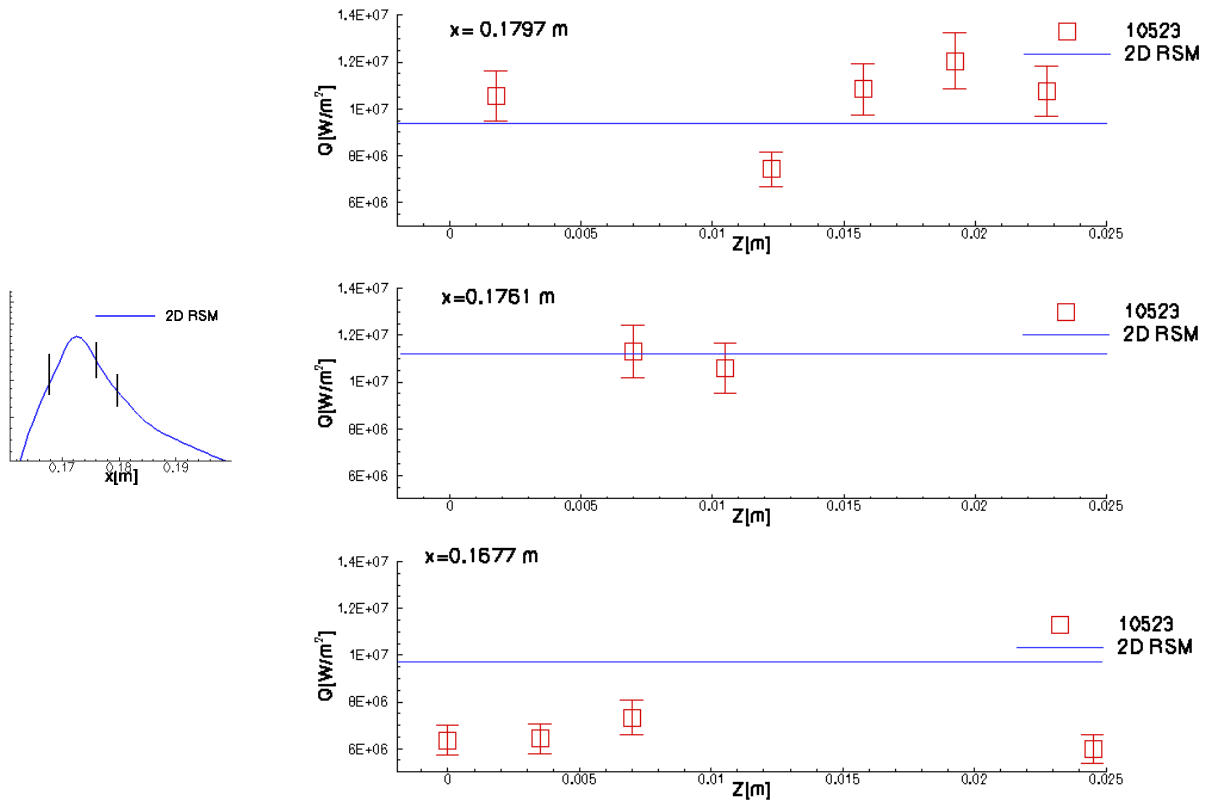


Figure 7.29. Heat flux distribution for a 40 degrees compression corner at $M=6.38$ and $Re=5.51 \times 10^6$ 1/m. On the left a zoom of the numerical peak heating region is given and the locations of the three lines shown on the right figure are highlighted. On the right the heat flux distribution along these three crossflow lines is presented. Runs without boundary layer trip.

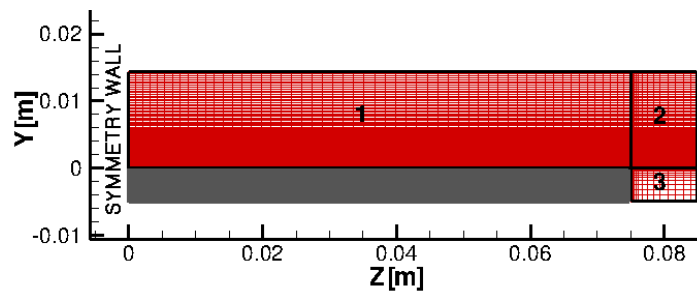


Figure 7.30. Computational domain along a plane orthogonal to the flow for a 15 degrees compression corner at $M=6.35$ and $Re=9.65 \times 10^6$ 1/m and at $M=6.38$ and $Re=5.51 \times 10^6$ 1/m. The numbers refer to the different blocks.

originated at the location of the (numerical) laminar to turbulent transition, where the boundary layer thickness has a sudden increase. At the kink, a shock wave is generated due to the presence of the compression ramp. This shock wave interacts with both the leading edge shock wave and the transition shock wave and two slip lines are visible behind the shock

	k- ω SST	k- ω Wilcox	EARSM	RSM
Iterations	90771	94347	90921	89114
CPU Time [s] (1000 it)	2.17×10^2	2.08×10^2	2.62×10^2	4.08×10^2
CPU Time [s]	1.97×10^4	1.96×10^4	2.38×10^4	3.64×10^4

Table 7.11. Comparison of turbulence models performance for the 15 degrees compression corner.

wave which originated from two triple points.

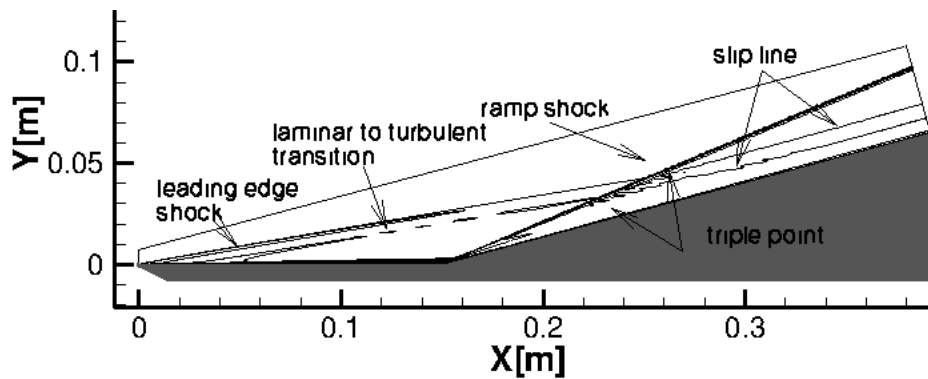


Figure 7.31. Computational domain showing the main flow features for a 15 degrees compression corner and fully turbulent conditions at $M=6.35$ and $Re=9.65 \times 10^6$ 1/m.

In Figure 7.32, the experimental findings for the pressure along the pressure line (23 mm away from the center line) and heat flux along the center line are compared with different turbulence models. Looking at the experimental results for the pressure, a first remark is necessary. The last two measurement points along the compression ramp show a pressure value substantially higher than the previous ones. Considering that, in that region, the pressure should remain constant and be equal to the value computed using the inviscid shock theory and reported in the picture with a black horizontal line, there is no physical reason why the pressure should increase in that region. This behavior has been observed also for the other test cases at 15 degrees and is probably due to the reflection of the expansion shock wave, originated at the nozzle exit, on the test section wall and its successive impingement on the model surface. For this reason, only measurements from the first three pressure gauges along the ramp are displayed for the following test cases. The pressure measurements along the plate show the behavior expected for an attached boundary layer and along the ramp the pressure measured by the first three gauges agrees excellently with the inviscid solution. From the numerical point of view, all the turbulence models show the same pressure distribution and no differences are visible between the two-dimensional result obtained with the RSM and the three-dimensional result using the same model but considering the line corresponding to the exact location of the pressure sensors along the model. The heat flux distribution presents only small differences between the turbulence models. The discrepancies visible along the flat plate have been discussed in Section 7.3.1. The agreement

with the numerical solution is excellent at each location.

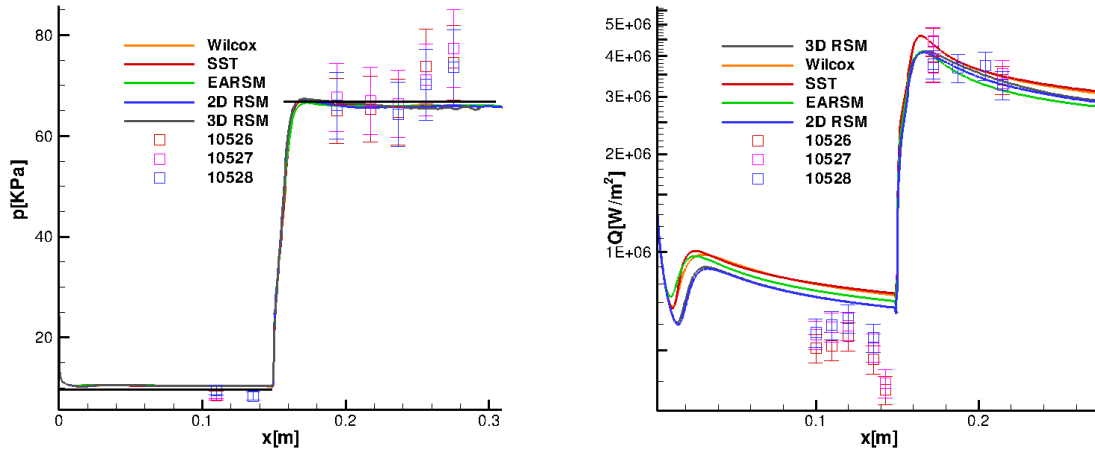


Figure 7.32. Pressure (left) and heat flux distribution (right) for a 15 degrees compression corner at $M=6.35$ and $Re=9.65 \times 10^6$ 1/m along the pressure line (23 mm away from the center line) and along the center line, respectively. Runs with boundary layer trip.

The results shown in Figure 7.32 (right) are more difficult to interpret. The first three TFG show the typical increasing behavior noticed before for the 40 degrees test case where a boundary layer trip was used. The third measurement point approaches the turbulent level from below. Moving toward the kink, an abrupt decrease of the heat flux is visible. However, the measured values are well above the laminar one for a flat plate at those conditions. In addition, the pressure measurement show that the boundary layer is attached in the region where the decrease occurs. The heat flux values along the ramp are in perfect agreement with the numerical solutions at each locations showing that there the boundary layer is fully turbulent.

The same phenomenon observed in the heat flux along the center line manifests itself along the measurement line at the side, as can be seen in Figure 7.33 (left). Also in this case, the heat flux increases along the first three measurement points closely approaching the turbulent level and then, starting from the fourth location the heat flux at the wall decreases steadily showing values in-between the turbulent and the laminar level. The good agreement between the data collected from different runs indicates the repeatability of this behavior. In Figure 7.33 (right) the heat flux along a line orthogonal to the flow is shown. The third measurement from the right corresponds to the sixth TFG along the plate in the left picture. The lower value registered by this gauge in comparison with its neighbors is visible. This value can show either a problem with the gauge during the runs or the presence of a vortex generated by the boundary layer trip. The latter could be the cause of the decrease of the heat flux along the ramp near the kink region.

Finally, in Figure 7.34 the heat flux along four lines on the compression ramp is compared with the results obtained from the 3D simulation. The numerical results show that for the

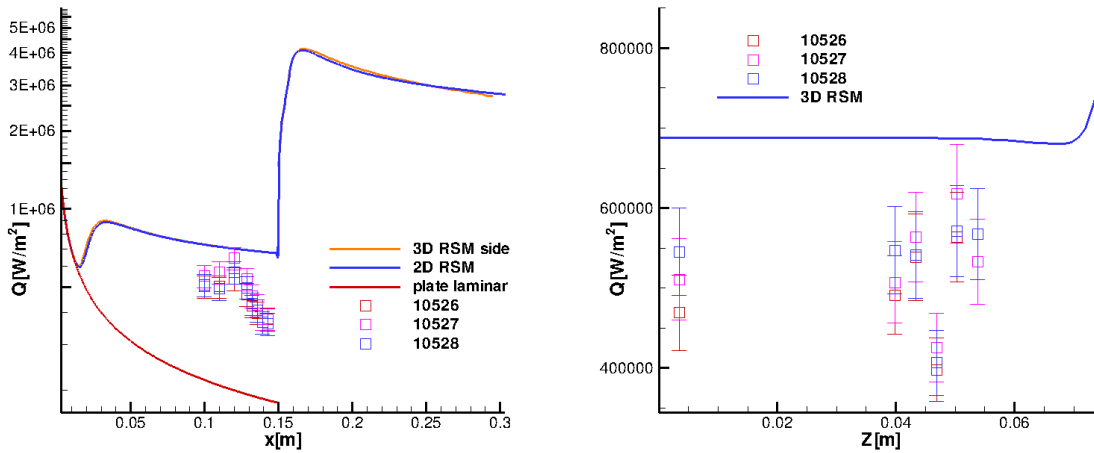


Figure 7.33. Heat flux distribution for a 15 degrees compression corner at $M=6.35$ and $Re=9.65 \times 10^6$ 1/m along a line parallel to the center line (left) and in the crossflow direction (right). Runs with boundary layer trip.

portion of the flow where the gauges are located the effect of the flow spillage is not felt. The agreement is excellent at each location and for each run supporting the assumption that the boundary layer along the plate is attached everywhere. This test case shows that using a boundary layer trip a turbulent behavior can be obtained in terms of pressure profile. The heat flux distribution differs from the one expected for a fully turbulent condition but there are evidences in the heat flux along the ramp and in the pressure measurements that show that the boundary layer does not undergo a separation. The numerical solutions from different turbulent models do not show appreciable differences and the agreement with the measurement is excellent at each location apart from the region near the kink where an unexpected decrease in the heat flux takes place.

7.4.2. 15 degrees 3 mm Condition with Boundary Layer Trip

The results obtained using the lower Reynolds number condition in combination with a boundary layer trip show the same features observed for the higher Reynolds number case. In Figure 7.35 (left), the experimental pressure distribution is shown and compared with the numerical result obtained using the RSM. The pressure values measured along the ramp show that the boundary layer in that region is attached. The only measurement available along the ramp is in agreement with the inviscid theory for this configuration. At all three locations the agreement between the experimental findings and the numerical simulation is good.

The heat flux along the flat plate, shown in Figure 7.35 (right), display the same behavior observed at the higher Reynolds number for the first three measurement locations. The last measurement displays a value below the laminar flat plate level. This probably indicates a problem with the respective gauge that stopped working after the run 10533. However, the

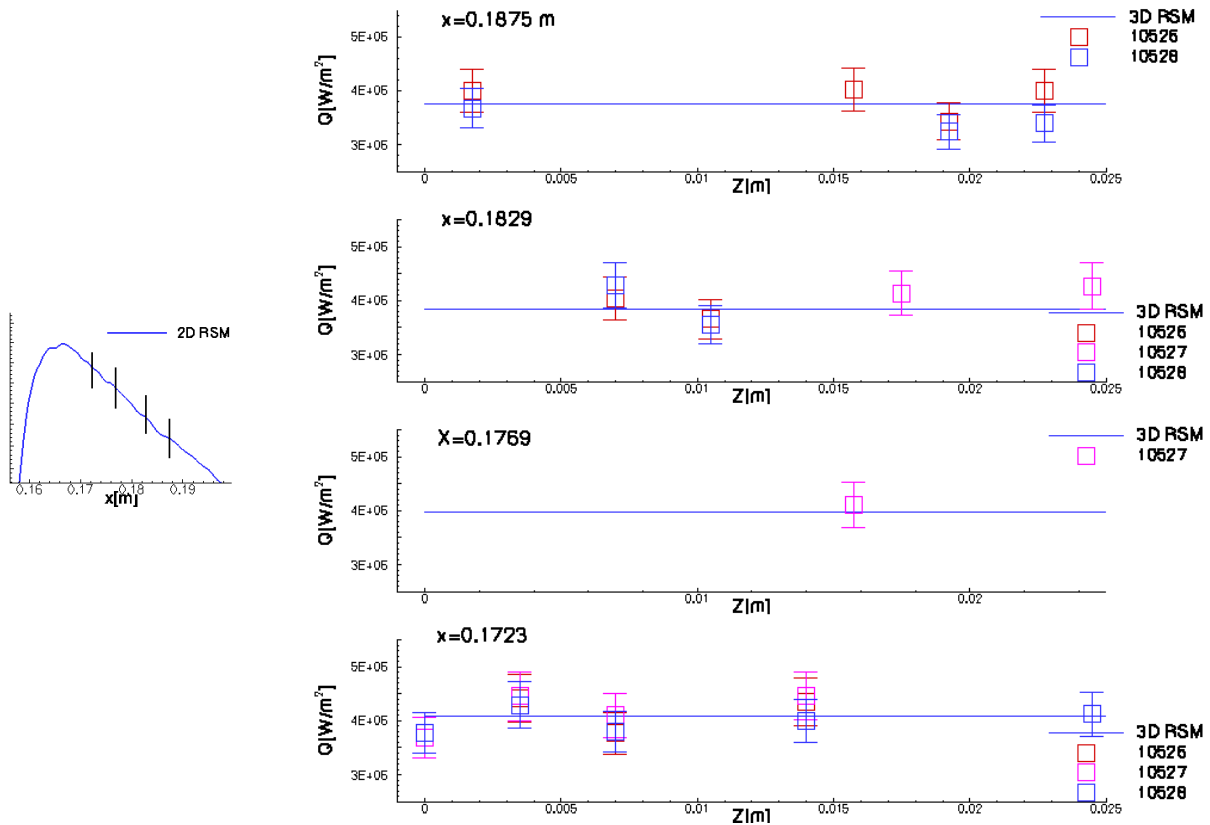


Figure 7.34. Heat flux distribution for a 40 degrees compression corner at $M=6.35$ and $Re=9.65 \times 10^6$ 1/m. On the left a zoom of the numerical peak heating region is given and the locations of the four lines shown on the right figure are highlighted. On the right the heat flux distribution along these four crossflow lines is presented. Runs with boundary layer trip.

measurement is shown here for completeness. The heat flux along the compression ramp shows an excellent agreement between measurement and numerical solution.

The heat flux along a line parallel to the center line is shown in Figure 7.33 (left) together with the measurements in the cross flow direction (right). The results in the flow direction show features similar to the higher Reynolds number case. From the measurements, it is clear that the flow is in the transitional regime between laminar and turbulent, thus it is difficult to predict the exact behavior of the boundary layer in the region of strong adverse pressure gradient.

For what concerns the measurement along the ramp, the heat flux is presented in Figure 7.37; the measured values are in qualitatively good agreement with the numerical solution but a spreading of the experimental results can be seen. As for the previous test case, the agreement between the experiment and the numerical solution for the pressure and the heat flux along the ramp is very good but the behavior of the heat flux along the plate is not reproduced by the simulation.

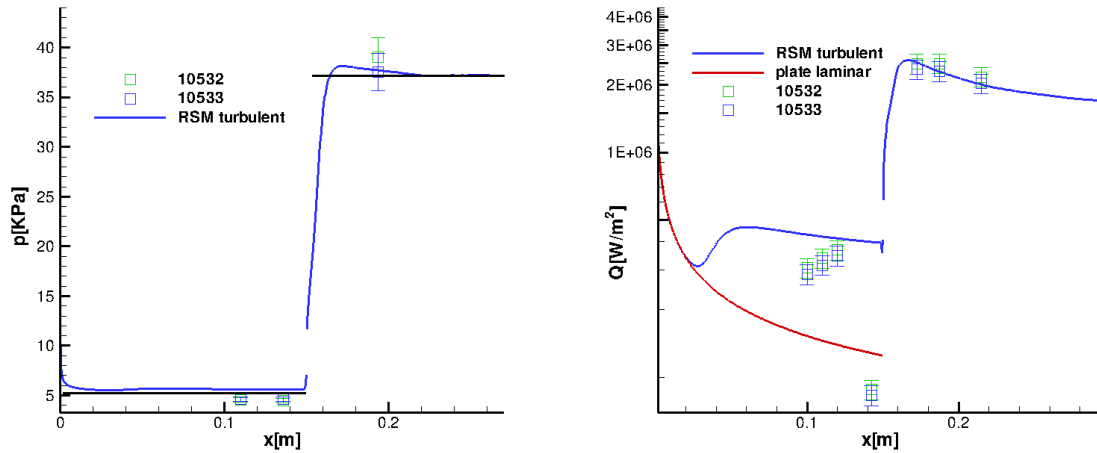


Figure 7.35. Pressure (left) and heat flux distribution (right) for a 15 degrees compression corner at $M=6.38$ and $Re=5.51 \times 10^6$ 1/m along the pressure line (23 mm away from the center line) and along the center line, respectively. Runs with boundary layer trip.

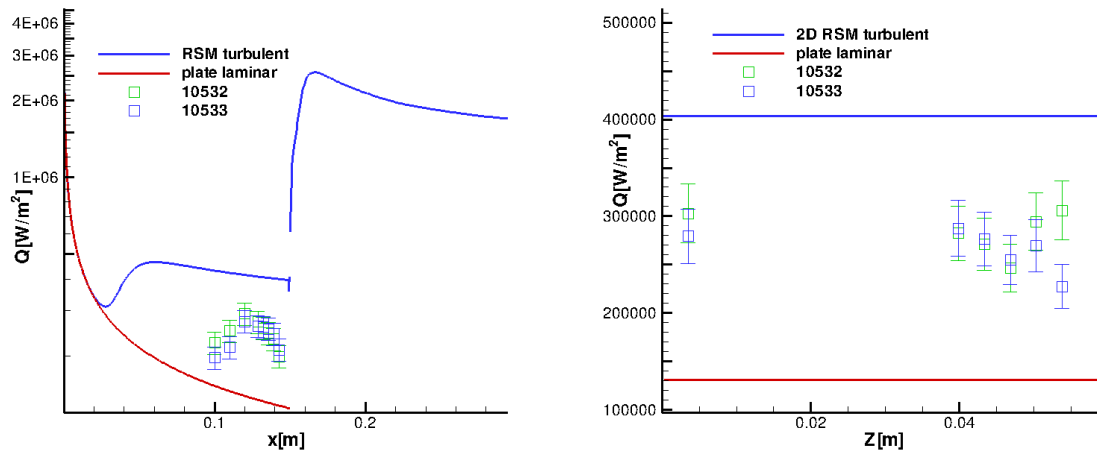


Figure 7.36. Heat flux distribution for a 15 degrees compression corner at $M=6.38$ and $Re=5.51 \times 10^6$ 1/m along a line parallel to the center line (left) and in the crossflow direction (right). Runs with boundary layer trip.

7.4.3. 15 degrees 6 mm Condition without Boundary Layer Trip

The results from the high Reynolds number condition without the use of a boundary layer trip are discussed in this section. The pressure distribution is shown in Figure 7.38 (left). The measurements show that the boundary layer undergoes a separation in a location between the two kulite sensors. Along the ramp, the pressure from the run 10525 shows a slight decrease as expected for a separated boundary layer when it reattaches along the ramp. Downstream, the values are in good agreement with the inviscid solution. The experiment is compared

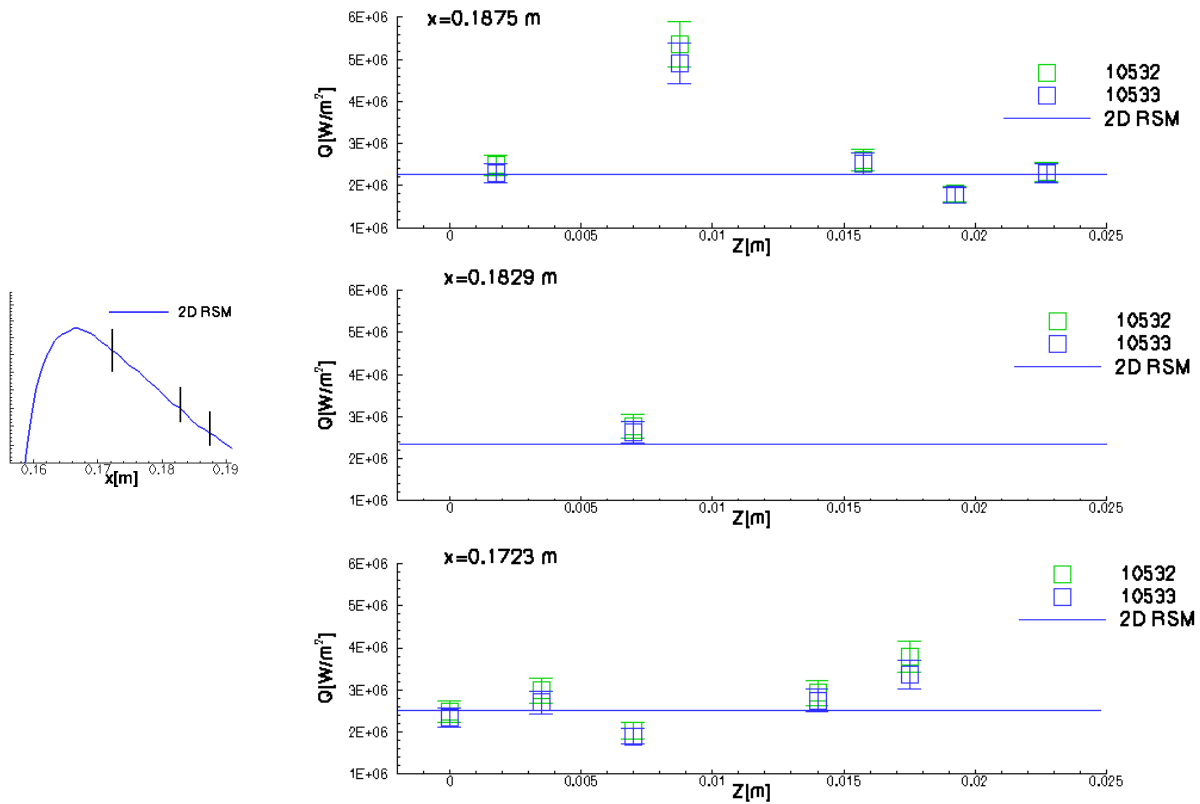


Figure 7.37. Heat flux distribution for a 40 degrees compression corner at $M=6.38$ and $Re=5.51 \times 10^6$ 1/m. On the left a zoom of the numerical peak heating region is given and the locations of the three lines shown on the right figure are highlighted. On the right the heat flux distribution along these three crossflow lines is presented. Runs with boundary layer trip.

with a fully turbulent solution, a laminar one and a laminar/turbulent solution where the transition point has been set at the kink. The fully turbulent solution clearly does not predict the boundary layer separation while the laminar one overpredicts it. The laminar/turbulent solution correctly predicts an attached boundary layer at the first measurement point and a separation at the location of the second sensor. However, the pressure rise computed numerically is higher than in the experiment. The cause can be in the inflow pressure that is higher than in the experiment as visible from the first pressure measurement that lies below the laminar value. Also, along the ramp, the simulation overestimates the pressure rise with respect to that measured in the experiment.

The heat flux measurements, in Figure 7.38 (right) clearly show that the boundary layer undergoes a separation. The heat flux decreases well below the laminar value and starts to increase again moving toward the kink. At the reattachment the heat fluxes are turbulent. As observed above the fully turbulent solution does not predict the boundary layer separation so that the values along the plate are extremely higher than in the experiment. However, the flow turns to turbulent inside the interaction region and the heat flux at reattachment and along the ramp are in excellent agreement with the fully turbulent solution. The laminar solution

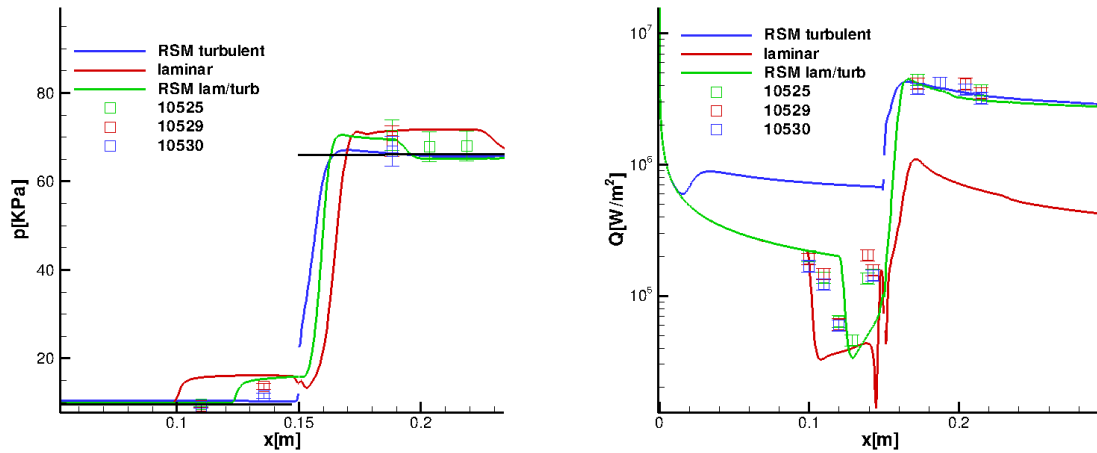


Figure 7.38. Pressure (left) and heat flux distribution (right) for a 15 degrees compression corner at $M=6.35$ and $Re=9.65 \times 10^6$ 1/m along the pressure line (23 mm away from the center line) and along the center line, respectively. Runs without boundary layer trip.

seems to predict a correct separation size but the heat fluxes along the ramp are too low. The laminar/turbulent simulation predicts the separation a bit later than what the experiment shows, probably indicating that the laminar to turbulent transition occurs further downstream than at the kink allowing a larger separation to develop. Along the ramp, the simulation is in excellent agreement with the experimental results.

The heat flux distribution along a line parallel to the center line and 46.85 mm at its side, is presented in Figure 7.39 (left). The experimental findings show that the boundary layer undergoes a separation. Since the heat flux level at the separation onset is laminar, the heat flux in the separated region shows the characteristic decrease below the laminar value for a flat plate. With respect to the measurements along the center line, here it seems that the separation size is larger and in both cases the separation size captured by the heat flux measurement is larger than what is seen by the pressure sensors. The differences are not substantial but, while the second TFG shows a clear separated value, this is not the case for the first kulite (the two gauges are aligned along the crossflow direction). This can indicate that the flow along the plate is less uniform than in the case where the boundary layer trip is used and differences can be observed in a plane orthogonal to the flow. Once more the laminar solution seems to correctly predict the separation size but the correct decrease and successive increase along the plate is not shown in the simulation. The heat flux values shown on the crossflow line inside the separated region indicate that the measurements are well below the laminar value for a flat plate. The only value collected by the TFG in near the center line is considerably lower than the others. This is most certainly due to a problem with the gauge.

Finally, the heat flux values along four lines in the crossflow direction located at the beginning of the ramp are displayed in Figure 7.40. The measurements are in qualitatively good agreement with the fully turbulent numerical solution. However, a spread of the results

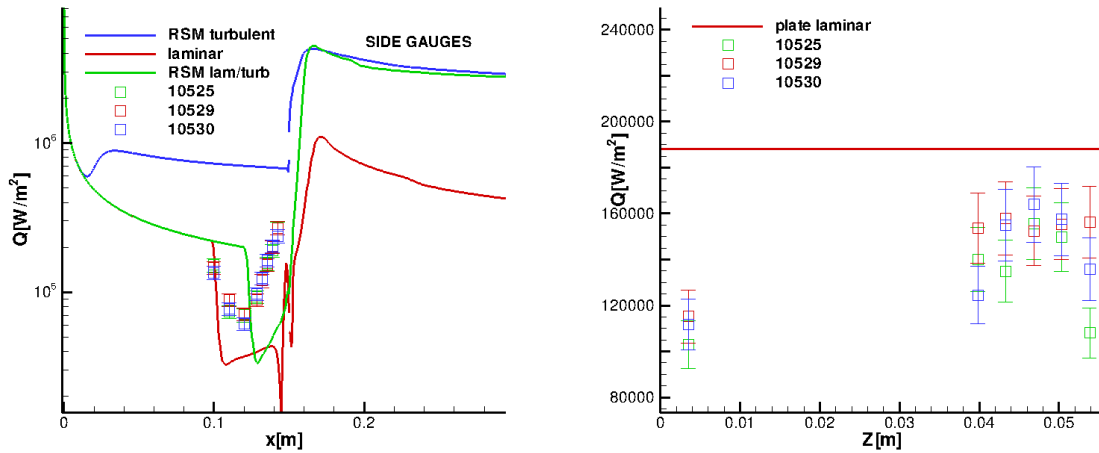


Figure 7.39. Heat flux distribution for a 15 degrees compression corner at $M=6.35$ and $Re=9.65 \times 10^6$ 1/m along a line parallel to the center line (left) and in the crossflow direction (right). Runs without boundary layer trip.

can be observed for each location. This can once more be due to some non-uniformities of the flow.

It is interesting to notice that the results obtained without the use of a boundary layer trip show a different state of the separation for changing ramp angle. In the case of a 40 degrees compression ramp the flow shows turbulent characteristics and the heat flux never approaches the laminar level. On the contrary, for the 15 degrees cases, a clear laminar separation takes place. Along the ramp, both conditions show turbulent results. The reason for this has to be found in the differences in the strength of the shock wave generated by the compression ramp. It is known that a turbulent amplification occurs when the flow passes through a shock and that this change in the flow nature can be transmitted upstream of the shock through the subsonic part of the boundary layer. This is the reason why the flow that undergoes a transition, shows a reduced separation size with respect to fully laminar flow. In the case of a strong shock (40 degrees compression ramp), the amplification is larger and affects the flow further upstream of the shock wave than in the case of a weak shock (15 degrees compression ramp). The same feature is observed in the low Reynolds number case presented in the next section.

7.4.4. 15 degrees 3 mm Condition without Boundary Layer Trip

The last test case to be discussed is the compression corner at 15 degrees at the lower Reynolds number condition without boundary layer trip. The pressure distribution is shown in Figure 7.41 (left). The experimental results show that the boundary layer is separated at both measurement locations along the flat plate. The pressure along the ramp shows a decrease down to the inviscid solution. For what concerns the prediction of the separation

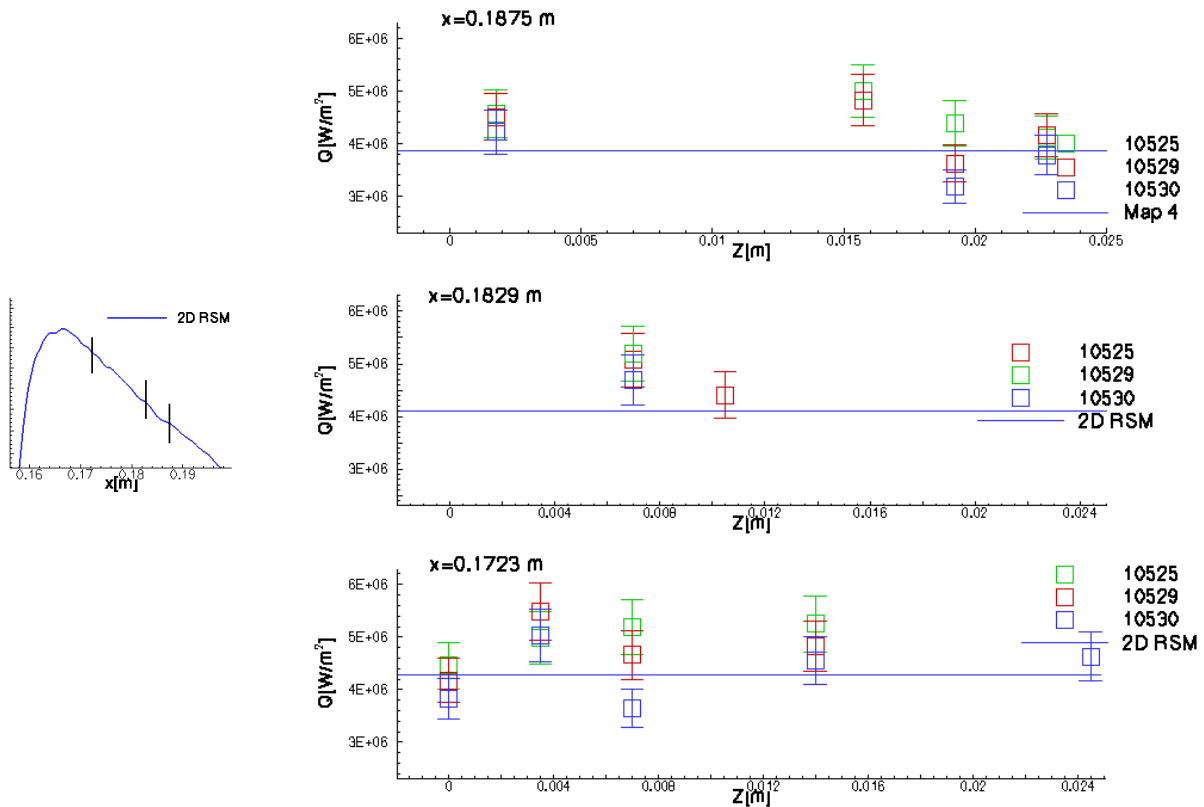


Figure 7.40. Heat flux distribution for a 40 degrees compression corner at $M=6.35$ and $Re=9.65 \times 10^6$ 1/m. On the left a zoom of the numerical peak heating region is given and the locations of the three lines shown on the right figure are highlighted. On the right the heat flux distribution along these three crossflow lines is presented. Runs without boundary layer trip.

size, only the laminar solution displays a separated value for both measurement locations but the pressure plateau is higher in the simulation. The pressure decrease detected along the ramp is not predicted by this solution.

The distribution of the heat flux along the wall presented in Figure 7.41 (right) detects a laminar separation of the boundary layer and once more the separation size is well predicted by the laminar solution which on the contrary does not match the heat flux values along the ramp. The fact that the laminar/turbulent solution underpredicts the separation size is visible both at separation and at reattachment where the heat flux peak detected in the experiment is shifted further downstream than in the simulation.

The same heat flux distribution, along a line parallel to the center line and 46.85 mm at its side, is presented in Figure 7.42 (left). In contrast with the previous test case, the separation size cannot be estimated neither from the pressure nor the heat flux measurement so that the possible influence of a non uniform inflow cannot be analyzed here. In the crossflow direction, in Figure 7.42 (right) the heat fluxes measured in the experiment are lower than the one predicted for a laminar flat plate confirming that the boundary layer there is separated.

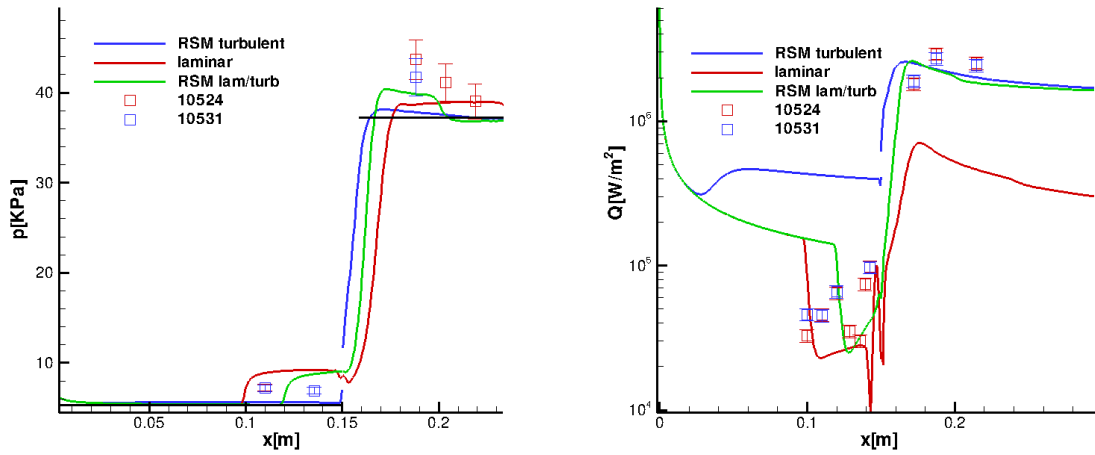


Figure 7.41. Pressure (left) and heat flux distribution (right) for a 15 degrees compression corner at $M=6.38$ and $Re=5.51 \times 10^6$ 1/m along the pressure line (23 mm away from the center line) and along the center line, respectively. Runs without boundary layer trip.

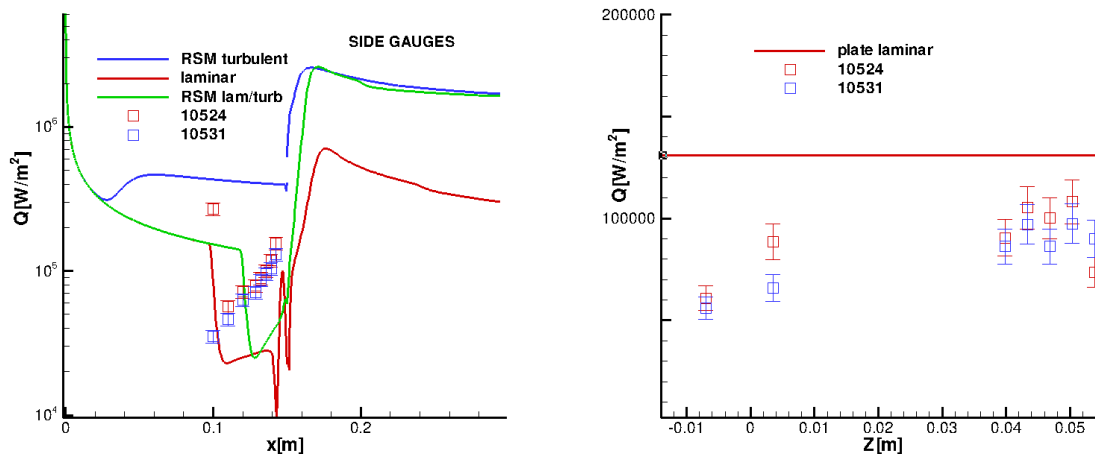


Figure 7.42. Heat flux distribution for a 15 degrees compression corner at $M=6.38$ and $Re=5.51 \times 10^6$ 1/m along a line parallel to the center line (left) and in the crossflow direction (right). Runs without boundary layer trip.

Along the compression ramp, the values measured along four crossflow lines, and shown in Figure 7.43 does not agree so well with the fully turbulent simulation due to the different locations of the peak heating along the wall.

The results presented in the last two sections show that for cases where the flow is transitional along the interaction region a laminar/turbulent simulation is necessary to correctly predict the flow features in both laminar and turbulent regions. However, in order to perform this kind of simulations a pre-knowledge of the transition point is needed which

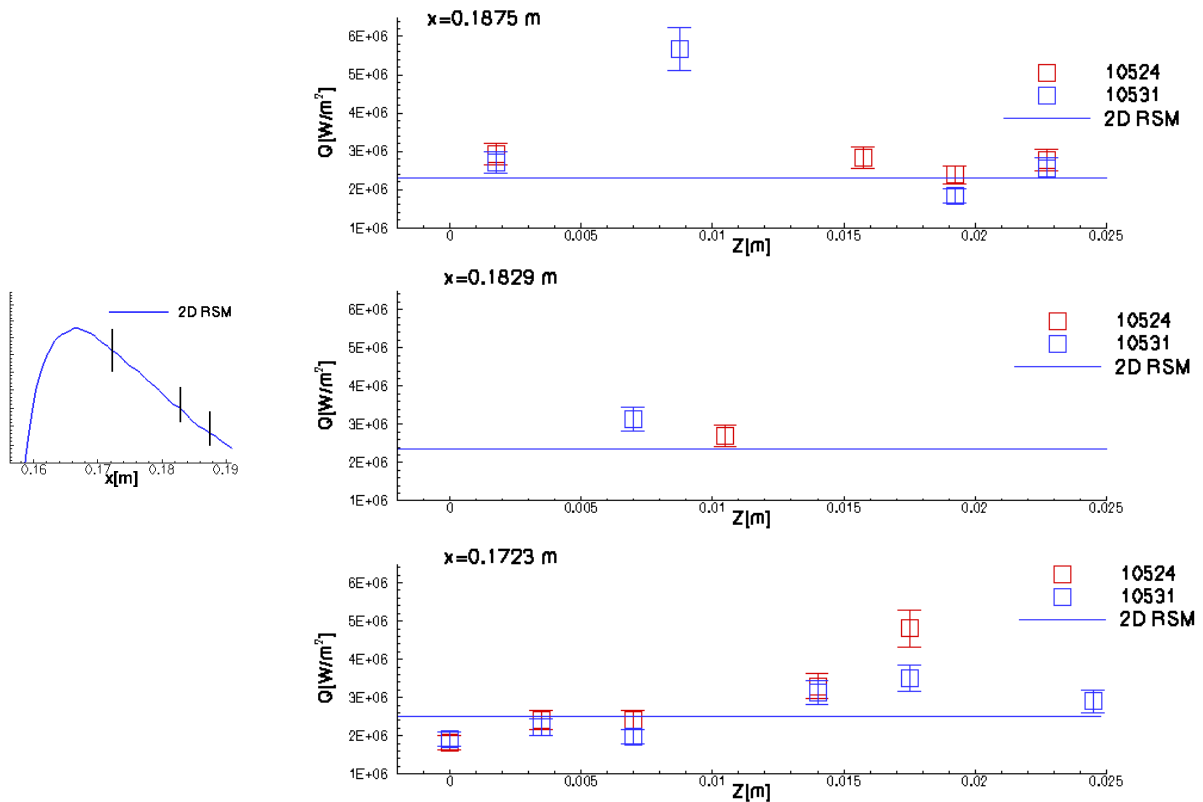


Figure 7.43. Heat flux distribution for a 40 degrees compression corner at $M=6.38$ and $Re=5.51 \times 10^6$ 1/m. On the left a zoom of the numerical peak heating region is given and the locations of the three lines shown on the right figure are highlighted. On the right the heat flux distribution along these three crossflow lines is presented. Runs without boundary layer trip.

is generally not available in experimental results.

7.5. Investigation Using an Adaptive Procedure

The compression corner at 15 degrees for fully turbulent inflow conditions has been studied using an adaptive grid. The inflow conditions relative to the high Reynolds number case are used here. The adaptive procedure has been performed using $L=4$ refinement levels. This number guarantees that, at the finest refinement level, the grid at the wall has a resolution equal to the optimal one determined in Section 5.2.2. A threshold value of $\epsilon=10^{-3}$ has been chosen as suggested in Section 5.2.4. The adaptation is triggered when the residual of the density drops below 10^{-2} . The variables used for grid adaptation are the variables from the Navier-stokes equation plus the first component of the Reynolds stress tensor.

The results obtained from the adaptive simulation are compared with the ones obtained on a uniform grid at the maximum refinement level. In addition, the solution obtained on the structured grid, and presented in the previous sections, is given for completeness. The

7. Three-dimensional hypersonic SWBLI

structured grid and the uniform grid are similar in terms of number of cells and spacing but do not coincide. All the simulations are run explicit in time using a maximum CFL number of 3.

	adaptive	uniform L=4	structured
Iterations	77010	108150	89114
CPU Time [s]	9.08×10^3	2.71×10^4	3.64×10^4
Cells	55612	107520	119700

Table 7.12. Comparison of performances for adaptive, uniform and structured grids for a 15 degrees compression corner at $M=6.35$ and $Re=9.65 \times 10^6$ 1/m.

Table 7.12 shows a comparison of the performances obtained using the different grids in terms of number of iteration, CPU times and number of cells. For what concerns the adaptive simulation, the number of cells refers to the finest grid. From a computational point of view, the adaptive grid allows the resolution of the problem using approximately half of the grid cells required at the finest refinement level or for the structured grid. The reduction in the total number of cells results in a total computational time which is one third of the one required for the uniform grid.

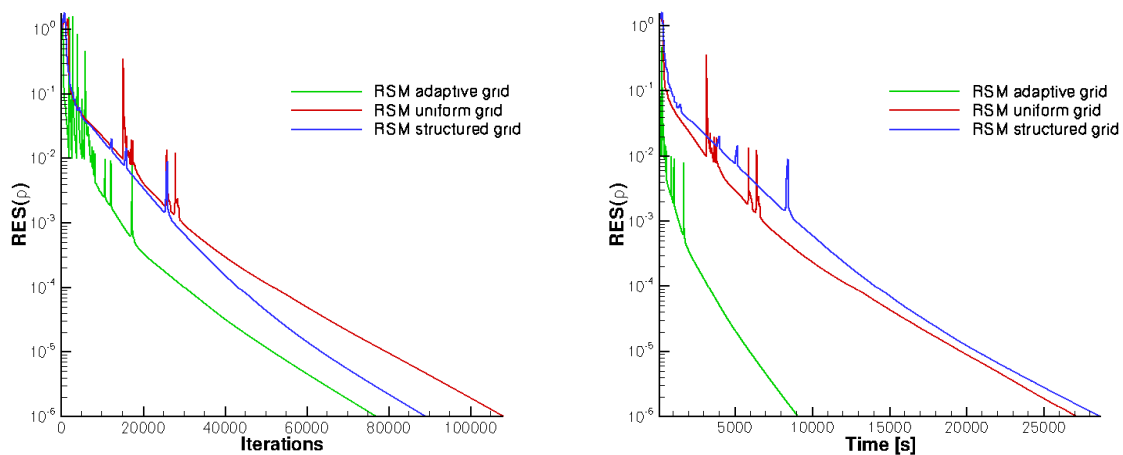


Figure 7.44. Comparison of convergence rate in terms of number of iterations and computational time for adaptive, uniform and structured grid. Test case: 15 degrees compression corner and fully turbulent conditions at $M=6.35$ and $Re=9.65 \times 10^6$ 1/m.

Figure 7.44 (left) shows the convergence rate for the three grids. The adaptive simulation and the uniform simulation show the same convergence rate. This behavior is expected since this quantity depends on the problem and on the grid used. What can be seen in this picture is that the adaptive procedure accelerates the convergence in the first part of the simulation when the grid is coarse especially in the boundary layer. After this phase the two lines run almost

parallel. In Figure 7.44 (right) the computational time is analyzed. From this picture the main advantage of the adaptive procedure shows up: the time required for a single iteration on the adaptive grid is greatly reduced, with respect to the uniform grid, due to the lower number of cells.

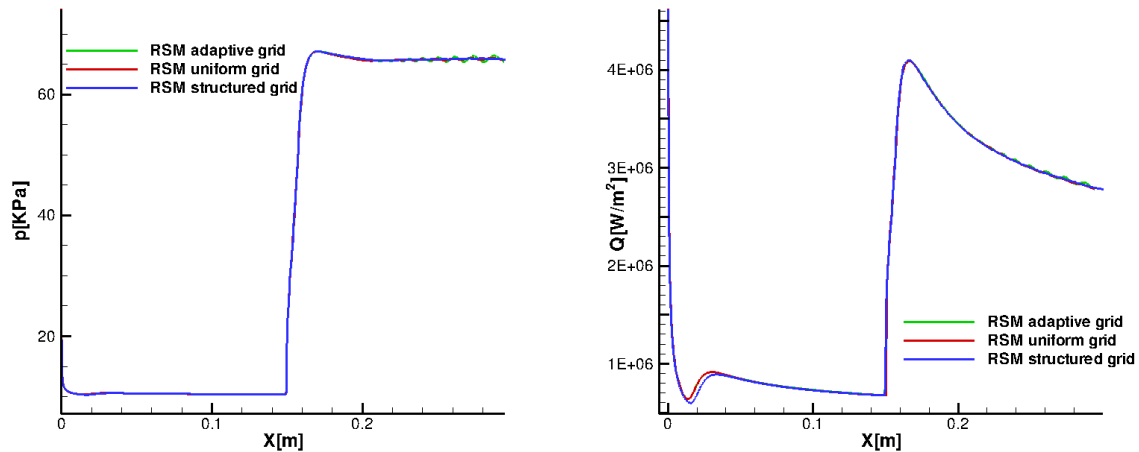


Figure 7.45. Pressure (left) and heat flux (right) distribution for a 15 degrees compression corner at $M=6.38$ and $Re=5.51 \times 10^6$ 1/m for different type of grids.

The results obtained for pressure and heat flux are shown in Figure 7.45. Both distributions show an excellent agreement between the three numerical solutions. However the adaptive solution shows some small oscillations in both quantities at the end of the ramp. The oscillations reduce on the uniform grid and reduce further on the structured grid but never disappear. The reason why these oscillations appear is still unclear. It can be related to the boundary conditions. At the outflow wall, supersonic outflow conditions are imposed. However, in the subsonic part of the boundary layer, this boundary condition is not properly defined. Due to a finer resolution in the leading edge region, the solutions on the adaptive grid and on the uniform grid at $L=4$ show a (numerical) laminar to turbulent transition occurring slightly upstream.

8. Conclusions

The simulation of hypersonic flows characterized by shock wave boundary layer interaction at real flight Reynolds number is a challenge for computational fluid dynamics. On the one hand the high Mach number generates large gradients in the thick boundary layer and makes this kind of problem extremely grid sensitive. On the other hand because of the high Reynolds number, turbulence has to be taken into account in the numerical simulations. In the literature review it has been shown that, despite more than 50 years of study of SWBLI and the improvement in computational capabilities, the numerical results achievable in turbulent regime, as of interest here, is still far from being satisfactory. One reason for this is that the eddy viscosity models, which are the standards for industrial codes, rely on the Boussinesq hypothesis of a linear dependence between the Reynolds stress tensor and the strain rate tensor. However, the assumption fails for wall dominated flows characterized by thick boundary layers and strong shock wave boundary layers interaction with separation.

For this reason a differential Reynolds stress model has been implemented into the in-house code QUADFLOW. In contrast to eddy viscosity models, this class of models solves a transport equation for each component of the Reynolds stress tensor and thus naturally includes the effects of streamline curvature and rotation and accounts for the normal stress anisotropy close to the wall.

The choice of the Reynolds stress model to be implemented has been taken on the analysis of the available results from the same model over different configurations from subsonic up to hypersonic. The model chosen, the SSG/LRR- ω model, has the advantage of combining the use of an ω -equation near the wall and of an ϵ -equation in the far-field. In this way the model overcomes the shortcoming of using an ϵ -equation in the wall region but maintains its good features of being only marginally sensitive to variations in the incoming turbulence. However the ω -equation introduces a singularity related to the definition of its value at the wall, which should be infinity, so that numerically prescribing a wall condition is not trivial.

The implementation of the Reynolds stress model has been extensively validated primarily on hypersonic test cases. For zero pressure gradient flows the model has proven to be able to accurately predict wall quantities such as the skin friction coefficient, when compared to both experimental data and a theoretical solution based on the reference temperature method. In addition, the Mach number and temperature distributions inside the boundary layer showed an excellent agreement with the experimental results available. For the prediction of the Reynolds stresses, the subsonic flow over a flat plate has been simulated and the results obtained were in agreement with previous findings obtained with the same turbulence model.

Parametric studies have been performed to assess the sensitivity of the model to free stream turbulence and grid resolution. As expected by its formulation, the model is only slightly

sensitive to the prescribed incoming turbulence. Different formulations of the boundary condition for the ω -equation at the wall have been tested and consistent results have been obtained when using parameters in the range suggested by the authors. For what concerns grid sensitivity, as generally known for hypersonic flows, it was hard to obtain a grid-converged solution for quantities like the heat flux. However the results showed evidence that the simulations always approximate the heat flux from below and that the difference between the chosen grid and the finest grid, where a converged solution was obtained, was less than 5% at the peak heating.

Successively, geometries characterized by shock wave/boundary layer interaction have been analyzed at hypersonic flight inflow conditions. Despite the known decrease in the stability of the model with respect to eddy viscosity models, the RSM has been successfully employed for the simulation of a double wedge configuration at Mach 8.3. The obtained results verify the ability of the model to predict both the pressure coefficient and the Stanton number distribution in agreement with experimental findings and with the SST model implemented in the same code. In addition, the RSM was tested in combination with a grid adaptation procedure showing that the grids generated with an adaptive strategy can further improve the agreement with the experimental findings and that the Reynolds stress model can successfully be used in combination with grid adaptation. The use of the model for the computation of a three dimensional Scramjet intake configuration showed that Reynolds stress models can be employed for the investigation of complex geometries.

In order to test the model on a fully turbulent test case and to collect data from critical flow regions, such as at separation and at reattachment, an experimental campaign has been initiated. A compression corner with two different ramp angles has been chosen to generate turbulent flow characterized by an attached boundary layer, for the lower ramp angle, and separated boundary layer, for the higher ramp angle. As expected, the results showed that for an attached boundary layer, the RSM as well as the eddy viscosity models were able to provide results in excellent agreement with the experimental data. However fundamental differences were found in the cases where a boundary layer separation occurred. The eddy viscosity models failed to predict the separation and consequently the main flow structures. The RSM and an EARSM predicted boundary layer separation proving the superiority of Reynolds stress based model for flows characterized by adverse pressure gradient. Different flow structures in terms of shock-shock interaction were found between the two models. However the Reynolds stress model showed a better agreement with the experimental findings for both pressure and heat flux.

Throughout this work, the chosen RSM has proven to be robust and accurate to be used for the simulation of high Reynolds number hypersonic flows. The superiority of the model, with respect to standard eddy viscosity models, in the prediction of flows characterized by turbulent separation and strong shock interaction makes it a valuable tool for the design of hypersonic vehicles.

Appendix A.

Sensor Positions

The correct position of each sensor along the model is given in this section. A distinction is made between the gauges along the plate and the gauges along the ramp. For the flat plate, the set of coordinates used considers z as the spanwise direction and x as the flow direction, consistently with the results sections. For the ramp, a relative system of coordinates is used considering the kink as $x_{rel} = 0$ and the ramp at 0 angle. For computing the location of the sensors with respect to the global system of coordinates (in millimeters) the following formula must be applied considering α the ramp angle:

$$\begin{cases} x = x_{rel}\cos\alpha + 150 \\ z = z_{rel} \end{cases} \quad (\text{A.1})$$

Sensor	x-coordinate (mm)	z-coordinate (mm)
K1	110	-23
K2	135.7	-23

Table A.1. Kulite pressure transducers positions along the flat plate

Sensor	x_{rel} -coordinate (mm)	z_{rel} -coordinate (mm)
K2	50	-23
K3	70	-23
K4	90	-23
K5	110	-23
K6	110	-23
K7	130	-23
K8	155	-23
K9	175	-23
K10	50	-23

Table A.2. Kulite pressure transducers positions along the ramp.

Sensor	x-coordinate (mm)	z-coordinate (mm)
TFG 1	0	100
TFG 2	0	110
TFG 3	0	120
TFG 4	0	128.7
TFG 5	0	132.2
TFG 6	0	135.7
TFG 7	0	139.2
TFG 8	0	142.7
TFG 9	7	135.7
TFG 10	3.5	135.7
TFG 11	-3.5	135.7
TFG 12	-7	135.7
TFG 13	46.85	100
TFG 14	46.85	110
TFG 15	46.85	120
TFG 16	46.85	128.7
TFG 17	46.85	132.2
TFG 18	46.85	135.7
TFG 19	46.85	139.2
TFG 20	46.85	142.7
TFG 21	53.85	135.7
TFG 22	50.35	135.7
TFG 23	43.35	135.7
TFG 24	39.85	135.7

Table A.3. Thin film gauges positions along the flat plate

Sensor	x_{rel} -coordinate (mm)	z_{rel} -coordinate (mm)
TC 1	19.25	27.85
TC 2	22.75	27.85
TC 3	0	23.15
TC 4	3.5	23.15
TC 5	7	23.15
TC 6	10.5	23.15
TC 7	14	23.15
TC 8	17.5	23.15
TC 9	21	23.15
TC 10	24.5	23.15
TC 11	14	34.15
TC 12	17.5	34.15
TC 13	21	34.15
TC 14	24.5	34.15
TC 15	-1.75	27.85
TC 16	1.75	27.85
TC 17	5.25	27.85
TC 18	8.75	27.85
TC 19	12.25	27.85
TC 20	15.75	27.85
TC 21	1.75	38.85
TC 22	5.25	38.85
TC 23	8.75	38.85
TC 24	12.25	38.85
TC 25	15.75	38.85
TC 26	19.25	38.85
TC 27	22.75	38.85
TC 28	3.5	34.15
TC 29	7	34.15
TC 30	10.5	34.15
TC 31	0	71.85
TC 32	0	67.15
TC 33	0	60.85
TC 34	0	56.15
TC 35	0	49.85
TC 36	0	45.15
TC 37	-1.75	38.85
TC 38	0	34.15

Table A.4. Thermocouples positions along the ramp.

Appendix B.

Thermocouples Calibration

The values collected from the calibration of the thermocouples are reported in Table B.1. The variables refers to the equation 7.2 and ΔV is defined as the change in voltages registered at the TC surface.

	T_w	T_s	ΔV	TP
TC 32	5	48	526	8930
TC 32	5	50	520	9540
TC 32	5	49	542	8650
TC 32	5	50	536	9200
TC 3	5	51	516	9800
TC 3	5	50	534	9250
TC 3	5	50	520	9540
TC 3	5	49	518	9340
TC 25	5	49	520	9290
TC 25	5	50	530	9330
TC 25	5	51	512	9720
TC 25	5	51	520	9790
TC 27	5	50	532	9290
TC 27	5	50	528	9330
TC 27	5	50	512	9720
TC 27	5	49	510	9790
TC 21	5	51	536	9290
TC 21	5	50	528	9370
TC 21	5	51	516	9710
TC 21	5	50	522	9510

Table B.1. Data from the thermocouples calibration.

Bibliography

- [1] <http://www.maplesoft.com/products/maple/>. 2010.
- [2] <http://www.swl.rwth-aachen.de/en/industry-solutions/thin-films/>. 2010.
- [3] N. A. Adams. Numerical Simulation of Turbulent Boundary Layer along a Compression Ramp at $M=3$ and $Re_\theta=1685$. *J. Fluid Mech*, 402, 2000.
- [4] J. D. Anderson. *Hypersonic and High Temperature Gas Dynamics*. McGraw-Hill, 1989.
- [5] J. D. Anderson. *Fundamentals of Aerodynamics*. McGraw-Hill, 2001.
- [6] J. D. Anderson. *Fundamentals of Aerodynamics*. McGraw-Hill, 4th edition, 2006.
- [7] D. Arnal and J Détery. Laminar-turbulent transition and shock wave/boundary layer interaction. In *RTO-EN-AVT-116*, 2004.
- [8] G. A. Ashford. *An Unstructured Grid Generation and Adaptive Solution Technique for High-Reynolds-Number Compressible Flows*. PhD thesis, University of Michigan, 1996.
- [9] J. Ballmann, M. Behr, K. Brix, W. Dahmen, C. Hohn, R. Massjung, S. S. Melian, S. Müller, and G. Schieffer. Parallel and adaptive methods for fluid-structure interactions. In W. Schröder, editor, *Summary of Flow Modulation and Fluid-Structure Interaction Findings - Results of the Collaborative Research Center SFB 401 at the RWTH Aachen University*, volume 109 of *Numerical Fluid Mechanics and Multidisciplinary Design*, pages 265–294. 2010.
- [10] J. P. Batham. An experimental study of turbulent separating and reattaching flows at a high Mach number. *J. Fluid Mech.*, 52(3):425–435, 1972.
- [11] P. Batten, M. A. Leschziner, and U. C. Goldberg. Average-State Jacobians and Implicit Methods for Compressible Viscous and Turbulent Flows. *J. Comput. Phys.*, 227:254–272, 1997.
- [12] J. J. Bertin. *Hypersonic Aerothermodynamics*. AIAA Education Series, 1994.
- [13] M. Bleilebens and H. Olivier. On the influence of elevated surface temperatures on hypersonic shock wave/boundary layer interaction at a heated ramp model. *Shock Waves*, 15:301–312, 2006.

- [14] P. B. Bookey, C. Wyckham, J. A. Smits, and M. P. Martin. Experimental Data of STBLI at DNS/LES Accessible Reynolds Numbers. *AIAA Journal*, (2005-309), 2005.
- [15] A. Bosco and B. Reinartz. Study of Compressible and Quasi-Incompressible Flows with QUADFLOW Flow Solver. In *Proceedings of NIC Symposium*, pages 349–355, 24-25 February 2010.
- [16] A. Bosco, B. Reinartz, and R. Boyce. Experimental and numerical analysis of an hypersonic compression corner for testing the prediction capability of a Reynolds Stress Model. In *8th International ERCOFTAC Symposium on Engineering Turbulence Modelling and Measurements, Marseille*, 9-11 June 2010.
- [17] A. Bosco, B. Reinartz, and S. Müller. Differential Reynolds Stress Model and grid adaptation for hypersonic double wedge simulations. In *6th International Symposium on Turbulence, Heat and Mass Transfer, Rome*, 14-18 September 2009.
- [18] A. Bosco, B. Reinartz, and S. Müller. Computation of hypersonic shock boundary layer interaction on a double wedge using a differential Reynolds Stress Model. In *27th International Symposium on Shock Waves, St. Petersburg*, 19-24 July 2009.
- [19] A. Bosco, B. Reinartz, S. Müller, L. Brown, and R. Boyce. Reynolds stress modeling for hypersonic flow. In *Proceedings of the iTi Conference in turbulence 2010, 19-22 September Bertinoro*, Progress in Turbulence. Springer, to be published.
- [20] F. Bramkamp. *Unstructured h-Adaptive Finite-Volumes Schemes for Compressible viscous Fluid Flow*. PhD thesis, RWTH Aachen, 2003.
- [21] F. Bramkamp, P. Lamby, and S. Müller. An adaptive multiscale finite volume solver for unsteady and steady state flow computations. *Journal of Computational Physics*, 197:460–490, 2004.
- [22] F. D. Bramkamp, B. Gottschlich-Müller, M. Hesse, Ph. Lamby, S. Müller, J. Ballmann, K.H. Brakhage, and W. Dahmen. H-Adaptive Multiscale Schemes for Compressible Navier-Stokes Equations-Polyhedral Discretization, Data Compression and Mesh Generation. In *Flow Modulation and Fluid-Structure-Interaction at Airplane Wings*, volume 84 of *Numerical Notes on Fluid Mechanics*, pages 125–204. Springer, 2003.
- [23] K. Brix, S. S. Mogosan, S. Müller, and G. Schieffer. Parallelisation of multiscale-based grid adaptation using space-filling curves. In F. Coquel, Y. Maday, S. Müller, M. Postel, and Q. H. Tran, editors, *European Series in Applied and Industrial Mathematics*, volume 29, pages 108–129, 2009.
- [24] L. Brown. Intrinsic three-dimensionality of laminar hypersonic shock wave/ boundary layer interactions. Number AIAA 2009-7205. 16th AIAA-DLR/DGLR International Space Planes and Hypersonic Systems and Technologies Conference, October 2009.

-
- [25] D. R. Buttsworth. Assessment of effective thermal product of surface junction thermocouples on millisecond and microsecond time scales. *Experimental Thermal and Fluid Science*, (25):409–420, 2001.
- [26] G. V. Candler, N. Ioannis, and M. S. Holden. Computational analysis of hypersonic laminar viscous-inviscid interactions. In *Aerospace Sciences Meeting and Exhibit*, number 2000-0532. AIAA, 2000.
- [27] D. R. Chapman, D. M. Kuehn, and H. K. Larson. Investigation of separated flow in supersonic and subsonic streams with emphasis on the effect of transition. Technical Report TN-3869, NASA, 1957.
- [28] A. Cohen, S. M. Kaber, S. Müller, and M. Postel. Fully Adaptive Multiresolution Scheme for Conservation Law. *Mathematics of Computation*, 72(241):183–225, 2003.
- [29] G. T. Coleman and J. L. Stollery. Heat transfer from hypersonic turbulent flow at a wedge compression corner. *J. Fluid Mech.*, 56(4):741–752, 1972.
- [30] T. Coratekin. *Numerical Simulation of Turbulent Shock/Boundary-Layer Interactions in Hypersonic Flows*. PhD thesis, RWTH Aachen, 2000.
- [31] T. Coratekin, J. van Keuk, and J. F. Ballmann. Performance of Upwind Schemes and Turbulence Models in hypersonic Flows. *AIAA Journal*, 42(5):945–957, 2004.
- [32] A. G. Dann. *Boundary Layer Separation in Hypersonic Ducted Flows*. PhD thesis, The University of Queensland, 2009.
- [33] M. Delanaye. *Polynomial Reconstruction Finite Volume Schemes for the Compressible Euler and Navier-Stokes Equations on Unstructured Adaptive Grids*. PhD thesis, Université de Liège, 1996.
- [34] J. Détery and J. P. Dussauge. Some physical aspects of shock wave/boundary layer interactions. *Shock Waves*, 19:453–465, 2009.
- [35] J. Delery and J. G. Marvin. *Shock-wave boundary layer interactions*. AGARDograph, 1986.
- [36] D. S. Dolling. Fifty Years of Shock-Wave/Boundary-Layer Interaction Research: What Next? *AIAA J.*, 39(8):1517–1531, 2001.
- [37] M. C. Druguet, G. V. Candler, and I. Nemeplis. Effect of Numerics on Navier-Stokes Computations of Hypersonic Double-Cone Flows. *AIAA J.*, 43(3):616–623, 2005.

- [38] J. P. Drummond, C. E. Cockrell Jr., G. L. Pellett, G. S. Diskin, A. H. Auslender, R. W. Guy R. J. Exton, J. C. Hoppe, R. L. Puster, R. C. Rogers, C. A. Trexler, and R. T. Volland. Hypersonic Airbreathing Propulsion - An Aerodynamics, Aerothermodynamics, and Acoustic Competency White Paper. Technical Report TM-2002-211951, NASA, 2002.
- [39] B. Edney. Anomalous heat transfer and pressure distribution on blunt bodies at hypersonic speeds in the presence of an impinging shock. Technical Report FFA Report 115, Aeronautical Research Institute of Sweden, Stockholm, 1968.
- [40] J. R. Edwards and S. Chandra. Comparison of Eddy Viscosity-Transport Turbulence Models for Three-Dimensional, Shock-Separate Flows. *AIAA J.*, 34:756–763, 1996.
- [41] B. Eisfeld. Implementation of Reynolds stress models into the DLR-FLOWer code. Technical Report IB 124-2004/31, DLR, December 2004.
- [42] B. Eisfeld. Computation of Complex Compressible Aerodynamic Flows with a Reynolds Stress Turbulence Model. In G. Rapin G. Lube, editor, *Int. Conference on Boundary and Interior Layers*, 2006.
- [43] B. Eisfeld and O. Brodersen. Turbulence Modelling and Stress Analysis for the DLR-F6 Configuration. In *23rd AIAA Applied Aerodynamics Conference*, number 2005-4727, June 2005.
- [44] G. M. Elfstrom. Turbulent hypersonic flow at a wedge-compression corner. *J. Fluid. Mech.*, 53(1):113–127, 1972.
- [45] H. H. Fernholz and P. J. Finely. *A Critical Compilation of Compressible Turbulent Boundary Layer Data*. Number No. 223. AGARDograph, 1977.
- [46] J. Frölich, D. von Terzi, E. Séverac, and R. Vaibar. Hybrid LES/RANS simulations: State of the Art and Perspectives. In *8th International Symposium on Engineering Turbulence Modelling and Measurements*, 2010.
- [47] C. Fureby, N. Alin, N. Wikström, S. Menon, N. Svanstedt, and L. Persson. Large-Eddy Simulation of High-Reynolds-Number Wall-Bounded Flows. *AIAA J.*, 42(3), 2004.
- [48] U. Gaisbauer, B. Weigand, and B. Reinartz. Research Training Group GRK 1095/1: Aero-Thermodynamic Design of a Scramjet Propulsion System. In *Proceedings of the 18th ISABE Conference*. International Symposium of Air-Breathing Engines (ISABE), 2007.
- [49] W. K. George. *Lectures in Turbulence for the 21th Century*. 2008.
- [50] U. Goldberg. Hypersonic Flow Heat Transfer Prediction Using Single Equation Turbulence Models. *J. Heat Transfer*, 123, 2001.

-
- [51] B. Górecki. Numerical simulation of hydrogen-air mixing in a hypersonic non-equilibrium flow. Bachelor Thesis, Warsaw University of Technology, 2010.
- [52] J. Häberle and A. Guelhan. Internal Flowfield Investigation of a Hypersonic Inlet at Mach 6 with Bleed. *J. Propul. and Power*, 23(5):1007–1017, September-October 2007.
- [53] J. Häberle and A. Gülhan. Experimental Investigation of a Two-Dimensional and Three-Dimensional Scramjet Inlet at Mach 7. *J. Propul. Power*, 24(5):1023–1034, 2008.
- [54] J. Häberle and A. Gülhan. Investigation of Two-Dimensional Scramjet Inlet Flowfield at Mach 7. *J. Propul. Power*, 24(3):446–459, 2008.
- [55] A. Hadjadj and J. Dussauge. Shock wave boundary layer interaction. *Shock Waves*, 19:449–452, 2009.
- [56] V. Hämäläinen. Implementing an explicit algebraic Reynolds stress model into the three-dimensional Finflo flow solver. Technical Report Report B-52, Helsinki University of Technology, 2001.
- [57] H. Heiser and T. Pratt. *Hypersonic Airbreathing Propulsion*. AIAA, 1994.
- [58] A. Hellsten. New Advanced $k-\omega$ Turbulence Model for High-Lift Aerodynamics. *AIAA J.*, 43(9), 2005.
- [59] M. S. Holden. Boundary-Layer Displacement and Leading-Edge Bluntness Effects on Attached and Separated Laminar Boundary Layers in a Compression Corner. Part 11: Experimental Study. *AIAA Journal*, 9(1):84–93, 1971.
- [60] P. G. Huang, P. Bradshaw, and T. J. Coakley. Turbulence Models for Compressible Boundary Layer. *AIAA J.*, 32(4), 1994.
- [61] C. Jessen, M. Vetter, and H. Grönig. An experimental investigation of surface thermometry and heat flux. *Z. Flugwis. Weltraumforsch.*, (17):73–81, 1993.
- [62] R. M. Kirchhartz. *Upstream Wall Layer Effects on Drag Reduction with Boundary Layer Combustion*. PhD thesis, The University of Queensland, 2009.
- [63] M. Koschnitzki. Strömungsbeeinflussung und Strömungs-Struktur-Wechselwirkung an Tragflügeln. Studienarbeit RWTH Aachen, 2008.
- [64] M. Krause. *Numerical Analysis of Transition Effects for Hypersonic Intake Flows*. PhD thesis, RWTH Aachen University, 2009.
- [65] M. Krause and J. Ballmann. Application of a Correlation-Based Intermittency Transition Model for Hypersonic Flows. In *DGLR Kongress 2008*, 2008.

- [66] M. Krause, B. Reinartz, and J. Ballmann. Numerical Computations for Designing a Scramjet intake. In *ICAAS 2006 25th International Congress of the Aeronautical Sciences*, 2006.
- [67] R. M. Krek and P. A. Jacobs. Shock tube and nozzle calculations for equilibrium air. Technical Report 2/93, The University of Queensland, 1993.
- [68] N. Kroll, C. C. Rossow, K. Becker, and F. Thiele. The MEGAFLOW Project. *Aerospace Science and Technology*, 4(4):223–237, 2000.
- [69] S. Kumar. *Numerical Simulation of Chemically Reactive Hypersonic Flows*. PhD thesis, RWTH Aachen, 2006.
- [70] M. I. Kussoy and C. C. Horstman. An experimental documentation of a hypersonic shock-wave turbulent boundary layer interaction flow: with and without separation. Technical report, NASA, 1975.
- [71] P. Lamby. *Parametric Multi-Block Grid Generation and Application to Adaptive Flow Simulations*. PhD thesis, RWTH Aachen University, 2007.
- [72] B. E. Launder, G. J. Reece, and W. Rodi. Progress in the development of a Reynolds-stress turbulence closure. *J. Fluid. Mech.*, 68:537–566, 1975.
- [73] S. G. Mallinson, S. L. Gai, and N. R. Mudford. The interaction of a shock wave with laminar boundary layer at a compression corner in high-enthalpy flows including real gas effects. *J. Fluid Mech.*, 342:1–35, 1997.
- [74] W. E. Meador and M. K. Smart. Reference Enthalpy Method Developed from Solutions of the Boundary-Layer equations. *AIAA J.*, 43(1):135–139, 2005.
- [75] D. J. Mee. Boundary-Layer Transition Measurements in Hypervelocity Flows in a Shock Tunnel. *AIAA J.*, 40(8):1542–1548, 2002.
- [76] D. J. Mee. Dynamic Calibration of Force Balances. Technical Report Research report 2002/06, The University of Queensland, 2002.
- [77] F. Menter and R. Langtry. A Correlation-Based Transition Model Using Local Variables Part 1 - Model Formulation. In *Proceedings of ASME Turbo Expo 2004 Power for Land, Sea and Air*, 2004.
- [78] F. R. Menter. Two-Equation Eddy-Viscosity Turbulence Models for Engineering Applications. *AIAA J.*, 32(8):1598, 1605 1994.
- [79] T. Neuenhahn. *Investigation of the shock wave boundary layer interaction of scramjet intake flows*. PhD thesis, RWTH Aachen, 2010.

- [80] T. Neuenhahn and H. Olivier. Influence of the wall temperature and the entropy layer effects on double wedge shock boundary layer interactions. In *14th AIAA/AHI Space Planes and Hypersonic Systems and Technologies Conference*, number AIAA 2006-8136, 2006.
- [81] R. D. Neumann. Special Topics in Hypersonic Flow. In *Aerodynamic Problems of Hypersonic Vehicles*. AGARD Lecture Series no. 42, 1972.
- [82] T. T. Q. Nguyen, M. Behr, and B. U. Reinartz. Numerical Investigation of Compressible Turbulent Boundary Layer Over Expansion Corner. In *16th AIAA/DLR/DGLR International Space Planes and Hypersonic Systems and Technologies Conference*, number AIAA 2009-7371, Bremen, October 2009.
- [83] J. Olejniczak, M. J. Wright, and G. V. Candler. Numerical study of inviscid shock interactions on double-wedge geometries. Technical Report UMSI 97/15, University of Minnesota, 1997.
- [84] M. E. Olsen, R. P. Lillard, and T. J. Coakley. The Lag Model Applied to High Speed Flows. Technical Report NAS 05-005, NASA, 2005.
- [85] G. Park, S. L. Gai, and A. J. Neely. Heat transfer measurements on a circular cylinder in hypersonic flow. In *16th Australasian Fluid Mechanics Conference*, 2007.
- [86] S. Pirozzoli and F. Grasso. Direct numerical simulation of impinging shock wave/turbulent boundary layer interaction at $M=2.25$. *Physics of Fluids*, 18, 2006.
- [87] B. U. Reinartz. Performance analysis of a 3D scramjet intake. In *Proceedings of the 26th ICAS Conference*. International Congress of the Aeronautical Sciences, 2008.
- [88] B. U. Reinartz, J. Ballmann, and R. R. Boyce. Numerical Investigation of Wall Temperature and Entropy Layer Effects on Double Wedge Shock / Boundary Layer Interaction. In *Proceedings of 14th AIAA International Space Planes and Hypersonic Systems and Technologies Conference*, number 2006-8137, 2006.
- [89] M. Ringuette, M. Wu, and M. P. Martin. Low Reynolds Number Effects in a Mach 3 Shock/Turbulent-Boundary-Layer Interaction. *AIAA J.*, 46(7), 2008.
- [90] C. C. Rossow and N. Kroll. Numerical Simulations - Complementing Theory and Experiment as the Third Pillar in Aerodynamics. In *Hermann Schlichting - 100 Years*, volume 102 of *Notes on Numerical Fluid Mechanics and Multidisciplinary Design Vol 102*. Springer, 2009.
- [91] J. C. Roy and F. G. Blottner. Review and assessment of turbulence models for hypersonic flows. *Progress in Aerospace Sciences*, 42:469–530, 2006.

- [92] R. Rudnik. Untersuchung der Leistungsfähigkeit von Zweigleichungs-Turbulenzmodellen bei Profilmströmungen. Forschungsbericht 97-49, Deutsche Zentrum für Luft- und Raumfahrt, 1997.
- [93] C. L. Rumsey, B. A. Patterson Reif, and T. B. Gatski. Arbitrary Steady-State Solutions with the k - ϵ Model. *AIAA J.*, 44(7):1586–1592, 2006.
- [94] T. Rung and F. Thiele. Computational modelling of complex boundary layer flows. In *Proc. 9th Intern. Symposium on Transport Phenomena in Thermal-Fluid Engineering, Singapore*, pages 321–326, 1996.
- [95] G. Schieffer, J. Ballmann, and M. Behr. Validation of advanced turbulence models in QUADFLOW. In *Turbulence, Heat and Mass Transfer 6*, September 2009.
- [96] G. Schieffer, M. Engel, L. Reimer, M. Behr, and H.-G. Reimerdes. *Simulation of the fluid-structure interaction between an elastic panel and an oblique impinging shock*, volume Annual Report of the SFB/TRR 40, pages 201–214. N. Adams and B. Weigand and R. Radespiel and T. Sattelmayer and W. Schröder, 2009.
- [97] G. Schieffer, R. Saurya, F. D. Bramkamp, M. Behr, and J. Ballmann. An Adaptive Implicit Finite Volume Scheme for Compressible Turbulent Flows about Elastic Configurations. In *Summary of Flow Modulation and Fluid-Structure Interaction Findings*, volume 109 of *Notes on Numerical Fluid Mechanics and Multidisciplinary Design*. Springer Verlag Berlin Heidelberg, 2010.
- [98] H. Schlichting. *Boundary Layer Theory*. McGraw-Hill, 1979.
- [99] D. L. Schultz and T. V. Jones. *Heat transfer measurements in short-duration hypersonic facilities*. Number No. 165. AGARDograph, 1973.
- [100] G. S. Settles and L. J. Dodson. Hypersonic Shock/Boundary-Layer Interaction Database. In *AIAA 22nd Fluid Dynamics, Plasma Dynamics and Laser Conference*, 1991.
- [101] K. Sihna, K. Mahesh, and G. V. Candler. Modeling the Effect of Shock Unsteadiness in Shock/Turbulent Boundary-Layer Interaction. *AIAA J.*, 43(3), 2005.
- [102] J. Smagorinsky. General circulation experiments with the primitive equations: I. The basic experiment. *Mon. Weather Rev.*, 91:99–164, 1963.
- [103] A. L. Smith. *Multiple component force measurement in short duration test flows*. PhD thesis, The University of Queensland, 1993.
- [104] A. L. Smith. *Multiple Component Force Measurements in Short Duration Test Flows*. PhD thesis, The University of Queensland, 1999.

-
- [105] A. J. Smits, M. P. Martin, and S. Girimaji. Current Status of Basic Research in Hypersonic Turbulence. In *39th AIAA Fluid Dynamics Conference and Exhibit*, January 5-8 2009.
- [106] P. R. Spalart and S. R. Allmaras. A One-Equation Turbulence Model for Aerodynamic Flows. Number 92-0439, 1992.
- [107] C. G. Speziale, S. Sarkar, and T. B. Gatski. Modelling the pressure-strain correlation of turbulence: an invariant dynamical system approach. *J. Fluid Mech.*, 227:245–272, 1991.
- [108] H. Tennekes and J. Lumley. *A First Course in Turbulence*. MIT Press, Cambridge, Massachusetts, 1972.
- [109] J. C. T. Turner. *An Experimental Investigation of Inlet Fuel Injection in a Three-Dimensional Scramjet Engine*. PhD thesis, The University of Queensland, 2010.
- [110] J van Keuk. *Numerische Analyse und Bewertung von Upwind-Verfahren für die Anwendung auf mehrdimensionale Über- und Hyperschallströmungen von Gasen*. PhD thesis, RWTH Aachen, 2000.
- [111] V. Venkataktishnan. Convergence of Steady State Solutions of the Euler Equations on Unstructured Grids with Limiters. *J. Comput. Phys.*, 118:120–130, 1995.
- [112] Y. Wada and M. S. Liou. 32nd Aerospace Science Meeting and Exhibit. In *AIAA Paper 94-0083*, number AIAA Paper 94-0083, January 1994.
- [113] D. C. Wilcox. *Turbulence Modelling for CFD*. DCW Industries Inc., 1993.
- [114] D. C. Wilcox. Formulation of the k - ω Turbulence Model Revisited. *AIAA J.*, 46(11):2823–2838, 2008.
- [115] C. Windisch. Numerische Simulation von Hochgeschwindigkeitsströmungen im Nichtgleichgewicht. Master's thesis, RWTH Aachen, 2009.
- [116] M. Wu and M. P. Martin. Direct Numerical Simulation of Supersonic Turbulent boundary Layer over a Compression Ramp . *AIAA J.*, 45(4), 2007.

Curriculum Vitae

Personal Information

Name	Arianna Bosco
Date of birth	11th of February 1983
Place of birth	Cuneo (Italy)

School Education

1989 - 1994	Primary School: Scuola Elementare Statale 'Gianni Rodari' (Italy)
1994 - 1997	Middle School: Scuola Media Statale 'Sandro Pertini' (Italy)
1997 - 2002	High School: Liceo Scientifico Statale 'Leonardo Cocito' (Italy) degree: Diploma

University Education

09/2002 - 10/2005	Bachelor of Science in Model and Systems Engineering at Università di Roma Tor Vergata (Italy) degree: Bachelor Degree (Laurea Triennale)
09/2005 - 07/2007	Master of Science in Mathematical Engineering at Politecnico di Torino (Italy), degree: Master Degree (Laurea Specialistica)

Career

12/2007 - today	PhD Student at the Aachen Institute for Advanced Study in Computational Engineering Science of Prof. Behr, RWTH University, Germany.
10/2009 - 04/2010	Occupational Trainee at the Centre for Hypersonics, The University of Queensland, Australia

Aachen, 31th of January 2010
Arianna Bosco